Laser-plasma interaction with ultra-short laser pulses

Inaugural-Dissertation

zur

Erlangung des Doktorgrades der

Mathematisch-Naturwissenschaftlichen Fakultät

der Heinrich-Heine-Universität Düsseldorf

vorgelegt von

Ralph Jung

aus Wermelskirchen

Mai 2007

Aus dem Institut für Laser- und Plasmaphysik
der Heinrich-Heine-Universität Düsseldorf

Gedruckt mit Genehmigung der
Mathematisch-Naturwissenschaftlichen Fakultät der
Heinrich-Heine-Universität Düsseldorf.

Referent:	Prof. Dr. O. Willi
Koreferenten:	Prof. Dr. K.-H. Spatschek
	Prof. Dr. H. Ruhl

Tag der mündlichen Prüfung: 16. November 2007

Zusammenfassung

Mit der Erfindung der *Chirped Pulse Amplification* (CPA) Technik im Jahre 1985 wurde es möglich, die Intensität ultra-kurzer Laserpulse extrem zu steigern. So stehen heutzutage an internationalen Groß-Laboratorien bereits Laser mit Leistungen von Petawatt zur Verfügung. An Universitäten können ultra-kurze Pulse von nur wenigen Schwingungen des optischen Feldes mit Hilfe kompakter "Table-Top"-Systeme auf mehrere zehn Gigawatt verstärkt werden. Diese Pulse bieten ideale Bedingungen für die Untersuchung ultra-schneller Prozesse.
In dieser Arbeit wurde ein Puls mit einer Länge von unter 10 fs in einen Gasjet unter hohem Druck fokussiert. Im Fokus wurden Intensitäten von über 10^{16} W/cm^2 erreicht. Hierbei kommt es zur Feldionisation des Materials. In einem "Pump-Probe"-Experiment wurde die vom Laser induzierte Ionisationsfront und der entstehende Plasmakanal mittels Schattenbildern und Interferometrie untersucht. Erstmals konnte das Voranschreiten der Front und die Entstehung des Kanals optisch mit einer Genauigkeit von weniger als 10 fs aufgelöst werden. Die Resultate stehen in hervorragender Übereinstimmung mit dreidimensionalen, numerischen Particle-In-Cell (PIC) Simulationen.

In einer weiteren Messung wurde die Propagation und Filamentierung eines Laser-produzierten Elektronenstrahls durch ein überkritisches Plasma untersucht. In diesem Experiment, ausgeführt am VULCAN Petawatt Laser des Rutherford Appleton Laboratoriums (UK), standen Intensitäten von $5 \cdot 10^{20}$ W/cm^2 zur Verfügung. Im Fokus des Lasers wurden Elektronen auf Energien von mehreren MeV beschleunigt. Der entstehende Elektronenstrahl propagierte daraufhin durch ein Plasma über eine Länge von mehreren hundert Mikrometern. Die Struktur des Strahls wurde anhand des an der Rückseite des verwendeten Targets emittierten Lichts beobachtet. Hierbei konnte gezeigt werden, dass der Strahl stark filamentiert. Die beobachtete ringförmige Anordnung der Filamente wurde mit Hilfe von 3D Particle-In-Cell Simulationen bestätigt.

Abstract

With the invention of the *Chirped Pulse Amplification* (CPA) technique in 1985, it became possible to amplify ultra-short laser pulses to high intensities. Nowadays, at international laboratories lasers are available that produce pulses of petawatt power. On an university's scale, however, ultra-short pulses containing just a few optical cycles can routinely be amplified to several tens of Gigawatt using compact "table-top" systems. These pulses provide ideal conditions for the study of ultra-fast processes. In this thesis, laser pulses of sub-10-fs in duration were focused into a gas jet of high pressure. In the focus, intensities above 10^{16} W/cm^2 have been achieved. This leads to optical field-ionization of the material. In a "pump-probe" experiment, the ionization front and the plasma channel generated were studied by optical shadowgraphy and interferometry. For the first time the propagation of the front and the channel evolution has been resolved optically with sub-10-fs time resolution. The results are in excellent agreement with three-dimensional Particle-In-Cell numerical simulations.

In another measurement, the propagation and filamentation of a laser-produced electron beam through an over-dense plasma were studied. In this experiment, conducted at the VULCAN Petawatt laser at the Rutherford Appleton Laboratory (UK), intensities of $5 \cdot 10^{20}$ W/cm^2 were obtained. In the focus of the laser, electrons have been accelerated to energies of several MeV. The electron beam generated propagated through a plasma of several hundreds of microns in length. The structure of the beam was observed by imaging the light produced at the rear side of the target. It has been found that the beam undergoes strong filamentation. Particularly a ring-like structure has been observed which has also been found in 3D Particle-In-Cell simulations.

Diese Arbeit wurde gefördert durch die
Gründerstiftung zur Förderung von Forschung und wissenschaftlichem
Nachwuchs an der Heinrich-Heine-Universität Düsseldorf
(*Düsseldorf Entrepreneurs Foundation*)

Contents

1. Introduction

The topic of this thesis is the laser-plasma interaction with ultra-short laser pulses. Particularly the ionization dynamics and subsequent plasma channel evolution as well as the filamentation of a relativistic electron beam in an over-dense plasma were studied. These experiments have become possible with recent advances in laser technology, especially in terms of the increase in light intensity. Figure 1.1 depicts schematically the development of focused laser intensity over the years from the invention of the laser. The quiver energy of a free electron exposed to the laser field is also indicated. The rapid increase in intensity in the sixties was supported by the invention of the technique of "Q-switching" [1] and "mode-locking" [2]. This also led to a decrease of pulse duration which dropped from microseconds, the typical duration of flashlamp discharges, to nanoseconds and picoseconds respectively. Soon an intensity level was reached in which nonlinear effects became crucial to optics and amplifiers. Particularly the intensity-dependent nonlinear index of refraction of the material, first expe-

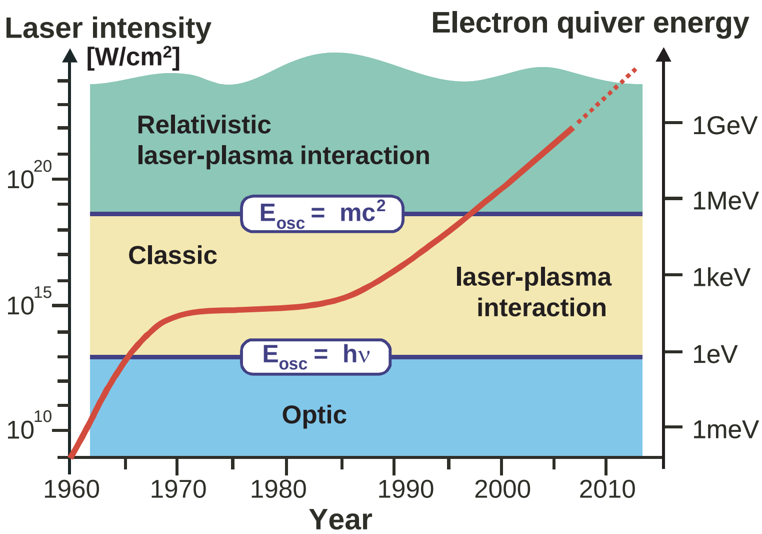

Figure 1.1: Progress in intensities and electron quiver energies since the invention of the laser in 1960 [3].

rimentally demonstrated in 1964 [4], distorted the wavefront of the laser beam. If this distortion becomes too large, beam filamentation and self-focusing occurs and causes damage in the laser chain. This problem was solved by the invention of a technique called CHIRPED PULSE AMPLIFICATION (CPA) by Gérard Mourou *et. al.* in 1985 [5, 6]. Their idea was to "stretch" the pulse in time by controlled dispersion of its spectral components. Stretching reduces the intensity while the energy remains constant. So the beam distortion can be kept below a critical value. (Quantitatively this is expressed by what is called the "B-integral" which measures the accumulation of the wavefront distortion due to the nonlinear refractive index). After the stretched pulse is amplified, it is "re-compressed" by an inverse dispersive process. So the energy of a pulse can be increased by 6 to 12 orders of magnitude while the pulse duration is kept similar to that of the seed [3]. Nowadays, lasers are available which produce pulses of sub-10-fs duration that could be fed into CPA amplifier systems. This extremely short durations of just a few optical cycles became possible with technological advances in mode-locking technique [7]. So the combination of femtosecond-oscillator, pulse stretcher, amplifier and compressor is the standard set-up of today's high-power laser systems. On a laboratory-scale, "table-top"-size, high-power lasers produce routinely pulses of several hundreds of Terawatt at pulse durations of about 20 fs. The final pulse duration is, however, limited to about 20 fs due to limited spectral bandwidth of the amplifier material (commonly Ti:sapphire) and gain narrowing reasons. In combination with extra compression schemes, such as a combination of a gas filled hollow fibre and a chirped mirror compressor, however, nowadays few-cycle pulses at a power level of several hundred Gigawatt are available. In the focus, intensities of the order of 10^{18} W/cm^2 [8] are obtained.

In addition to the attempt to generate pulses which contain just about one optical cycle, super-high-power lasers up to the petawatt level (10^{15} W) have been developed with the help of the CPA technique. (For comparison: the power of the sun light which is incident on earth is of the order of 170 PW). Nowadays, ultra-high intensity sources which produce focused intensities in the range of $I \sim 10^{18} - 10^{21}$ W/cm^2 are routinely available. With it, the new regime of relativistic laser-plasma interaction has attracted great interest of the scientific community. For example, it allows particles to be accelerated to relativistic energies using the PONDEROMOTIVE POTENTIAL of the pulse. This has opened many applications in science, medicine and technology. Simultaneously, ultra-short laser pulses (i.e. $\tau_L < 1$ ps) with durations close to the optical limit of just a few cycles of the carrier wave (i.e. a few fs), allow experimentalists the study of highly transient processes which have only been made accessible recently. Milestones in this ultra-fast scientific context are, for example, the generation of coherent XUV radiation using higher harmonics of the laser fundamental, the production of atto-second pulses, and the observation of inner-molecular transitions [9, 10, 11, 12, 13, 14, 15].

In the first part of this thesis, a 800 nm Titan-Sapphire laser system producing sub-10-fs laser pulses containing few hundreds of micro-Joule was used. In the experiment, the pulses were focused into a neutral jet of various gases. Due to a very high intensity contrast ($\sim 10^8$), no pre-plasma was present prior to the main interaction of the laser pulse with the target material. This and the ultra-short pulse duration make the experimental separation of laser-induced ionization process from the subsequent plasma dynamics possible. In particular, as will be shown, though the ponderomotive potential of the laser pulse is about 600 eV, almost none of this energy is transferred into kinetic electron motion of the plasma during such a short time. Both inverse bremsstrahlung and ponderomotive heating are reduced to such an extend that they effectively can be ignored. Nonlinear effects such as $\vec{j} \times \vec{B}$-heating are of minor importance at an intensity of 10^{16} W/cm^2. Consequently, a highly ionized but low temperature plasma is generated. The evolution of this plasma was studied using optical probing. For these studies, an optical probing system was developed and an ultra-short probe pulse at variable time delay generated. For the first time, snapshots and time-series of the ionization front and the subsequent evolution of a plasma channel were recovered with sub-10-fs temporal resolution.

One of the goals of this work was to achieve the highest possible resolution. Spatially, a close to diffraction limited resolution of ~ 1 µm was obtained. The temporal resolution of such a pump-probe experiment is, however, limited by the pulse duration of the probe. Limited probe pulse duration always causes a smearing of the object along the direction of motion is seen in the images. This effect is well known as motion blur. This is particularly important when imaging an object that is moving at a velocity close to light speed. In this experiment, the spatial resolution in the direction of motion of the propagation front could be increased to ~ 3 µm and is hence of the order of the diffraction limit of the imaging optics.

Recently, Gizzi *et. al.* have reported time resolved interferograms of laser induced ionization of helium using 130 fs probe pulses [16]. They found a significant loss of visibility in fringe contrast and spatial resolution. This effect was called PULSE TRANSIT EFFECT. In this thesis, in contrast, no smearing of fringe contrast has been observed. Furthermore, it was possible to correlate the pulse duration of the probe pulse *a posteriori* with the contrast transition been observed in focused shadowgrams. A duration of sub-10-fs has been confirmed.

The experimental observations were analyzed with the help of 3D-Particle-In-Cell (PIC) simulations using the Plasma Simulation Code (PSC) written by Hartmut Ruhl [17]. These simulations include the ionization dynamics and the influence of collisions. Important plasma parameters such as the electron temperature have been obtained from the numerical data. A good agreement between the experimental observations and the simulations has been achieved.

In the second part of this thesis, the transport and filamentation of a high-energetic (several tens of MeV) laser-generated electron beam through an over-dense plasma ($15 - 30\ n_{cr}$) were studied experimentally. The propagation of laser-accelerated, high-energetic electrons through an over-dense plasma is of fundamental importance to the FAST IGNITOR concept relevant for laser fusion as well as astrophysics. The experiment was performed at the VULCAN Petawatt laser at the Rutherford Appleton Laboratory (UK), a "large scale" system designed to deliver laser pulses with an energy of 500 J and a pulse length of 500 fs.

Today, there are basically two concepts for controlled thermonuclear fusion as an almost un-exhaustable energy reservoir. The first one is the magnetic confinement fusion approach; here a dilute ($\sim 10^{14}$ cm^{-3}) deuterium-tritium plasma is heated and magnetically confined for such a long time that a net energy gain is obtained by initializing the thermonuclear reaction process

$$\mathrm{D} + \mathrm{T} \rightarrow \mathrm{He} + \mathrm{n} + 17.6\ \mathrm{MeV}. \tag{1.1}$$

Thus, the reactants are fused to an alpha particle (helium). The total kinetic energy of 17.6 MeV is distributed between the charged helium particle with an energy of 3.5 MeV and a neutron with an energy of 14.1 MeV. Besides many other possible fusion reactions with equivalent or even higher energy gain, the D-T reaction is the most feasible one because of its relatively large reaction cross section at accessible temperatures (about 10 to 40 keV). In huge fusion machines such as Tokamaks, several tens of m^3 of plasma are magnetically confined and thermally isolated by magnetic fields. Recently, the International Thermonuclear Experimental Reactor (ITER) has been commissioned. The machine, which will be built in Cadarache (France), is designed to confine more than 800 m^3 of plasma.

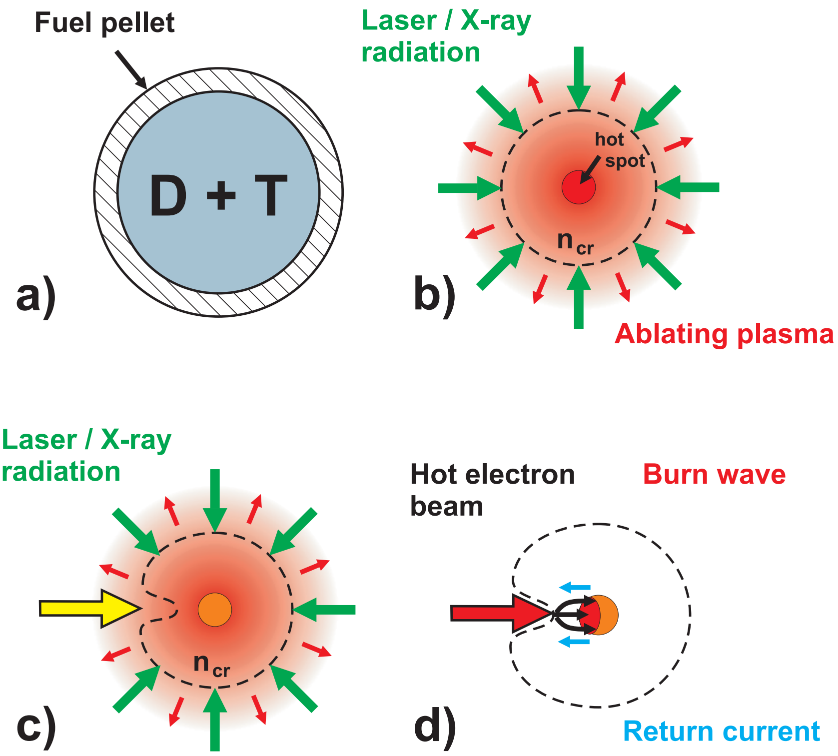

Figure 1.2: Schematic of "classical" inertial fusion energy concept and fast ignition. a) A fuel pellet (schematically) consists of a micro-balloon filled with liquid or a cryogenic mixture of deuterium and tritium. b) The fuel is compressed to high densities by the ablating plasma, and the core is heated hydrodynamically using well-timed shock waves. In the final stage, a hot spot is in pressure balance with the surrounding plasma which is colder but denser (isobaric). After ignition, a radial burn wave propagates through the surrounding fuel. c) In the fast ignitor approach, however, the fuel is compressed uniformly (isochoric) and an intense laser pulse bores a hole into the plasma corona. So the critical density is pushed closer to the fuel center. d) A separate ignitor pulse is focused in the channel and generates high currents of energetic electrons. Depositing their energy in the core, the "spark" is rapidly heated and the fusion process locally ignited. The distance that the electrons have to overcome is of the order of 100 µm.

The aim is to demonstrate a performance in which ten times more fusion power is produced than is consumed by heating.

In the second approach, the fuel is confined by inertia. A pellet containing deuterium and tritium is externally compressed and heated by X-rays, particles or laser radiation. At the moment, various techniques exist such as the Z-pinch [18, 19], heavy-ion beams [20] and direct and indirect laser drive [21]. In this thesis, however, we concentrate on the laser-based inertial confinement fusion (ICF) approach.

ICF-programs using intense lasers attracted public attention when Nuckolls published an article in NATURE magazine in 1972 [22]. Following this scheme, a fuel pellet of only the dimension of millimeters in diameter is compressed to extreme densities by several laser beams which are symmetrically focused onto its shell. Due to the fact that laser radiation of a given wavelength, λ, can only penetrate into a plasma up to a critical electron density, n_e [cm^{-3}] $\approx 1 \cdot 10^{21}/(\lambda\ [\mu\text{m}])^2$, a part of the laser energy is absorbed at the outer shell of the fuel. So the surface material is rapidly heated and ablated. As a result of momentum conservation, the inward push of ablating plasma makes the pellet implode. This configuration is called DIRECT DRIVE since the driving lasers are directly focused onto the ablator shell. For this, a high uniformity of the driver beams on the surface is required. In the INDIRECT DRIVE scheme, the fuel pellet is placed in a hohlraum of material with high atomic number such as gold. The beams are incident on the inner walls of the hohlraum and the laser energy is first converted to X-rays. The intense radiation field of X-rays inside the hohlraum drives the ablator. This configuration is advantageous because of its more homogeneous radiation field and a reduced sensitivity of the implosion to hydrodynamic instabilities [23]. In the simplest configuration, however, the target is uniformly compressed and the fuel will fuse homogeneously over the volume when densities of the order of 1000 g/cm^3 and temperatures of the order of 10 keV are reached. As volume ignition requires an extreme amount of laser energy (of the order of 10^6 MJ), the "HOT-SPOT" ignition scenario was developed, where only a small fraction of fuel is brought to high temperatures by well-timed shock waves [24]. Here a hot inner region is surrounded by colder but denser fuel plasma, both being in a pressure balance (isobaric model). After a self-sustaining burn wave is generated in the center, the fusion reaction propagates outwards through the surrounding fuel. Calculations predict a significant higher gain with respect to volume ignition, but still Mega-Joule of driver energy are required [25]. As the core has to be compressed to densities of ~ 1000 g/cm^3, hydrodynamic instabilities such as the RAYLEIGH-TAYLOR instability become important. These instabilities significantly reduce the effectiveness of the compression and hence reduce the energy gain [26, 27].

In 1994, Tabak proposed to use an external energy source to trigger ignition. This would relax the demands on heating and compression. In the first stage of this FAST IGNITOR scheme, the hot spot is compressed to densities of about $300-400$ g/cm^3. Then a high-intensity, ultra-short laser pulse with an intensity of $\sim 10^{19}$ W/cm^2 and a duration of about 100 ps is used to push the critical surface of the plasma corona closer to the dense core. This process is known as HOLE BORING and makes use of the high light pressure of the intense pulse [28, 29, 30]. Finally, an "ignitor laser" pulse, which is shorter (about 1 to 10 ps, limited by the disassembly time of the fuel) but more intense ($\sim 10^{20}$ W/cm^2), propagates in this channel and is stopped at the critical density. There a significant part of its energy is converted into a strong (i.e. Mega-Ampere) current of hot ($\sim$ MeV) electrons. These high energetic electrons are able to penetrate deeply into fuel and are stopped at the high compressed ($\sim 10^{25}$ cm^{-3}) core. So, according to the scenario, a part of the fuel, the "spark", is rapidly heated and ignition of the thermonuclear fuel is initiated. The particular advantages of this concept are high gain and significantly reduced requirements on driver energy (kJ instead of MJ) [31, 32]. Recently, Kodama *et. al.* have experimentally given evidence of fusion in a pre-compressed fuel using an ultra-intense, short-pulse laser when measuring the neutron yield [33]. In their experiment, a special geometry was used to shorten the distance between the implosion center and the critical surface by inserting a gold cone into the shell of about 50 µm. The cone also made the guiding of the ignitor pulse possible.

Though these first results are very encouraging, the problem of simultaneous compression and heating is still unsolved and questions concerning the transport and energy deposition of the electron beam remain unanswered. The transport of the electrons to the pre-compressed core involves currents of the order of $100 - 1000$ MA through regions of over-dense plasma. These currents exceed the critical Alfvén limit given by $J_A = 17.1\ \beta\gamma$ kA, where $\beta = v/c$ denotes the speed of the electrons normalized to light speed, and γ is the relativistic Lorentz factor of the beam [34]. The transport is only possible if return currents, formed by the thermal background electrons of the plasma, play a significant role in neutralization. Under these conditions, i.e. in presence of a large flow of fast electrons and a counter-streaming flow of cold electrons, kinetic instabilities like the WEIBEL INSTABILITY [35] can grow. 2D- and 3D-PIC simulations have clearly predicted that the transport of the relativistic electron beam will not be homogenous and filamentary structures will occur. Magnetic fields up to 100 MG will surround the filaments [28, 36]. The arrangement of the filaments propagating through the region of over-dense plasma is of great interest because it determines the amount of energy that can be deposited in the fuel. Processes such as collective stopping of the hot electrons, coalescence of the current filaments and energy dissipation due to heating of the surrounding plasma may be crucial [37, 38]. Therefore the understanding of the propagation mechanisms of the relativistic electrons through dense plasmas is essential for the success of the FI scheme.

A number of experiments investigating the propagation and filamentation of laser-produced relativistic electron beams were performed using metal and plastic foils or glass slabs [39, 40, 41, 42, 43, 44, 45]. In this thesis, in contrast to former studies, pre-heated low density foam targets were used since they offer a different approach to study electron beam transport through dense plasmas over long distances. The experimental results presented in this thesis clearly show that the electron beam undergoes strong filamentation, which was identified to be of the Weibel type. The obtained data are presented and are analyzed with the help of 3D-PIC simulations performed by A. Pukhov and S. Kiselev. Both the experiments and the 3D-PIC simulations show that the filaments organize in ring like structures. The divergence of the beam is similar to that one observed in other experiments using different targets [33, 46]. Moreover, the observations are in agreement with recent numerical simulations performed by other groups [47].

The thesis is structured as follows: First the ionization processes relevant for the understanding of the channel formation are reviewed. They are also of general importance for high-intensity laser interaction with matter because they dominate the evolution of a pre-plasma. Then the interaction of laser radiation with plasma electrons is described as it plays an important role for the energy transfer into randomized as well as directed kinetic motion of the electrons. In addition, the physics relevant for the super-high intensity interaction is described. In both experimental campaigns, data was obtained using optical diagnostics. Therefore the diagnostic is presented and performance factors are addressed. An important aspect of channel formation studies in gases, however, was the availability of an appropriate gas target. For these experiments, a special gas target was designed. It is briefly described and key parameters such as gas density and response time are given. Then the experimental results obtained on the propagation of the ionization front induced by sub-10-fs laser pulses in gases are presented. In order to interpret the data, 3D-PIC simulations were performed using the Plasma Simulation Code (PSC) written by H. Ruhl. The last chapter deals with the experiment conducted to study the electron beam filamentation. The data obtained are presented. Also here, they are interpreted with the help of 3D-PIC simulations.

2. Interaction of strong laser pulses with matter

The starting point of any laser-plasma interaction is the transition of the target material into plasma state due to the presence of the laser electric field. Experimentally, laser-induced ionization was observed shortly after the invention of the laser in the sixties already. With advances in laser technology, however, higher intensities, different wavelengths and shorter pulse durations became available. Depending on the laser parameters used, different ionization processes such as Multi-photon ionization, Above-threshold ionization and Barrier suppression ionization were discovered. The role of "nonlinear radiation forces" was investigated, what lead to what is today called ponderomotive force of a laser pulse [48]. Numerous theoretical models have been developed with the aim to quantify the ionization rates and to predict the kinetic energy of the electrons. And of course, during more than 40 years since the invention of the laser, a multitude of publications exist which cover experimental and theoretical aspects of laser-induced ionization and the role of the ponderomotive potential of a laser pulse. Particularly an overview over the various theoretical methods is given by several extensive review articles available [49, 50, 51, 52]. But even today there are many challenges and open questions left. For example, the quantum mechanical simulation of the ionization process induced by a picosecond laser pulse in which an electron is accelerated to energies up to several times of the photon energy (a process termed Above Threshold Ionization [53]) is extremely difficult despite of today's computational power [49].

In this chapter, the present standard of knowledge of the ionization process of matter is reviewed. Key results are summarized which are in particular relevant for the interpretation of the experimental data obtained in this thesis. The various ionization models are presented and the influence of the laser pulse duration is discussed. The emerge of the ponderomotive force is described as a result of the motion of an electron in a spatially inhomogeneous laser field. The non-relativistic as well as the relativistic case are considered.

2.1. Ionization processes

Multi-photon ionization

Soon after the realization of the optical laser in 1960 [54, 55, 56], the intensity of light could be increased in such a way that the field of classical optics was left behind. Various nonlinear optical effects were demonstrated experimentally, e.g. the nonlinear optical index of refraction [4] and the generation of high harmonics [57]. The electric field strength produced in the focus of those lasers was still weak compared to that responsible for the binding of an electron in an atom. Also the energy of the photons was too low to induce direct photo-ionization. Nevertheless, it was soon observed that those lasers could induce optical breakdown of material [58, 59, 60]. Responsible for the transition of neutral matter into plasma state is the simultaneous energy contribution of several photons to liberate an electron from its parent atom or ion. This effect has been referred to as MULTI-PHOTON IONIZATION (MPI) [60] and has been predicted theoretically by Göppert-Mayer in 1931 already [61]. The underlying principle of MPI is that the light intensity, I, of a laser is increasing with the photon flux density through an area, A, (e.g. the laser focus) according to

$$I = \frac{\mathcal{E}}{\Delta t \cdot A} = \frac{n\hbar\omega}{\Delta t \cdot A}. \tag{2.1}$$

Here $\mathcal{E}$ denotes the optical energy which is incident onto an area during a time interval Δt. The energy depends on the number, n, and the angular frequency, ω, of photons; $\hbar$ denotes Planck's constant, h, divided by 2π. According to Einstein, who quantum-mechanically explained the photo-ionization in 1905 (and for this he received the Nobelpreis in 1921) [62], a bound electron can be liberated if it absorbs the quantum energy $h\nu = \hbar\omega$ as given by the famous equation

$$\mathcal{E}_{\text{kin}} = h\nu - \mathcal{E}_{\text{ion}}, \tag{2.2}$$

where ν is the frequency of the photon and $\mathcal{E}_{\text{ion}}$ the ionization energy. In MPI, ionization is induced if many $(n \cdot h\nu)$ photons are absorbed simultaneously. The remaining energy, $\mathcal{E}_{\text{kin}}$, is given to the electron in form of kinetic energy. The ionization process itself is based physically on the existence of short-living virtual electronic states having life-times of the order given by Heisenberg's uncertainty principle, $\Delta\mathcal{E} \cdot \Delta t \geq \hbar$, with $\Delta\mathcal{E} = \hbar\omega$ being the energetic distance between two of these states and Δt the life-time (typically sub-fs). An electron, which is lifted into such a state by absorbing a photon, has to absorb the next within a time of the order of the life-time of the state to proceed to the next level. This is the reason why the radiation field has to present a photon density high enough such that a positive non-zero probability for MPI occurs. In turn, the Heisenberg criterion preserves neutral matter from being ionized at lower light intensities and long wavelengths. In order to illustrate the mechanism, figure 2.1 a) depicts the electrostatic potential of a proton and an electron bound by this potential. The electron is shown as wave-packet. In b), an external electric field is present which is the laser electric field. Though it has little influence on the atomic potential, the electron can be lifted into the continuum via multi-photon ionization. In the case of virtual states are located energetically close to real ones, the ionization probability can be increased drastically due to resonances.

If more photons are absorbed by the electron than required for overcoming the binding energy of the atom, the electron spectra show characteristic maxima separated by the energy $m \cdot \hbar\omega$ (with an integer $m > 0$). Hence the kinetic energy of the electron is larger than the photon energy, $\mathcal{E}_{\text{kin}} > \hbar\omega$. In the extended version of the Einstein equation, photo-ionization is given by

$$\mathcal{E}_{\text{kin}} = (n + m)\hbar\omega - \mathcal{E}_{\text{ion}}. \tag{2.3}$$

This ionization process was termed Above Threshold Ionisation (ATI) [53, 63]. A typical ATI-electron spectrum shows characteristic maxima with the distance of the photon energy. The ionization process can experimentally be studied by analyzing the energy and momentum distribution of the electrons. Various theories have been developed in order to describe ATI processes. In the case of laser intensities below $\sim 10^{13}$ W/cm^2, the electron spectra can be calculated using multi-order perturbation theory. Several non-perturbative theories have been developed to describe ATI at higher field intensities, e.g. the KFR-theory by Keldysh, Faisal and Reiss [64, 65, 66, 67, 68]. An overview over the various theoretical approaches to describe ATI is given in the review article by Burnett (1993) and citations within [49].

Particularly the observation of high harmonic generation (HHG) of the laser fundamental strengthened the interest in ATI mechanism. High harmonics are emitted by electrons that recombine with the parent ion after being in a high energy continuum state where they could absorb several photons above the ionization potential [69, 70, 71, 72]. Here the photon energy of the laser is converted into VUV, XUV and recently also into keV X-ray regime [73]. Due to the high degree of coherence of this radiation and the discovery of a plateau in the spectra (where adjacent harmonics are emitted at similar intensity), various applications have been suggested. So it is possible to overlap multiple frequencies (orders) coherently of one pulse train to generate attosecond pulses or use HHG as a coherent XUV-source of high brilliance for lithography applications [11].

The Barrier Suppression Ionization model

It is interesting to ask at what intensities the laser electric field is comparable to that of the atom (and hence no small perturbation of the atomic field any more). As the simplest case, assume the Bohr model of a hydrogen atom in which an electron is on its orbit around a proton at a distance of a Bohr radius, a_B. The electric field strength, E_a, that keeps the electron on the orbit, can be calculated classically. One finds

$$a_B = \frac{\hbar^2}{m_e e^2} = 5.3 \cdot 10^{-9}\ \text{cm} \ \rightarrow \ E_a = \frac{e}{4\pi\epsilon_0 a_B^2} \approx 5.1 \cdot 10^{11}\ \text{V/m} \tag{2.4}$$

where m_e denotes the electron mass, e its charge and ϵ_0 the vacuum permittivity. Formally, this field is equivalent to an atomic unit of intensity, I_a, of

$$I_a = \frac{\epsilon_0 c}{2} E_a^2 \approx 3.45 \cdot 10^{16}\ \text{W/cm}^2. \tag{2.5}$$

As usual, c denotes the vacuum speed of light. If the atom is placed in a laser field with an intensity of $I_a = 3.45 \cdot 10^{16}$ W/cm^2, formally a complete suppression of the atomic Coulomb potential would be induced. Equation (2.4) can be written in the form

$$E = 2.74 \cdot 10^3 \sqrt{I\ [\text{W/cm}^2]}\ \ \frac{\text{V}}{\text{m}}\ , \tag{2.6}$$

where I_L is the light intensity. Higher ionization rates have been observed experimentally for lower intensities than predicted by this approximation already. That leads to the conclusion that at intensities which are lower than I_a the electric field of the laser must have a significant effect on the atomic potential already. In a simple model developed by Bethe and Salpeter, ionization is explained by the distortion of the atomic binding potential due to the electric field of the laser [74]. The model predicts an "APPEARANCE INTENSITY", I_{app}, at which ionization occurs. The starting point is the superposition of the nuclear potential and a static external electric field. In one dimension this superposition reads

$$V(x) = -\frac{Ze^2}{x} - eEx \tag{2.7}$$

with Z being the charge of the ion which will be produced and E the external electric field strength. Energetically, the region of lower energy for the electron is separated by a reduced potential (see figure 2.1). The position of the barrier, $x_{\max}$, can be derived by setting $\partial V(x)/\partial x = 0$, yielding $x_{\max} = Ze/E$. By claiming $V(x_{\max}) = E_{\text{ion}}$, the critical field electric strength, E_{crit}, is given by

$$E_{\text{crit}} = \frac{\mathcal{E}_{\text{ion}}^2}{4Ze^3}. \tag{2.8}$$

The particular ionization energy is given by $\mathcal{E}_{\text{ion}}$. Since in this case, the electric laser field is so strong that the Coulomb barrier is suppressed, the electron can escape freely. This ionization process is termed Barrier Suppression Ionization (BSI). The minimum laser intensity required is given by

$$I_{\text{BSI}} = \frac{\pi^2 c \epsilon_0^3 \mathcal{E}_{\text{ion}}^4}{2Z^2 e^6} \approx 4 \cdot 10^9 \left(\mathcal{E}_{\text{ion}}[\text{eV}]\right)^4 Z^{-2} \ \frac{\text{W}}{\text{cm}^2} \ . \tag{2.9}$$

This relation has been confirmed experimentally over several orders of magnitude of intensity using nobles gases [75]. For the example, in the case of a hydrogen atom ($Z = 1$, $\mathcal{E}_{\text{ion}} = 13.6$ eV), one finds

$$I_{\text{BSI}} = \frac{I_a}{256} \approx 1.37 \cdot 10^{14} \ \frac{\text{W}}{\text{cm}^2} \ . \tag{2.10}$$

As stated above, a significant lower electric field amplitude is required to ionize the atom than predicted, if only the undisturbed ionization potential is considered. A table of ionization thresholds predicted by BSI-theory for some materials relevant for this thesis is given in Appendix B.

Tunnel-ionisation and ionisation rates

The laser intensities at which ionization is predicted by the BSI theory are in good agreement with experimental observations. Nevertheless, the BSI theory states thresholds but no ionization rates. Those rates can be derived by quantum-mechanical calculations of the tunnel probability of the electron wave packet through the barrier. The tunnel-ionization process is schematically illustrated in figure 2.1 c). Here the Coulomb barrier is lowered by the electric field of the laser and the wave packet may tunnel through. Calculations have been performed by Keldysh in 1965 and were extended by Perelomov later [64, 76, 77] (refer also to [78]). The requirement for tunneling to occur is given by a quasi-static electric field and potential, respectively, what is assumed for the calculation. This is fulfilled for low laser frequencies and long Kepler times. Here the electron has enough time to tunnel through the barrier. Tunneling is hence a quasi-static (adiabatic) scenario. To distinguish quantitatively whether ionization due

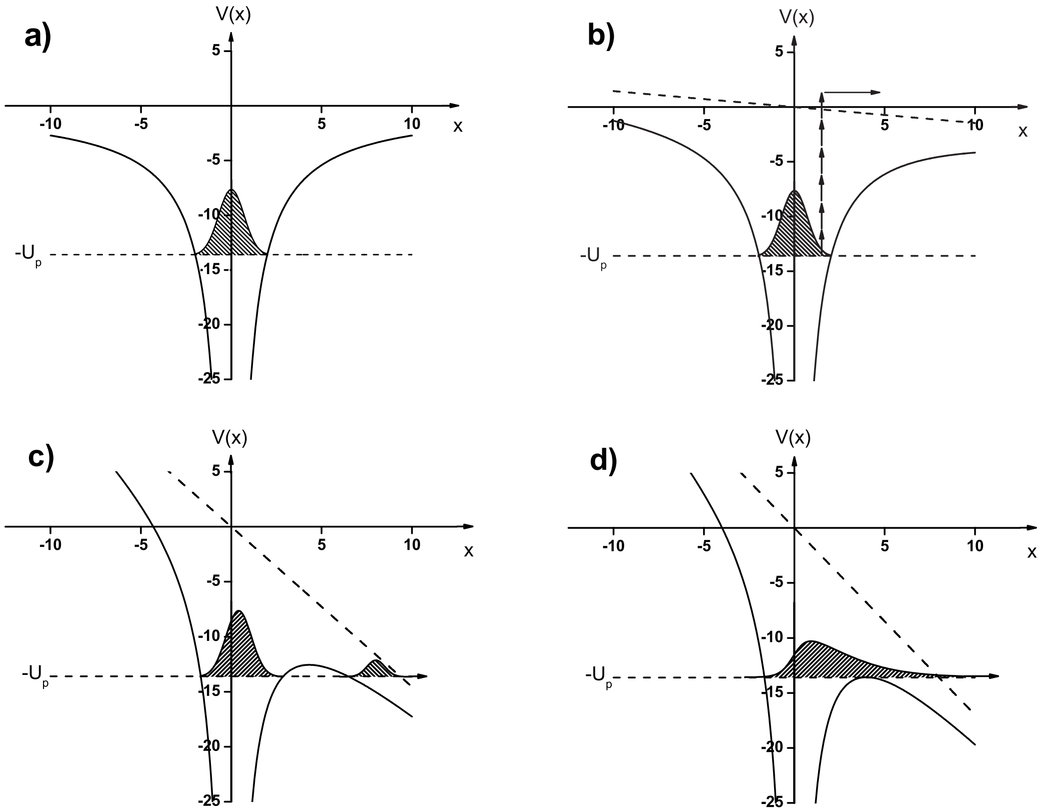

Figure 2.1: a) Electrostatic potential, $V(x)$, of an ion with $Z = 1$ with no laser field present. The electron bound to the ion is illustrated by a wave-packet. The binding potential is $-U_p$. In b) - d) an external static electric field is added which is increasing in strength and deforms the potential. The units chosen are Bohr radii and eV, respectively. The electric field strengths correspond to the peak values obtained at light intensities of 0, $1 \cdot 10^{12}$, $1 \cdot 10^{14}$ and $3.45 \cdot 10^{14}$ W/cm^2, respectively. The ionization processes illustrated are hence due to multi-photon, tunneling and barrier suppression.

to tunneling or above threshold ionization is more likely, Keldysh introduced a dimensionless parameter, termed the Keldysh-Parameter,

$$\gamma = \omega_L \sqrt{\frac{2\mathcal{E}_{ion}}{I_L}}. \tag{2.11}$$

Here I_L denotes the laser intensity and ω_L the angular frequency of the radiation. In the case of $\gamma < 1$, tunneling ionization is dominant. This condition is fulfilled for strong fields and long wavelengths. For $\gamma > 1$, the time needed by the electron for tunneling is larger than the laser period. Here the quasi-static approximation is clearly invalid and ATI is the dominant ionization process. The regime in between, where $\gamma \approx 1$, is rather a characteristic regime then a sharp boundary ("non-adiabatic tunneling" regime [79]). For the outer electrons of noble gases, it is entered at focused laser intensities of $\sim 10^{14}$ W/cm^2 and a wavelength of $\lambda = 800$ nm.

Following Keldysh, the ionization rates, Γ, are given for hydrogen-like systems by

$$\Gamma = 4\omega_a \left(\frac{\mathcal{E}_{\text{ion}}}{\mathcal{E}_h}\right)^{5/2} \frac{E_a}{E(t)} \cdot \exp\left[-\frac{2}{3}\left(\frac{\mathcal{E}_{\text{ion}}}{\mathcal{E}_h}\right)^{3/2} \frac{E_a}{E(t)}\right], \qquad (2.12)$$

where $\mathcal{E}_{\text{ion}}/\mathcal{E}_h$ is the fraction of the ionization potential with respect to that of hydrogen, E_a the atomic electric field (equation (2.4)) and $\omega_a = me^4/\hbar^3 = 4.16 \cdot 10^{16}$ s^{-1} the atomic frequency. In an extended version developed by Ammosov, Delone and Krainov, the ionization rates are derived for complex atoms and ions and for arbitrary quantum numbers of the electronic configuration (ADK-THEORY, [80]). Experimentally, the electron yield predicted by ADK-theory has been confirmed for the noble gases helium, argon, neon and xenon in an intensity range from 10^{13} W/cm^2 up to 10^{18} W/cm^2 using 1 ps pulses ($\lambda = 1.053$ nm) in [75].

Influence of pulse duration

Experiments have clearly shown that besides the pulse intensity, the pulse duration is an important parameter with respect to which ionization process is relevant. Particularly using ultra-short pulses with durations of < 1 ps, tunneling rather than ATI was observed [10, 75, 81]. Here the experiments show that the characteristic modulations in the electron spectra (i.e. the separation of the maxima by the distance of the photon energy) were suppressed. In addition, a shift in the energetic position of the levels has been reported. This shift has been explained by the fact that the electrons can gain almost no energy from the PONDEROMOTIVE POTENTIAL of the laser because of the short interaction time using ultra-short pulses (see below). Also individual resonances in the electron yield per eV, which are typical for ATI, were suppressed [50, 51, 82].

Another important factor is the pulse contrast. If the intensity is increasing too slowly or pre-pulses are present, population depletion occurs via MPI prior the tunneling regime is entered. So it is possible that the ionization saturates at an intensity, I_{SAT}, which is lower than I_{BSI} [49]. That happens if the life time of the electronic state is shorter than the rise time of the field intensity. Conclusively, in order to induce tunnel ionization, the pulses have to be ultra-short, high-intense and must be of high contrast.

Recapitulating, the level of ionization induced by a laser pulse depends not only on the ionization potentials of the material, but also on the pulse intensity, duration and wavelength. Different ionization channels are possible such as multi-photon ionization (MPI and ATI, respectively), or tunneling (BSI) ionization. The number of electrons produced until a time t, is given by the integration of the relevant ionization rate,

$$N(t) = 1 - \exp\left(-\int_{-\infty}^{t} \Gamma(\tau)\,\mathrm{d}\tau\right). \tag{2.13}$$

So actually a long laser pulse at rather low intensity can produce an equal number of electrons with respect to a high intensity pulse with shorter duration. In turn, though the thresholds stated by BSI theory for "instantaneous" tunnel ionization may be exceeded, it is possible that the pulse duration is too short to liberate a significant number of electrons. Particularly it is observed in Particle-In-Cell simulations of the interaction of a sub-10-fs pulse with gases that the average ionization state is relatively low. This is discussed in chapter 6.

2.2. The non-relativistic ponderomotive potential and force

After the electron has been released from the parent atom or ion, the dynamic of motion is given by the Lorentz equation,

$$\frac{\mathrm{d}\vec{p}}{\mathrm{d}t} = m_e \cdot \frac{\mathrm{d}\vec{v}}{\mathrm{d}t} = -e \cdot \left(\vec{E} + \vec{v} \times \vec{B}\right). \tag{2.14}$$

Here the time-dependent electric field of the laser at the position of the electron is denoted by $\vec{E}$, the magnetic field by $\vec{B}$. The velocity of the electron is termed $\vec{v}$, its momentum $\vec{p}$. In the non-relativistic scenario, i.e. $v/c \ll 1$, the influence of the magnetic component can be neglected and the equation of motion is reduced to

$$\frac{\mathrm{d}\vec{p}}{\mathrm{d}t} = -e\vec{E}. \tag{2.15}$$

A plane electromagnetic wave with an electric field component of

$$\vec{E}(\vec{r}, t) = \vec{E_0} \cdot \cos(\omega t - \vec{k} \cdot \vec{r}) \tag{2.16}$$

at the position $\vec{r}$ and at a time t will cause the electron to oscillate with a quiver velocity,

$$v_q = \frac{eE_0}{m_e \omega}. \tag{2.17}$$

The angular frequency of the oscillation is denoted by ω, the k-vector by $\vec{k}$. The QUIVER ENERGY, U_p, stored in this oscillation is given by

$$U_p = \frac{e^2 E_0^2}{4 m_e \omega^2}. \tag{2.18}$$

Here $U_p = < \frac{1}{2} m_e v_q^2 >_{\text{cycle}} = \frac{1}{2}\mathcal{E}_{\text{kin,max}}$ was used. This energy is also called the PONDEROMOTIVE POTENTIAL of the laser. In practical units it reads

$$U_p = 9.33 \cdot 10^{-14} \cdot (\lambda[\mu\text{m}])^2 \cdot I[\text{W/cm}^2] \;\; \text{eV}. \tag{2.19}$$

For example, a pulse with an intensity of $1 \cdot 10^{16}$ W/cm^2 has a ponderomotive potential of $U_p = 596$ eV.

Due to the radial intensity profile in focus, however, the electric field of the laser is far from being a homogeneous plane wave. Assuming a Gaussian intensity distribution, the peak intensity is achieved on the beam axis and a gradient across the field distribution is present (compare also Appendix A). This gradient leads radially to an additional acceleration of the quivering electrons into the direction of lower intensities. By averaging the dynamics over the cycle, a PONDEROMOTIVE FORCE can be identified. Its origin is usually a spatial gradient in laser intensity due to focusing.

To derive the strength of the ponderomotive force, assume a plane electromagnetic wave traveling in z-direction with the electric field component in y-direction. The strength of the E-field may vary with y due to focusing (i.e. $E_0(y, z = 0) = E_{0,\text{max}} \cdot \exp(-y^2/w^2)$ with a Gaussian width w and a peak electric field strength of $E_{0,\text{max}}$), hence

$$\vec{E}(\vec{r}) = E_y(y, z) \cdot \vec{e_y} = E_0(y, z) \cdot \cos(\omega t - kz) \cdot \vec{e_y}. \tag{2.20}$$

Thus the equation of motion of the electron placed in this field becomes

$$\frac{\mathrm{d}v_y}{\mathrm{d}t} = -\frac{e}{m_e} \cdot E_y(y, z). \tag{2.21}$$

Following [83, 84], and using $\psi = \omega t - kz$, after a TAYLOR expansion of the electric field, it reads

$$E_y(\vec{r}) = E_0(y, z) \cdot \cos\psi + y \cdot \frac{\partial}{\partial y} E_0(y, z) + \ldots \tag{2.22}$$

The solution of equation (2.21) for the lowest order term yields

$$v_y^{(1)} = -v_q \cdot \sin\psi \;,\; y^{(1)} = \frac{v_q}{\omega} \cdot \cos\psi. \tag{2.23}$$

This can be re-inserted into (2.21), giving

$$\frac{\partial v_y^{(2)}}{\partial t} = -\frac{e^2}{m_e^2\omega^2} E_0 \frac{\partial E_0(y)}{\partial y} \cdot \cos^2 \psi. \tag{2.24}$$

After multiplying by m and averaging over a cycle, the PONDEROMOTIVE FORCE is obtained,

$$F_\mathrm{p} = \left\langle m_e \frac{\partial v_y^{(2)}}{\partial t} \right\rangle = -\frac{e^2}{4m_e\omega^2} \cdot \frac{\partial E_0^2}{\partial y}. \tag{2.25}$$

Comparing with equation (2.18) shows that the ponderomotive force is given by the negative gradient of the ponderomotive potential,

$$F_p = -\nabla U_p, \tag{2.26}$$

and scales with the negative gradient of the intensity, $-\nabla I$. Note that in the non-relativistic case, the effective acceleration is in the $\pm y$-direction only, i.e. perpendicular to the $\vec{k}$-vector of the wave.

Left of figure 2.2 depicts the spatial intensity distribution of a laser pulse with a wavelength of $\lambda = 800$ nm and a pulse duration of $\Delta t_I = 50$ fs, which is focused to a spot of 5 μm in diameter (both FWHM of intensity). The pulse is shown at focal position ($t = t_0$). The peak intensity is $I_0 = 1 \cdot 10^{16}$ W/cm^2. The iso-intensity lines indicate the spatial inhomogeneity of the pulse due to focusing. The influence of the pulse on an electron which is initially at rest close to focal position is illustrated on the right side of figure 2.2. The y-position of the electron is plotted as a function of time. Initially, it is at rest in the focal plane ($z = 0$ μm) with a small distance to the optical axis ($y_0 = 500$ nm). The dynamics of the electron under the influence of the transiting laser pulse has been obtained by numerical integration of the equation of motion. As the pulse arrives, the electron starts to quiver in $\pm y$-direction and is accelerated radially out of focus. At the time $t = 0$, the amplitude of the $\vec{E}$-vector is largest and thus also the quiver velocity v_q. Finally, the net energy transferred to the electron ($\mathcal{E}_\mathrm{kin} \approx 1.04$ eV) is only a small fraction of the ponderomotive potential of the pulse ($U_P \approx 595$ eV). This is due to the short pulse duration. In this example, the maximum quiver velocity on axis is $v_q = 6.8 \cdot 10^{-2}\, c$ and the amplitude of the motion about ± 9 nm. If in contrast the laser pulse duration is long enough so that the electron can slip down the potential completely, almost all of the oscillatory energy in the field can be transformed into directed motion. The final velocity observed is then up to $v \sim v_q$ and the maximum gain of kinetic energy is given by the ponderomotive potential of the laser. Experimentally this was first confirmed

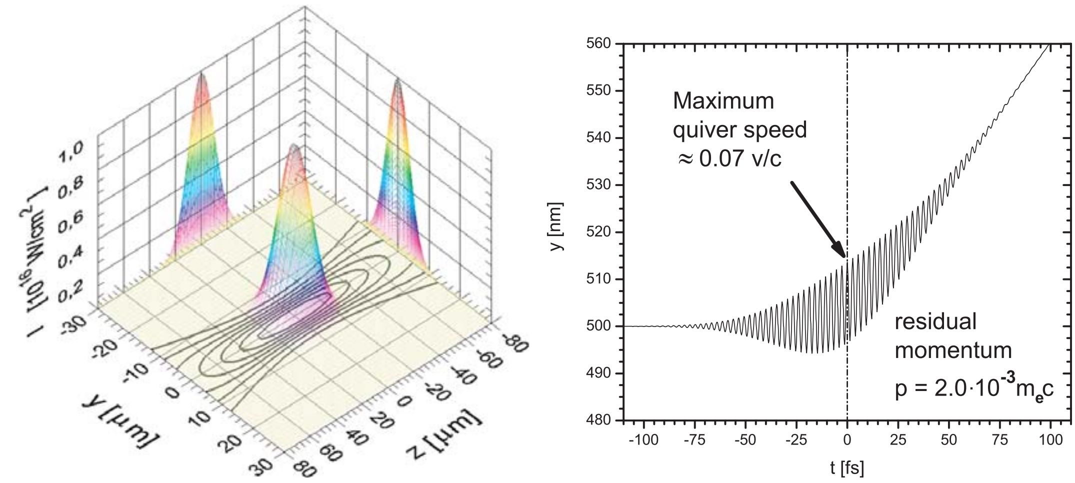

Figure 2.2: Left: 2D-intensity distribution of a $\Delta t_I = 50$ fs laser pulse focused to a spot of 5 μm in diameter (FWHM). The iso-intensity lines indicated are 86, 74, 62, 50, 37, 25 and 12 percent of $1 \cdot 10^{16}$ W/cm^2. Right: quiver motion an electron initially located at a distance $y_0 = 0.5$ μm with respect to the optical axis. The ponderomotive force, $F_\mathrm{p} = -\nabla U_\mathrm{p}$, accelerates the electron radially along the gradient of intensity.

by ATI photoelectron spectra [50]. If the laser pulse is ultra-short, however, the electron gives its quiver energy back to the laser field adiabatically and has hence gained almost no kinetic energy after the pulse has passed. As clearly shown by the simulation depicted in figure 2.2, at an intensity of $I = 1 \cdot 10^{16}$ W/cm^2 and a pulse duration of $\Delta t_I = 50$ fs, the net energy transfer can already be neglected. This effect is even more sustained if pulses of sub-10-fs duration are used.

2.3. Relativistic motion of a free electron in an em-wave

In the relativistic case, the magnetic field component in the Lorentz equation (equation (2.14)) becomes strong enough to induce a significant change in the electron dynamics which becomes nonlinear. Approaching the relativistic regime, it is common to introduce a dimensionless variable

$$a_0 = \frac{v_\perp}{c} = \frac{eE_0}{\omega m_e c}. \tag{2.27}$$

The speed of an electron transverse to the k-vector of the light wave is denoted by $v_\perp$. Physically, a_0 can be read as a normalized vector potential which corresponds to the classical velocity of a free electron oscillating in a linearly polarized electric laser field. In terms of irradiance it reads

$$a_0 = \left(\frac{1}{2\pi^2\epsilon_0}\frac{e^2}{m_e^2c^5}\lambda_L^2 I\right)^{1/2} \quad (2.28)$$

$$= 0.85\cdot\lambda_L[\mu\mathrm{m}]\cdot\sqrt{I_{18}}. \quad (2.29)$$

Following the definition given by equation (2.27), the relativistic regime is entered and the dynamics becomes nonlinear when the normalized vector potential approaches $a_0 \sim 1$. In terms of IRRADIANCE, this happens when the value of the intensity-wavelength product exceeds

$$I\lambda_L^2 \approx 10^{18}\,\frac{\mathrm{W}}{\mathrm{cm}^2}\,\mu\mathrm{m}^2. \quad (2.30)$$

Note that the laser wavelength, λ_L, is an important parameter. Using longer wavelengths, e.g. $\lambda_L = 10.6$ µm of a CO_2 laser, a_0 equals unity at intensities of about $I \approx 1.2\cdot 10^{16}$ W/cm^2. This is the reason why various nonlinear laser-plasma effects have originally been observed with CO_2 laser pulses of ns duration, such as relativistic self-focusing [85], high-order-harmonic generation on solid targets [86], and laser particle acceleration [87].

The amplitudes of the electric and the magnetic field components as well as the intensity can be expressed formally in terms of the normalized vector potential, a_0:

$$E_0 = \frac{a_0}{\lambda\,[\mu\mathrm{m}]}\cdot\,32.2\,\frac{\mathrm{GV}}{\mathrm{cm}} \quad (2.31)$$

$$B_0 = \frac{E_0}{c} = \frac{a_0}{\lambda\,[\mu\mathrm{m}]}\cdot 107\ \mathrm{MG} \quad (2.32)$$

$$I_0 = \frac{\epsilon_0 c}{2}E_0^2 = \frac{a_0^2}{\lambda^2\,[\mu\mathrm{m}^2]}\cdot 1.37\cdot 10^{18}\,\frac{\mathrm{W}}{\mathrm{cm}^2} \quad (2.33)$$

Since the dynamics of an electron in high amplitude fields has to be described relativistically, the RELATIVISTIC GAMMA-FACTOR,

$$\gamma = \left(1+\frac{p^2}{m^2c^2}\right)^{\frac{1}{2}}, \quad (2.34)$$

becomes relevant. Particularly the momentum of the electron is given by $\vec{p} = \gamma m\vec{v}$. The nonlinearity in the dynamics is caused by the magnetic force, $-e\vec{v}\times\vec{B}$, in the Lorentz equation (2.14), which turns the direction of the electron momentum. Note that the Keldysh-adiabaticity parameter is also termed γ due to historical reasons.

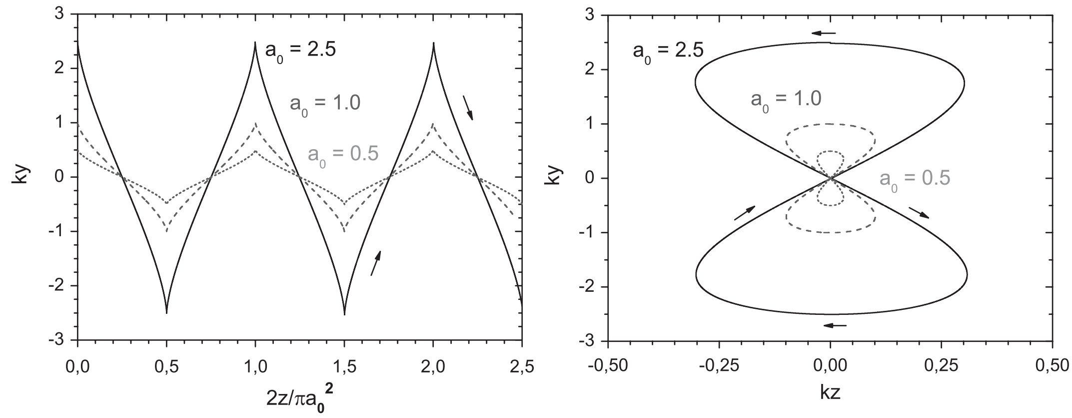

Figure 2.3: Left: Orbits of a free electron oscillating in a linearly polarized plane wave as observed in the laboratory rest frame for different normalized amplitudes, a_0. Right: Same orbits as seen in a co-moving average rest frame. Here typically a "figure of eight" motion is observed. The normalized amplitudes correspond to laser intensities of $5 \cdot 10^{17}$ W/cm^2, $2 \cdot 10^{18}$ W/cm^2 and $1.4 \cdot 10^{19}$ W/cm^2 at a wavelength of $\lambda = 800$ nm.

The fully relativistic equations of motion of an electron oscillating in a plane electro-magnetic wave can be solved exactly [78, 88, 89]. While in the case of low amplitude the momentum of the oscillation is perpendicular to the laser direction, at high field amplitudes the orbits reveal a more complicated geometry. So also a momentum component parallel to the direction of the laser pulse is observed. As an example, consider an electron which is under the influence of a super-intense, linearly polarized laser field, $\vec{E} = \vec{E_0} \cdot \sin(\omega t - kz) \cdot \vec{e}_y$, propagating in z-direction. The momenta in the laboratory frame are given by

$$p_x = 0 \ , \ \ p_y = a_0 \cos \Psi \ , \ \ p_z = \frac{a_0^2}{4}[1 + \cos 2\Psi]. \tag{2.35}$$

As above, the phase factor is $\psi = (\omega t - kz)$. The electron is pushed parallel to the propagation direction of the laser and carries a z-momentum, p_z, that is pulsing with twice the laser frequency. The average drift velocity, v_D, is here given by

$$\frac{v_D}{c} = \frac{a_0^2}{4 + a_0^2}. \tag{2.36}$$

The parallel drift of an electron in a super-intense electromagnetic field was first noticed by Brown and Kibble in 1965 [90]. (A short derivation of the motion of the electron for arbitrary polarized fields can be found in [83].)

In order to illustrate the relativistic dynamic of an electron placed in a super-intense electro-magnetic wave, the relativistic equation of motion of an electron was solved numerically. The orbits observed in the laboratory frame and in the co-moving frame are illustrated in figure 2.3. The particle trajectories were calculated using the BUNEMAN PARTICLE-PUSHER which is used in numerous Particle-In-Cell codes [83, 91]. Co-moving with the averaged center of momentum, the periodic motion of the electron is seen as a "figure-of-eight". (In the case of circularly polarized light, however, the electron describes a circle with a radius $a_0/\sqrt{2}\gamma_0$ in the average rest frame and a helical orbit in the laboratory frame).

Consequently, a super-intense, ultra-short pulse (in the form of a plane wave) will accelerate an electron both transversally as well as longitudinally. As the electron is overtaken by the pulse, it is decelerated again. After the interaction, the electron is left behind the pulse at zero momentum. Here it is displaced along the laser propagation axis. Note that as long as the symmetry of acceleration and deceleration are undisturbed, the electron gains no net energy.

2.4. The ponderomotive force in the relativistic regime

So far it was assumed that the super-intense laser field was a plane wave. In the focus of a "relativistic laser pulse", i.e. at irradiances above $I\lambda^2 \approx 10^{18}$ Wcm^2, however, an electron will be expelled from regions of high intensity towards lower intensity in a similar way as in the non-relativistic case. Differences in the dynamics arise from the fact of relativistic mass increase at high quiver velocities and the non-vanishing $\vec{B}$-component in the Lorentz force. A RELATIVISTIC GENERALIZATION OF THE PONDEROMOTIVE FORCE was derived by Bauer *et al.* as well as Quesnel and Mora [92, 93]. It is given by

$$F_p = -\frac{e^2}{4\overline{\gamma} m_e \omega^2} \nabla \vec{E}_0^2, \tag{2.37}$$

where $\overline{\gamma}$ is the local relativistic, cycle-averaged γ-factor in a linearly polarized wave according to

$$\overline{\gamma} \approx \sqrt{1 + \frac{a_0^2}{2}}. \tag{2.38}$$

The relativistic ponderomotive force is responsible for the average electron motion observed in the laboratory frame and can be written as the negative gradient of a RELATIVISTIC PONDEROMOTIVE POTENTIAL,

$$U_p = \frac{m_e c^2}{4\overline{\gamma}} a_0^2. \tag{2.39}$$

Quesnel and Mora have shown with the help of 3D-simulations, that in the relativistic case the electrons are pushed isotropically out of focus. This was observed independently from the polarization direction of the strong, linearly polarized laser pulse simulated. Complicated 3D trajectories are reported. Besides a radial acceleration, the electrons are accelerated also in laser propagation direction. Here the electrons, which are scattered out of focus, can gain a maximum kinetic energy, $\mathcal{E}_{\text{kin}} = (\gamma - 1)m_e c^2$, of the order of the ponderomotive potential of the laser.

3. Laser-induced plasma processes

Once a plasma is produced by the leading edge of an ultra-short laser pulse due to one of the ionization processes described above, the fundamental parameters relevant for the description of the plasma phenomena are essentially the electron density and temperature. A key question of interest is hence what is the energy transfer from the laser pulse into the plasma. This energy which is stored in kinetic motion of the electrons and which - after thermalization via collisions - defines an initial temperature, forms the energy reservoir to drive other processes like collisional ionization and hydrodynamic expansion of the plasma created. Therefore, in this section the absorption processes relevant for both the understanding of the absorption mechanism and the interpretation of the numerical analysis results are reviewed.

3.1. Laser absorption and heating processes

ATI-heating

In the ATI-regime, the electron spectra recorded experimentally indicate that the electrons gain their kinetic energy during the ionization process via multiple photon absorption. Typically energies of the order of few eV are reported at laser intensities of $10^{13} - 10^{14}$ W/cm^2 [50].

In the BSI regime, ionization occurs due to tunneling and the electrons are born with initially zero momentum into the laser field [83]. The kinetic energy an electron can gain from the laser depends upon at which moment it was born into the field. To illustrate this, assume an electron was born already before the laser pulse arrives. As the electric field strength is increasing at the leading side of the pulse, a quiver motion is induced. The maximum kinetic energy of the electron at the center of the pulse is about $2 \cdot U_p$. At the tailing side, the electron is decelerated and when the pulse has left it behind, its momentum is zero again. This is the classic result, that a free electron cannot gain kinetic energy from the wave without a collision process being involved. In contrast, if the electron is born under the influence of the laser pulse, any phase-mismatch between the peak of the linearly polarized electric laser field and the point of birth of the electron will lead to a residual kinetic energy. Analytically, an electron which is born with zero momentum at the time t_0 will follow classically a sinusoidal pulse, $E(t) = E_0 \cdot \sin(\omega_0 t)$, with a quiver velocity

$$v_q = \frac{eE_0}{m_e \omega_0} \left(\cos \omega_0 t - \cos \omega_0 t_0 \right). \tag{3.1}$$

The cycle-averaged kinetic energy is given by

$$\langle \mathcal{E}_{\mathrm{kin}} \rangle = \frac{1}{2} m_e \left\langle v_q^2 \right\rangle = U_p \cdot (1 + 2 \cdot \cos^2 \omega_0 t_0), \tag{3.2}$$

where the first term on the right hand side is the coherent quiver energy of the oscillation (compare equation (2.18)), the second the remaining energy due to dephasing which is therefore termed ATI-ENERGY or DEPHASING ENERGY [94, 95]. Integrating over a laser cycle, the gain in energy is given by

$$\mathcal{E}_{\mathrm{ATI}} = \frac{2U_p \cdot \int_0^{2\pi} \Gamma_i(\phi) \cos^2 \phi \, \mathrm{d}\phi}{\int_0^{2\pi} \Gamma_i(\phi) \phi \, \mathrm{d}\phi}, \tag{3.3}$$

where Γ_i denotes the intensity-dependent ionization rate and ϕ the phase of the electric laser field. In particular in the context of ultra-short pulses, however, one

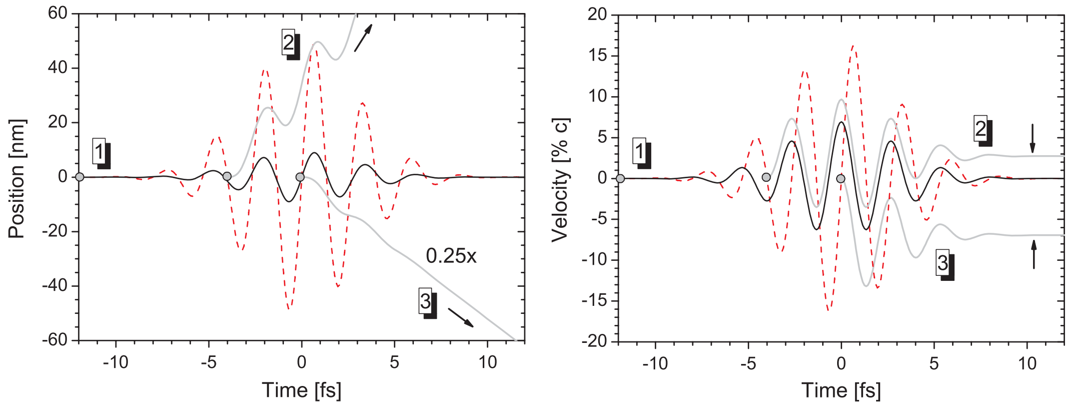

Figure 3.1: Position (left) and velocity (right) of electrons born with zero momentum at different times with respect to the pulse maximum. A sinusoidal electric field is indicated by the red dashed line (arbitrary units). The simulated laser intensity is $1 \cdot 10^{16}$ W/cm^2 and the pulse duration is 5 fs (FWHM). The trajectories were integrated numerically. While electron (1) is already present before the pulse has arrived and gains no net energy, electrons (2) and (3) are born under the influence of the pulse with a phase shift of zero with respect to the wave. Their net energy gain is 0.2 and 1.2 keV, respectively. Note that the phase shift chosen is such that the kinetic energy gain is maximum for each electron. Nevertheless, ionization at such a point is unlikely due to low field strength. Generally, electrons from highest ionization stages will contribute most to the final plasma temperature [94].

has to take into account the fast change of the temporal intensity profile. Here the ATI energy gain of an electron is given by

$$\mathcal{E}_{\text{kin,ATI}} = 2 \cdot U_p \cdot e^{-4 \cdot \ln 2 \left(\frac{t-t_0}{\Delta t_I}\right)^2 \Gamma_i(\Phi) \cos^2 \Phi}, \tag{3.4}$$

where again a sinusoidal wave is assumed with the maximum of its envelope located at $t = t_0$. The relation between phase and time is simply $t = \Phi/\omega$. Note that arbitrary phase relations between the carrier wave and the peak of the envelope are controlled by the choice of t_0 with respect to Φ. To obtain the total residual energy, $\mathcal{E}_{\text{ATI}}$, the integration has to be extended over the entire laser pulse. Figure 3.1 shows trajectories of electrons born at different times with respect to the maximum of an ultra-short (5 fs FWHM) laser pulse. Electron (1) is present already before the laser pulse arrives, electrons (2) and (3) are born under the influence of the pulse. The maximum energy gain of (3) is twice the laser ponderomotive potential, i.e. about 1.2 keV, while in contrast the gain for (2), which is born one and a half laser cycles before the pulse maximum, is just about 200 eV.

One characteristic of the ATI energy is that the velocity distribution of the electrons is non-Maxwellian. Subsequent thermalization of ATI energy is due to electron-electron collisions. After thermalization, the relation between the electron temperature, T_e, and the ATI energy, $\mathcal{E}_{\mathrm{ATI}}$, can be defined via [94]

$$\mathcal{E}_{\mathrm{ATI}} = \frac{3}{2} k_B T_e. \tag{3.5}$$

Inverse bremsstrahlung

In the model of ATI-heating it was implied that the oscillating electrons are always in phase with the laser electric field. A cloud of electrons follows instantaneously the driving field and any collisions are neglected. Since the ions are too heavy to be significantly accelerated by the field, they form a stationary background. Now, taking collisions of the electrons with the ions into account, a fraction of the quiver energy is transferred into random motion. This leads to collisional heating due to the physical effect of nonlinear inverse bremsstrahlung.

To estimate the amount of energy which is transferred, the electron-ion collision frequency has to be considered. In the case of a Maxwellian velocity distribution, it is given by the Spitzer formula,

$$\langle \nu_{ei} \rangle \ = \frac{4\sqrt{2\pi}}{3} \cdot \frac{Z^2 n_i e^4 \cdot \ln \Lambda}{(4\pi\epsilon_0)^2 \sqrt{m_e} \cdot (k_B T_e)^{3/2}}, \tag{3.6}$$

where Z is the degree of ionization (charge state), n_i the density of ions (in m^{-3}, $Z^2 n_i = Z n_e$) and T_e the electron temperature[1]. In practical units it reads

$$\langle \nu_{ei} \rangle \ = 2.91 \cdot 10^{-6} \cdot \frac{n_i[\mathrm{cm}^{-3}] \cdot Z^2}{(T_e[eV])^{3/2}} \cdot \ln \Lambda \ \ \mathrm{s}^{-1}, \tag{3.7}$$

where $\ln \Lambda$ is the Coulomb logarithm given by

$$\ln \Lambda = \ln \left(\frac{12\pi}{Z} \lambda_D^3 \cdot n_e \right). \tag{3.8}$$

The Debye length is defined by

$$\lambda_D = \sqrt{\frac{\epsilon_0 k_B T_e}{n_e e^2}}, \tag{3.9}$$

and gives a characteristic plasma length over which the electrostatic field of a charged particle is attenuated to $1/e$ due to shielding of other mobile charges.

[1] Note that the Spitzer equation requires a temperatures of at least ~ 5 eV [94].

Note that a Maxwellian velocity distribution is assumed. In practical units the Coulomb logarithm reads

$$\ln\Lambda = \ln\left(1.55 \cdot 10^{10} \cdot \frac{T[\mathrm{eV}]^{3/2}}{Z \cdot \sqrt{n_e[\mathrm{cm}^{-3}]}}\right). \tag{3.10}$$

At high laser intensities ($I > 10^{15}$ W/cm^2), the electron velocity is dominated by the quiver motion in the laser field, such that the quiver energy becomes comparable to the thermal energy (compare equation (2.18)). Hence the Spitzer formula has to be corrected to take the non-Maxwellian behaviour into account. This is usually done by a correction factor,

$$F = \left(1 + \frac{\langle v_q^2 \rangle}{3 v_{th}^2}\right)^{-3/2}, \tag{3.11}$$

where $v_{th} = \sqrt{2k_B T_e / m_e}$ is the electron thermal velocity [96]. A cycle-averaged power absorption rate can be defined [97] by

$$P = 2 \cdot U_p \cdot \langle \nu_{ei} \rangle . \tag{3.12}$$

For a laser intensity of the order of 10^{16} W/cm^2, a wavelength of 800 nm and an electron density of $n_e \approx 10^{19}$ cm^{-3}, the absorption rate is of the order of ten eV/ps [94]. Generally, due to the fact that electron-ion collisions become more and more unlikely with increasing electron temperature, the absorption rate also scales with $I^{-3/2}$ [98].

Energy transfer

Once the relevant processes for coupling of laser energy into electron kinetic motion are identified, it is important to focus on the energy transfer in the OFI-produced plasma. Large-angle scattering due to Coulomb collisions is responsible for the energy transfer and will lead to thermalization (i.e. relaxation of the velocity distribution into a Maxwellian). The energy relaxation time, that is the time needed by a particle to transfer most of its kinetic energy ($\Delta E/E \approx 1$) to a collision partner, is basically given by the large angle scattering collision time, τ. For the energy loss of electrons due to collisions with other electrons one finds [98]

$$\tau_{\mathrm{ee}} = \frac{3\sqrt{6}}{8} \frac{\sqrt{m_e}(k_B T_e)^{3/2}}{\pi e^4 n_e \ln\Lambda}, \tag{3.13}$$

what in practical units reads

$$\tau_{\mathrm{ee}} \approx 1.07 \cdot 10^{-11} \left(\frac{10^{20}}{n_e[\mathrm{cm}^{-3}]}\right) \left(\frac{10}{\ln\Lambda}\right) \left(T_e\ [\mathrm{keV}]\right)^{3/2} \quad \mathrm{s}. \tag{3.14}$$

Since the different mass of electrons with respect to the ions and the (average) charge state of the ions are important for the effectiveness of the energy transfer, different energy relaxation times are found for different species:

$$\tau_{\text{ii}} \approx \frac{1}{Z^3}\left(\frac{m_i}{m_e}\right)^{1/2} \tag{3.15}$$

$$\tau_{\text{ei}} \approx \frac{1}{Z}\left(\frac{m_i}{m_e}\right), \tag{3.16}$$

where τ_{ii} denotes the time scale the ions need to thermalize, τ_{ei} that required by electrons and ions to thermalize, respectively. Since the energy transfer between species with different masses is rather inefficient, the time required until the electron velocity distribution becomes Maxwellian is short compared to that until electrons and ions thermalize. As can be seen from equations (3.14) and (3.15), at electron densities of the order of 10^{20} cm^{-3} and electron energies of few tens of eV, a laser pulse duration of sub-10-fs is significantly shorter than typical energy transfer times in the plasma. Consequently, on timescales relevant for the development of the plasma, a sub-10-fs laser pulse appears like a delta-function excitation. Hence it is expected that the ionization process is well separated from the development of the plasma due to the ultra-short pulse duration. This is the basis for the experimental observation of the laser-induced ionization front reported in chapter 6.

Resonance absorption

So far absorption, that is an effective transfer of laser energy into plasma electron motion simultaneously to a damping of the light wave, was considered only as a collisional process. At high laser intensities, i.e. above $\sim 10^{16}$ W/cm^2, however, collisions between electrons and ions become unlikely due to an $I^{-3/2}$ scaling of the Spitzer formula (compare equations (3.6) and (3.11)). In the special case of a linearly p-polarized laser which is incident obliquely onto a steeply rising plasma density profile, a high fraction of laser energy may be absorbed by RESONANCE ABSORPTION, which is a non-collisional process. The incoming wave may have an angle, Θ, with respect to the direction of the gradient. Solving Maxwell's equations in conjunction with the linear electron density ramp yields a standing wave field which is formed by the incoming and reflected wave [84, 98]. Particularly the wave has its turning point at a density of $n_{cr} \cdot \cos^2\Theta < n_{cr}$.

A part of the electric field can tunnel to a layer close to the critical density. Here electron plasma waves are driven resonantly, i.e. $\omega_{\mathrm{pe}} = \omega_L$, by the electrostatic field component parallel to the electron density gradient. Analytically this is due to a singularity in the solution for the electric field at the position of the critical density in case of p-polarization [99, 100]. Freidberg has shown with Particle-In-Cell simulations that the electron plasma waves grows over a few cycles and a supra-thermal electron tail is produced as it breaks. This happens subsequently at the critical surface every full laser cycle. Wave breaking in the collision-less regime damps the amplitude of the oscillation which is equivalent to absorption of the wave energy [101]. This driving field is responsible for high absorption though the electron-ion collision frequency may be small. Resonance absorption is sensitive to both the incidence angle and the steepness of the density profile. If the angle is close to normal incidence, the driver field parallel to the density gradient vanishes. If the angle is too large, the distance for tunneling of the electric field close to the region of critical density is too large. At high laser irradiance, a steepening of the density profile near the critical density can make resonance absorption less sensitive to the incidence angle, Θ, due to a shortening of the tunneling distance [102]. Moreover, since in contrast to inverse bremsstrahlung that leads to a heating of all electrons, in resonance the laser energy is transferred to only a small fraction of electrons which therefore can be accelerated to high kinetic energies ("supra-thermal" electrons). Experimentally it was found that collision-less absorption at intensities of 10^{16} W/cm^2 and above could be more than 50% (a summary of absorption measurements since 1988 can be found in [83]). Typically a bi-Maxwellian electron temperature is observed in which the "hot" component can significantly exceed the characteristic plasma thermal electron temperature, T_e . Numerical simulations were used to predict an effective temperature of the supra-thermal electrons which can be produced by resonance absorption. Particularly a Boltzmann distribution with a temperature scaling according to

$$T_{\mathrm{res}} = 0.1 \; (I_{17}\lambda_L^2)^{1/3} \;\; \mathrm{MeV} \tag{3.17}$$

is expected, where λ_L is the wavelength of the driving laser in µm and I_{17} the intensity in terms of 10^{17} W/cm^2, respectively [103]. As a result of the direction of the electron density gradient and the (parallel) component of the electrostatic driving laser field, the electrons will be accelerated every full cycle in direction normal to the target surface.

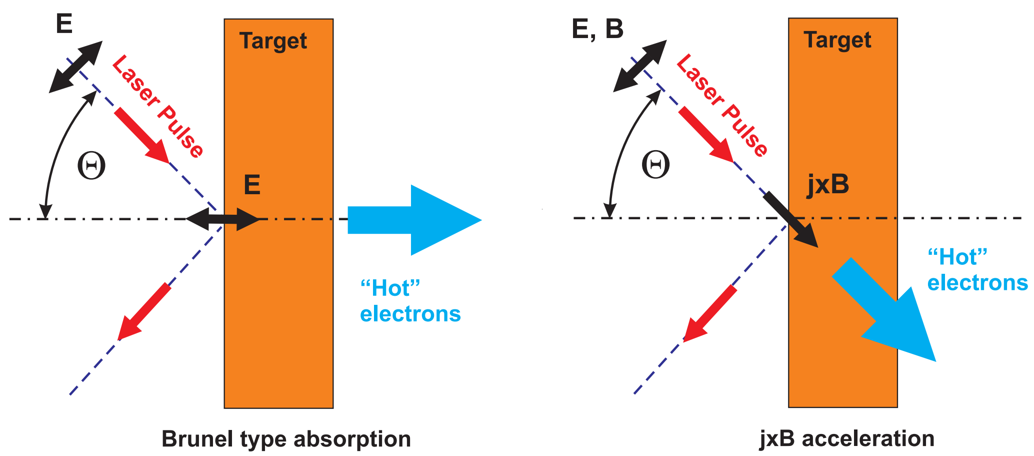

Figure 3.2: Schematic of different laser absorption mechanisms that lead to electron acceleration.

Brunel type absorption and j×B-acceleration

In the context of high-intensity, ultra-short laser pulses interacting with a solid target, other absorption mechanisms besides classical collisional and resonance absorption may occur. While in early ICF research rather long (ns) pulses were used and the dimension of the pre-plasma was of the order of hundreds of microns, with the availability of sub-ps pulses, the pre-plasma was significantly reduced as a consequence of higher contrast. This scenario is even dramatized if the surface is deformed by the light pressure and pushed in laser direction, which is known as hole boring effect [29, 30]. Hence steep density gradients allow the laser field to interact with plasma electrons close to the critical surface, i.e. in the case of high-contrast, sub-10-fs pulses even more or less directly with a plasma at solid density [104].

In the Brunel model of absorption (also referred to as VACUUM HEATING), the p-polarized laser is obliquely incident on a steep density gradient, where it interacts with electrons at the critical surface. An electron can be pulled out of the target into vacuum well beyond the thermal Debye sheath, $\lambda_D = v_{th}/\omega_{pe}$, where v_{th} is the thermal velocity of the plasma electrons. During the second half of the cycle it is thrown back in again. Because the laser field cannot follow inside over-dense plasma region but penetrate only into a skin depth of $\sim c/\omega_{pe}$, the electron can move unhindered into the plasma. In such a way a population of "hot" electrons is produced in about every cycle. The driving electric field is perpendicular to the surface and the electron acceleration is hence normal to the target surface. The Brunel type of absorption is schematically illustrated on the left side of figure 3.2. It is evident that the mechanism tends to be more efficient with increasing strength of the driving field and also greater incidence angles. Note that the geometry of the model is similar to that in classical resonance absorption but the mechanism is different. Particularly it requires a large density gradient and is moreover complementary to classical resonance absorption, that breaks down in the case of too steep density gradients. It is interesting to note that the original title of the work by Brunel is "*not-so-resonant, resonance absorption*".

Another absorption mechanism which is of relevance at relativistic laser intensities is $\vec{j} \times \vec{B}$-HEATING. This mechanism was theoretically predicted by Wilks *et. al.* [105] and experimentally confirmed by Malka and Miquel [106]. Here an electron is accelerated by the Lorentz force induced by the magnetic field component of the laser, as described above already. Without plasma, it is decelerated by the second half of the pulse. In the presence of a steep density gradient, however, electrons which are pushed into the over-dense plasma region cannot be followed by the wave. They continue their motion and form a hot electron tail in the spectrum. The characteristics of the $\vec{j} \times \vec{B}$ mechanism is that it works with arbitrary polarization direction (except circular) and will accelerate the electrons in laser propagation direction twice every full laser cycle. The energy gain of the electrons is of the order of the ponderomotive potential of the laser field

$$
\begin{aligned}
T_h \approx mc^2(\gamma - 1) &= mc^2 \left[\left(1 + \frac{2U_p}{mc^2} \right)^{1/2} - 1 \right] && (3.18) \\
&\approx 0.511 \left[\left(1 + \frac{I_{18}\lambda_L^2}{1.37} \right)^{1/2} - 1 \right] \text{ MeV.} && (3.19)
\end{aligned}
$$

The $\vec{j} \times \vec{B}$ mechanism will be most effective for normal incidence where the laser electric field vector is parallel to the density gradient [83]. This is supported by 2D-PIC simulations with step-like density profiles [105, 107]. As shown in simulations by Pukhov [28], the mechanism will also work in the context of extended density ramps, i.e. relaxed requirements on the steepness of the profile. Here the laser pulse drives electrons in a snow-plough manner prior it reaches the critical surface. The electrons which are pushed beyond the critical surface, keep their kinetic energy.

Though various absorption models exist (such as vacuum heating, anomalous skin effect etc.), and each covers different regimes of density scale lengths, polarization properties and incidence geometries, due to the complex dynamics of the interaction process it is even today a challenge to investigate the relevant processes contributing to a single experimental result. For example, if at relativistic intensities $\vec{j} \times \vec{B}$ acceleration might be the dominant process, Brunel absorption may occur at the sides of the hole. Here Particle-In-Cell simulations play an important role and have widely been used to cover the effects such as nonlinear propagation, energy transport and fast particle generation (see [83] and references within).

3.2. The Alfvén limit

So far, the conversion efficiency of laser energy into a directed electron beam was related to the irradiance of the laser. If the laser pulse energy is increased, the amount of electrons produced is increased. Indeed, the fast ignitor scheme is based on the assumption that extremely high currents exceeding the order of Mega-Ampere can be produced and at least a fraction of their kinetic energy can be deposited in the pre-compressed core [31]. Nevertheless, in 1939 already a fundamental limit for the current that can in principle be transported was proposed by Alfvén [34]. The ALFVÉN LIMIT was originally derived in the context of the motion of cosmic rays (charged particles) through cosmic space. The situation described is similar to that in a laser-plasma experiment, since these currents are propagating through a background of charged particles of cosmic space that provides a good conductor and screens out any electric field and space charge, respectively. As a result, the space charge of the moving particle beam is neutralized by return currents in the surrounding medium. The beam travels under the influence of its magnetic field itself. By solving the equation of motion, Alfvén found that particles beyond a critical radius of the beam axis are turned in opposite direction due to the influence of the surrounding magnetic field. Consequently, the maximum current in a direct beam is fundamentally limited by its own magnetic field. In the relativistic formulation, this limit for the current reads

$$J_A = \frac{4\pi\epsilon_0 \cdot m_e c^3}{e} \cdot \beta\gamma_b \ \ \text{kA} \approx 17.1 \ \beta\gamma_b \ \ \text{kA}, \tag{3.20}$$

where $\gamma_b = 1/\sqrt{1-\beta^2}$ is the relativistic gamma factor of the beam. The beta-factor is given by $\beta = v/c$. Note that the limit is proportional to the beam energy and is independent of the current density or cross section of the beam. Physically this can be understood by the fact that the limiting factor is given by the magnetic field alone. Hence, if a beam consists of equal parts of oppositely charged particles such that the *magnetic field* of the beam is zero, no limit in the number of particles is found. As already pointed out by Alfvén, such a beam is unstable to small disturbances, e.g. due to a magnetic field, that give rise to an instability to grow as a result of further increase of the magnetic field.

3.3. Weibel Instability

In the fast ignitor concept proposed by Tabak *et. al.* in 1994, the fuel is ignited by energy deposition of high energetic laser-produced electron beams in a hot-spot geometry. To deliver the required amount of energy to the center of the fuel, currents of the order of 10^3 to 10^4 Mega-Ampere are required. In vacuum, a current is fundamentally limited to the Alfvén current given by $J_A = 17.1\,\beta\gamma$ kA, because above the self-generated magnetic fields turn the flow and lead to a self-limitation of maximum current. In a plasma, however, the beam can be neutralized by a return current that is induced to maintain charge neutrality of the plasma. Nevertheless, though the Alfvén limit can be exceeded, in the situation of a high energetic (and hence generally collision-less) current that is counter-streamed by another (colder) one, instabilities may favourably grow. These instabilities possibly disturb the beam transport through the over-dense plasma in such a way that they affect the collimation of the beam and thus reduce the amount of energy that can be deposited in the core. This will have a direct influence on the potential success of the fast ignitor concept.

Generally, instabilities which are known in the context of energetic beams propagating through a neutralizing background plasma, are the (resistive) hose instability and the sausage instability [108]. Both are macroscopic instabilities. Microscopic instabilities are the two-stream and Buneman-instability as well as the electromagnetic filamentation (Weibel) instability. The WEIBEL INSTABILITY was first predicted in 1959 for a non-relativistic plasma produced by an anisotropy in the distribution function [35]. Recently the Weibel instability of relativistic beams has again gained importance due to the fast ignitor scheme. The instability is also attributed to play a major role in astrophysical phenomena such as the generation of filamented current densities and magnetic fields in relativistic cosmic jets which further lead to particle acceleration and emission of jitter radiation [109, 110, 111, 112].

To illustrate the physical mechanism of the Weibel instability, consider a spatial homogeneous electron beam which is charge-neutralized by a counter-propagating one in a plasma with fixed ion background. The situation is illustrated in figure 3.3 a). The beams travel parallel to the z-axis in opposite directions and have initially homogeneous densities labelled $n_{e,\mathrm{left}}$ and $n_{e,\mathrm{right}}$, respectively. Hence the net current is zero. In b), an infinitesimal fluctuation is added in the form of a magnetic field $B_y(x) = B_0 \cos(kx)$. As a result, the Lorentz force, $-e\vec{v} \times \vec{B}_y$, will deflect moving electrons in such a way that current sheaths are formed. This is equivalent to an anisotropy in the distribution function, here

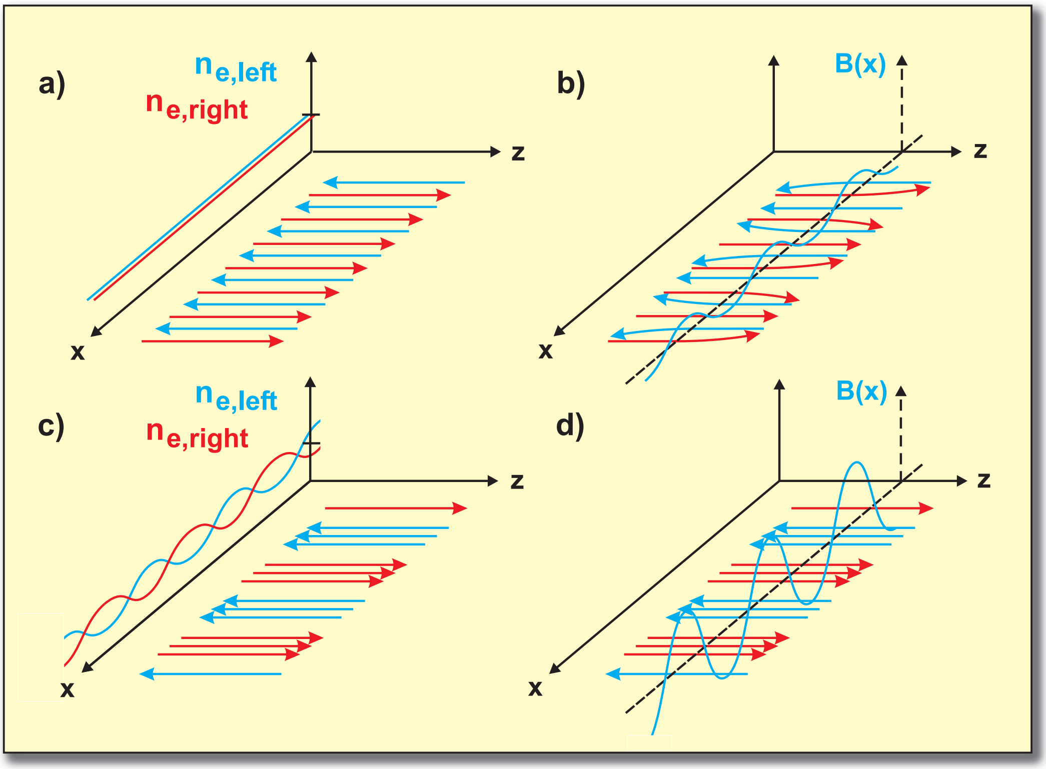

Figure 3.3: Illustration of the development of Weibel instability of two counter-propagating electron beams. Details on the mechanism are given in the text.

in space, and the density is modulated as illustrated in c). The current inhomogeneities now close the instability loop as the magnetic field, which caused the modulation, is increased (d). A hallmark of the instability is hence the production of current filaments (with a typical transverse dimension of the collision-less skin depth, c/ω_{pe}), surrounded by magnetic fields in the plane perpendicular to the direction of the flow. The modulation grows and leads to a further concentration of current density. As can be seen, Weibel instability is a pure kinetic instability.

Filamentation of electron beams undergoing Weibel instability was recently studied numerically using both PIC and Fokker-Planck hybrid codes [37, 38, 113, 114, 115, 116]. Growth rates were deduced from linearization of relativistic two-stream relativistic Vlasov-models [113, 115, 116, 117, 118, 119]. In simple form, the growth rate of Weibel instability, γ_{W}, it is given by

$$\gamma_{\mathrm{W}} = \omega_{be} \left(\frac{n_b}{\gamma_b n_e} \right)^{1/2} \frac{v_b}{c}, \tag{3.21}$$

where ω_{be} is the electron plasma frequency, n_b/n_e the contrast in density of the beam with respect to the neutralizing background plasma, v_b the beam velocity and γ_b the relativistic Lorentz factor of the beam [39, 120, 121]. Note that the growth rate is proportional to the square root of the beam contrast, i.e. fraction of beam density and background density. This was the motivation for recent experimental studies of laser accelerated electron beams in under-dense plasmas using a combination of solid and gas targets [39].

The filamentation is self saturating if the energy due to the anisotropy is completely transferred to the magnetic field. In the saturation stage, the current filaments of same sign may attract each other and eventually merge, what leads to an decrease of magnetic energy. This was often found in simulations and led to more organized, larger filaments, sometimes with a quasi-regular structure [17, 36, 37, 38].

Up to now, a transverse temperature of the current was neglected, which in fact can reduce or even suppress the growth of the instability. In the simple model depicted above, a transversal temperature (in x-direction) of the beam electrons tends to stabilize the flow. More quantitatively, a threshold for the instability was derived by Silva using a relativistic kinetic theory [122] (see also [115]). He found a threshold given by $n_b/n_e > \gamma_b \left(p_\perp/p_\parallel\right)^2$, which increases with laser intensity, i.e. the beam kinetic energy expressed by γ_b, and the transverse momentum, $p_\perp$. This is in particular important for the fast ignitor, since the electron density rises from $\sim n_{cr}$ to $\sim 1000 \cdot n_{cr}$ during a propagation length of the order of 100 µm.

Résumé

Recapitulating, the laser-plasma processes relevant for the experimental part of this thesis have been summarized. Important absorption mechanisms in the context of the study of the ionization front propagation in gaseous targets are ATI-heating and inverse bremsstrahlung. Since the energy transfer from the laser pulse into kinetic energy of plasma electrons depends on the pulse duration, in the context of sub-10-fs pulses, most of the energy transfer from the laser into the plasma is due to ATI-heating. This is confirmed by Particle-In-Cell simulations as detailed in chapter 6.

In contrast, resonance absorption and $\vec{j} \times \vec{B}$-type absorption are of particular relevance in the second experiment, i.e. the study of the filamentation of relativistic electron beams in over-dense plasmas. Here electrons are accelerated to MeV energies by the ponderomotive potential of the laser. The theoretical background to identify the relevant laser absorption mechanism was presented. Finally, the Weibel instability, which was identified as the origin for the filamentation of the electron beam observed experimentally, was explained. Important analytical formulas and scaling laws were summarized which will be used in chapter 7.

4. Optical diagnostic

The data in this thesis was mainly obtained by optical imaging and optical probing, respectively. Hence a major task in the conceptual phase of the experiments was to achieve high spatial resolution - especially for the study of electron beam filamentation in over-dense plasma - and also temporal resolution, as needed for the study of the ionization front propagation in gaseous targets. In this chapter, the diagnostics used are presented. Performance factors like resolving power are addressed, which have been obtained by a careful characterization of the set-ups.

4.1. Optical diagnostic for the study of electron beam filamentation in over-dense plasma

One of the central experiments in this thesis concerns the study of the filamentation which an electron beam produced by an ultra-intense laser pulse undergoes while it propagates a significant length through over-dense plasma. To examine the structure of the electron current at the rear side of the laser irradiated target, a high resolution optical imaging diagnostic was set up. Here the physical effect was used that high-energetic charged particles (i.e. the electrons with kinetic energies up to several tens of MeV) produce electromagnetic radiation when transiting the plasma-vacuum interface at the rear side of the target. The particular radiation is called Transition radiation. A visible part of the emission was used to image the spatial distribution of the current density. The beam was expected to filament with a diameter of the order of the skin length [115]. The goal was to resolve the finest structures imprinted by the current filaments. Therefore the optical resolution was optimized. In the following, important characteristics of the transition radiation used for imaging are summarized, then the imaging system itself is presented and fundamental definitions for optical performance parameters are summarized which form the background for the characterization and analysis.

Transition radiation

Coherent and incoherent transition radiation, respectively, have been used in a number of experiments in the context of detection and diagnosing of electron beams [40, 123, 124, 125]. Generally, transition radiation is produced by high energetic charged particles during the transition between media with different dielectric properties. It was first theoretically described by Ginzburg and Frank in 1946 [126]. The underlying physical effect is that the moving charge causes a polarization of the material. If spatially a variation of the dielectric properties is given (e.g. the charge is transiting the border between two with different polarization properties such as the metal-vacuum boundary), a transient polarization is produced which gives rise to a fast changing polarization current. Latter is the origin of the emission of electromagnetic radiation which can cover a wide spectral range (far infrared, Terahertz, optical).

In the ideal situation that a single electron is emerging from a semi-infinite metallic surface (or high-density plasma, i.e. $\omega_{pe}^2 \gg \omega^2$) into vacuum normal to the surface, the energy, $\mathcal{E}$, emitted per unit frequency dω and per solid angle, dΩ, is given by

$$\frac{\mathrm{d}^2 W_e}{\mathrm{d}\omega \mathrm{d}\Omega} = \frac{r_e m_e c}{\pi^2} \frac{\beta^2 \sin^2 \Theta}{(1-\beta^2 \cos^2 \Theta)^2}, \tag{4.1}$$

where Θ is the observation angle with respect to the electron trajectory, $r_e = (4\pi\epsilon_0)^{-1} e^2/(m_e c^2) \approx 2.818 \cdot 10^{-15}$ m, the classical electron radius and $\beta = v/c$ the velocity of the electron normalized to the light speed [127, 128]. Here the dielectric constant, ϵ, changes rapidly from $\epsilon = 1 - \omega_{pe}^2/\omega^2$ in the plasma to $\epsilon = 1$ in vacuum (step transition), where ω_{pe} denotes the electron plasma frequency. The angular emission structure is cone-shaped having a maximum at $\Theta \sim 1/\gamma$ in the case of highly relativistic electrons $\gamma \gg 1$. Here γ denotes the relativistic Lorentz factor of the electrons. The differential energy distribution that is emitted is depicted in figure 4.1.

If many, N, electrons contribute to a net current, the total optical energy emitted generally adds incoherently (addition of intensity) and scales therefore according to $W_{\mathrm{ITR}} \approx N \cdot W_e$. In the context of laser-accelerated electrons, however, the electron current is produced during the interaction time of the radiation. As a result, the electron current is strongly modulated and, as will be seen later, at high laser intensities significantly bunched. If the bunch length is short compared to the particular wavelength of the emitted radiation, the electric fields have to be added coherently and the energy emitted is then $W_{\mathrm{CTR}} \approx N^2 \cdot W_e$. In general, both COHERENT TRANSITION RADIATION (CTR) and INCOHERENT TRANSITION RADIATION (ITR) contribute to the total energy emitted. The particular distribution dependents on the spatial-temporal structure of the electron current. But in principle, however, the spatial electron beam distribution can be obtained from the spectra of the radiation emitted. A study of optical emission with particular focus on quantitative information on the calibrated emission recorded have

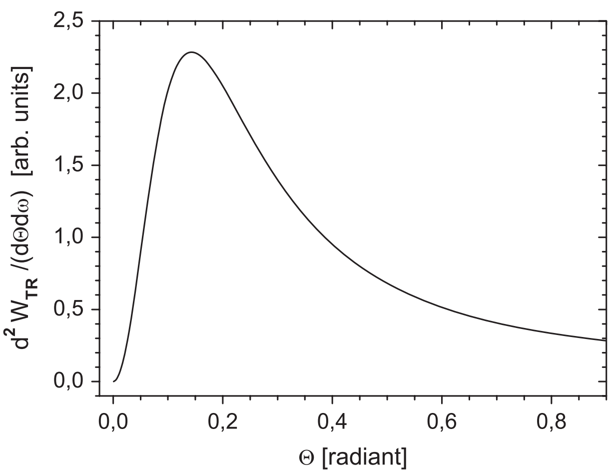

Figure 4.1: Differential energy distribution of transition radiation vs observation angle Θ emitted by an electron crossing the plasma-vacuum interface perpendicularly with a velocity v = 0.99 c.

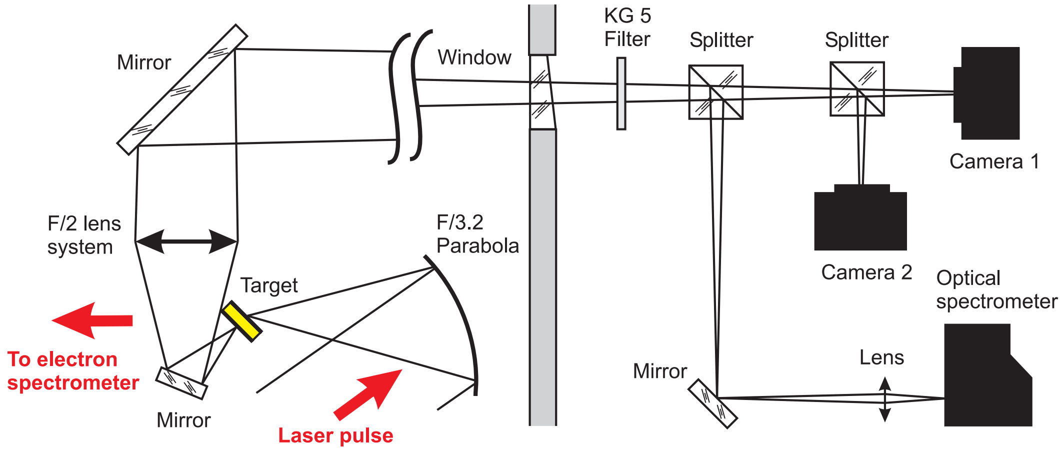

Figure 4.2: Imaging system used for diagnosing electron beam filamentation. To keep the optical axis of the main pulse clear, the beam path was folded twice inside the target chamber. To allow precise focusing of the lens, the lens holder was equipped with a motorized translation stage.

been performed by [44]. A detailed theory of the emitted radiation produced by electron bunches with arbitrary spatial and momentum distribution was recently presented by Schroeder *et. al.* by solving the Maxwell equations [127]. Note that besides transition radiation different other mechanisms potentially exist, which contribute also to an emission of radiation produced by the electron current. One candidate is synchrotron radiation, if, for instance as a result of magnetic fields or strong surface electric fields are present, the electron trajectory is bent.

The imaging system

The imaging system is depicted in figure 4.2. The multi-layered target which is described in more detail below was placed under an angle of 45° with respect to the direction of the petawatt laser pulse in order to avoid back reflections of laser energy by the plasma into the laser chain.

The laser pulse was focused with an f/3.2 off-axis parabola onto the target front side. The rear side was imaged with an f/2 projection lens (Carl Zeiss) with an effective focal length of $f = 100$ mm onto Ilford HP5-Plus black-and-white film. The magnification was $\sim 42\times$. To keep the main beam axis clear, the optical axis of the diagnostic channel was folded twice inside the target chamber using high-quality flat aluminium mirrors[1]. Stray light of the petawatt pulse was

[1]This in addition allowed to place a debris shield between the target and the projection lens.

blocked using KG 5 filters. Non-polarizing cubic beam splitters (50:50) were used to operate simultaneously cameras and optical spectrometers. In order to achieve high resolution, the spectral window of one camera was limited to a bandwidth of 10 nm around the second harmonic of the laser (527 nm) by using an interference filter[2]. The second camera integrated over the visible spectral range. Spectra of the light emitted were recorded with an optical spectrometer operating at the central wavelength of 527 nm and were detected with a 16-bit CCD camera. The spectral sensitivity range of the imaging system was about 400 to 700 nm.

Note that at high magnification, the depth of focus of the lens was of the order of microns. A measure for the tolerance on defocusing is given by Rayleigh's QUARTER WAVE CRITERION which predicts a quasi-optimum image within $\partial f = \lambda/(2U^2)$, where $U = n \cdot \sin\alpha$ is the NUMERICAL APERTURE (NA) of the lens and α the half angle between the optical axis and the outermost ray transmitted by the lens [129, 130]. In addition, the effective focal length is changing under evacuation of the target chamber. This has to be compensated during pre-shot preparations. To drive the lens to best focal position and to minimize defocus induced aberrations, an additional optical alignment set-up was added (not shown here, applied for German patent). A detailed calibration approved that the focal position of the lens could be optimized within the diffraction limited depth of focus, $\Delta z = 2\partial f \approx 11.2$ µm.

Resolving power

According to Fourier theory of optical imaging (Abbe theory), the resolution is the result of limits in the transfer capabilities of the imaging system for spatial frequencies of the object into image space. Particularly, image blurring will occur due to a damping of high frequencies. So the optics acts as a low-pass filter. The transfer capabilities of a system is related to the acceptance angle (i.e. the numerical aperture) of the optics. Mathematically this can be described by an OPTICAL TRANSFER FUNCTION (OTF), which in general is a complex function that contains an absolute value given by the MODULATION TRANSFER FUNCTION (MTF) and a phase term, the PHASE TRANSFER FUNCTION (PTF),

$$g_{\mathrm{OTF}}(\nu) = g_{\mathrm{MTF}}(\nu) \cdot e^{i g_{\mathrm{PTF}}(\nu)}. \tag{4.2}$$

[2]Note that equation (4.1) is independent from the particular frequency what indicates that broadband emission is expected. Limiting the bandwidth was advantageous as the projection objective used was not chromatically corrected.

In the case of incoherent illumination, the optical transfer function is defined in the frequency space by the Fourier transform of the intensity of the POINT SPREAD FUNCTION (PSF). Latter is the intensity distribution in the focal plane as the response of the imaging system to homogeneous illumination. For a system with a circular aperture and which is free of additional aberrations, it is the well known AIRY PATTERN. In principle, the form of the optical transfer function is characterized by a decrease from $g_{\mathrm{OTF}}(0) = 1$ to zero at the threshold frequency, ν_g, whereas the function can exhibit a more or less complex behaviour [131]. Above ν_g, no frequencies are transferred by the optics and therefore cannot contribute to information achieved in the image. The OTF of an ideal aberration-free system with a circular pupil is given by

$$g_{\mathrm{OTF}}(\nu) = \frac{2}{\pi}\left[\arccos\left(\frac{\nu}{2\nu_0}\right) - \left(\frac{\nu}{2\nu_0}\right)\cdot\sqrt{1-\left(\frac{\nu}{2\nu_0}\right)^2}\,\right], \tag{4.3}$$

with the normalized spatial frequency $\nu_0 = a/(\lambda f)$ and the CUT-OFF FREQUENCY

$$\nu_g = 2\nu_0 = \frac{2a}{\lambda f} = \frac{2\mathrm{NA}}{\lambda} = \frac{1}{\lambda f/\sharp}. \tag{4.4}$$

Here a is the radius of the lens and $f/\sharp = f/(2a)$ is the F-NUMBER of the system [131].

To determine the resolving power of the imaging system used, the relevant (contrast-) modulation transfer function was measured including beam splitters, filters and mirrors. The MTF characterizes the performance of an optical system in transfer of intensity contrast of a sinusoidal grating object pattern with the spatial frequency ν according to $g_{\mathrm{MTF}} = (I_{max} - I_{min})(I_{max} + I_{min})$. For this, the set-up was reconstructed in Düsseldorf using original components used in the experiment (except the wedged target chamber window). Details on how to measure the MTF of an optical system are given in [131, 132].
Both the theoretical and the measured MTF for the imaging system used are presented in figure 4.3 a). The curves show that the resolving power was better than 2 µm. In addition, in order to contribute to the coherent emission of optical transition radiation as observed in the experiment, the imaging quality was also checked using coherent 527 nm illumination. Figure 4.3 b) shows line outs taken from imaged using powder with grain sizes down to the micron range. The powder was imaged using incoherent (c) and coherent (d) back illumination. The interference pattern in d) is produced by the object slide. Note that the diameter of the smallest particles that could be resolved is consistent with those of the smallest filaments observed in the experiment (2.3 µm FWHM).

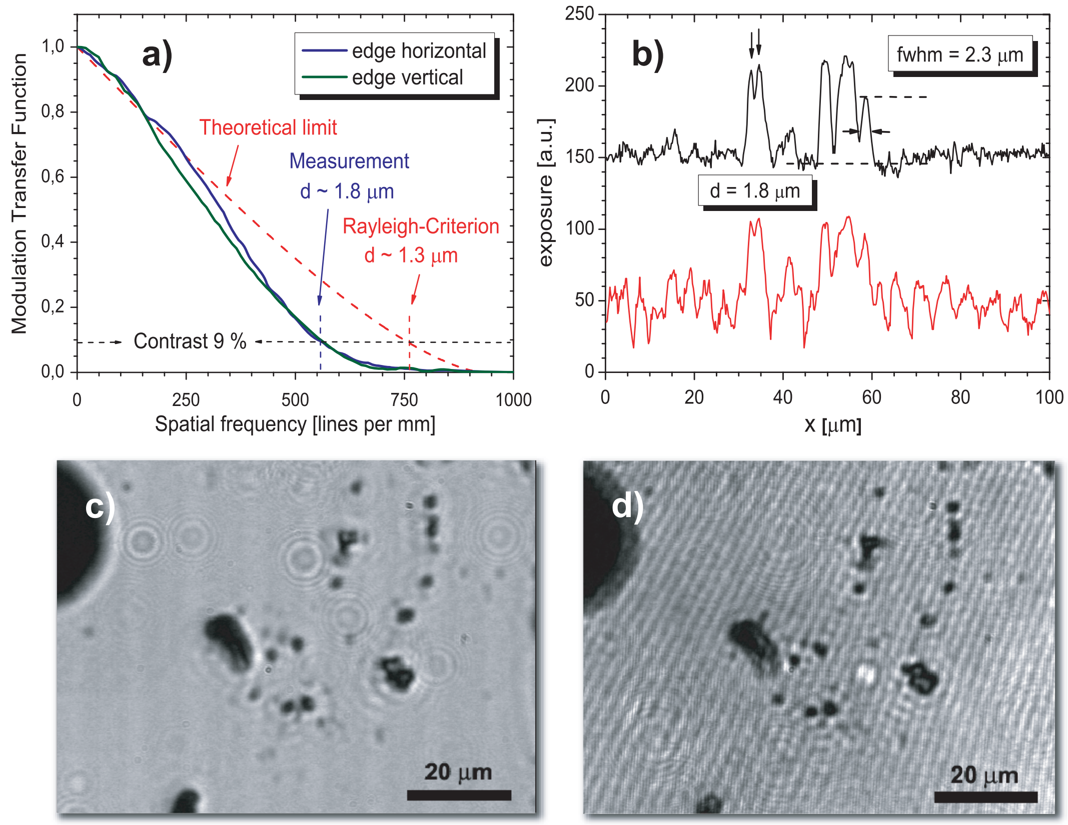

Figure 4.3: a) Modulation transfer function for the optical system used in the experiment using incoherent illumination at 527 nm. b) Lineouts taken from images obtained with grain powder using incoherent (c) and coherent (d) illumination.

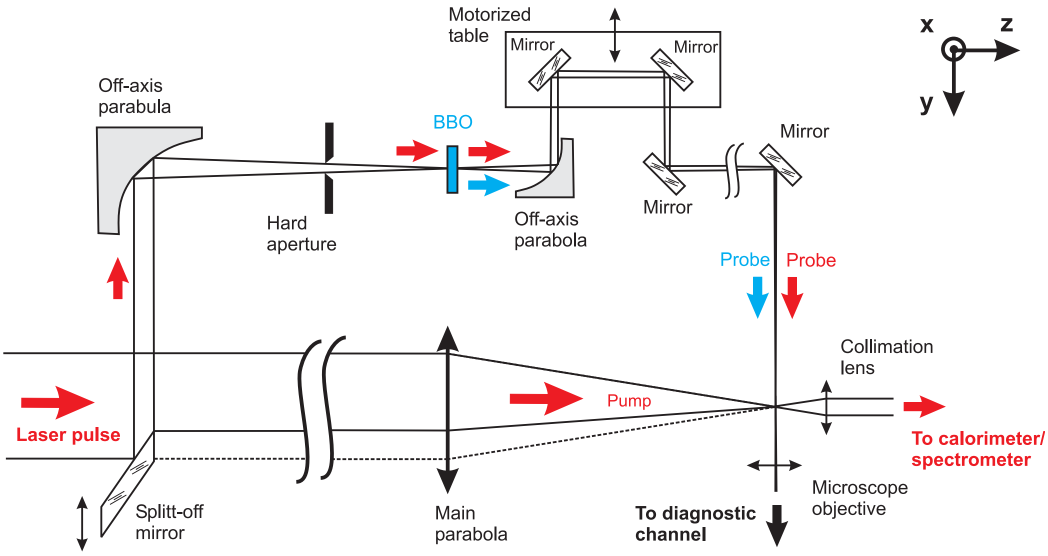

Figure 4.4: Set-up of pump-probe experiment.

4.2. Optical diagnostic for the study of ionization front propagation in gaseous targets

To examine the onset and development of a plasma channel produced by a high-intensity, ultra-short laser pulse in gaseous media, an optical probe line was set up. The diagnostic should be capable to localize the ionization front and the subsequent evolution of density gradients with high spatial and temporal resolution. Also quantitative information on the electron density had to be obtained on a timescale of femtoseconds. To meet these challenges, the techniques of time resolved shadowgraphy and interferometry were applied. In the following, the probe line and the diagnostic are presented and performance factors are addressed. Important optical properties of an under-dense plasma are summarized which describe the influence on the ultra-short probe pulse used.

The imaging system

The set-up used is depicted in figure 4.4. The probe beam was generated under vacuum by splitting off an outer part of the main beam by a moveable mirror. This happened inside the target chamber and close to the interaction region in order to improve the pointing stability of the probe beam. Then the pulse was focused by a gold-coated 90° off-axis parabola with an effective focal length of 152.4 mm and 2” in diameter. In the focus of the parabola the pulse was frequency doubled in a 40 µm thick, linear BBO crystal. The plane where the harmonic generation takes place was imaged by a second, aluminium-coated 90° off-axis parabola of 1" in diameter and a focal length of 25.4 mm into the plane of the interaction located at target chamber center (TCC). Since only a small outer part of the beam was used, diffraction was an issue. To both reduce the peak intensity on the crystal and to smooth the beam spatially, high spatial frequencies were removed by a hard aperture placed close to the Fourier plane of the first parabola. So the line-like shape of the probe beam was transformed to an ellipse and simultaneously the depth of focus of the second parabola was enlarged (order of cm). A mechanical high-precision delay line using aluminium mirrors allowed to add up to 100 mm optical path length, equivalent to a delay of $\sim 1/3$ ns of the probe with respect to the pump pulse. The position of the slider was controlled using a high-precision calliper with a resolution of ± 0.5 µm and a reproducibility of ± 1 µm. Piezo-electric driven micro-actuators allowed to control the beam position under vacuum conditions. Finally, a resolution of ± 1 µm and a reproducibility of $< \pm 2$ µm equivalent to ± 7 fs was achieved. Great care was taken not to lengthen the probe pulse in time by dispersive effects in materials by using reflective instead of refracting optics before the interaction with the plasma created by the pump pulse. Note that the lengthening due to group velocity dispersion of the pulse in the very thin BBO can virtually be neglected (refer to equation (6.5)). More important, however, is to conserve spectral bandwidth with respect to the duration-bandwidth product using broadband reflective mirrors etc. Spectroscopic measurements show hat the bandwidth of the 400-nm probe pulse was about 25 nm. This is, according to equation (6.2), sufficient for a duration of sub-10-fs. Note that the remaining infrared part of the probe beam was also transferred by the optics and could be used for probing, depending on the filter configuration used.

The plasma was imaged onto an intensified CCD. The lens used was an infinity-corrected Plan-M-Apo 10× microscope objective (Mitutoyo) with a resolving power of 1 µm and a long working distance of 33.5 mm. The depth of focus was 3.5 µm. Note that using laser gas targets in contrast to solids, no additional debris shield was needed. The effective pixel size of the camera (4 Quick E, Stanford Computer Optics) was $(11\ \mu\text{m})^2$. The modulation transfer function of a pixelated sensor is given by $g_{\text{MTF}}(\nu) = |\sin(\pi\nu\Delta x)/(\pi\nu\Delta x)|$, when Δx is the pixel size in one dimension which is related to the cut-off frequency, ν_g, via $\nu_g = 1/\Delta x$ (compare equation (4.3)) [131]. To match the Nyquist frequency, $\nu_{\text{Ny}} = 0.5 \cdot \nu_g$, with the design resolution of the optics of 1000 lpmm (lines per mm) equivalent to a resolving power of better than 1 μm at 400 nm, a magnification of $M \sim 44\times$ was chosen. This was equivalent to a sampling of 1 pixel = 1/2.06 μm on the camera[3]. From the design point this gave a resolution of better than 1 μm over a field of view of 0.37×0.28 mm^2. Again, due to the high magnification it was important to use a focusing telescope instead of a collimating one to collect sufficient light on the camera (note that a magnification of $M = 44$ means to reduce the intensity by a factor of $1/44^2 \approx 5 \cdot 10^{-4}$ if a collimated beam was used for probing). For alignment, a 50 μm in diameter tungsten wire was glued onto an edge of the gas nozzle and used to locate the best focal position. The focus could be optimized using also a separate retro-diagnostic set-up. After optimization, the position of the gas nozzle was varied and monitored by high-precision callipers attached to the translation stage.

Optical properties of plasma channel

The electromagnetic wave equation for monochromatic electric, $\vec{E}(\vec{r}, t)$, and magnetic, $\vec{B}(\vec{r}, t)$, fields can be derived from Maxwell equations (e.g. see [98]). For a homogenous plasma with an electron density, n_e, and with stationary background of ions, the wave equations are (in Gaussian units)

$$\left(\nabla^2 + \frac{\omega^2 \epsilon}{c^2}\right) \vec{E}(\vec{r}) = 0 \quad \text{and} \quad \left(\nabla^2 + \frac{\omega^2 \epsilon}{c^2}\right) \vec{B}(\vec{r}) = 0, \tag{4.5}$$

where ϵ is the dielectric function

$$\epsilon = 1 - \frac{\omega_{pe}^2}{\omega^2} = 1 - \frac{n_e(\vec{r})}{n_{cr}}, \tag{4.6}$$

of the plasma. Solutions of the wave equation are given by

$$\vec{E}(\vec{r}, t) = \vec{E}_0 \cdot e^{i(\vec{k} \cdot \vec{r} - \omega t)} \text{ and } \vec{B}(\vec{r}, t) = \vec{B}_0 \cdot e^{i(\vec{k} \cdot \vec{r} - \omega t)}, \tag{4.7}$$

respectively.

[3]The magnification is matched with the sampling theorem saying that to avoid undersampling, i.e. an overlap of the frequency spectra in Fourier space, the maximum spatial frequency, $\nu_{\max}$, contained in the signal has to be sampled according to $2\nu_{\max} = 2\nu_{\mathrm{Ny}} < 1/\Delta x$. Here $\nu_{\mathrm{Ny}} = 1/(2\Delta x)$ is referred to as the NYQUIST FREQUENCY when Δx is the size of a pixel. Note that at ν_{Ny}, the contrast transfer is decreased to about 64% and becomes zero at the cut-off frequency of the sensor, which is given by $\nu_{\mathrm{cutoff}} = 1/\Delta x$ [131].

For the electro-magnetic wave the plasma behaves like a dielectric medium in which the dispersion relation

$$\omega^2 = \omega_{pe}^2 + k^2 c^2 \tag{4.8}$$

is valid. The index of refraction of the plasma is

$$n = \sqrt{\epsilon} = n_{\mathrm{re}} + i n_{\mathrm{im}} \tag{4.9}$$

with a real and imaginary part and ϵ the dielectric function similar to a dielectric medium in classical optics [98]. In the case of an UNDER-DENSE PLASMA, where the electron plasma frequency, ω_{pe}, is smaller than the frequency of the em-wave, ω, the radiation can propagate without significant absorption and the (local) refractive index is related to the (local) electron density by

$$n(\vec{r}) = \sqrt{1 - \frac{n_e(\vec{r})}{n_{cr}}}, \tag{4.10}$$

where $n_e(\vec{r})$ is the (local) electron density and n_{cr} the critical density, respectively. In practical units, the critical density to be inserted in equation (4.10) reads

$$n_{cr} = \frac{1.1 \cdot 10^{21}}{(\lambda_L[\mu\mathrm{m}])^2}\ \mathrm{cm}^{-3}. \tag{4.11}$$

In the case of an OVER-DENSE plasma, i.e. $\omega < \omega_{pe}$, the plasma electrons can short-circuit the E-field and the wave is effectively damped. This means that it decays exponentially due to a non-vanishing imaginary refractive index, in_{im}. Note that so far a linear response of the plasma electrons on the electric field of the wave was assumed. This is valid if the intensity of the light wave is not too high (relativistic amplitude $a_0 \ll 1$). If the electrons accelerated by the E-field approach speeds close to light speed, c, the critical density has to be corrected as a result of relativistic mass increase of the quivering electrons,

$$n_{cr,\mathrm{rel}} = n_{cr}\sqrt{1 + \frac{a_0}{2}}. \tag{4.12}$$

Consequently, the laser beam can propagate through densities which are higher than for non-relativistic intensities. This effect is referred to as RELATIVISTIC INDUCED TRANSPARENCY [133, 134]. In the case of focal intensities of the order of 10^{16} W/cm^2, however, the interaction of both the pump as well as the probe beam with the plasma channel can be treated as non-relativistic.

Due to the spatial inhomogeneous intensity distribution of the focused laser pulse, an axis-symmetric plasma channel is produced with the maximum electron density close to the optical axis. The probe beam, which can be assumed to be a bunch of parallel rays covering the interaction region, is deflected according to the local refractive index. Latter is given by the local electron density, according to equation (4.10). Rays which are missing the plasma outside are not affected by electron density gradients, but eventually by changes in the refractive index of the background gas.

In the geometric-optical limit, the beam path of a probe ray through the channel can be described by the solution of the ray equation for a medium with homogeneously varying refractive index field $n = n(\vec{r})$,

$$\begin{aligned} \frac{\mathrm{d}}{\mathrm{d}s}(n\vec{u}) &= \operatorname{grad} n \\ \Leftrightarrow \frac{\mathrm{d}}{\mathrm{d}s}\left(n\frac{\mathrm{d}\vec{r}}{\mathrm{d}s}\right) &= \operatorname{grad} n, \end{aligned} \tag{4.13}$$

where $\vec{u} = \mathrm{d}\vec{r}/\mathrm{d}s$ is the tangent vector along the beam path. The index field is related to the spatial variation of the local electron density of the (under-dense) plasma. The direction of $\vec{u}$ is always parallel to the wave vector $\vec{k}$. The trajectory of the ray is bent due to gradients of the index field. Equation (4.13) shows that in the case of a (Gaussian) cylinder-symmetric plasma with a radial index distribution, i.e. $n(\vec{r}) = n(r)$, the plasma acts as a dispersing lens. In the wave picture, the phase fronts of the light wave, $\Phi(\vec{r})$, are always orthogonal to $\vec{k}$. Hence a phase front deformation (as detected by an interferometer) is equivalent to a deflection of the rays and vice versa.

Shadowgraphy

Due to the refractive index gradients, the intensity profile of the probe beam is modulated by the plasma channel. To introduce a coordinate system with the origin at target chamber center (TCC), let $+z$ be the direction of the pump pulse and $+y$ the direction of the probe pulse, respectively. Both beams are linearly polarized in the yz-plane[4]. The plasma channel is produced along the $z-$direction with a radial electron density distribution, $n_e(r)$, seen in the xy-plane. The deflection of the initial parallel probe rays leads to an increase and decrease of the intensity observed in a xz-plane located in a distance, L, behind

[4]The polarization direction of the probe beam was turned twice, first during the frequency doubling process and second due to changing the beam height (x-plane) using a periscope at the position of the second motorized mirror.

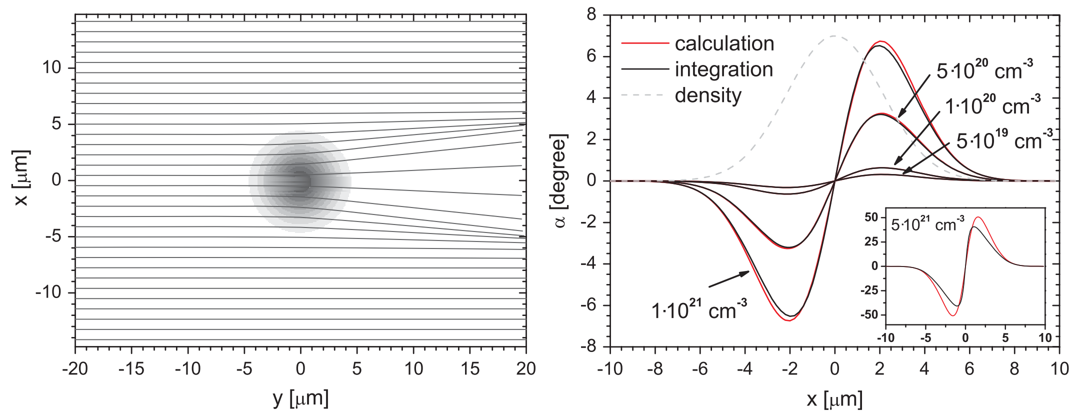

Figure 4.5: Left: Raytrace of beam deflection within a Gaussian electron density profile. The peak density is $1 \cdot 10^{21}$ cm^3, the diameter 5 μm (FWHM). Right: Comparison of the angle of deflection derived using equation 4.14 and obtained by numerical integration of the beam path. the result is shown for different peak electron densities.

the deflecting object. In the case of small deflection angles, α (in units of radiant) is given by

$$\alpha = \int \frac{1}{n} \cdot \frac{\partial n}{\partial x} \, \mathrm{d}y. \tag{4.14}$$

Here it is assumed that no rays are absorbed by the plasma. The intensity profile can in principle be detected on a film plate or detector placed in the probe beam at some distance behind the channel. This technique is called PARALLEL LIGHT SHADOWGRAPHY and has a successful history in which it usually was used to localize density gradients produced in the atmosphere by ballistic objects and combustion physics [135]. In particular, the intensity distribution in a plane located at the distance L behind the object (in the $+y$-direction) is the given by

$$\frac{\Delta I}{I_0} = \frac{\partial \alpha}{\partial x} \cdot L \propto \frac{\partial^2 n_e}{\partial x^2} \cdot L. \tag{4.15}$$

In FOCUSED SHADOWGRAPHY, however, an imaging optic is used to relay the plane onto a detection system located somewhere else. This is advantageous since the plane of interest can easily be shifted with respect to the object axis (variation of L) and further optical elements such as filters etc. can be placed in between. Here the technique of focused shadowgraphy was applied using the imaging lens to relay the plasma channel shadowgram strongly magnified onto a gated CCD.

Figure 4.5 (left) illustrates the deflection of parallel rays propagating in $+y$-direction due to a refractive index field produced by Gaussian shaped electron density distribution of 5 μm in diameter (FWHM). The beam paths were obtained by numerical integration of the ray equation using a peak electron density of 10^{21} cm^{-3}. The maximum deflection angle is about 6.5°. Figure 4.5 (right) depicts the deflection angles for different peak electron densities obtained on the same profile. The red curve illustrates the result of the integration along a straight line according to equation (4.14) and the black curve the result of a 2D numerical integration of the ray equation (4.13), respectively. For small deflection angles of about $< 10°$, equation (4.14) is a good approximation. Here the deflection angle is directly proportional to the electron density. At larger deflection angles, discrepancies due to the strong bending of the probe rays have been observed. Note that at very steep density gradients also diffraction effects are expected which eventually have to be taken into account. These are usually neglected in the geometrical approach. It is important, however, that all rays which are deflected are transferred by the imaging optics, i.e. the numerical aperture of the lens is adopted. The slope of the initial refractive index field can, in principle, be reconstructed by integration of the intensity profiles. Nevertheless, though high resolution images of the location of density gradients are obtained, it is usually difficult to reconstruct the absolute number density of plasma electrons. Therefore the technique of interferometry was used.

Plasma interferometry

In contrast to shadowgraphy, the technique of interferometry is effective in determination of plasma electron densities. This is based on the fact that in interferometry the optical path length of the rays are measured and compared, i.e. the signal is a measure of the integral $\int n \, dl$ instead of the spatial derivative of n. Nevertheless it is important to keep in mind that a non-uniform phase front deformation is physically equivalent to a deflection. As the plasma channel deflects the rays which are to be compared, experimentally a proper imaging of the plasma is of paramount importance. This requires that the imaging lens is properly focused with respect to the plasma axis.

The information obtained from an interferogram is encoded in the phase difference, $\Delta\Phi$, between a probe and a reference beam with a frequency ω according to

$$\Delta\Phi = \frac{\omega}{c} \int (n-1) \; \mathrm{d}l. \tag{4.16}$$

In the context of sub-10-fs pulses, a proper timing of the probe and the reference pulse is of paramount importance. Here the geometry of the modified Nomarski-

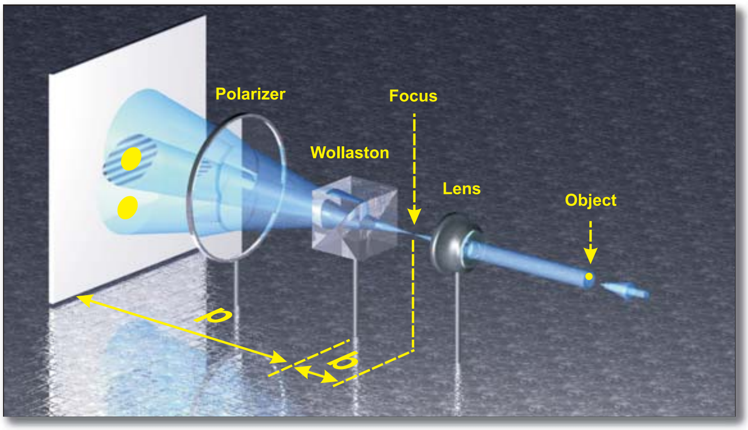

Figure 4.6: A modified Nomarski interferometer.

interferometer is advantageous due to its intrinsic symmetry. The core of the modified Nomarski interferometer is a birefringent Wollaston crystal which consists of two cemented prisms with different refractive indexes for the ordinary and extraordinary beam (refer to figure 4.6). The Wollaston is orientated in such a way that the linearly polarized probe beam is split to orthogonal polarized beams of equal intensity which are leaving the crystal under an angle ϵ. Depending on the beam diameter and the angle ϵ, both beams are partially overlapping in the image plane. If in addition a polarizer is placed behind the Wollaston which is orientated parallel to the probe beam, an interference patten is observed in the overlap region. Latter is due to the fact that the beams exiting the crystal are both polarized at 45° with respect to the original polarization direction and the polarizer, respectively. The distance of the fringes, δ, can be adjusted by choosing the distances b and p (refer to figure 4.6) according to

$$\delta = \frac{\lambda}{\epsilon} \frac{p}{b}, \tag{4.17}$$

where λ is the wavelength of the radiation used. In a modified Nomarski interferometer, basically one half of beam is used as the probe and the other half as the reference beam of the interferometer. The object to be diagnosed is placed in one half of the beam to appear in the center of the overlapping region. Note that in contrast to a classical Mach-Zehnder interferometer set-up no extra time synchronization of the arms is needed what is due to the symmetry of the interferometer. This is very advantageous in the context of ultra-short laser pulses. In the experiment, the Wollaston polarizer crystal was inserted into the beam path after the microscope objective inside the target chamber and a polarizer was placed before the camera to obtain a fringe pattern outside. Assuming radial-symmetry, the electron density can be derived from the phase shift measured by performing an Abel inversion.

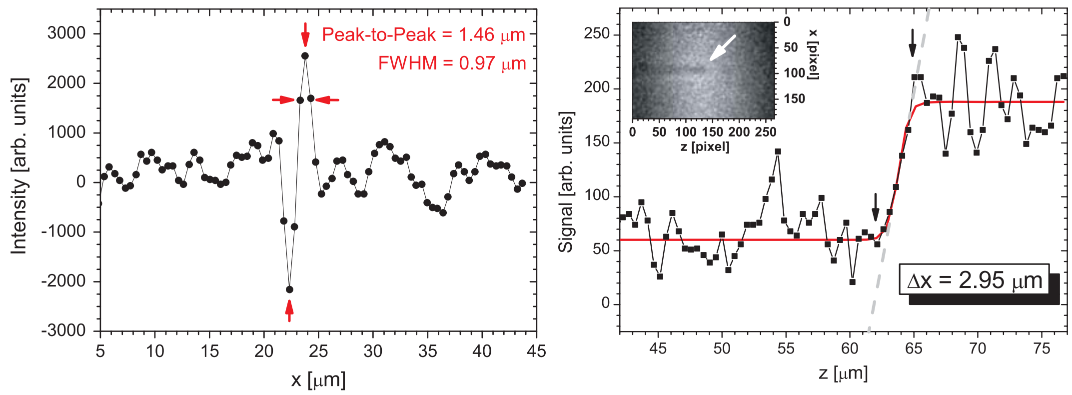

Figure 4.7: Left: Line-out across intensity pattern observed in nitrogen plasma channel using the 400 nm probe pulse. Right: Lineout along the pump pulse propagation axis during laser interaction with neutral neon. The plasma channel is shown in the inset. Maximum contrast is reached over 6 pixel as indicated by arrows.

System performance

The optical resolution of the diagnostic channel (including mirrors, apertures, filters and target chamber window) was verified under experimental conditions using the 400 nm probe pulse. Structures observed in the shadowgrams of the plasma channel with a size (FWHM) of 1 μm could be resolved. This is demonstrated on the left side of figure 4.7.

The temporal resolution obtained can be estimated from the motion blur of the plasma front itself. Due to the fact that the speed of the object is known ($\sim c$) and the ionization process itself can be approximated by a step transition, the optical resolution is reduced due to the duration of the probe pulse. This is supported by the fact that according to ADK theory, field ionization probabilities are peaked at the maxima of the electric driver field. Hence subsequent ionization of the gas will occur approximately every half-cycle at the leading edge of the 800 nm pulse as soon as an appropriate intensity is reached. Note that this sub-cycle dynamics cannot be resolved here because the duration as well as the wavelength of the 10 fs, 400 nm probe pulse is too large. Here attosecond XUV-pulses would be required.

Figure 4.7 (right) depicts the on-axis intensity observed in a typical shadowgram obtained in neon. In the inset, the main pulse is propagating from the left to the right and the position of the ionization front is close to the center of the image. A plasma channel is seen on the left side. A line-out of the signal was taken along the channel axis. The maximum contrast is reached over a distance of 6 pixel or less than 3 μm. This is equivalent to the motion blur that is expected to be produced by a sub-10-fs probe pulse, if for simplicity a rectangular pulse shape is assumed. To quantify this result, the contrast transfer function on the profile (red line) was calculated in analogy to equation (4.3), yielding a temporal resolution limit between ~ 8 fs (10%) and ~ 13 fs (50%), respectively. This result *a posteriori* confirms that a temporal resolution of about 10 fs was obtained during the experiment.

The resolution limit of the interferometer is basically determined by the minimum resolvable phase shift on the one hand and the critical density on the other. Note that due to the relatively short length, Δl, over which the probe interacts with the plasma and that is of the order of the focus diameter (i.e. < 10 µm), an error can occur as a result of a small $\Delta\Phi \propto n \cdot \Delta l$. To estimate the minimum resolvable electron density, equation (4.16) can be expanded for the plasma refractive index $n = (1 - n_e/n_{cr})^{1/2} \approx 1$, yielding

$$\Delta\Phi \approx \frac{\pi}{\lambda}\frac{n_0 \cdot Z_{av}}{n_{cr}} \cdot \Delta l, \tag{4.18}$$

where n_0 is the neutral gas density and Z_{av} the average ionization state (hence $n_e = n_0 \cdot Z_{av}$). In practical terms this yields

$$\frac{\Delta\Phi}{2\pi} \approx 5 \cdot 10^{-3} \cdot \Delta l \cdot Z_{av} \cdot p \text{ [atm]}, \tag{4.19}$$

where p denotes the local pressure of the background gas. For helium at a pressure of 1 atmosphere (1 atm $\mathrel{\widehat{\approx}} 2.69 \cdot 10^{19}$ cm^{-3}) and at an average ionization state of 2, a phase shift of 2π is obtained after a propagation length of $\Delta l \approx 100$ µm. In the interferogram this is seen as one fringe shift. In turn, assuming that the minimum detectable phase shift is about 0.1π and the channel has a diameter of about ~ 5 µm, the minimum detectable ionization is $Z_{av} = 0.7$. Hence the interferometer is insensitive to electron densities below $\sim 7 \cdot 10^{18}$ cm^{-3}.

In addition, the effect of the interaction length, Δl, for the case of constant electron density was estimated. Therefore a cone shaped volume was simulated which was filled with an electron density of $1 \cdot 10^{19}$ cm^{-3}. The phase shifting of a 400 nm probe pulse was calculated. The same fringe distance (5 µm) and spatial resolution (1 pixel $\widehat{=}$ 1/2.06 µm) as in the experiment were used. The simulated interferogram was analyzed in the same way as the experimental data. The result of the subsequent analysis is depicted in figure 4.8 and shows that at small channel diameters ($5 - 10$ µm), the electron density is generally underestimated. For a diameter of 5 µm, the uncertainty of the method is about 50%.

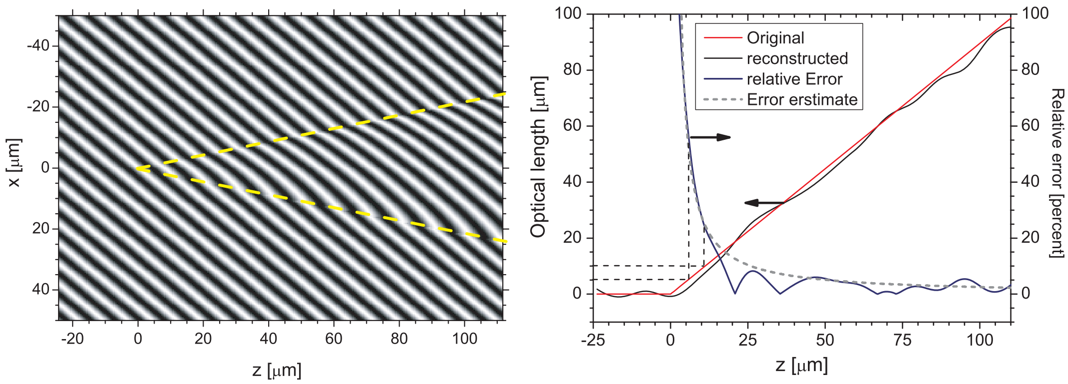

Figure 4.8: Left: Simulation of an interferogram which would be produced by a cone-shaped volume filled with a constant electron density of $8 \cdot 10^{19}$ electrons per cm^3. The tip of the cone is located at position $(0, 0)$, the diameter is increasing from zero to 48.5 µm at the right side. The interferogram has the same spatial frequency of the fringes as observed in the experiment and was also analyzed in the same way as the experimental data. Right: Estimation of the error which results from the resolution limit of the interferogram analysis. Here an electron density of $1 \cdot 10^{19}$ cm^{-3} was used.

Energy absorption measurements

To determine the fraction of the laser pulse energy which is absorbed due to ionization of the neutral gas atoms and during the interaction with plasma electrons generated, separate absorptions measurements have been performed using fast photodiodes and an Ulbricht sphere. Experimentally, the divergent laser beam behind the focus was re-collimated using a near infrared achromatic doubled with a focal length of 30 mm and less than 0.5 % reflection in the spectral range between 700 and 1000 nm. A small f-number of f/0.85 was chosen in order to collect also those rays which have potentially been deflected due to ionization induced defocusing. After re-collimation, the beam passed an un-coated BK7 window and was dumped into an Ulbricht sphere of 9.5 cm in diameter and an entrance hole of 3.0 cm in diameter. The inner of the sphere was painted with white Barium Sulphate ($BaSO_4$) having a high diffuse reflectivity of better than 95 % in the spectral range between 300 nm and 1.300 nm. The fraction of the energy that is re-emitted by the inner surface of the Ulbricht sphere was measured by a fast silicon photodiode with 1 ns rise time in photoconductive operation mode and reversed biased with 60 V. Simultaneously, the laser energy was monitored using a second fast silicon detector with a bandwidth of 2 GHz and internally biased for a minimum rise time of 175 ps. The fraction of the light reflected by an AR-coated quartz window of 1 mm thickness through which the

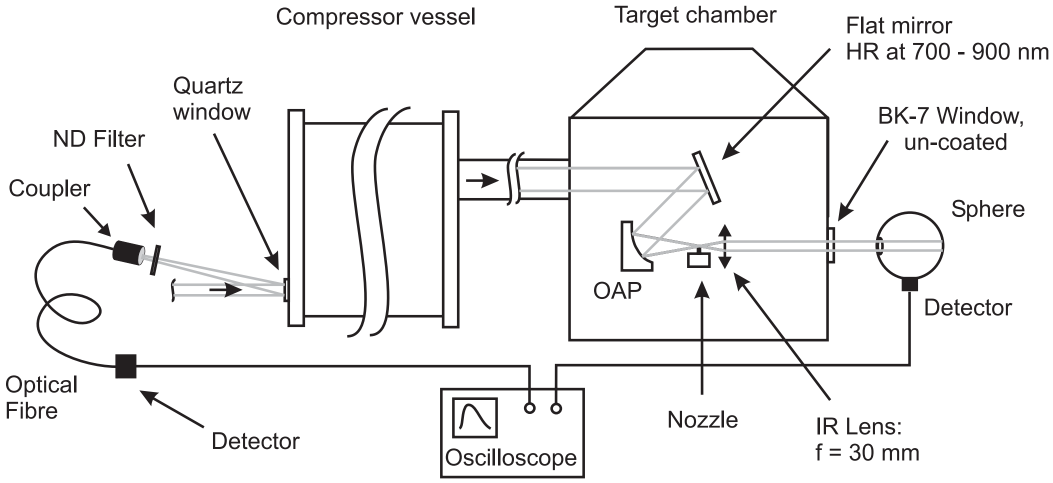

Figure 4.9: Schematic of the experimental set-up for the absorption measurements.

beam enters the compressor was coupled into an optical fibre connected to the diode. Due to the pressure difference, the entrance window of the compressor was slightly bent so that the reflected light was focused. The entrance of the fibre was placed at the focus. The diode signal gave a reference for the pulse energy per shot and was used to monitor the temporal stability of the laser energy. To keep the absorbed energy on a level below detector saturation would occur, the energy of the beam was attenuated by calibrated ND grey filters. The response of the diodes was both recorded by a 2 GHz oscilloscope. A schematic of the experimental set-up is shown in figure 4.9.

The linearity of the response of the photodiodes was carefully checked in the relevant energy range, i.e. up to 150 μJ on target. In order to reduce typical noise contained in the data, each diode signal was post-processed and fitted by an asymmetric double sigmoid peak function. A program was written to perform the fits where a Marquardt optimization algorithm was used. By taking the peak value and the area under the curve of the fit function, however, the noise could be well reduced. In addition, each data point was averaged over at least ten shots.

Since ionization of the gas can lead to ionization-induced defocusing of the driving beam, it was also important to check if the laser pulse was deflected in such a way that it missed the entrance of the Ulbricht sphere. Therefore the sphere was shifted to different positions (+30 cm and +60 cm, respectively) and the energy collected was measured for different backing pressures up to 52 atmospheres. Here argon was used as test gas due to its low BSI-intensities what should lead to strong ionization defocusing of the pump pulse. As the same signal was obtained at different positions, ionization induced defocusing had no effect on the absorption measurements.

Optical spectroscopy and calorimetry

In order to measure the effect of the plasma interaction on the main pulse, the Ulbricht sphere was removed and the beam was coupled into a symmetrical Czerny-Turner spectrometer using a hollow fibre. The spectrometer had a focal length of 75 mm (AvaSpec-2048) and was equipped with a grating of 300 lines per mm that was blazed at 300 nm. With a fixed slit size of 10 μm, a spectral range of about 350 to 1100 nm was covered with a resolution of 0.8 nm (line width FWHM). A calibrated halogen lamp was used for intensity calibration, a green, red and infrared laser for wavelength calibration.

Single pulse energy measurements were obtained using a large-area amplified pyroelectric detector (Molectron J50LP-4A-2K), connected to an energy meter (EPM1000 by Coherent). The typical calibration uncertainty was of the order of 2 percent.

5. Laser gas target development

In this chapter, the laser-gas target used in the experimental part of the thesis is described. Generally, pulsed gas targets are applied whenever laser intensity or pulse duration require to guide the beam in vacuum prior to the laser-gas interaction. Particularly using sub-10-fs pulses, it was needed in order to avoid an increase in pulse duration due to group velocity dispersion. In this context, a supersonic, high-density laser-gas target was developed and optimized for both a high mass flow and a short response time. In particular, a commercial valve was modified in such a way that it was applicable to drive supersonic nozzle types recently suggested by Semushin and Malka [136]. These nozzles were ascribed to produce a close to flat-top density profile with steep density gradients at the edges. The spatial gas jet profile generated was analyzed independently by 2D computational fluid simulations and interferometry. Because the nozzles required a high mass flow rate, a short response time of the gas jet target was of paramount importance to maintain good vacuum conditions. This was in particular relevant for the set-up because the target chamber volume used was relatively small. In order to optimize the response time, a semi-analytical model for the time dependence of the mass-flow was developed. The model has clearly shown that the volume between the valve and the nozzle throat is critical parameter for the response time. An optimized gas target was constructed by introducing a compact combination of valve and nozzle. Time-resolved interferometry of the gas jet produced shows that the built-up time of the flow could be reduced to < 3 ms while simultaneously densities of $3 \cdot 10^{20}$ cm^{-3} using a Mach 3.3 expansion (evaluated at a height of 500 μm above nozzle exit) were obtained. In addition, the design allowed an easy exchange of the expansion rates (Mach numbers) during an experiment. A repetition rate of 0.2 Hz using high backing pressures of ~ 50 bars was obtained.

5.1. The gas target design

A gas target consists of a reservoir of gas under high pressure (typically few atmospheres), an electrically controlled valve and a nozzle close to the laser focus. If the valve is fired, a gas flow driven by the backing pressure of the reservoir into the target chamber is triggered. As soon as a steady-state flow has developed, the laser is fired into the gas which exits at the nozzle and expands into vacuum. So locally, gas densities of up to few 10^{21} particles per cm^3 can be produced in the vacuum vessel [137, 138, 139].

The density profile of the jet can be shaped by the nozzle geometry. In the simplest case of a circular orifice, a sub-sonic (”free”) expansion into vacuum is produced. The density drops exponentially along the flow direction with increasing distance from the orifice. In the perpendicular direction, the profile has a Gaussian shape which is increasing in width. The disadvantage of this geometry is clearly the inhomogeneity of the density profile. In addition, if a high intensity laser pulse is focused into the gas jet, ionization induced defocusing may occur in the wings of the density profile. This potentially limits the focusability of the beam.

To obtain a more homogeneous density profile, Semushin and Malka recently suggested numerically optimized nozzle geometries in order to produce supersonic expansions which show a plateau-like density profile close to the jet axis together with steep gradients at the edges [136]. This profiles are in particular useful to keep the gas density constant over long (i.e. several mm) interaction lengths. The ”edge” of the gas jet is defined by the location of the largest density gradient.

The homogeneity implies that a stable (i.e. steady state) gas flow has developed prior to the laser is fired. From applications using technical gases it is known, that this requires a passage of at least 0.5 mm in diameter through which the gas can stream from the high to low pressure side. In smaller passages, high frequency density modulations develop which lead to a self-clogging of the flow [140]. (This is also the reason for characteristic high frequency noise produced by a gas under high pressure that can escape through a small leakage of a compressed air bottle). This limit, in turn, defines high demands on the mass flow capability of both the duct and the valve. Hence for the design of a supersonic gas target it is important that besides the gas jet shaping also the performance of the flow system is considered.

Governing equations for compressible fluid flow

In order to quantify the relevant parameters such as mass flow, $\dot{m}$ (in kg/s), temperature, T (in Kelvin), pressure, p (in Pascal), and density, ρ (in kg/m^3), in the following the governing equations for compressible fluid flow are reviewed. Using an 1-dimensional model, the flow is guided through a duct with a variable cross section, A. It was assumed that the compressible fluid is a perfect gas (that is justified in the case of noble gases) and that the flow is isentropic (i.e. adiabatic and frictionless). The maximum velocity at which pressure disturbances can be transported in the fluid is given by the sound speed,

$$a = \sqrt{kR_S T}, \tag{5.1}$$

where $k = c_p/c_v$ is the ratio of the specific heats of the gas at constant pressure and constant volume, respectively, and R_S the specific gas constant. The ADIABATIC CONSTANT, $k = 1 + 2/f$, is given by the number of the degrees of freedom, f, in the molecules. Values of k and R_S for the gases used during the experiment are listed in table 5.1. If the gas is at rest (e.g. sealed in the reservoir), p_0, ρ_0 and T_0 denote the STAGNATION PRESSURE, DENSITY and TEMPERATURE, respectively. The inner energy of the gas is stored in form of random kinetic motion of the particles (when potential energy is neglected) and is measured as temperature. In a flow, a part of this random kinetic energy is transformed into directed motion and the (local) temperature of the gas decreases accordingly. The MACH-NUMBER is defined by the velocity of the flow, v, with respect to the sound speed, $M = v/a$. The flow is called sub-sonic for $M < 1$, sonic for $M = 1$ and super-sonic for $M > 1$, respectively. Due to energy conservation, if at any point in the duct a probe of the fluid is brought to rest and tested, the stagnation values are obtained. This is the reason why M^2 can be interpreted physically as the ratio of directed kinetic energy to random kinetic energy. Note that the Mach number is usually associated with super-sonic flow, but it is well defined also in the sub-sonic regime.

Under the assumption that the flow is isentropic, the variables of state, i.e. temperature, T, pressure, p, and density, ρ, become one-dimensional functions of the local Mach number [141]. The property ratios for the steady one-dimensional isentropic flow of a perfect gas are given by

$$\frac{T_0}{T} = \left(1 + \frac{k-1}{2} M^2\right) \tag{5.2}$$

$$\frac{p_0}{p} = \left(1+\frac{k-1}{2}M^2\right)^{k/(k-1)} \quad (5.3)$$

$$\frac{\rho_0}{\rho} = \left(1+\frac{k-1}{2}M^2\right)^{1/(k-1)}. \quad (5.4)$$

Note that gases with the same adiabatic constant k will behave similar. Hence the properties of the expansion are similar if different noble gases are used.

To optimize the design of a laser-gas target, it is of fundamental importance to consider that a maximum Mach number of $M = 1$ is obtained at the location of the minimal cross section, $A^\star$, of the duct. Here the speed of the gas equals the local sound speed. To illustrate this, let the valve separate two reservoirs which are initially at the same pressure, p_0 and p_1, respectively and which both are connected by a pipe system. If the valve is opened and the background pressure p_1 is reduced, a flow is started. As already mentioned above, the pipe system (including valve, connectors and nozzle) may be described as an one-dimensional duct with variable cross section, A. Let the minimal cross section, A^*, be located somewhere in the duct. The isentropic mass flow rate, $\dot{m}$, between the two reservoirs is then given by [141]

$$\dot{m} = \frac{\mathrm{d}m}{\mathrm{d}t} = \frac{p_0 \Psi A^*}{\sqrt{k R_S T_0}}, \quad (5.5)$$

with a flow factor, Ψ. Latter is a function of the expansion ratio, p_1/p_0, and given by

$$\Psi = \left[\frac{2k^2}{k-1}\left(\frac{p_1}{p_0}\right)^{2/k}\left[1-\left(\frac{p_1}{p_0}\right)^{(k-1)/k}\right]\right]^{1/2}. \quad (5.6)$$

With increasing pressure difference, the Mach number and hence the mass flow is increased until the gas is accelerated to sound speed, $M = 1$, at the location of $A^\star$. The mass flow, $\dot{m}$, cannot be increased by further expansion of the gas; the flow is "chocked". The physical reason for this is that pressure disturbances

Table 5.1: Adiabatic constant and specific gas constant for gases used in the experiment.

	Helium	*Neon*	*Argon*	*Nitrogen*
k	1.667	1.667	1.667	1.4
R_S [J/(kg·K)]	2077	411.9	208	296.6
ρ [mg/mol)]	4.003	20.18	39.94	28.02

such as a rarefaction wave are transported with the sound speed. Consequently, when the pressure p_1 is below the critical pressure, the rarefaction front cannot propagate upstream the throat. Hence a further reduction of the background pressure has no effect on the flow speed. The flow factor saturates at a maximum of

$$\Psi^* = k \left(\frac{2}{k+1} \right)^{\frac{(k+1)}{2(k-1)}} . \tag{5.7}$$

The maximum mass flow rate is hence fundamentally limited by the minimal cross section, $A^\star$, and the gas type. Explicitly, for an one-dimensional isentropic flow it is given by

$$\dot{m} = \sqrt{\frac{k}{R_S}} \frac{p_0}{\sqrt{T_0}} \left(\frac{2}{k+1} \right)^{\frac{(k+1)}{2(k-1)}} A^\star . \tag{5.8}$$

In turn, the local Mach number at any point of the duct, is completely described by the local cross section. The area-Mach relation for isentropic flow of a caloric perfect gas is given by

$$\frac{A}{A^*} = \frac{1}{M} \left[\left(\frac{2}{k+1} \right) \left(1 + \frac{k-1}{2} M^2 \right) \right]^{\frac{k+1}{2(k-1)}} . \tag{5.9}$$

If $M = 1$ is satisfied at the nozzle throat (with a given diameter), the expansion characteristics of the flow can easily be derived from the CRITICAL VALUES,

$$T^* = \left(\frac{2}{k+1} \right) T_0 \tag{5.10}$$

$$p^* = \left(\frac{2}{k+1} \right)^{k/(k-1)} p_0 \tag{5.11}$$

$$\rho^* = \left(\frac{2}{k+1} \right)^{1/(k-1)} \rho_0 \tag{5.12}$$

$$a^\star = \sqrt{k R_S T^\star} . \tag{5.13}$$

Physically this means that the conditions at the nozzle throat are fully determined by the stagnation values of the gas (i.e. backing pressure of the valve at *closed* position). This illustrates the importance in the design to ensure that the minimum cross section of the duct is the nozzle throat (and e.g. not inside the valve). Since supersonic nozzles require a Mach number of $M = 1$ at their throat, an important design criterion for a laser gas target is to ensure an optimum mass flow rate for a given valve-nozzle system. If a smaller cross section is present anywhere else in duct, the mass flow and the maximum achievable density at a given backing pressure p_0 are limited. Equation (5.8) shows also that the best way to increase the density of the gas jet is to increase the backing pressure of the valve.

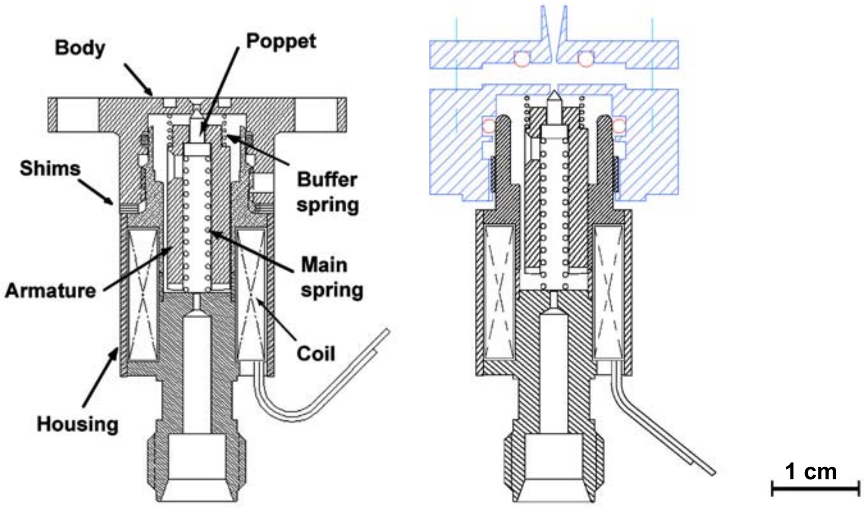

Figure 5.1: Left: Schematic of series 9 valve [142]. Right: modified valve with supersonic Mach 5.5 nozzle (shims are not drawn). The vertical lines indicate the position of fixing screws which allow for a quick exchange of the nozzle type.

5.2. Optimization of gas flow

To control the gas flow, a fast valve with a low leak rate was required. Chosen was a commercial solenoid pulse valve produced by Parker Hannifin (series 9) [142]. It meets the requirements of both a fast response time of a few hundreds of microseconds and a high-level vacuum sealing so that it is suited for applications in ultra-high vacuum. In addition, it is delivered with a control unit including a delay generator that produces a high-voltage sequence adapted to the coil impedance in order to shorten the opening cycle. Figure 5.1 (left) shows a cross section of the valve. The sealing is performed by a Teflon poppet closing an orifice in the flange body which had a diameter of (0.78 ± 0.01) mm. The valve is specified to operate at backing pressures of up to 85 atmospheres (1 atm = 14.7 psi) and high repetition rates up to 120 Hz. The drawback of the series is that it supported either high mass flow or high backing pressure. The factory specification for the mass flow was > 1 l/min for nitrogen at 981 mbar backing pressure.

Though the orifice diameter of the valve was nominally larger than that of the nozzle throat (0.5 mm in diameter), the effective cross section and net mass flow were more relevant. In order to determine $A^\star$ and to clarify that the flow through nozzles would not be choked, the maximum mass flow of the valve was validated experimentally. In a first step, a calibrated mass flow regulator and a precise membrane pressure gauge was used to determine the volume of the target chamber, V_{Ch}, by monitoring the increase of pressure with time. Using the ideal gas law and the mass flow known one obtains

$$V_{\mathrm{Ch}} = \left(\frac{\Delta p}{\Delta t}\right)^{-1} \frac{\Delta N}{\Delta t} k_B T_0, \tag{5.14}$$

where $\Delta p/\Delta t$ denotes the pressure increase (in mbar/s), $\Delta N/\Delta t$ is the number of molecules conveyed per second, T_0 the room temperature of about 293 K and k_B the Boltzmann constant. A relatively low flow of 1 standard liter per minute was chosen in order to avoid energy losses due to friction or turbulence. The advantage of this procedure is that it produces small error bars due to a linear fit can be applied. The volume of the target chamber was obtained as $V_{\mathrm{Ch}} = (0.369 \ \pm 0.017)$ m^3.

In a second step, the fact was used that the mass flow is limited by the minimum cross section, $A^\star$ (equation (5.8)). The pressure inside the evacuated chamber rises with time due to the "leak" that is introduced when the valve is opened. The leak rate is defined by the product $\Delta p \cdot V$ divided by the time interval Δt. Since the volume of the chamber was known, the size of the "leak", i.e. $A^\star$, could be obtained from the pressure increase with time, $\Delta p/\Delta t$. One finds

$$\frac{\Delta p}{\Delta t} V = \sqrt{k R_S T_0} \cdot \left(\frac{2}{k+1}\right)^{k+1/2(k-1)} \cdot p_0 A^\star \,. \tag{5.15}$$

In order to validate the performance of the valve, the flow with and without poppet was measured. Different gas types were used and the flow was normalized to atmospheric pressure, i.e. $p_0 = 1$ atm. Without poppet, a good agreement between the measurement and the prediction of the mass flow formula for a throat diameter of 0.78 mm has been obtained. If the poppet was inserted, however, an effective throat diameter of only ~ 0.3 mm has been obtained. This shows that the maximum mass flow was significantly reduced by the popped what leads to a lower measured throat diameter.

On the left side of figure 5.2 the leak rates obtained are shown. Note that using air at atmospheric pressure, a leak rate of 18.6 mbar l/s was observed, what is in good agreement with the factory specifications. The mass flow rate of the valve was therefore lower than that required for the use in combination with nozzles with 0.5 mm throat diameter as suggested by Semusin and Malka. A more detailed examination has shown that the reason for this is given by the design of the valve, in particular by a limit in the stroke of the armature. Latter could not be increased simply due to the fact that the magnetic force of the magnet on the armature was limited and furthermore dependent on the rest position within the valve. (This position could be varied by changing the number of shims, compare

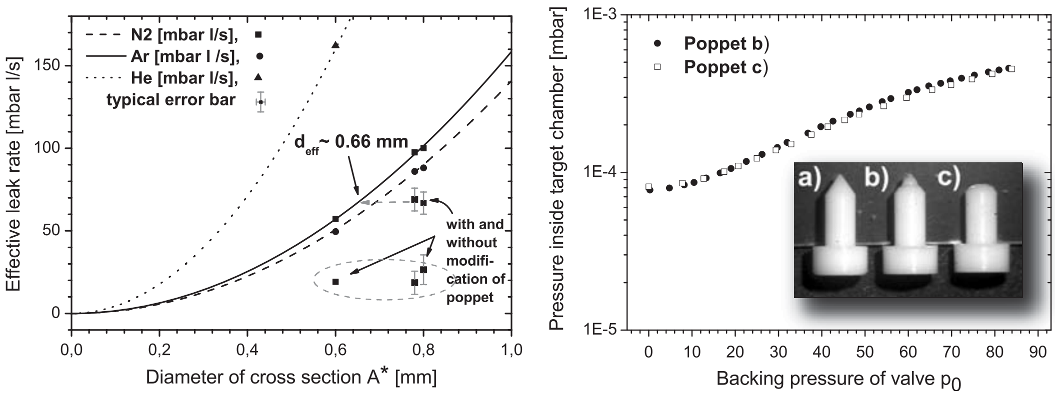

Figure 5.2: Left: Leak rate due to the mass flow into the target chamber for different gases as a function of the diameter of the duct. Measurements using the original flange correspond to a diameter of 0.78 mm, those using the modified flange to a diameter of 0.8 mm. If the nozzles are attached, the diameter is reduced to 0.6 mm. A significant higher mass flow is observed if the poppets are modified as described below. Right: Target chamber pressure at different backing pressures of the valve using an original and a modified poppet. Inset: Virgin poppet (a), same after several hundreds operating cycles of the valve (b) and after subsequent modification (c).

figure 5.1). The optimum working point was the result of a force balance given by the gas pressure and the orifice diameter on the one hand and the magnetic and spring forces on the other.

In order to optimize the mass flow, both the flange body and the sealing poppet were modified. Therefore a series of design variations was tested experimentally. In addition, the settings for the electric high-voltage sequence generated by the driver unit were adapted. The modified flange body is illustrated on the right side of figure 5.2. The orifice had a slightly larger diameter of 0.8 mm what was limited by the maximum tractive force of the magnet and the gas pressure, respectively. After several minutes of operation, a virgin poppet was cut above the contact point with the flange body. The inset in figure 5.2 shows a virgin poppet (a) beside one after several hundreds of opening cycles (b). The deformation of the material due to mechanical pressure forces that leads to the sealing can clearly be observed. The third poppet shown (c) was modified by cutting the overlapping tip under a microscope. The result was a significant increase of the leak rate to 69.7 mbar l/s with a good reproducibility. The gas outflow of the valve could be increased to 3.7 l/min at 981 mbar. A very good reliability of the mass flow performance and a linear increase with increasing backing pressure was observed up to about 90 atmospheres. The sealing capability of the valve was not affected. This is illustrated on the right side of figure 5.2. Here the chamber

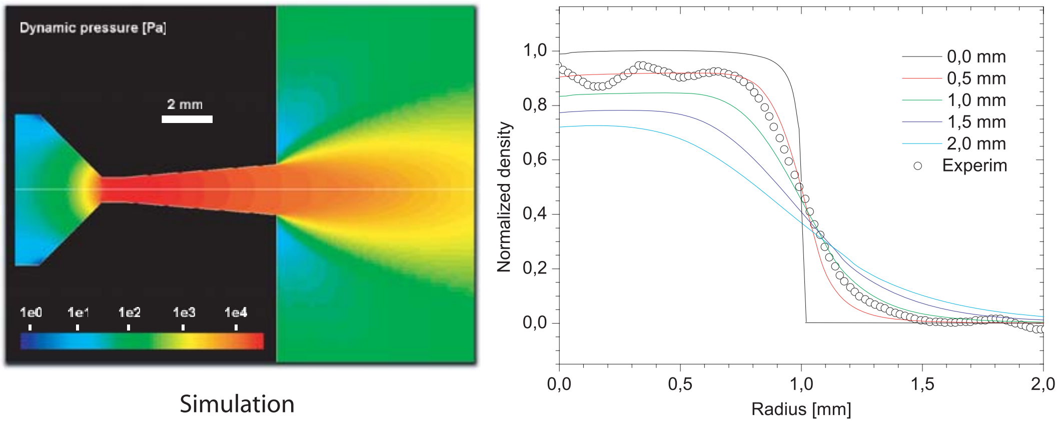

Figure 5.3: Left: Dynamic pressure of supersonic (Mach 3.5) nozzle suggested by [136] obtained by CFD-simulation. Right: Density profiles in radial direction obtained from simulation for different heights above the nozzle exit and experiment.

pressure after ten minutes pumping with the turbo-molecular pump connected to the chamber is shown. In both cases of using the original and the modified poppet, the same leak rate has been observed.

2-Dimensional fluid flow

To calculate the maximum mass flow and the properties of the gas within the duct, the model of 1-dimensional frictionless fluid flow of a perfect gas can be used. To obtain spatial profiles across the stream, however, one has to rely on numerical fluid simulations. This technique is called COMPUTATIONAL FLUID DYNAMICS (CFD). Compressible fluid flow simulations in 2D geometry (due to the axial symmetry of the problem) were performed with the industrial simulation tool FLUENT. In particular, FLUENT solves iteratively the full steady-state and transient Navier-Stokes equations in two- or three-dimensional geometries on a grid using a finite volume method. The coupled set of partial differential equations includes conservation of mass, momentum and energy. In a first step, the geometry and the grid is defined which forms a computational domain to solve the flow equations. Then the materials and boundary conditions are set. According to the flow conditions (viscid, laminar, Reynolds number etc.), an appropriate solver is chosen and the solution iterated. Finally, the result is analyzed by a post-processor and can be visualized.

On the left side of figure 5.3, a map of dynamic pressure obtained from 2D-CFD simulation is depicted. The divergent part of the nozzle is conically shaped and the diameter increases from 1 mm at the throat to 2 mm at the exit. The length of the divergent passage is 6 mm. A jet with a Mach number of $M = 3.5$ is produced at the exit. The expansion characteristic of the jet into vacuum is clearly supersonic. On the right side of figure 5.3 the density profiles obtained for different heights above the exit are shown. The result of the interferometrical measurement is also shown. The density was evaluated at a height of 500 µm. A good agreement between simulation and experiment is observed.

5.3. Optimization of time response

Usually, valve and nozzle form separate parts of a laser-gas target and are both mechanically connected by some duct (e.g. compare figure 7 in [136]). This volume is under vacuum prior the valve is fired, and to obtain maximum mass flow through the nozzle, first a pressure similar to p_0 must been built up in there. The time required for the pressure to built-up depends on the volume size, the speed of the valve and the mass flow in and out, respectively. Hence both the mass flow of the valve and the geometry of the connection with the valve have direct influence on the response time of the target.

In order to describe the dynamics of a gas target, the governing differential equations for the mass flow trough the valve on the one hand and through the nozzle on the other were coupled and solved numerically. Parameters were the size of the volume, the dimensions of the constrictions and the gas type. The valve was treated as converging duct with a (time-dependent) effective annulus given by the poppet position. Thus the effect of choking mass flow rate was fully included in this model for all times. The division of the problem in flow and stagnation zones is illustrated in figure 5.4. Using the ideal gas law and writing the pressure increase as a function of mass flow, the corresponding differential equations are obtained:

$$\frac{\mathrm{d}p_0(t)}{\mathrm{d}t} = 0 \tag{5.16}$$

$$\frac{\mathrm{d}p_1(t)}{\mathrm{d}t} = \frac{\mathrm{d}m_1\big(p_0, p_1(t), A_1(t)\big)}{\mathrm{d}t} \cdot \frac{N_A}{m_{mol}} \cdot \frac{k_B T_0}{V_1} \tag{5.17}$$

$$\frac{\mathrm{d}p_2(t)}{\mathrm{d}t} = \frac{\mathrm{d}m_2\big(p_1(t), p_2(t), A_2\big)}{\mathrm{d}t} \cdot \frac{N_A}{m_{mol}} \cdot \frac{k_B T_0}{V_1}. \tag{5.18}$$

The stagnation pressures p_1 in the volume V_1 and p_2 in the target chamber with the volume V_2 depend on the mass flow (equation (5.8)) through the valve and the nozzle, respectively. To define a pressure inside volumes V_1 and V_2, simply $T = T_0$ was assumed. Moreover, since the valve is connected to a gas reservoir with constant stagnation pressure p_0, $V_0 \gg V_1 + V_2$ was assumed.

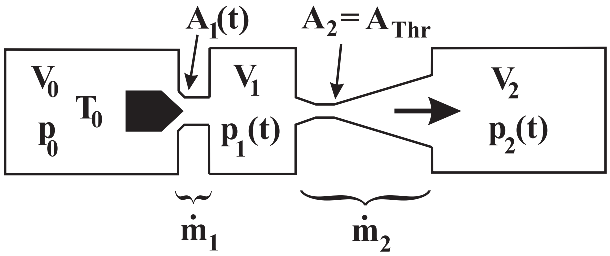

Figure 5.4: Model of flow and stagnation zones for a given valve-nozzle combination. The volume of the connection is denoted as V_1, whereas p_0, T_0 are the stagnation pressure and temperature in the gas reservoir V_0.

Decoupling the flow regimes and the stagnation values in V_0 to V_2 allows to solve the differential equation for the stagnation values. A model for the time dependence of the poppet position inside the valve was prior deduced from an experiment. In particular, a wire was attached to the poppet tip and imaged onto a gated CCD. Then a time series of the poppet position as function of delay time between triggering the valve and the camera gate was taken. From this measurement, $A_1(t)$ was obtained. The result was that the armature is accelerated after a delay of $\sim$ 350 µs with respect to the moment when the driver receives a trigger signal. The armature and the poppet arrive at the end-position at about 2 ms after the trigger signal. Hence the minimum delay between firing the laser pulse into the gas jet is of the order of 2 ms, if just the mechanic of the valve was considered. In contrast, the simulation clearly shows that if a realistic cross section of about 0.66 mm in diameter for the valve is assumed, together with nozzles having throats of 0.5 mm in diameter, a connection volume of about 1 cm^3 leads to an increase of several tens of milliseconds already. Hence to optimize the response time, the volume in between valve and nozzle was minimized. In the modified version of the gas target, the nozzles were attached to the flange in a way illustrated on the right side of figure 5.1. Here the volume of the connection was about 1 mm^3.

In order to validate this result experimentally, two different gas target set-ups were analyzed. The reference system was an (un-modified) series 9 valve connected to a Mach 3.5 nozzle with a throat diameter of 1 mm and an exit diameter of 2 mm. The set-up is shown in figure 5.5. Here a volume of about 1 cm^3 remains between the valve exit and the nozzle throat. The second target was the modified valve with nozzles connected closely to the flange body as depicted on the right side of figure 5.1. The throat diameters of the supersonic nozzles attached were 0.6 mm instead of 0.5 mm as suggested by Semushin and Malka.

This was the lower limit at which the mechanic workshop could guarantee a symmetric orifice. Note the difference in the size of reference and the modified target set-up. Time resolved interferograms of the gas jet were obtained using a modified Nomarski interferometer [143]. The nozzles were imaged with a resolution of 50 pixels per mm onto a gated high speed CCD camera using an expanded 532 nm diode laser beam and an achromatic lens with a focal length of 300 mm. The time resolution was 1 μs, set by the gating interval. The target chamber was evacuated to at least 10^{-1} mbar between the shots. In the experiment, the backing pressure was 41 ± 1 atmospheres of argon and the gas densities were evaluated 500 μm above the nozzle exit. The result is shown in figure 5.6. In the case of the reference system, the delay until a stationary flow regime was obtained is about 30 ms (a). In contrast, with the modified flange body, the delay is of the order of 3 ms (c). Note that a density of about $3 \cdot 10^{19}$ particles per cm^3 is obtained though the throat diameter is about 0.6 mm instead of 1 mm and a higher Mach number is used (5.5 instead of 3.5). As also shown in figure 5.6, the maximum density using the reference system could be doubled by modifying the poppet as described above (b). The dynamics is not affected as the build-up time of the flow remains unchanged. Nevertheless, the Mach 3.5 nozzle is still under-performing due to that the flow is chocked by the valve. Note that a density of $1.8 \cdot 10^{20}$ particles per cm^3 was predicted at the nozzle exit [136].

The results obtained from the model calculation are also shown in figure 5.6. To extrapolate the densities at the nozzle exit to that at a height of 500 μm above, the density gradient obtained from the interferograms was used. Table 5.2 depicts the parameters chosen in order to reproduce the measurement. Though the model of 1-dimensional isentropic flow is rather simple, a good agreement between measurement and computation is observed. The difference in the estimate

Figure 5.5: Mach 3.5 nozzle head connected to series 9 valve. The inset shows the modified head applied with a Mach 5.5 nozzle. The outer diameters of the nozzles are 4.1 and 2.1 mm, respectively.

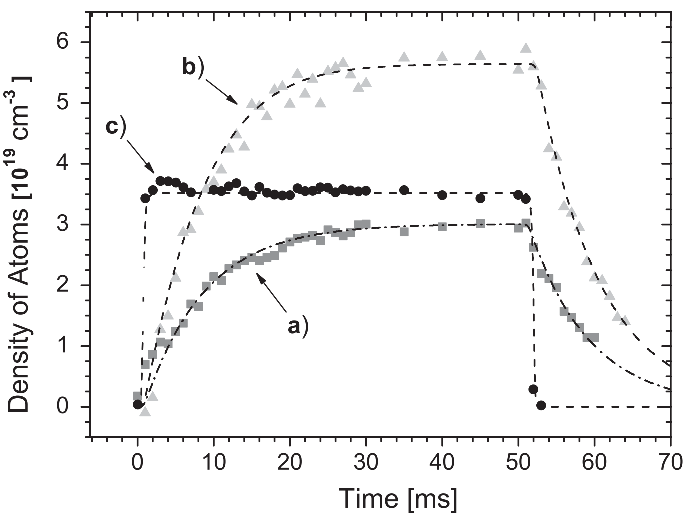

Figure 5.6: Figure 4. Measured and calculated history of atomic density at 500 µm above nozzle exit for a) M = 3.5 nozzle and using an unmodified poppet, b) same but using a modified poppet, c) M = 5.5 nozzle and modified head as well as flattened poppet.

of V_1 from the calculation in (c) is ascribed to the breakdown of the model in the case of small volumes V_1. Since the kinetic energy of the flow is neglected, the temperature is over-estimated and hence the volume. Nevertheless, both model and experiment clearly show that a high density as well as a fast response time were achieved [138]. It is worth to mention that the gas target was successfully applied in an experiment in which high harmonics of an ultra-short laser pulse were generated and where the target chamber volume was less than 10 liters.

As mentioned above, the nozzles finally used had a throat of 0.6 mm in diameter (instead of 0.5 mm). As a result, the interferograms show that the profile is affected in such away that a donut-shaped density profile is produced with a slightly lower density on the jet axis instead of a flat-top. For the experiments in this thesis, however, this is even advantageous since the density gradient at the edge is increased. Due to the fact that the focusing of the laser pulse is strong (f/3.15), the Rayleigh length is significantly shorter than the gas jet diameter.

Table 5.2: Parameters used to simulate the time dependent mass flow through the gas target. p_0 denotes the backing pressure, r_1 the radius of the valve constraint, r_2 of the nozzle throat, respectively.

parameter	*(a)*	*(b)*	*(c)*
p_0 [atm]	40.5	41.5	42.5
r_1 [mm]	0.315	0.40	0.33
r_2 [mm]	0.5	0.49	0.30
V_1 [cm^3]	1.12	1.12	$5 \cdot 10^{-3}$

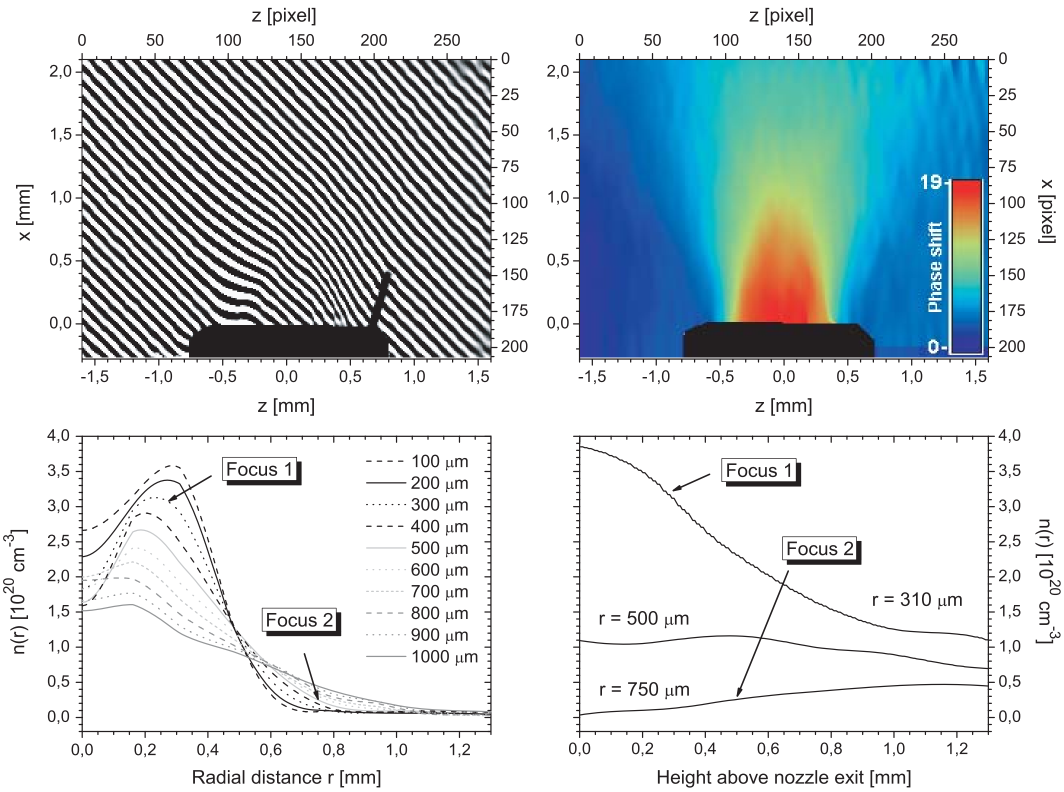

Figure 5.7: Gas density profiles produced by Mach 3.3 nozzle. Top left: Interferogramm obtained using argon, the shadow of the nozzle head and a wire attached for laser alignment purposes is also shown. Top right: Map of phase shift calculated from fringe shift. Bottom left: Using an Abel inversion, the radial density at various heights above the nozzle exit was calculated. Bottom right: Scans of density profile at a fixed radius as a function of distance to the nozzle exit. "Focus 1" and "focus 2" indicate laser focal positions used in this thesis. All densities are observed for a backing pressure of 50 atmospheres.

Hence the experiments are not affected by this.

Figure 5.7 shows the interferometry results of Mach 3.3 nozzle with an exit diameter of 1 mm in diameter. An interferogram obtained using argon is shown top left, top right depicts the phase map obtained by Abel inversion. Bottom left of figure 5.7 shows the measured density profile at different heights above the nozzle exit, whereas bottom right shows the density profile scanned in height at a fixed radius of the jet axis. The different focal positions of the laser are indicated by "focus 1" and "focus 2", respectively.

6. Ionization dynamics of sub-10-fs pulse in gases

In this chapter, experimental results on the propagation of a laser-induced ionization front through gaseous media and the subsequent evolution of a plasma channel are presented. An ionization front is formed at the moment of electronic breakdown of the target gas caused by optical field ionization. The optical properties of the plasma generated differ from those of the surrounding gas. Particularly the refractive index depends on the local density of electrons in the plasma. So an optical probing of the spatial-temporal evolution of the electron density becomes possible. Due to the fact that the ionization front propagates with a velocity that is close to the speed of light, the accuracy of such a pump-probe technique depends significantly on the duration of the probe. Here for the first time the front was probed with a time resolution of better than 10 femtoseconds. The study of the ionization front reported here became in particular possible because of a high contrast of the laser. As clearly seen in the data and also observed in other experiments using solid targets, no pre-plasma was present [104].

In the following, the laser system is described and the data obtained via optical shadowgraphy and interferometry are presented. The energy transfer from the laser into the plasma was studied with the help of absorption measurements and spectroscopy of the laser pulse. Particle-In-Cell simulations of the laser-gas interaction and the interaction of the probe with the plasma have been performed. The numerical results are presented and compared with the experimental data.

6.1. Giga-Watt sub-10-fs laser system

The generation of multi-Giga-Watt high-contrast, sub-10-fs pulses used for the experimental studies in this work was based on a commercially available laser system (Femtopower Compact Pro, Femto Lasers GmbH). First ultra-short pulses with a duration of less than 12 fs containing about 5 nJ optical energy were generated by a mirror-dispersion-controlled Ti:Sapphire oscillator. Then, using the CPA technique [5, 6], the pulses were amplified up to 800 μJ and a pulse length of about 25 fs, and finally compressed to durations of less than 10 fs using an additional hollow-fibre-compressor combination. Taking all the transport losses into account, the pulse energy on target was about 150 μJ (15 GW).

The heart of both the oscillator and the amplifier was a crystal of Ti-doped sapphire (Ti:Al_2O_3), a material which has turned out to provide ideal optical properties for the generation of ultra-short and high-intensity pulses in combination with the CPA technique, in particular due to its spectrally broad amplification profile ranging from 650 to 850 nm. According to the underlying physical principle of the generation of ultra-short pulses, a broadband spectrum is required to obtain short pulses. Quantitatively, the relation between the pulse duration,

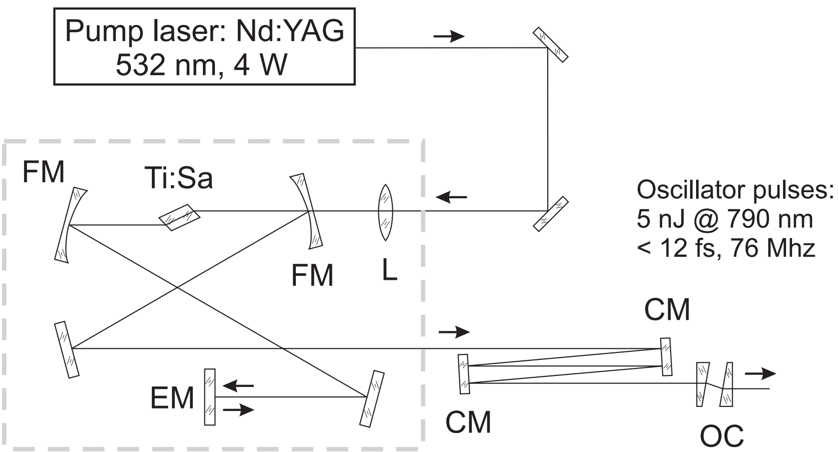

Figure 6.1: Layout of the Femtosource Scientific Pro mirror-dispersion-controlled Ti:sapphire oscillator (Femto Lasers GmbH). A highly doped Ti:Sa crystal is pumped by a frequency-doubled Nd:YAG laser whose output is focused into the crystal (lens L). A linear optical resonator is established by the end mirror (EM) and the output coupler (OC). Focusing mirrors (FM) with their foci located inside the crystal sustain the optical Kerr-effect used for mode-locking of resonator modes around the maximum of the crystal's gain curve. Group velocity dispersion is intra-cavity compensated by chirped mirrors (CM). The output coupler is double-wedged to avoid back reflections.

$\Delta\tau_p$ (FWHM of the intensity profile), and its spectral width, $\Delta\nu_p$ (FWHM of the spectral intensity in frequency space), is given in the form of a duration-bandwidth product in analogy to the Heisenberg uncertainty principle,

$$\Delta\tau_p \cdot \Delta\nu_p \geq \kappa. \tag{6.1}$$

Here κ is a numerical constant of the order of 1 that depends on the actual pulse shape [144]. If equality holds, the pulse is called BANDWIDTH LIMITED or FOURIER TRANSFORM LIMITED. In the special case of a temporally and spatially Gaussian shaped pulse, equation (6.1) reads [145]

$$\Delta\tau_p \cdot \Delta\lambda_p \geq \frac{2\ln 2}{\pi} \cdot \frac{\lambda_0^2}{c}, \tag{6.2}$$

where λ_0 is the central wavelength, $\Delta\lambda_p$ the spectral width (both in nm) and c the speed of light. Hence, to generate ultra-short pulses, sufficient sidebands next to the carrier frequency, ω_0, need to be generated and amplified. For an laser wavelength of $\lambda_0 = 800$ nm, a duration of $\Delta\tau_p = 10$ fs requires a spectral width of at least $\Delta\lambda_p = 95$ nm.

Another important aspect is that dispersion effects become important as soon as the pulse propagates through dispersive material (even though the Ti:Sa crystal itself). The frequency dependence of the medium refractive index, $n(\omega)$, induces a change in both the temporal width and the general form of the pulse. The principle behind this behaviour is that a bandwidth-limited pulse with a duration $\Delta\tau_p$ and a spectral width $\Delta\omega_p = 2\pi\Delta\nu_p$ can be understood as a wave packet consisting of several groups of waves, where each one is centered around a frequency ω. In a dispersive medium, each group propagates with an individual group velocity, $v_g(\omega)$, and the pulse spreads as a result of the different group velocities above the pulse spectrum. While the entire wave packet propagates with constant group velocity, v_g, according to

$$k' = \frac{1}{v_g} = \left.\frac{\mathrm{d}k}{\mathrm{d}\omega}\right|_{\omega_0} = \frac{n_0}{c} + \frac{\omega_0}{c} \cdot \left.\frac{\mathrm{d}n}{\mathrm{d}\omega}\right|_{\omega_0}, \tag{6.3}$$

higher order terms in the Taylor series expansion of $k(\omega)$ are responsible for pulse distortion[1]. In particular, temporal pulse broadening is governed by the second derivative of k in respect of the frequency ω,

$$k'' = \frac{\mathrm{d}^2k}{\mathrm{d}\omega^2} = \frac{2}{c} \cdot \left.\frac{\mathrm{d}n}{\mathrm{d}\omega}\right|_{\omega_0} + \frac{\omega}{c} \cdot \left.\frac{\mathrm{d}^2n}{\mathrm{d}\omega^2}\right|_{\omega_0}, \tag{6.4}$$

[1]The first term on the right side of equation (6.3) describes the phase delay per unit length in the medium and the second the change in the carrier to envelope phase per unit length.

while the pulse shape is affected by higher order terms [144]. The effect of temporal pulse broadening per unit length and spectral width is called GROUP VELOCITY DISPERSION. Table 6.1 shows the group velocity dispersion for some materials that were important for the experimental set-up. The central wavelength was $\lambda_0 = 800$ nm. The increase in duration with propagation length, z, of a bandwidth limited pulse due to group velocity dispersion in a material is

$$\Delta\tau'(z) = \Delta\tau \cdot \left[1 + \left(4 \cdot \ln 2 \cdot \frac{z[\mathrm{mm}] \cdot \mathrm{GVD}}{(\Delta\tau[\mathrm{fs}])^2}\right)^2\right]^{1/2} \text{ fs.} \tag{6.5}$$

This is the reason why the compressor and all following optical elements for guiding and focusing of the pulse onto target have been placed in vacuum. Group velocity dispersion became also important in the context of generating an ultrashort probe pulse (refer to chapter 4).

To generate ultra-short pulses, however, both a sufficient spectral width and the careful compensation of group velocity dispersion effects are of paramount importance. In the oscillator, the spectral width has been achieved by the production of side-bands, in particular by passive mode-locking of several modes of the optical resonator using the optical Kerr-lens effect [146], that is the intensity-dependent change in the refractive index of the Kerr medium (here the Ti:Sapphire crystal itself). Figure 6.1 shows a schematic of the MHz-laser oscillator. The group velocity dispersion of the pulse in the crystal was compensated by CHIRPED MULTI-LAYER DIELECTRIC MIRRORS which allow the generation of femtosecond pulses due to an adaptable negative group velocity dispersion in combination with a high broadband reflectivity [147]. So pulses of < 12 fs were produced at a repetition rate of 76 Mhz. Each pulse contained about 5 nJ optical energy [148].

The oscillator pulses have been ultra-short but did not contain enough energy to drive laser-plasma processes which were of interest here like noble gas ionization (focused to a spot of 5 µm in diameter FWHM, the intensity would have been of the order of $5 \cdot 10^{11}$ W/cm^2). To improve the energy, the pulses

Table 6.1: Group velocity dispersion of different optical materials [145]

Material	[fs^2/mm]	*Material*	[fs^2/mm]
Air at 1 atm	0.02	Glass (BK7)	44.6
Sapphire	58.0	Quartz	36.1
BBO	37.0	SF14	178.3

are amplified by a factor of about $2 \cdot 10^5$ in energy by a femtosecond amplifier. The commercial Femtopower Compact Pro amplifier used is a modular system consisting of the oscillator described above, a stretcher unit followed by a 9-pass Ti:Sa amplification stage and a prism compressor. A schematic of the system is presented in figure 6.2. Note that the repetition rate of the system is reduced to that of the pump laser, which is running at 1 kHz.

To compress the pulses to duration of sub-10-fs, the bandwidth of the pulse is increased using the nonlinear effect of SELF PHASE MODULATION (SFM), that is the coherent generation of side bands as a result of the temporal intensity profile at high intensities accoording to [8]

$$\delta\omega = \omega(t) - \omega_0 = -\frac{1}{2} \cdot \frac{\omega_0 n_2}{c} \cdot z \cdot \frac{\partial I(t)}{\partial t}. \tag{6.6}$$

Here n_2 is the nonlinear part of the refractive index, $n = n_0 + n_2 \cdot I(t)$. Although at high intensities SFM is a very strong effect in solids, it spatially limits the usable beam area due usually the beam profile is a Gaussian. To homogenously modulate the frequencies over the radial profile and maximize the self phase modulation of the pulse, Nisoli *et. al.* proposed the usage of noble gases in combination with a guiding element in form of a hollow fiber [149, 150]. Experimentally the pulse was focused into a capillary of 1 m in length and about 250 μm in diameter filled with 2 atmospheres of neon. Noble gases are advantageous because of their high ionization threshold. The pulse was guided over a relatively large propagation length with relatively low losses. The transmission efficiency of the fiber used was measured to be better than 50 percent. The spectrum of the pulse was increased from about 50 nm in the prism compressor to about 135 nm (FWHM) in the fiber. This increase in bandwidth allows the pulse to be compressed to durations of less than 10 fs. Latter is done in the last stage by using a set of 8 chirped mirrors which also compensate for dispersion effects induced by the propagation through air and a quartz windows which was used to seal the capillary and the vacuum vessel of the compressor. The calculated minimal (Fourier-limited) pulse duration is $\Delta\tau_{p,F} \approx 7$ fs (FWHM). Measurements of the temporal pulse profile were performed in great detail elsewhere and confirm a duration of $\Delta\tau_p \approx 8$ fs [151] using a 2nd order autocorrelation set-up. Measurements of the optical bandwidth of the pulse behind the focusing parabola in the target chamber and additional autocorrelation measurements were performed to confirm that the temporal beam quality was not affected by the guiding optics.

The contrast in intensity of the system during the experiment was better than 10^8 on a ps time basis. As a result, no pre-plasma was produced prior to the main interaction. Shadowgraphic images have shown this (see below) and measurements on solid targets have also confirmed it independently. Particularly the absence of higher order lines in XUV spectra recorded on solids have clearly shown that a close-to-solid density plasma has been obtained [104, 152].

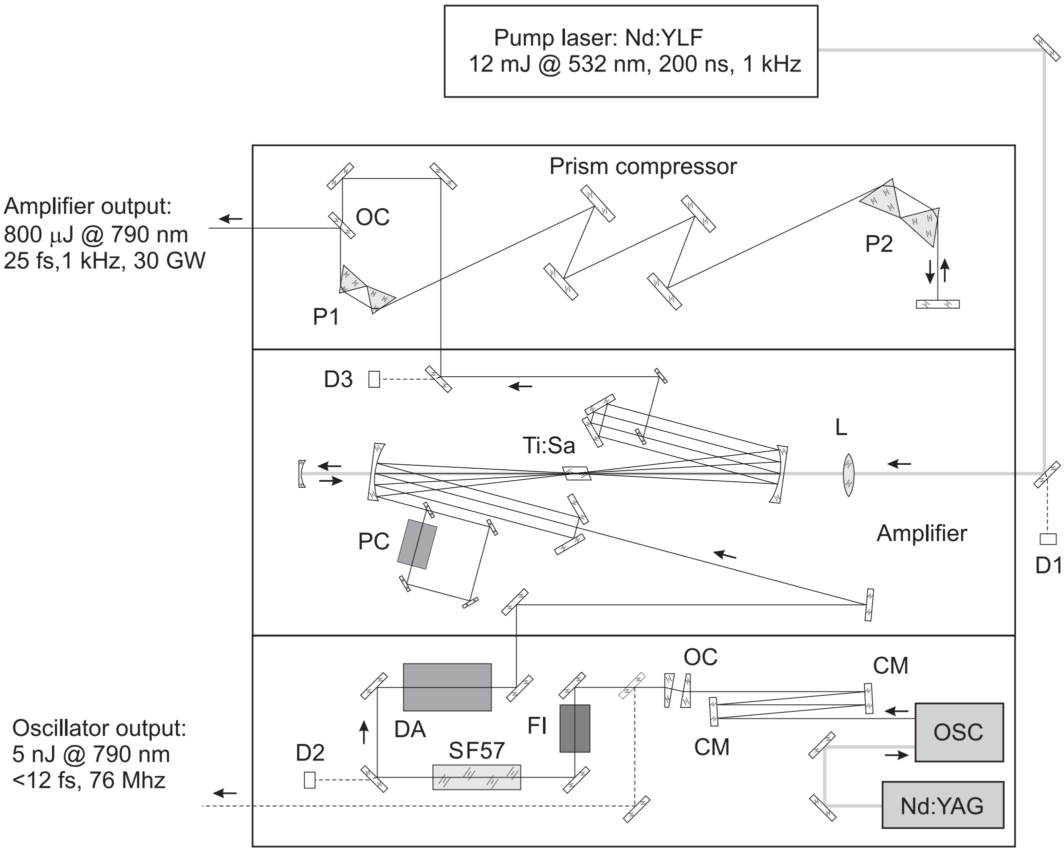

Figure 6.2: Schematic of the femtosecond multi-pass amplifier used (Femtopower Compact Pro, Femto GmbH). The oscillator part is optically isolated from the amplification stage by a Faraday isolator (FI). Before being amplified, the seed pulses are stretched to a duration of > 10 ps together with 5 cm glass (SF57) and shaped in amplitude and phase by an accusto-optic programmable filter (DA) (DAZZLER, Fastlite) [153]. The Ti:Sa amplifier crystal, which is in a vacuum (vacuum vessel not drawn here), is passed 9 times in total. The pockels cell (PC) is synchronized to the pump laser and reduces the train of oscillator pulses to one every millisecond after the 4th amplifier round trip. Here the repetition rate of the system is reduced to that of the pump laser, i.e. to 1 kHz. After re-compression by a double-pass prism compressor, the pulse duration is about 25 fs and each pulse carries about 800 µJ of optical energy. The diodes indicated (D1 to D3) are used for timing and alignment purposes.

6.2. Experimental set-up

The ionization dynamics induced by the driving laser beam takes place on the timescale of femtoseconds and the dimension of a focal spot diameter, i.e. of a few microns. To obtain time-resolved data of the onset and development of the plasma channel, a high temporal resolution and a high optical resolving power were of paramount importance. This also implied that the duration of the optical probe pulse had to be as short as possible. Additional frequency doubling was advantageous for the enhancement of the contrast between the signal and the stray light of the pump pulse. Moreover, the bandwidth of the probe pulse was reduced (compare equation (6.1)) and the signal could easily be separated from the optical self-emission of the plasma by using a narrow-band interference filter. Also the penetration depth of the probe into the plasma was increased as the critical density is quadratically increasing with the frequency of the light by

$$n_{cr} = \frac{m_e \epsilon_0 \omega^2}{e^2} = \frac{m_e \epsilon_0 (2\pi c)}{e^2 \lambda^2} \tag{6.7}$$

(yielding $n_{cr} = 6.97 \cdot 10^{21}$ cm^{-3} for $\lambda = 400$ nm radiation and $n_{cr} = 1.74 \cdot 10^{21}$ cm^{-3} for $\lambda = 800$ nm). To meet these challenges, a miniaturized delay line including a frequency-doubling crystal was developed and installed. The probe beam was generated under vacuum conditions inside the target chamber. Short beam paths are advantageous in order to achieve a precise synchronization with low jitter and stable beam pointing. Details of the set-up are given in chapter 4.

Characterization of focus

On solid targets, the focus is characterized by the lateral intensity distribution on the surface, whereas for gas targets it has to be treated fully 3-dimensional. This means that focusing in longitudinal direction has to be considered, too. The interaction zone is extended from a surface (in the case of solids) to a volume. This volume depends significantly on the focusing optics and also on the beam quality (characterized by the BEAM QUALITY PARAMETER M^2, see Appendix A). Moreover, the focus geometry can be altered during the interaction of the pulse with the plasma generated. This effect is referred to as IONIZATION INDUCED DEFOCUSING. This, however, is addressed later on. Here the results of the focus geometry under vacuum conditions are summarized.

The quality of focus of the parabola was carefully checked before each experiment using a separate diagnostic set-up. A high-quality aluminium mirror was placed on a translation stage at a distance of about 3 cm behind the focus. So it was possible to turn the beam into a separate diagnostic channel. A motorized projection lens (identical to those used in chapter 7) was used to image the focus onto a 8 bit CCD or a 12 bit beam profiler. The magnification was about 40×. Since a proper measurement of the size of the vacuum focus was important, the magnification of the focus diagnostic was cross-calibrated using a diffraction grating with 0.5 cm periodicity. The grating was placed in an expanded and collimated Helium-Neon laser beam that was co-linear with respect to the Ti:Sa beam and could be used for alignment purposes. The distances between the orders observed in focal position were measured. Knowing the laser wavelength of the Helium-Neon laser (532.8 nm, green) and the effective focal length of the parabola (f_{eff} = 119 mm), the angular spread of the orders was used to cross-calibrate the system magnification.

Axially, i.e. along the optical axis of the main pulse, the beam caustics were scanned with respect to the best focal position using the Helium-Neon laser and the 800 nm AMPLIFIED SPONTANEOUS EMISSION of the Ti:Sa laser. Therefore a precision length gauge was attached to the projection lens. Since the expectations were that the beam characteristics of a full energy shot would possibly differ from that obtained using ASE radiation, the focus of the main laser pulse was measured under full energy conditions. Therefore the intensity was attenuated by replacing the last high-reflective mirror which turns the beam onto the parabola by a wedged glass substrate with a reflectivity of about 4 percent. The results of the measurements are summarized in figure 6.3.

The first observation has been that the different radiation sources produce slightly different diameters of the focal spot. The smallest spot was produced by the Helium-Neon laser. Axially, the focal positions of the ASE and of the main pulse were shifted by more than 200 μm with respect to the Helium-Neon laser. This generally can be explained by a different divergence of the beams. Note that this was not crucial for the measurements since axially the focal position was simultaneously determined by focusing ASE on the tip of a wire, which was connected to the nozzle, and by imaging the self-emission of the plasma. More important was to take into account the different slopes of the Ti:Sa and the ASE beam radii because they have a direct influence on the size of the interaction volumes. The curves with the best fits were used to determine the beam quality parameter M^2. As shown by A. E. Siegman, arbitrary real laser beams can be

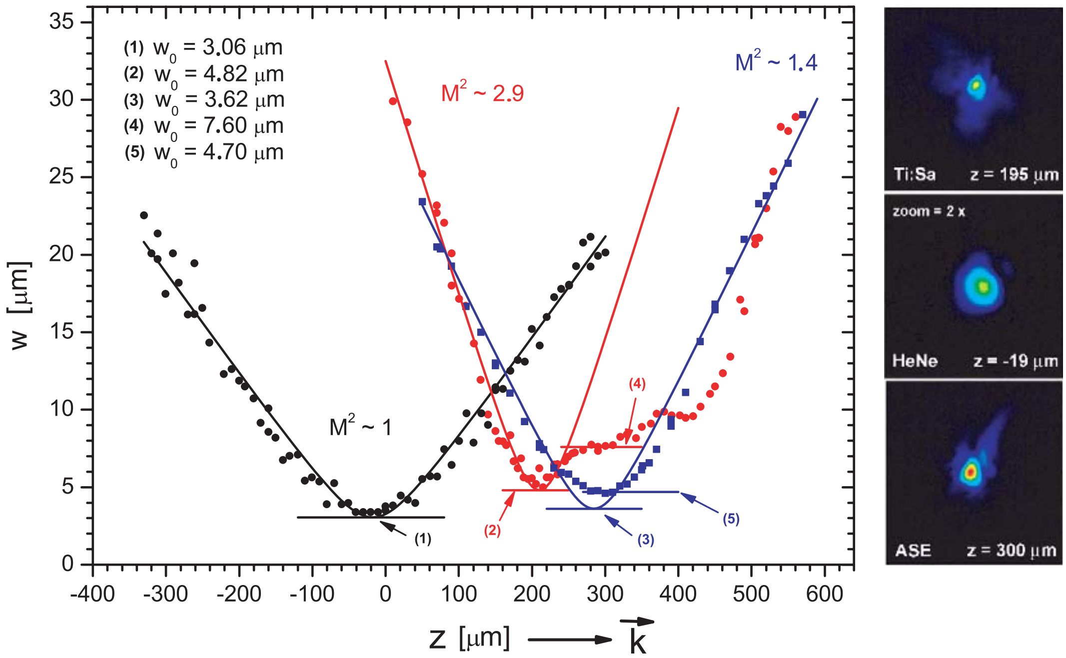

Figure 6.3: Beam caustics obtained with focus diagnostic. Black curve: caustic of 633 nm Helium-Neon laser; blue curve: of 800 nm ASE emission from Ti:Sa; red curve: of Ti:Sa main pulse. The beam quality parameter, M^2, was calculated by fitting the data using equation (20) in Appendix A. Right: typical images of best focus recorded with 12-bit beam profiler.

described using the Gaussian beam propagation formalism if the beam quality parameter M^2 is introduced (compare equations (20) to (22) in Appendix A) [154]. The beam profile of the Helium-Neon laser used for alignment has been close to a Gaussian ($M^2 \approx 1$), while the angular spreads of the Ti:Sa main pulse and ASE were larger ($M^2 > 1$). Particularly, a relatively high beam quality parameter of $M^2 = 2.9$ has been observed in the case of the main pulse. It might be over-estimated because in the near-field of the focus, a doughnut-shaped intensity distribution was observed, whereas the spot was always fitted by a Gaussian to obtain a value of the beam radius $w(z)$. This was independently confirmed by the fact that in front of the focus the self-emission data have shown ring-shaped plasmas. The caustic of the main pulse was axially non-symmetric and the best position of the focus was closer to the parabola than expected. Laterally, however, the focus diameter was comparable to that of the ASE, which was usually used to characterize the diameter of the focal spot and the intensity achieved.

Another possibility to validate the beam characteristics is to compare the beam diameter on the focusing element (i.e. between the last turning mirror and the parabola) with that in best focal position. This also yields a measure for the angle under which the beam is focused (f-number). In front of the parabola, a beam radius of $w \approx 12.0$ mm was measured using Polaroid film (compare figure 4 in Appendix A). As the parabola used had an effective focal length of $f = 119$ mm, the beam was focused using a f-number of $f_{\text{eff}}/\sharp = f_{\text{eff}}/(\pi \cdot w) \approx f/3.2$. According to Gaussian beam optics, a minimum beam radius at focal position of $w_0 \approx 2.52$ µm is predicted for a diffraction-limited, ideal Gaussian beam ($M^2 = 1$). Comparing this radius with those measured, while using Ti:Sa ASE and full energy pulse, the beam quality parameter for the real beam geometry can be derived (equation (20) in Appendix A). Particularly, M^2 (ASE) $= 3.64$ µm/2.52 µm $= 1.44$ and M^2 (Ti:Sa) $=$ 4.82 µm/2.52 µm $= 1.91$ were obtained. This is in good agreement with separate measurements reported in [151]. In the context of plasma generation, however, the Rayleigh length is important, which defines a characteristic length within a homogeneous plasma formation can be assumed. Using

$$z_R = \frac{\pi w_0^2}{M^2 \lambda}, \tag{6.8}$$

one finds similar results of $z_R \approx 36$ µm in the case of ASE ($M^2 = 1.44$ and $w_0 =$ 3.64 µm) and $z_R \approx 32$ µm at a full-energy shot ($M^2 = 2.9$ and $w_0 = 4.82$ µm).

6.3. Optical probing of plasma channel formation

Defining the plasma axis

The rays of the optical probe beam are deflected by the refractive index of the plasma as described theoretically in chapter 4. This deflection was measured by recording the intensity distribution of the probe beam at different positions with respect to the plasma. Therefore a microscope objective with a high numerical aperture of NA = 0.28 was used to image a thin "slice" of the probe beam, i.e. a plane perpendicular to its k-vector, with high resolution onto a camera. The "thickness" of the slice was of the order of the depth of focus of the microscope objective and was about 3.5 μm. The position was chosen with high precision by a controlled movement of the lens along the optical axis of the probe beam. The object plane of the imaging system was shifted accordingly. In the following the shift of the lens is labeled Δy with respect to optimum focal position (refer to figure 4.4). The change in magnification could be neglected due to the huge enlargement factor. This technique, however, required the proper definition of the zero position which is defined by the optical axis of the pump pulse and the center of the plasma channel, respectively. Therefore the optical self-emission of the plasma in the spectral range between 400 and 750 nm was recorded. A misalignment of the position of the lens with respect to the position of the plasma channel leads to a decrease of the maximum light observed. A blurring of the image is the result which can be measured as an increase in width of the self-emission profile. The increase in width of the plasma channel (which can be assumed to be axis-symmetric) was measured as a function of focal position of the lens. For each position, the intensity profile was recorded without an interference filter in front of the camera. The records have shown that the best fit to the profile is given by a Lorentz-profile,

$$S = S_0 + \frac{2A}{\pi} \frac{\Delta x}{4(x - x_0)^2 + \Delta x^2}, \tag{6.9}$$

where S is the signal, S_0 a constant offset, A the area under the curve, Δx the width and x_0 the center of the peak profile. The optimum focal position, y_0, of the lens is found when the width, Δx, is at a minimum. Figure 6.4 shows a typical profile obtained for the self-emission of a nitrogen plasma. The inset displays the area which was used to gather the intensity profile for the fit.

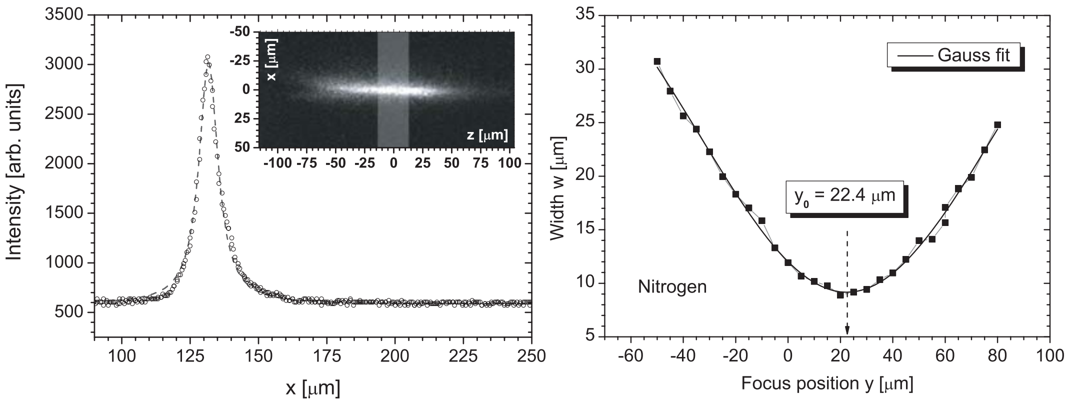

Figure 6.4: Left: Intensity profile due to optical self-emission of nitrogen plasma with 50 atmospheres backing pressure. The fit function chosen was a Lorentz profile. The inset shows the full image and the area chosen for averaging. Right: Width of Lorentz fits as the microscope objective is moved. The best focal position is indicated.

The optical self-emission was much weaker in the case of helium and neon than with argon and nitrogen. Nevertheless, the fits showed good measures of the position of the plasma axis. The remaining uncertainty for best focal position was estimated to be ±15 μm. In all cases, the backing pressure of the valve was 50 atmospheres.

Focused shadowgrams

Once the plasma axis was determined, shadowgrams were taken at different time delays of the probe pulse with respect to the main pulse for all four gases. Therefore a systematic focal shift, Δy (with respect to best focal position, y_0), of the microscope objective was used to control the contrast in the shadowgrams. Experimentally, the shift of the motorized microscope objective was controlled by a high-precision calliper. The principle of the FOCUSED SHADOWGRAPHY technique is detailed in chapter 4. Areas of brighter and darker regions have been observed which are a result of the spatial variation in refractive index gradients according to equation (4.14). If the lens images a plane behind the channel axis, rays are deflected outwardly and hence a dark inner region can be observed surrounded by brighter outer regions. If the object plane is in front of the plasma axis, the rays virtually cross in front of the plasma and hence a bright inner region with a dark outer region can be seen. Note that if the object plane of the lens is at the channel axis, no shadow structure is observed since rays which are deflected by refractive index gradients are "sorted" by the optical imaging element. For helium, where smallest deflections have been observed, the experimental result is

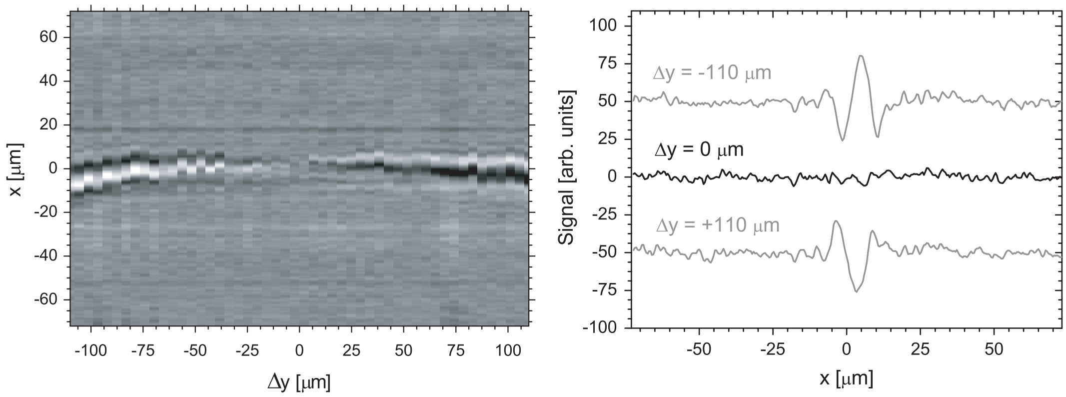

Figure 6.5: Left: Sequence of intensity patterns observed in shadowgrams taken using helium target gas under controlled shift, Δy, of the microscope objective with respect to the plasma channel axis. Right: Line-outs in the x-direction.

presented in figure 6.5. In the position of best focus, which is in agreement with the position estimated from the self-emission data, the deflection is minimal, and even when using argon and nitrogen as target gas, almost no structure is observed. Note that this confirms the capability of the optical imaging diagnostic since the rays were deflected within the numerical aperture of the lens.

Speed of ionization front obtained from shadowgrams

The position of the ionization front can be obtained from shadowgrams with high precision. Figure 6.6 depicts a time series obtained using helium at an atomic density of about $3 \cdot 10^{19}$ cm^{-3} (focal position (2) in figure 5.7). The focal shift of the microscope objective was $\Delta y = -100$ μm and $\Delta y = +100$ μm. The series shows one of the central measurements of this campaign. Note that helium has the highest ionization potentials for electrons of the outer shell compared to the other gases used here. This consequently means that it has the lowest deflection. Although a good contrast was obtained at high resolution. The diameter of the channel is below 10 μm, a fact that is consistent with focus measurements.

From the position of the ionization front it is possible to determine the velocity of the laser pulse with high precision. Here the shift in position of the front directly correlates to the optical path inserted in the probe beam path by moving the delay line. A separate cross-calibration was performed by comparing the position of the wire tip, obtained from the optical probe line using known magnification, with the reading of the calliper connected to the z-axis of the translation stage. The position of the ionization front seen in the images as a function of the optical path inserted into the probe line, is depicted in figure 6.7.

Within an uncertainty of a few percent, the velocity of the ionization front is the vacuum speed of light , i.e. $c \approx c_0$. Note that a change in the group velocity of the pulse due to the refractive index of the neutral gases is much below the uncertainty of the measurement.

Plasma channel evolution obtained from shadowgraphy

Using the shadowgraphy technique, an examination of the plasma channel formation (in form of a series of snapshots) was made possible. Since the deflection of the rays of the probe beam is sensitive to changes in the electron density gradients, both the position of the density gradients can be given with high accuracy and the slope of the electron density can be calculated by integrating the profiles. This is possible in the case of small gradients and simple profiles, which are given here. For the analysis, the assumption was that the density profile is approximately Gaussian-shaped. The profiles obtained from helium and neon were then fitted with the second derivative of a Gaussian. As a result, both the channel diameter (FWHM) and the relative electron density within the channel were obtained. The upper graphs in figure 6.8 show the time evolution of the channel diameter. In the case of helium, the lightest of the molecules probed here, the diameter remains constant for a few ps. Then the onset of a channel expansion has been clearly observed. This indicates that kinetic energy was transferred from the electrons to the ions, which subsequently gain in thermal kinetic energy. As a result, the channel was expanding. For the other gases rather than helium, however, no significant expansion of the channel was observed up to about 300 ps, what was the maximum delay of the optical probe. As an example, neon is shown.

In the lower part of figure 6.8, the contrast observed in the shadowgrams is depicted, which is given by the amplitude of the Gaussian fit function and proportional to the electron density inside the channel (compare figure 4.5). In the case of helium, the electron density is rapidly increasing in the moment the laser pulse ionizes the gas. After that, the signal remains constant. In contrast to this, in the case of neon, an increase of the signal is observed up to about 500 to 700 femtoseconds after the laser-gas interaction. This indicates that here the electron density is still increasing within the channel. A typical candidate responsible for this observation is collisional ionization. Also in the case of argon and nitrogen, an increase of the signal is observed on a similar timescale. This behaviour is confirmed independently by interferometric measurements (see below).

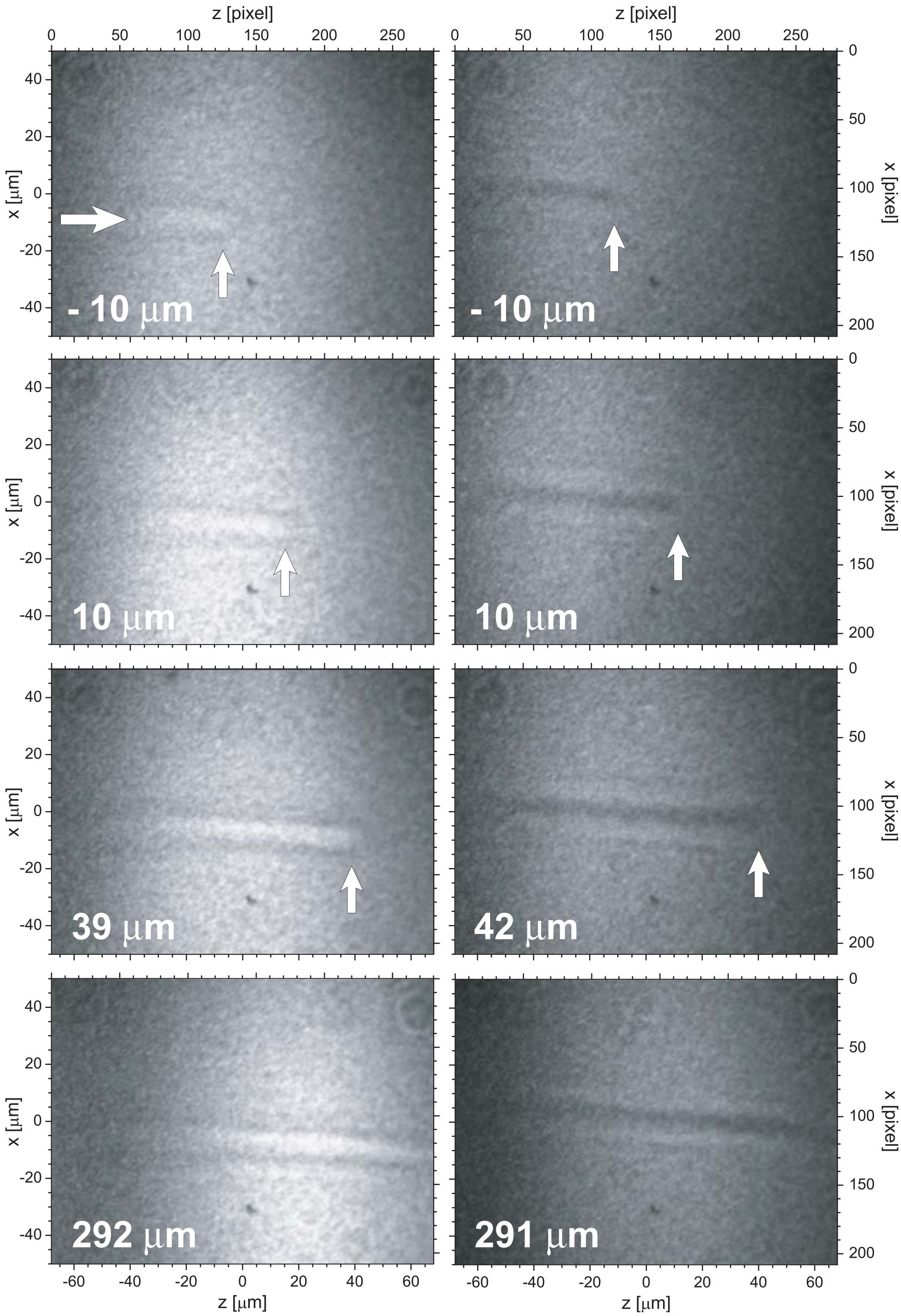

Figure 6.6: Series of high-resolution snapshots of the ionization front and the plasma channel taken with the 400 nm probe pulse for different delays. Left column: focus of microscope objective "before" (i.e. $\Delta y = -100$ µm) and "behind" (i.e. $\Delta y = +100$ µm) the optical axis of the main pulse. The optical path, which is inserted in the probe line, is indicated. The laser (indicated by an arrow) is incident from the left.

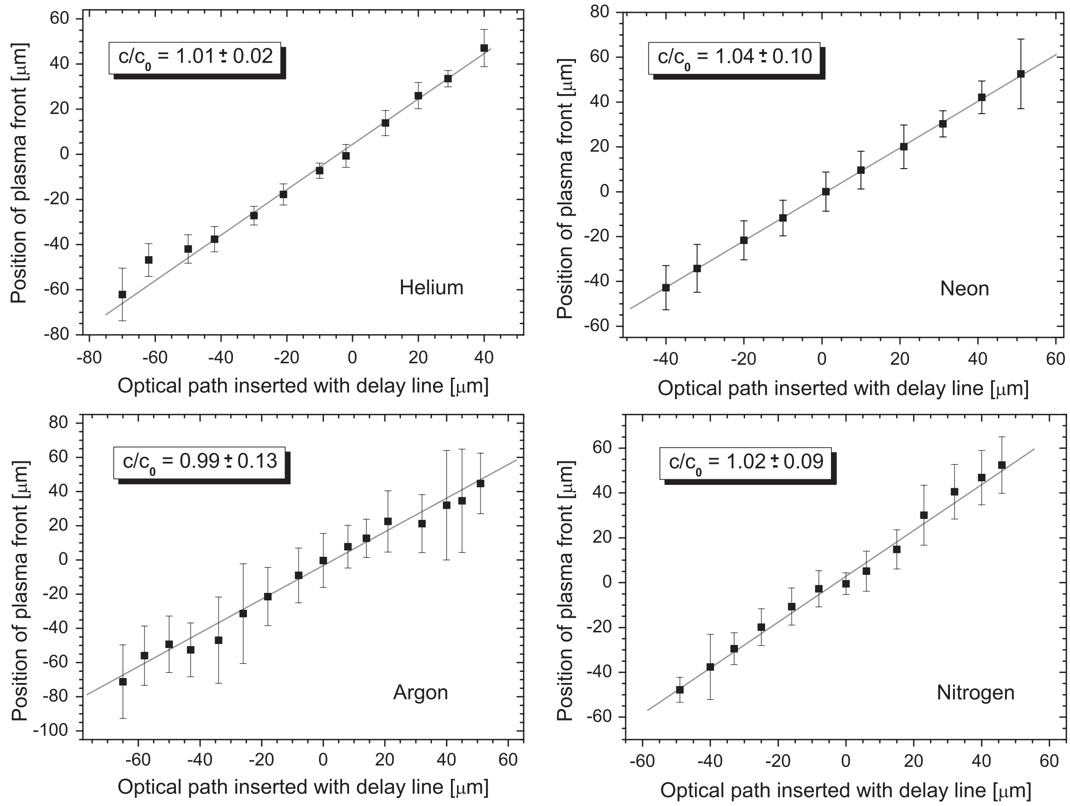

Figure 6.7: Position of plasma front obtained from the shadowgrams for different probe pulse delays and gases. The speed of the ionization front, c, was obtained by a linear fit of the data points; c_0 denotes the vacuum speed of light.

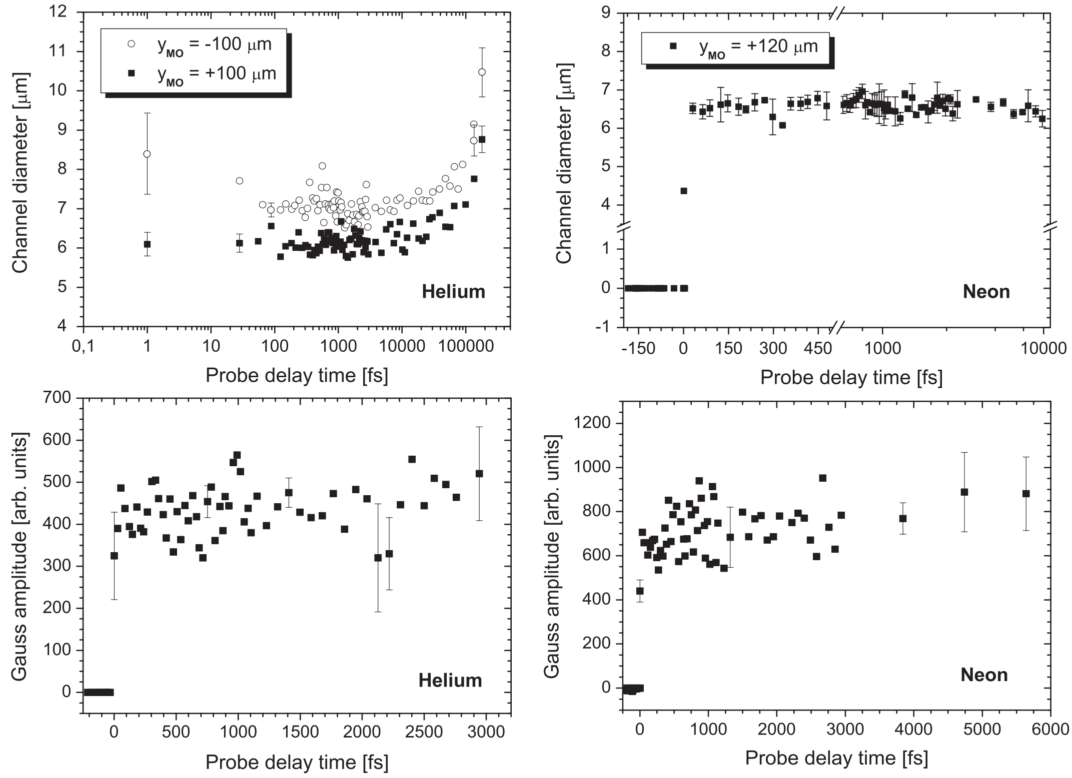

Figure 6.8: In the upper part of the figure, the diameter of the plasma channel for different delays of the probe with respect to the pump pulse is shown as observed in the shadowgrams. In the lower part, the signal strength (contrast) is depicted which is proportional to the electron density within the channel. On the left side of the figure, the data obtained using helium are shown, on the right side those using neon.

Time evolution of electron density

To obtain more quantitative information about the electron density within the plasma channel, time resolved interferometric measurements were performed. A modified Nomarski interferometer was used and details of the set-up are given above. Here, the object plane of the lens was shifted to the position of the plasma axis, i.e. $\Delta y = 0$. At focal position (2), however, almost no fringe shift was observable when using helium and neon. In order to increase the signal, the laser focus was shifted to a position of higher gas density indicated by position (1) in figure 5.7. The electron densities have been obtained from the phase shift with the help of an Abel inversion. The results are presented in figure 6.9.

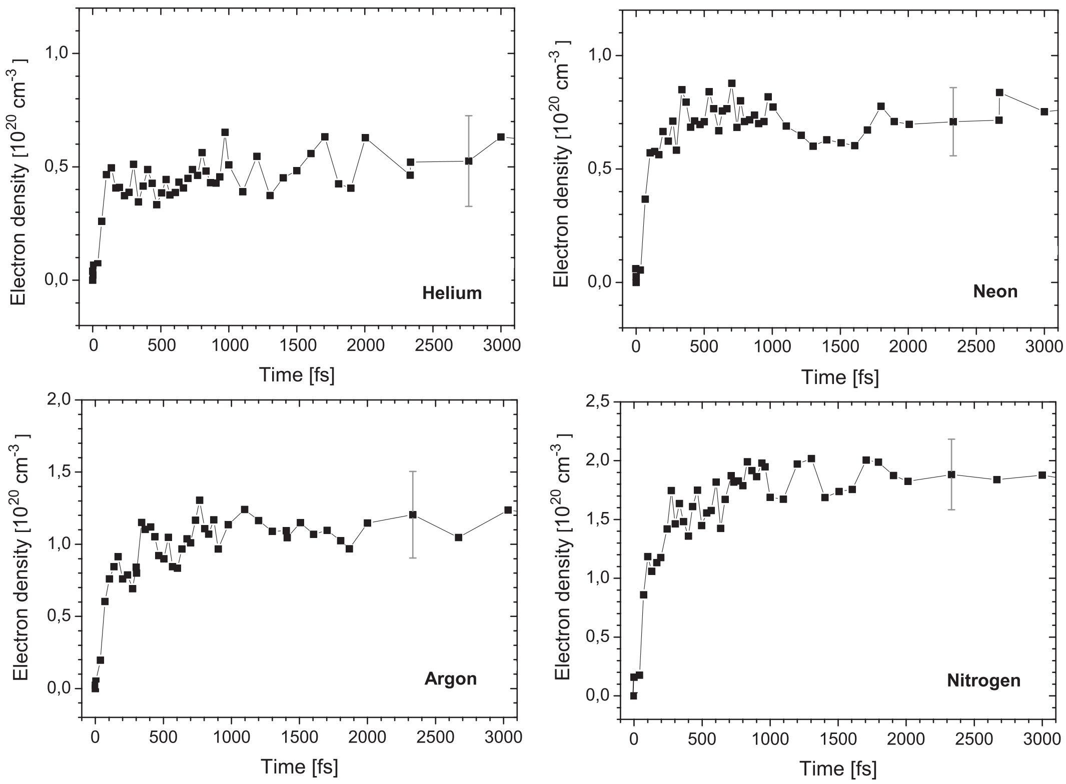

Figure 6.9: Time evolution of axial electron density in the channel for the four different gases used. The neutral gas density was about $3 \cdot 10^{20}$ cm^{-3}. Typical error bars are indicated.

Immediately after the laser-gas interaction, an electron density of about $4 \cdot 10^{19}$ cm^{-3} was observed in the case of helium and of about $6 \cdot 10^{19}$ cm^{-3} in the case of neon. This is below the densities that were expected according to BSI-theory if a neutral gas density of the order of 10^{20} cm^{-3} and a laser intensity of 10^{16} W/cm^2

in the focus is used. Also in the case of argon and nitrogen, the electron densities observed were of the order of $8 \cdot 10^{19}$ cm^{-3} and $1.1 \cdot 10^{20}$ cm^{-3}, respectively. Also here, a rather low ionization level was found, especially since both gases have significantly more electrons than helium and neon, which can be field-ionized at the given intensity. Moreover, the electron density is of the same order for both though the ionization potentials of the outer shell electrons are different (compare Appendix B). This is an indication that ionization induced defocusing took place and the electron density was limited due to a reduced focusability of the pulse. The effect of ionization induced defocusing is therefore discussed below. Nevertheless, the time evolution of the interferograms have clearly shown an increase of the electron density on a time-scale of 500 to 1000 femtoseconds after the laser-plasma interaction. While in the case of helium the electron density remains almost unchanged, in the case of neon a further increase by a factor of about 1.2× of the initial value is observed. This is even more dramatic in the case of argon (1.4×) and nitrogen (1.7×). This indicates that collisional ionization occurred and increased the average ionization level after the pulse. Moreover, the times required to reach the highest electron density are different. In the case of neon, the electron density saturates within about 600 fs after the pulse interaction and within about 1 picosecond in the cases of argon and nitrogen.

In order to estimate the effect of electron impact ionization on the time evolution of the electron density, a simple model was created and the assumption was that almost all atoms, A, have already been ionized by the laser and are in a charge state of +1. This is reasonable because of the high field ionization rates of about $\Gamma_i > 10^{16}$ s^{-1} at a focal intensity of $I \sim 10^{16}$ W/cm^2 (equation (2.12)) if defocusing is neglected. With an electron temperature present, the electron density will potentially increase in time due to binary collisions of the plasma electrons and the ions. Particularly the reaction $e + A^{1+} \rightarrow A^{2+} + e + e$ was assumed to happen. The collisional ionization cross section, $\sigma(v)$ (in cm^2), depends on the relative velocities of the reaction partners. Here the mean thermal velocity of the electrons was used which is given by [155]

$$\overline{v}_e = \left(\frac{8 k_B T_e}{\pi m_e}\right)^{1/2} \approx 6.7 \cdot 10^7 \left(T_e \text{ [eV]}\right)^{1/2} \quad \frac{\text{cm}}{\text{s}}, \tag{6.10}$$

where T_e is the electron temperature. The collisional ionization rate was approximated by

$$\left.\frac{\mathrm{d}n_e}{\mathrm{d}t}\right|_{\text{coll}} \approx n_i \cdot n_e \cdot \overline{v}_e \cdot \sigma(\overline{v}_e), \tag{6.11}$$

where n_i and n_e are the ion and electron density, respectively. They are equal in the model. The cross sections have their maximum for electron temperatures of around 100 eV. This is of the same order of magnitude as predicted by numerical simulations (see below) [156]. Using furthermore an ion density of $n_i \approx 3 \cdot 10^{20}$ cm^3 and an electron temperature of $T_e \approx 60$ eV, the collisional ionization rates are of the order of $1 \cdot 10^{32}$ cm^{-3}s^{-1} in the case of helium, $1 \cdot 10^{33}$ cm^{-3}s^{-1} in the case of neon and few 10^{33} cm^{-3}s^{-1} in the case of argon and nitrogen. Hence within 500 fs, about $1 \cdot 10^{19}$ cm^{-3} electrons will be ionized by collisions in the case of helium, about $1 \cdot 10^{20}$ cm^{-3} in the case of neon and few 10^{20} cm^{-3} in the case of argon and nitrogen. Note that the number of electrons is overestimated since a constant rate is assumed and level depletion as well as energy transfer were neglected. Nevertheless, in comparison to the initial electron density of $3 \cdot 10^{20}$ cm^{-3}, the results have shown that the increase in electron density due to collisions plays a minor role in the case of helium, whereas it qualitatively reproduces the experimental observations in the case of neon and the other two gases. They have also shown that on a time scale of the pulse duration the rates for collisional ionization are small compared to those for field ionization. Physically, this is based on the density of the target gas. At solid density, in contrast, collisional ionizations have to be taken into account when intense femtosecond pulses are used. This was for instance shown by collisional Particle-In-Cell simulations using helium at densities of the order of 10^{23} cm^{-3} [157, 158].

The rate for the inverse process, i.e. three-body recombination, Γ_{recomb}, was estimated to be [155]

$$\Gamma_{\text{recomb}} = b \cdot n_e \cdot n_i \tag{6.12}$$

with

$$b = \frac{8.75 \cdot 10^{-27} \cdot Z^3}{T_e[\text{eV}]^{9/2}} \cdot n_e \quad \frac{\text{cm}^3}{\text{s}}, \tag{6.13}$$

where Z is the effective charge state of the ion. For the approximation, $Z = 1$ was assumed, yielding a recombination rate of about 10^{24} cm^{-3}s^{-1}, i.e. about 10^{14} events within 100 ps. This is a small fraction of a total of $\sim 10^{20}$ cm^{-3}. Hence, on the timescale that was probed during this experiment, three-body recombination can be neglected.

Ionization induced defocusing

The ADK tunnel ionization rates predict that a significant number of atoms are ionized at the leading edge of the pulse already (compare also figure 6.18). Hence the major part of the pulse will travel through a plasma, even when a sub-10-fs pulse is used. This has clearly been demonstrated by simulations (see below). Due to the radial intensity profile of the pulse, however, most of the electrons have been produced on the propagation axis. Due to the fact that an increase of the electron density causes a decrease of the optical refractive index of the plasma, the plasma acts as a negative lens (compare equations (4.10) and (4.13)). In the geometrical picture, the rays are bent outwardly. So in contrast to vacuum, where the maximum intensity at focal position is dominated by diffraction and can be derived by the Gaussian beam formalism as detailed in Appendix A, IONIZATION INDUCED DEFOCUSING can affect the focusability of the pulse. To increase the gas density means to increase the total number of electrons. As a result defocusing becomes stronger. Ionization induced defocusing becomes important when defocusing of the plasma is comparable to the focusing of the beam optics. Then the intensity will be clamped at a certain maximum below the one obtained in vacuum. Hence the maximum charge state of the ions will be limited as well [159, 160].

A clear sign of the effect is the asymmetry of the plasma created as a direct result of the change in the slope of the beam radius due to diffraction (compare for example measurements reported by Monot *et. al.* [159]). To estimate the effect, the light emitted from the plasma due to self-emission and Thompson scattering of the pump was recorded. Figure 6.10 shows axial profiles of the signal obtained by removing the 400 nm interference filter and without the probe beam. As can be seen, the profiles show significant symmetry defects.

A simple geometrical estimate predicts that ionization induced defocusing becomes important in the case of [83]

$$\frac{n_e}{n_{cr}} > \frac{\lambda}{\pi z_R}. \tag{6.14}$$

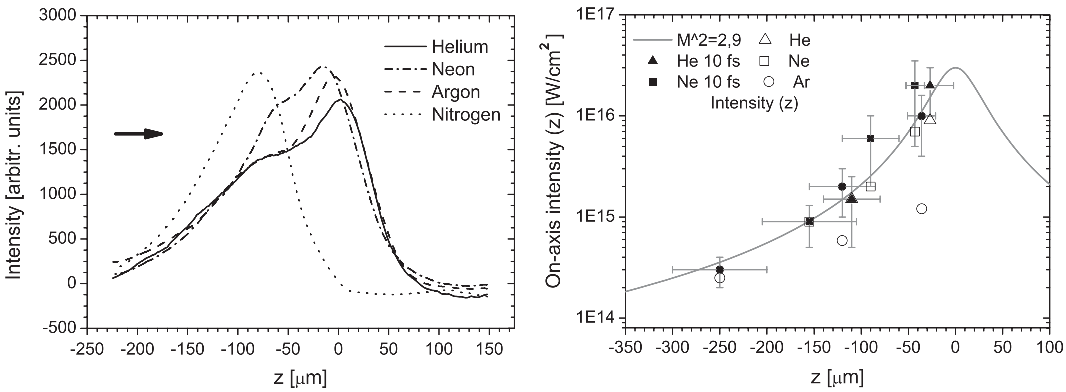

Figure 6.10: Left: Profiles of optical self-emission of the plasma channel obtained at focal position (1). Right: On-axis intensity profile and ionization steps estimated from self-emission data. The Keldysh-formula was used to estimate the intensity at which ionization steps occur (filled symbols). The threshold intensity given by the BSI-theory (valid for long pulses) is also indicated (open symbols) ($M^2 = 2.9, I = 2.95 \cdot 10^{16}$ W/cm^2, $n_0 = 3 \cdot 10^{20}$ cm^{-3}).

When using a Rayleigh length of $z_R \approx 35$ μm and $n_{cr} \approx 1.74 \cdot 10^{21}$ cm^{-3} for $\lambda =$ 800 nm, the electron density will be clamped at the order of $n_e \tilde{>} 1.5 \cdot 10^{19}$ cm^{-3}. A more detailed analytic model, which is based on a ray-optics description of the laser beam, is presented by E. E. Fill [160]. He derives a differential equation for the variation of the slope of the $1/e$-radius of the intensity of a Gaussian beam caused by diffraction and ionization defocusing and gives an estimate for the minimum beam radius and maximum intensity obtained in the focus. According to his model, a maximum electron density of

$$n_e = Z_{\max} \cdot n_0 = C^2 \cdot n_{cr} \tag{6.15}$$

can be produced if a focusing optic with a half-angle of convergence of $C = r/f$ is used. Note that the beam radius, r, at the position of the optical element with a focal length of f is here defined by $r = 2^{-1/2}w$. However, using the parameters given for this set-up and taking a realistic focusing into account, similar electron densities in the range of $n_e \approx 8.2 \cdot 10^{18}$ cm^{-3} ($M^2 = 1.4$) and $n_e \approx 3.5 \cdot 10^{19}$ cm^{-3} ($M^2 = 2.9$) are predicted. These are of the same order as above. Note that these are only estimates rather than exact calculations. Nevertheless, the estimates might explain the relatively low average ionization state seen in the interferometric data. To include a more realistic model of ionization and beam propagation, numerical modeling is required.

Energy absorption measurements

The fraction of the laser energy which is absorbed during the interaction was measured with an Ulbricht sphere. Details of the set-up are given in chapter 4. Figure 6.11 shows the signal detected by a diode attached to the sphere as a function of backing pressure of the gas target. In the case of helium and neon, a linear decrease has been observed up to 50 atmospheres of backing pressure. This shows that absorption is directly proportional to the number density of atoms in the focal volume. This observation is in agreement with the ionization model, in which the energy exchange between the wave and a *single* atom is described. Collective effects of the plasma electrons are neglected. To increase the background density means to increase the local density of atoms in the interaction volume and hence to increase the fraction of energy that is absorbed. In the case of argon and nitrogen, the same behaviour has been observed up to backing pressures of about 20 to 25 atmospheres. Beyond these pressures, the fraction of energy absorbed is still increasing but at a reduced rate. This change in behaviour is ascribed to the formation of clusters in the gas jet. Separate measurements of the Rayleigh scattering of low-intensity laser light have clearly shown that if a backing pressure of about 25 atmospheres is exceeded, clusters are formed. Particularly for the gas target used (Mach 3.3), an increase of scattered light has been observed. Clustering occurs if the temperature of the gas is lowered due to the expansion in such a way that the attractive potential due to Van-der-Waals forces can dominate over kinetic energy between the particles. Cluster in a gas do not change the refractive index and hence cannot be detected by interferometry. The mean size of a cluster is increasing with the square of gas density, which is a linear function of backing pressure [161]. From experiments on cluster targets a significant increase in absorption of laser light has been reported [162]. Assuming that the increase of absorption is equivalent to an increase in the number of electrons liberated, the observation can be interpreted by enhanced ionization induced defocusing due to an effectively lowered ionization potential of the medium due to clustering. This interpretation is supported by PIC simulations. Clustering is not included in the numerical model and a direct proportionality between the number density of atoms and the absorbed laser light is seen. The interaction between sub-10-fs laser pulses and clusters are beyond the scope of this work and studied in detail elsewhere [163].

According to the measurements, about 5 percent of the laser pulse energy were absorbed during the interaction in the case of helium and neon if a backing pressure of 25 atmospheres was applied. In the case of argon and nitrogen, an

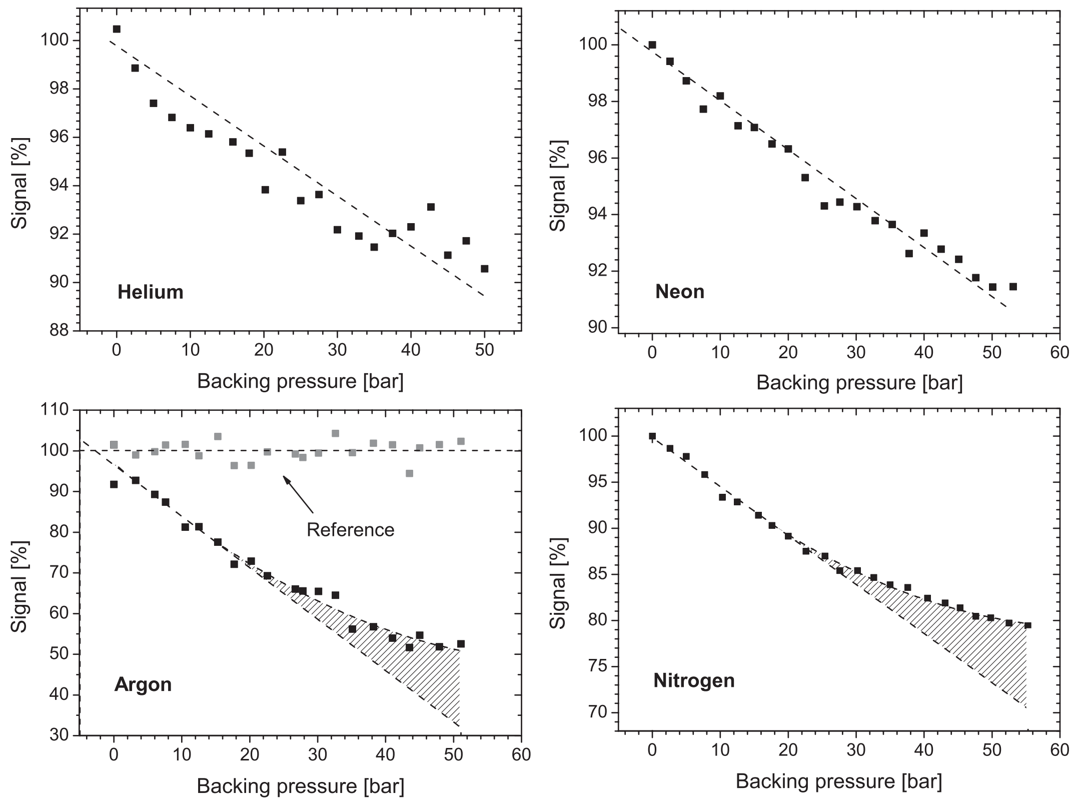

Figure 6.11: Signal detected with the Ulbricht sphere shown as as function of backing pressure for different gases. The change in the absorption characteristics in the case of argon and nitrogen relates to clusters in the expanding gas jet. Separate measurements have shown that clusters are produced at backing pressures of about 25 atmospheres and more.

absorption of about 35 and 15 percent respectively has been examined, applying the same pressure. This result was to compare with the energy required to ionize the atoms inside the focal volume. Therefore the volume was calculated in which the laser intensity is high enough to cause the ionization of an atom or ion with a charge state Z according to $A^Z \rightarrow A^{Z+1}$ (see equation (48) in Appendix A). The number density of particles inside the volume was given by the gas density, i.e. about $1.5 \cdot 10^{19}$ cm^{-3} at 25 atmospheres backing pressure of the valve (focal position (2)). Particularly the assumptions were $w = 4.82$ µm, $M^2 = 1.91$ and $I_0 = 2 \cdot 10^{16}$ W/cm^2. The intensity thresholds for the ionization were taken from figure 6.21. Hence the pulse duration was taken into account already. For example, in the case of helium the volume, in which the gas is ionized once, is about $12 \cdot 10^3$ µm^3. Using the ionization energies listed in Appendix B, a total laser energy of about 0.7 µJ is consumed by ionization. Assuming that the average

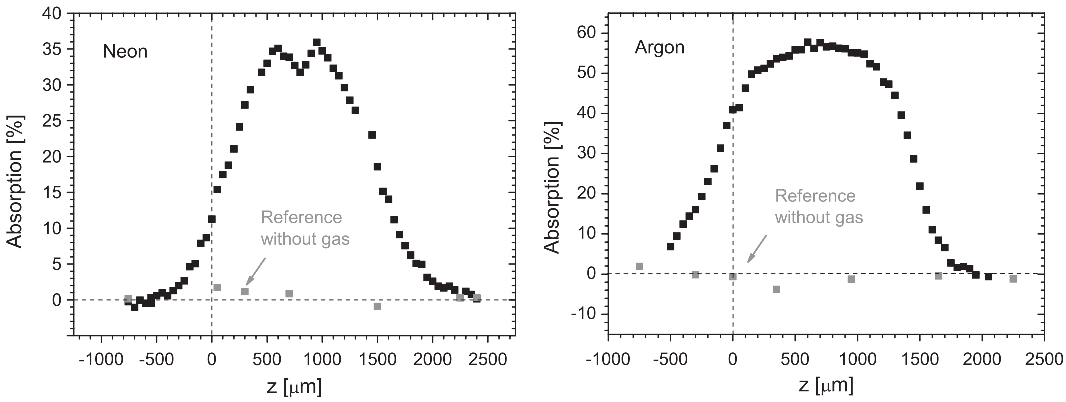

Figure 6.12: Absorption profiles for different focal positions in the gas jet. The height above the nozzle was kept constant (500 μm). The position $z = 0$ is equivalent to that denoted by "focal position 2" in figure 5.7. The backing pressure was 50 atmospheres.

kinetic energy of the plasma electrons is of the order of 50 eV, another 1.4 μJ are required for heating. In total, about 2.1 μJ or 4 percent of the initial pulse energy (about 60 μJ) are needed. This is in good agreement with the observation. The same calculation was performed for neon: about 1.2 μJ are consumed by the ionization process and about 3.2 μJ are needed to heat the plasma electrons to about 60 eV. This is a total of about 7 percent of the pulse energy. Here again, the estimate matches the observations made during the experiment. The same holds for argon, where in a volume of about $121 \cdot 10^3$ μm^3 an energy of 5.2 μJ is used for ionization and about 20 μJ for heating (to 50 eV). This means that about 33 percent of the pulse energy is required for the process. Note that this is a rough estimation. The reason for this inexactitude is the estimate of the ionization volume. As detailed above, the interaction volume is far from being governed by Gaussian beam formalism. Moreover, an influence of the refractive index of the plasma on the pulse propagation and hence the volume in which ionization occurs, is not included in the model. In addition, the electron temperatures were estimated (from the simulation). For a more precise measurement of the absorption of laser energy, however, a large f-number of the focusing beam optics is required to increase the Rayleigh length to multiples of the interaction length. Measurements of this kind are reported in [161], for example. Since the pulse energy was limited to a maximum of about 150 μJ, such experiments were not feasible and thus beyond the scope of this study. Nevertheless, using the measurements of the beam caustic above, a good agreement between estimation and experiment has been observed.

The influence of ionization induced defocusing on the absorption has been demonstrated by changing the focal position within the expanding gas jet. Since the density of the gas jet was known from interferometric measurements, it has been possible to compare it directly with the absorption data. Figure 6.12 shows the degree of absorption measured with the Ulbricht sphere as a function of the focal position of the pulse within the gas jet. Experimentally, the position of the valve was varied with respect to the focus, which was fixed. The height of the beam above the nozzle was kept at 500 µm. Neon and argon were used as target gas. While in the case of neon, the absorption is more or less proportional to the gas density profile (compare figure 5.7), in the case of argon a higher absorption has been observed (it saturates at a position of $z \approx 150$ µm). Moreover, the double-peak structure, which is well reproduced in the Rayleigh scattering signal obtained from the experiment to determine the cluster density [163], is not reproduced here. This is an indication that the focus has been affected by ionization induced defocusing. In this experiment, the backing pressure was 50 atmospheres.

Measurements of blue-shift

In addition to the fraction of laser energy that was absorbed, the optical spectrum of the laser pulse after the interaction was measured. Here a blue-shifting of the pulse spectrum has been observed. In general, a spectral blue-shift is caused by an increase of the electron density along the propagation axis of the pulse due to field ionization. As a consequence, the refractive index is changing rapidly across the pulse. This leads to self-modulation and blue-shifted frequency components in the spectrum with respect to the carrier wavelength. This is in analogy to the self-phase-modulation process caused by a non-linear refractive index medium (see above). Due to the fact that recombination and hence a reduction of the electron density can be neglected during the interaction time of the pulse, only a frequency up-shift has been observed. The spectral blue-shift, $\Delta\lambda$, with respect to the central wavelength, λ, of the pulse is given by [164]

$$\Delta\lambda = \int_0^L \frac{e^2 n_0 \lambda^3}{8\pi^2 \epsilon_0 m_e c^3} \cdot \frac{\mathrm{d}Z}{\mathrm{d}t}\,\mathrm{d}l. \tag{6.16}$$

Here the initial atomic density is denoted by n_0, and the ionization rate by $\mathrm{d}Z/\mathrm{d}t$, where Z is the average charge state produced. The blue-shift is increasing when the interaction length, L, is increasing and is proportional to the number of

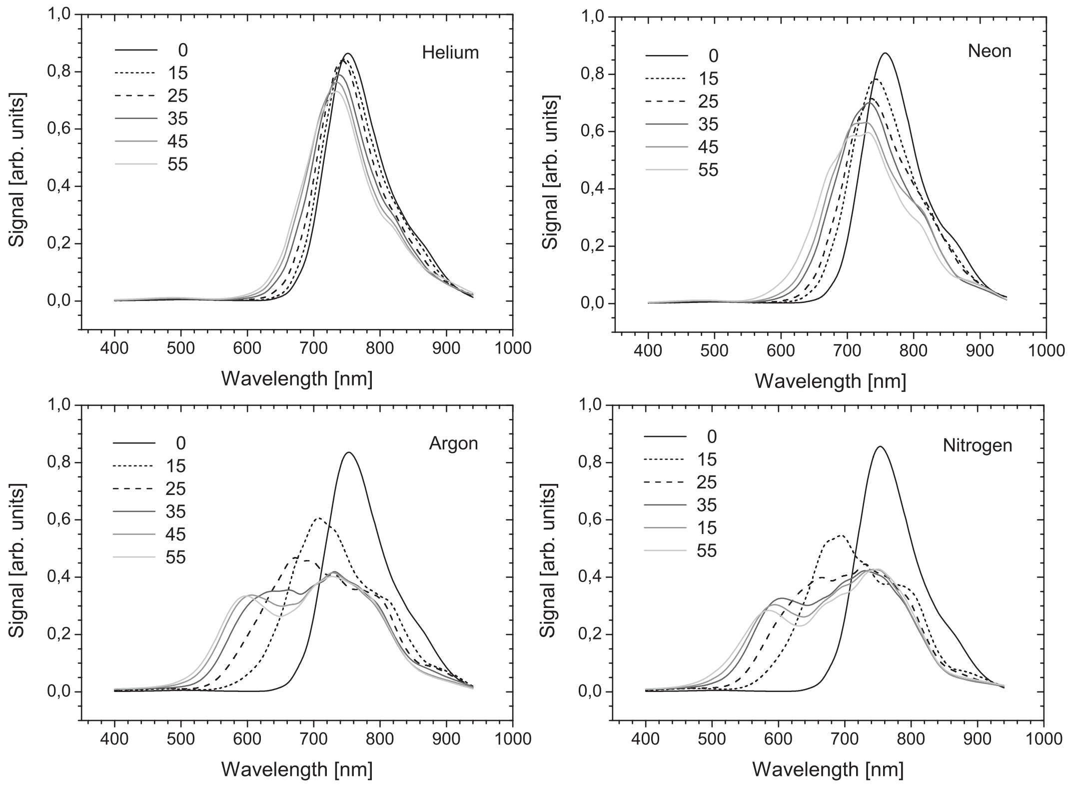

Figure 6.13: Optical spectra of the pump pulse after the interaction with different target gases. The backing pressures (in atmospheres) were varied during the experiments. A spectral blue-shift is observed.

electrons produced. The spectra obtained for the four gases studied here are presented in figure 6.13.

During the measurements, the backing pressure of the valve was increased up to about 50 atmospheres. At focal position (2), a local density of up to about $n_0 \approx 3 \cdot 10^{19}$ cm^{-3} was produced. In all cases, a significant blue-shift of the laser spectrum has been seen which increased with the background gas density. In order to quantify the effect, the wavelength at which the spectral intensity reached 10% of the normalized total intensity was recorded. The results are shown in figure 6.14. The spectra have been normalized. Note that in the literature sometimes different definitions of blue-shift are given, e.g. the shift of the center of the spectral intensity profile.

Comparing the slopes of the curves with the ones depicted in figure 6.11 (showing the absorption obtained with the Ulbricht sphere) reveals a significant similarity. The maximum blue-shift increases linearly for all test gases up to about 25 atmospheres. Beyond, argon and nitrogen have got a reduced rate with respect to an increase in background gas density. Hence the ionization-induced blue-shifting of the pulse qualitatively correlates to absorbed pulse energy. The laser intensity was not varied during this measurement, and so the volume, in which a certain laser intensity was achieved, was remained constant. This underlines the importance of defocusing.

In order to compare the observations with the theoretically expected blue-shift, equation (6.16) was simplified to

$$\frac{\Delta\lambda}{\lambda} \approx \frac{n_0 L}{2 n_{cr} c} \frac{\mathrm{d}Z}{\mathrm{d}t}. \tag{6.17}$$

Particularly $L \approx z_R$, $n_0 = 1.5 \cdot 10^{19}$ cm^{-3}, $n_{cr} = 1.74 \cdot 10^{21}$ cm^{-3} were used. The ionization rates $\mathrm{d}Z/\mathrm{d}t$ were estimated using the predicted charge state of the simulation (compare figure 6.21). The assumption was that this charge was produced within 10 femtoseconds. This yields a spectral blue-shift of $\Delta\lambda/\lambda \approx 0.1 - 0.2$ which is of the same order of magnitude as observed in the experiment. For a more detailed analysis, however, numerical 1D-PIC simulations have been performed (see below).

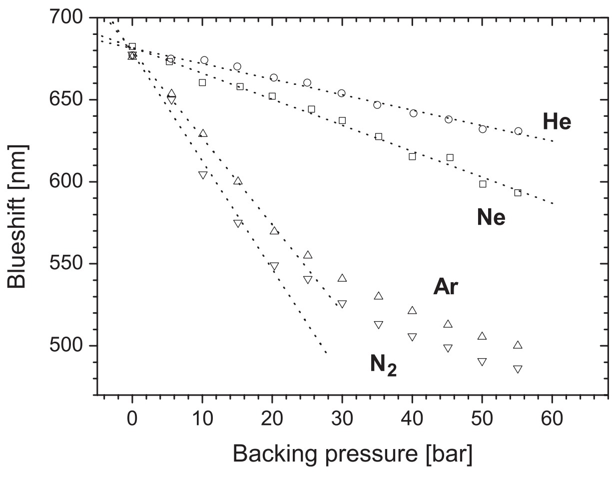

Figure 6.14: Blue-shift of the pump pulse after the interaction with various target gases. The shift is shown as a function backing pressure. See also figure 6.11.

Influence of femtosecond-pre-pulses

As explained above, the XUV-spectra obtained on solid targets have clearly shown that no pre-pulse was present. In order to investigate the effect of a controlled pre-pulse, however, the accusto-optical filter in the front-end (DAZZLER) was reprogrammed. So it was possible to use up to 20 percent of the pulse energy to generate a well-controlled pre-pulse. The delay was varied with femtosecond precision. Figure 6.15 shows a shadowgram obtained using argon at 50 atmospheres backing pressure at focal position (1). A pre-pulse containing 20 percent of the total pulse energy was present 100 fs prior to the main pulse. Note that the pre-pulse was also transferred to the diagnostic channel. Nevertheless, since frequency-doubling in the BBO crystal is a non-linear process, the conversion efficiency of the energy contained in the pre-pulse is low compared to that of the main pulse. Hence the double-exposure was negligible if the 400-nm bandpass filter was present. In the shadowgrams, the evolution of a shadow structure of about 30 μm in front of the beginning of the channel is clearly observed. Changing the programmable delay caused a linear change in the distance with respect to the main interaction. The inserted delay was in good agreement with the shift of the pre-plasma obtained in the images. The ionization threshold of argon is a few 10^{14} W/cm^2, hence the maximum intensity contrast detectable in the shadowgrams is less than 10^2. Nevertheless, in the cases of argon and nitrogen, a pre-pulse containing less than 10 percent of the pulse energy could still be detected.

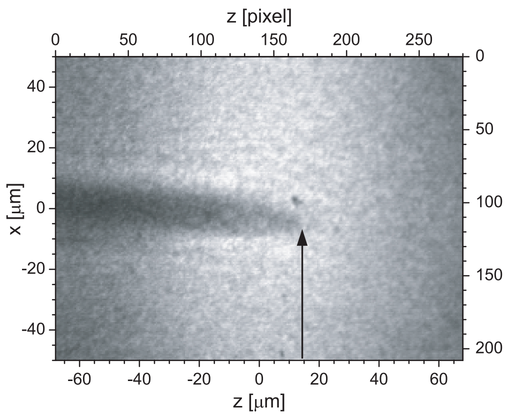

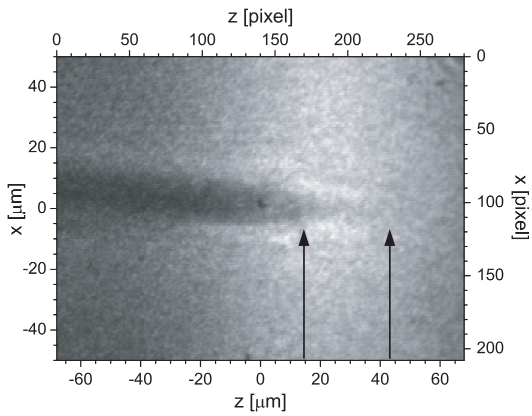

Figure 6.15: Shadowgrams of the ionization front produced in argon. Left: without pre-pulse, right: with a 100 fs pre-pulse present containing about 20% of pulse energy.

Evolution of Fresnel diffraction pattern

Increasing the distance between the diagnostic plane that was imaged with the microscope objective and the plasma axis, interference structures were observed in the shadowgrams. The fringe structure evolved parallel to the channel axis, and when using argon and nitrogen, a good contrast has been observed. A typical image is presented on the left side of figure 6.16, depicting a high-resolved image of the ionization front produced in nitrogen. The image was post-processed (enhancement in contrast) in order to improve the signal-to-noise contrast. The interference structure behaved similar to that of a Fresnel diffraction pattern, which is usually produced behind a sharp edge. For example, the dimension of the pattern increased with the distance Δy. At the onset of the channel, the structure developed at an angle of about 45 degrees with respect to the propagation direction of the pump pulse. This can be explained by optical retardation of the diffracted rays. Similar results are reported in [16].

In order to compare the dimension of the structures with that of the 10 fs laser pulse, an iso-intensity line indicating $2 \cdot 10^{14}$ W/cm^2 was added to the left picture of figure 6.16. This line defines the volume of the pulse within the background gas is being ionized. The BSI-thresholds for the first ionization state were used. They are similar for argon and nitrogen. The result is, however, that the pattern observed is significantly larger than the pulse diameter. This is further indication that the pattern was produced by Fesnel diffraction of the probe pulse on the plasma channel boundary.

Further, a comparison of the intensity distribution with a Fresnel diffraction pattern produced behind an edge was of interest and therefore a line-out was taken and compared with an analytic model. The findings are shown on the right side of figure 6.16. Here two patterns have been added in order to reproduce the intensity modulation on the upper and lower sides of the channel. A good agreement has been found. Particularly the distance from the edge at which the analytical model produces a similar pattern as seen in the shadowgrams was of the same order as Δy in the experiment. Note that the contrast of the diffraction pattern is small compared to the one observed in the shadowgrams used to analyze the change in the deflection angle of the probe rays due to the continuous change in the refractive index inside the channel. Especially when small distances Δy were chosen, the diffraction pattern was small and had no significant influence on the signal. Nevertheless, with increasing distance Δy, also the distance between the maxima in the Fresnel pattern was increased. So at large Δy, the pattern could be well resolved. The PIC-simulations explained

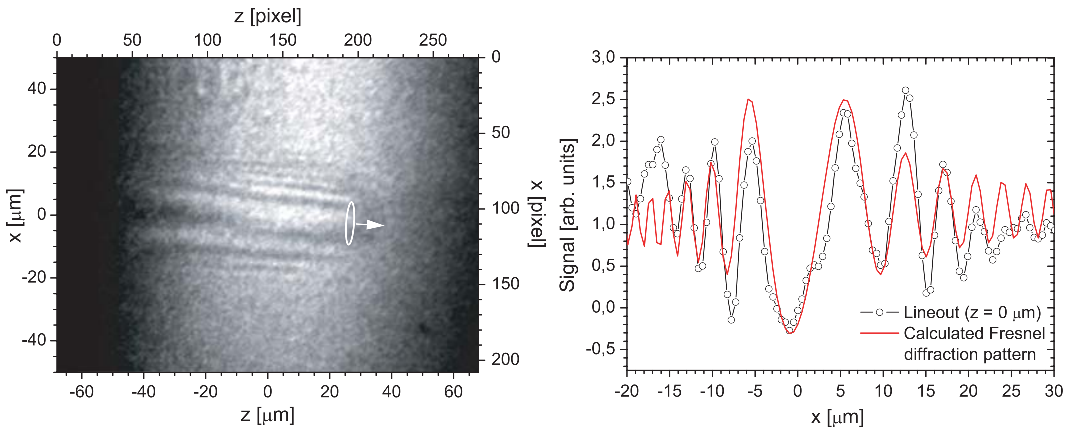

Figure 6.16: Left: Ionization front observed in nitrogen. A 10 fs pulse is indicated by an iso-intensity line of about $2 \cdot 10^{14}$ W/cm^2. A characteristic diffraction pattern is evolving under an angle of about 45 degree with respect to the direction of the main pulse. Right: line-out in the x-direction and comparison with calculated Fresnel-diffraction patterns.

below have clearly reproduced the patterns.

The occurrence of the diffraction pattern is induced by the strong focusing of the pump pulse. As a result of steep intensity gradients, the ionization rates increase rapidly at the edge of the pulse. If the electron density and hence the refractive index change on a scale length that is of the same order or less than the wavelength of the probe pulse, the rays are diffracted and Fresnel patterns are produced.

6.4. Numerical simulations

Numerical simulations of the dynamics of the ionization front produced in the target gas were performed with three-dimensional (3D) Particle-In-Cell (PIC) simulations. In general, PIC codes solve the relativistic equations of motion for a large number of particles under the influence of electric and magnetic fields together with Maxwell's equations [165]. Particle simulations are advantageous with respect to fluid simulations whenever kinetic effects are to be resolved. In contrast to fluid codes, which essentially require the existence of a local thermodynamic equilibrium to define fluid variables such as pressure and density, PIC codes are useful for the simulation of particle acceleration and other non-Maxwellian effects.

According to kinetic theory, the dynamics of a plasma can be modelled by calculating the individual trajectories of each particle in phase space. This, however, is impossible due to the large number of particles (i.e. typically 10^{23} cm^{-3} in a solid). In order to simplify the problem, a large number of real particles is represented by a QUASI or MACRO PARTICLE having a fixed charge and mass. Therefore in the numerical scheme, a spatial grid is introduced to the problem that is fixed in space. The quasi-particle can be understood as a charged cloud of the dimension of a grid cell. This is why the technique is also called CLOUD-IN-THE-CELL method. Solving the single-particle equation of motion in averaged electric and magnetic fields is equivalent to solve the VLASOV-EQUATION coupled to MAXWELL EQUATIONS. The Vlasov-equation describes the development of the distribution function, $f(\vec{x}, \vec{v}, t)$, of a single (quasi-) particle in phase space,

$$\frac{\partial f}{\partial t} + \vec{v} \cdot \frac{\partial f}{\partial \vec{x}} + \vec{a} \cdot \frac{\partial f}{\partial \vec{p}} = 0, \tag{6.18}$$

and gives a self-consistent description of the laser-plasma interaction [157]. Here $\vec{p} = m\gamma\vec{v}$ is the relativistic momentum of the (quasi-) particle, $\vec{a} = q(\vec{E} + \vec{v} \times \vec{B})$ the acceleration due to the Lorentz force and γ the relativistic Lorentz factor. If collisions are included, a collision term, $\left(\frac{\partial f}{\partial t}\right)_{\text{coll}}$, has to be added to the right side of equation (6.18) yielding the VLASOV-BOLTZMANN-EQUATION.

The basic cycle of a PIC-iteration starts with solving the Maxwell equations on the grid. The space charges and currents are obtained from the distribution and velocities of the quasi-particles. Then the center-of-charge of the cloud is propagated as described by the Lorentz equation (2.14). The fields at the positions of the particles are obtained by interpolation. The new positions and velocities obtained after a time step Δt are used to update the space charges and currents to be inserted in Maxwell's equation. Now the PIC-cycle starts again. During the calculation, the shape of the clouds remain the same and they can unhindered penetrate each other. The interaction is introduced indirectly via the fields. In general, a collision-less plasma is assumed in a standard PIC-code, i.e. collective effects dominate over small-scale collisions. Binary collisions have to be included separately. The time step of the iteration, however, has to be small enough to resolve the frequencies that occur in the problem (e.g. the external electric laser field and the electron plasma frequency). Also the spatial grid size has to be adapted to the problem accordingly in order to resolve typical scale length (such as the Debye length).

The Plasma Simulation Code PSC

In order to simulate the dynamics of the ionization front, the Plasma Simulation Code (PSC) code written by Hartmut Ruhl was used. The code solves the relativistic Vlasov-Boltzmann equations coupled to the Maxwell equations for an arbitrary number of species [17]. Binary collisions between the particles are included using a Monte-Carlo Particle-In-Cell (MCPIC) approach. Usually two separate meshes are used, one representing the Maxwell fields and the quasi-particles, which represent the distribution function, and one defining an interaction range for colliding particles. In the PSC, however, the same mesh is used for both. Field ionizations are included via the ADK tunneling rates for the neutral and ionic species. If ionization occurs, a new photoelectron is generated at the position of the ion and the charge state of the ion adapted accordingly. The photoelectron is initialized with zero velocity.

The code consists of various modules which can also be run stand-alone. So the Maxwell solver for the fields, the Monte-Carlo binary collision module as well as the solver for the Vlasov equation can be switched on and off prior to starting a run. Details of the code and the modules can be found in [17]. The simulations reported here were performed on a 64-bit server with two dual-core AMD Opteron processors running at 2.6 GHz and 24 GBytes RAM.

Simulation set-up

The coordinate system used in the simulation was similar to the one that described the experimental set-up. The simulation box had the dimensions of $20 \times 30 \times 20$ μm^3. The mesh size was 0.1 μm in the x-direction and 0.05 μm in the y- and z-direction, respectively. The region that was filled with particles was restricted to a volume of $10 \times 10 \times 20$ μm^3 centered on the optical axis of the pump pulse in order to save computational resources. The neutral particle density was $1 \cdot 10^{19}$ cm^{-3} if not stated otherwise. Each species was represented by 2 quasi-particles per cell. Outside the inner box, the density was set to zero. A linear p-polarized pump pulse with a central wavelength of 800 nm propagated in the positive z-direction, i.e. the electric field was oscillating in the $\pm y$-direction. To focus the pulse inside the simulation box, it was initialized with curved phase fronts, i.e. the k-vectors pointed towards a geometrical center. The pulse was focused under an angle of $\Theta = 9°$. As detailed in Appendix A, the focal diameter of a Gaussian beam is determined by the angle of divergence and the wavelength. In order to verify that the phase modulation imprinted on the pump pulse reproduced an intensity profile as predicted by the equations of Gaussian beam propagation, laser beam diffraction in vacuum was demonstrated. Particularly a focus with a radius of $w_0 = 1.35$ μm was obtained. The results are shown in figure 6.17 and are in good agrement with the analytic predictions. Note that the position of the beam waist of a focused Gaussian beam is shifted slightly towards the (virtual) focusing element due to the diffraction limit. This shift by Δf is usually negligible in real experiments. Nevertheless, here it gave a good test of the set-up and was it also observed in the simulation. The duration of the pulse was 10 fs (FWHM) and it was started in front of the simulation box. The focal intensity (cycle-averaged) was $I = 1.5 \cdot 10^{16}$ W/cm^2.

A Gaussian-shaped p-polarized probe beam with a wavelength of 400 nm was propagating in the $+y$-direction and initialized with a diameter of 10 μm (FWHM). The intensity of the probe beam was 0.05× that of the pump pulse in order to keep the intensity below the ionization threshold of the target material. The probe beam and the pump pulse were started simultaneously and both beams crossed each other in the center of the simulation box. A continuous wave beam was simulated in order to simplify timing purposes. To introduce a "delay" with respect to the pump pulse, an appropriate slice of the probe beam was analyzed. For the Maxwell fields, periodic boundary conditions were chosen in the x-direction as well as for the quasi-particles. Radiative boundary conditions were chosen for the fields in the y- and z-direction so that the radiation could escape freely while periodic boundary conditions were selected for the particles.

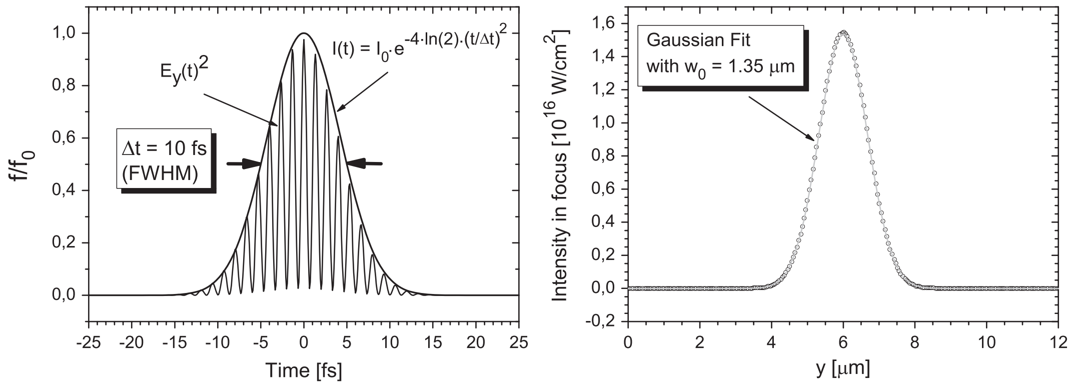

Figure 6.17: 3D-PIC simulation of laser beam diffraction in vacuum. Left: Pulse profile in the focus. The square of the electric field is plotted after 2000 time steps in a co-moving frame and compared with analytic expressions to check the set-up of the temporal pulse shape. The envelope for the intensity, $I(t)$, is given by equation (10) in Appendix A. Right: Focusing the pulse under an angle of $\Theta = 9°$, a beam waist of $w_0 = 1.35$ μm is achieved.

Simulation of shadowgrams

As soon as the pump pulse entered the simulation box, ionization of the background gas was observed. As an example, figure 6.18 shows the electron density produced in helium for different time steps in the simulation. The map represents a xz-cut along the optical axis of the pump pulse, i.e. at $y = 6$ μm. The position of the pulse is indicated, too. The beam caustic due to focusing has been well reproduced. A maximum average ionization state of about $Z = 1.5$ has been observed in the center of focus. Clearly the different ionization steps can be separated from each other. While an average ionization state of $Z = 1$ has already been generated at the leading edge of the pulse, a higher intensity is required to liberate the second electron. This happens close to the center of the pulse. Particularly the distance between the onset of the first and the second ionization state is less than 2 μm. Note the modulation in the electron density at the position of the pulse front, which corresponds to the intensity of the pump pulse over a cycle. From the simulation it is observed that the speed of the ionization front is the speed of light.

In this run, the collisional module was switched off because collisions had no impact on the electron density produced (collisional ionization was not included in the model and plays a minor role at these densities). The simulation was repeated for the other gases as well. Similar results have been obtained. In all cases, the ionization front propagated with the speed of light.

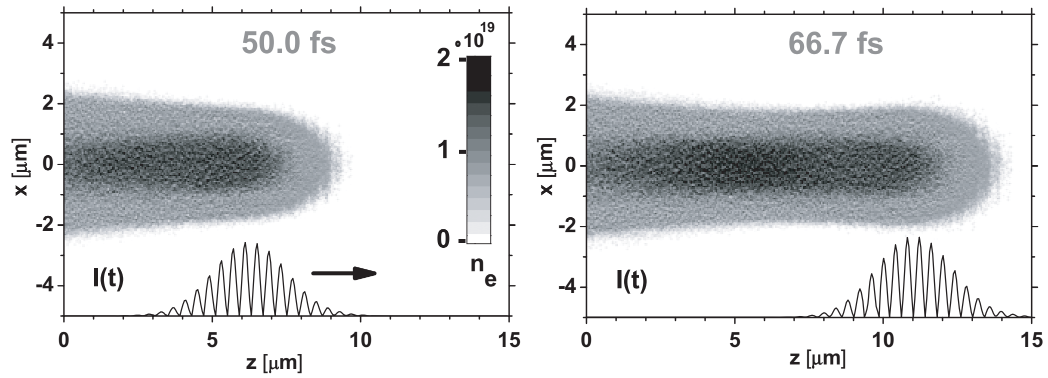

Figure 6.18: Electron density produced by 10 fs pump pulse for different times. The pulse position is indicated below. In the center of the focus, an average ionization state of about $Z \approx 1.5$ has been observed.

The shadowgrams were simulated by analyzing the Poynting flux of the 400 nm probe beam after the interaction with the electron density. Therefore a plane parallel to the one shown in figure 6.18 was chosen and shifted by $\Delta y = +6.5$ µm along the k-vector of the probe with respect to the plasma axis. The Poynting flux was averaged over 4 optical cycles of the probe. Without the field ionization module running, an undisturbed Gaussian intensity profile has been observed. With field ionization included, however, the intensity distribution was modified as depicted in figure 6.19. Here the reference given by the intensity profile without plasma was subtracted. In order to include the motion blur in the simulations, the spatial resolution in z-direction was limited. Therefore a filter calculated the "smearing" of the moving front over 8 fs or 2.7 µm in the images. The intensity modulation observed in the simulated shadowgrams is caused by the deflection of the rays on the electron gradients produced by the electron distribution. As expected, the plasma acts as a negative lens due to the fact that the high electron density on the channel axis leads to a reduced refracting index with respect to outer parts of the channel. Hence the rays are bent outwards and a dark central part is observed in the shadowgrams. On the upper and lower side of the channel, a Fresnel pattern is evolving similar to that observed in the experiment. The origin is the abrupt rise of the electron density at the position of about $x = \pm 2$ µm due to strong focusing. The electron density is increasing from zero to $1 \times n_0$ on a scale length shorter than the wavelength of the probe pulse. Hence a steep gradient in the optical refractive index is produced. This leads to a diffraction of the pulse. A similar structure is seen in figure 6.16.

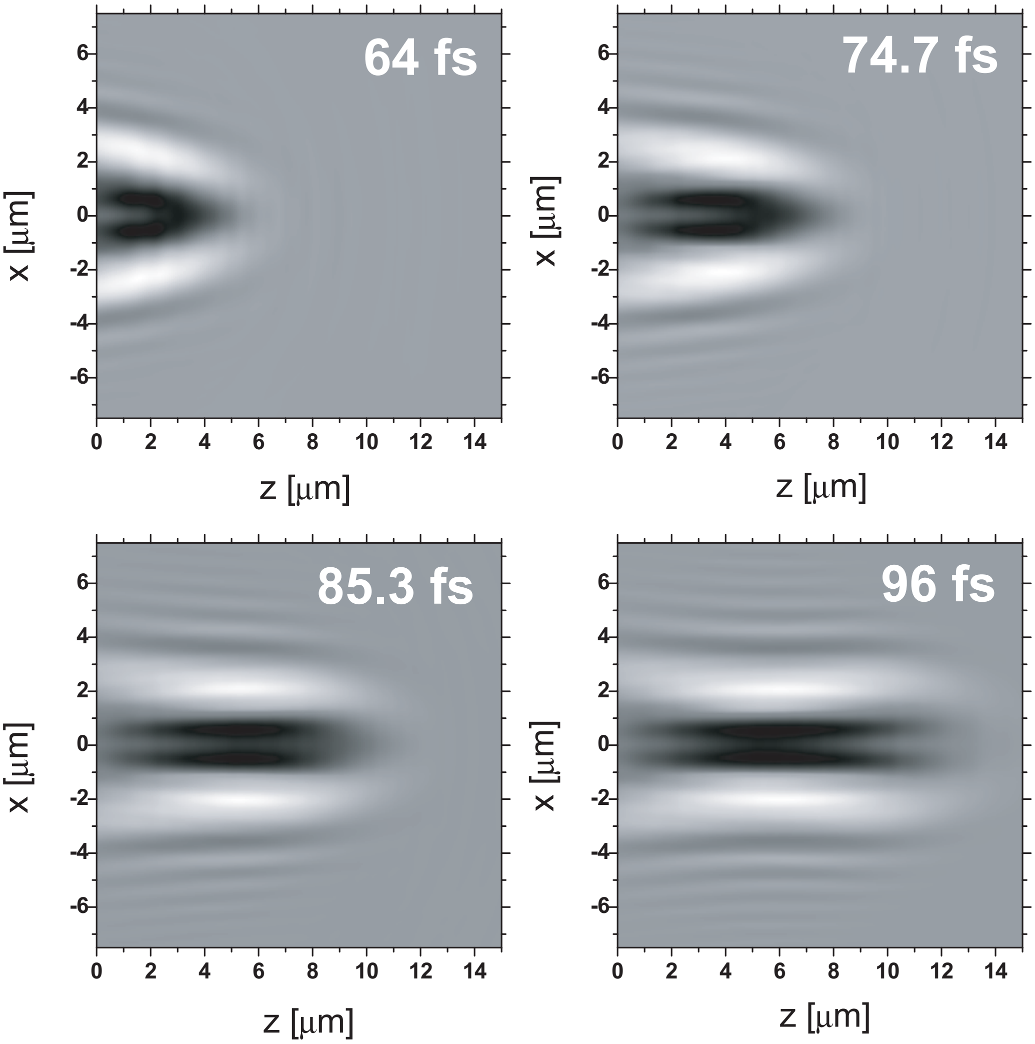

Figure 6.19: Shadowgrams gained from the 3D-PIC simulation for different times.

The intensity distribution given by the Poynting flux without the filter applied is shown on the left side of figure 6.20. A modulation has also been observed in front of the plasma channel. Here the diffraction of the probe on the instantaneous electron density distribution is resolved. Note that the period of the modulation is of the order of 400 nm and difficult to be resolved optically. On the right side of figure 6.20, only the x- and z-components of the Poynting flux that are detected in the plane of interest were plotted. Here it is clearly observed that the shadow structure seen in the shadowgrams is due to the fact that most of the rays are bent outwards, i.e. in positive and negative x-direction.

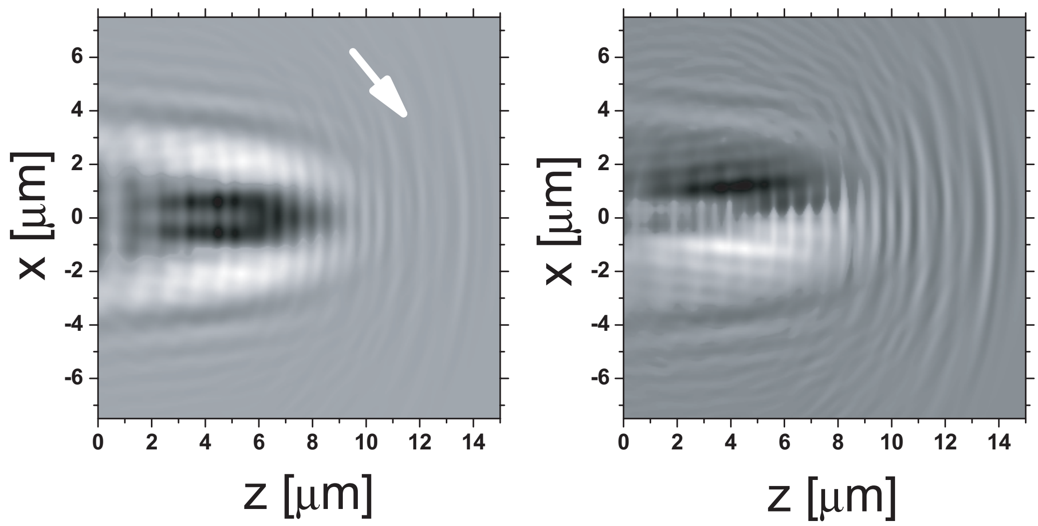

Figure 6.20: Shadowgrams obtained by analysis of the Poynting flux of the probe without 8 fs filter applied. Left: Total Poynting flux obtained in the simulation at the plane of interest. At the front of the channel, a fine structure has been observed (indicated by the arrow). The modulations on the left side are an artefact, caused by deflection of the probe beam on the wall of the simulation box. Right: Here only the x- and z-components of the Poynting flux are shown.

Moreover, at the front of the channel, a fine structure has evolved which is caused by the small-scale gradients occurring during the ionization process in z-direction. The comparison with the electron density distribution shown in figure 6.23 reveals a clear analogy (note that the ionization observed in neon and argon is quite similar. See also figure 6.18). This structure seen at the front of the channel, however, is smeared out in the experiment due to the pulse duration of about 8 fs. Nevertheless, this clearly shows that even the inner-cycle dynamics of the ionization front can be obtained from a shadowgram, in principle, if the spatial and especially the temporal resolutions are appropriate.

Simulation of ionization dynamics

The ionization front generated by the pump pulse depends strongly on the ionization rates of the target material. Especially in the context of sub-10-fs pulses, the pulse duration may have a direct influence on the average charge state produced. So even though high ionization rates are observed, the interaction period may be too short to cause depletion of an electronic level (compare equation (2.13)). Hence reduced average charge states are observed with respect to longer pulses at the same intensity.

In order to study the ionization dynamics more in detail, the simulation was performed in a simplified geometry (1D) and at increased resolution. Particularly a resolution of 20 cells per micron in the z-direction and a time step of 0.1 fs were used in order to guarantee that the ionization process over a cycle was resolved. The collisional module was switched off. Figure 6.21 shows the average ionization state, i.e. the average electron density divided by the background gas density, of the target gas that is produced by a 10 fs pulse as a function of pulse intensity. Helium, neon, argon and nitrogen (not shown) were the gases used. The background gas density was $1 \cdot 10^{19}$ cm^{-3}. The vertical lines indicate the ionization thresholds predicted by BSI-theory (equation (2.9)). As a few-cycle pulse was used, a lower average ionization state has been observed than predicted the BSI-thresholds. This is clearly an effect of the pulse duration, as demonstrated in the bottom right picture of figure 6.21. Here the average ionization state produced by a Gaussian pulse of 10 fs in duration and at an intensity of $I = 2 \cdot 10^{16}$ W/cm^2 is shown (curve a)). The pulse is propagating from left to right through a homogeneous background of neon. For comparison reasons, curve b) depicts the average ionization state produced by a temporal flat-top pulse which has an identical leading edge as the 10 fs pulse. The pulse itself is not drawn. In this run, the number of particles per cell was increased to 500 in order to achieve better statistics (reduced noise). An average ionization state of $Z = 3$ has been found in the case of the flat-top pulse. This is in agreement with the BSI-theory. In contrast, an average ionization state of about $Z \approx 2.4$ was produced by the 10 fs pulse. A saturation of the average ionization state has been observed after about 35 fs for the longer pulse. This result, however, shows that the proper rate equations have to be considered to explain the total number of electrons produced.

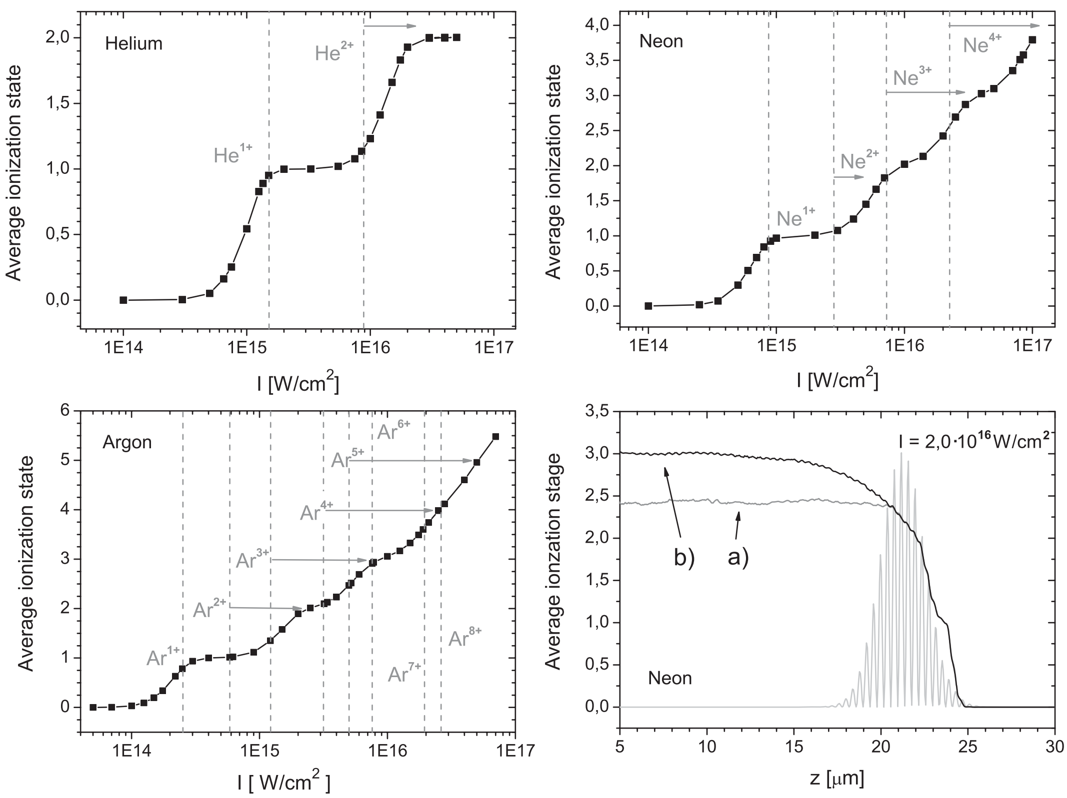

Figure 6.21: Average ionization states produced by 10 fs pulse as function of laser intensity for different gases. The BSI-intensities are indicated by vertical lines (compare Appendix B). Due to the ultra-short pulse duration, the average ionization state of the gas has been reduced. The underlying effect is illustrated bottom right and shows the average ionization state produced by a pulse with a duration of $\Delta t_I = 10$ fs (FWHM) and an intensity of $2 \cdot 10^{16}$ W/cm^2 (curve a)). Here $Z \approx 2.4$ is found. For comparison, curve b) has been produced by a pulse with a temporal top-hat profile with identical rise time and intensity. Here the average ionization state is $Z = 3$.

Simulation of the evolution of electron temperature due to ATI-heating and collisions

The strength of the electric field that is present at the moment when a photoelectron is produced determines the residual (ATI) energy the electron can gain from the laser field. After the passing of the pulse, binary collisions will lead to thermalization of the plasma electrons. In order to simulate this process, the same simulation set-up was used as before, but this time the collision module was turned on. The momenta of the electrons for the x-, y- and z-direction were stored and the distribution function of the kinetic energy computed. Particularly a slice of 10 μm in width was used within which the kinetic energy of the electrons was averaged. This was done for each time step. The energy spectrum obtained was fitted by an exponentially decreasing function to define a temperature. The result is depicted in figure 6.22. Here the electron temperature of the y-component is shown, i.e. the one parallel to the direction of the polarization of the laser field.

When a temperature was defined, i.e. the fit with an exponential function was possible, an initial temperature of about 200 eV was discovered. At this time, a part of the electrons was still oscillating in the trailing edge of the pulse and the energies of the x- and z-component (not shown here) were about zero. After the pulse had passed, however, the temperatures of the x- and z-component increased and the temperature of the y-component decreased until all three relaxed at the same value. This happened after about 250 fs in the case of helium and 450 fs in the case of neon. As detailed above, the kinetic energy of the plasma electrons is due to ATI. In order to compare the simulation with formula (3.3), the ATI energy was calculated using the ADK tunneling ionization rates. Using furthermore $k_B T_{\mathrm{ATI}} = 2/3\ \mathcal{E}_{\mathrm{ATI}}$ [94], similar temperatures as those observed in the simulation were found. Note that e.g. the time scales observed here are of the same order as those observed experimentally (compare figure 6.9, showing the increase in electron density after the interaction of the gas with the pulse). Although this effect was connected to collisional ionization, it indicates that electron energy, which was distributed somehow within the plasma, was present. The simulation as well as the experiment, however, have clearly shown that the pulse duration is short compared to the time required for thermalization.

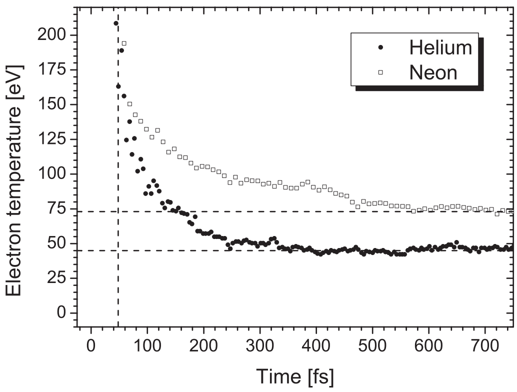

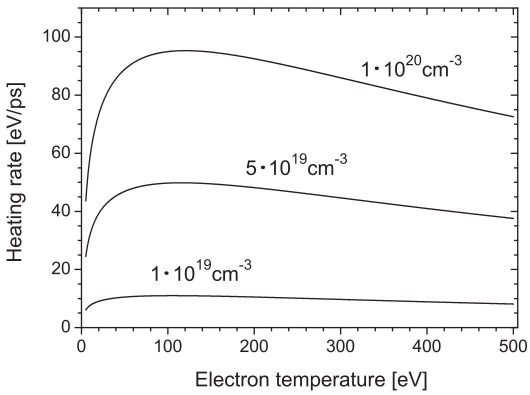

Figure 6.22: Left: Evolution of temperature defined via the energy spectrum observed for the y-component of motion of electrons produced by field ionization. Right: Calculated collisional heating rate for different electron densities. The average ionization state assumed is $Z = 1$. Note that the rate scales with $\nu_{ei} \propto Z \cdot n_e$ (equation (3.6)).

So far, only the energy contribution due to dephasing (ATI) was considered. To take into account the energy transfer from the quiver energy into random kinetic motion due to collisions with ions during the pulse interaction, the heating rate due to inverse bremsstrahlung was estimated. The right part of figure 6.22 depicts the heating rate calculated using equations (3.6) to (3.12), showing that the collisional heating effect can be neglected in the context of sub-10-fs pulses and at densities of the order as used during this experiment. This is a result of the rather low collision rates between the electrons and the ions being influenced by the ponderomotive potential of the laser. So, inverse bremsstrahlung is more effective at longer pulse durations and higher densities (e.g. such as in solids). The role of collisional ionization in helium at solid density was studied by PIC simulations in [157, 158].

Simulation of ionization-induced blue-shift

During the experiment, a significant blue-shift in the optical spectrum of the pump pulse after the interaction with the target gas has been observed. Blue-shifting was ascribed to the temporal change of the refractive index due to the increase in electron density over the pulse. So the relationship between the ionization rate and the frequency shift gives information about the electron density produced. The information obtained from the optical spectra were particularly useful for the estimate of the electron density produced within the channel. Note that due to the strong focusing of the laser pulse, the interaction length between the probe pulse and the electrons in the plasma channel was approximately of the diameter of the focal spot, i.e. about 5 μm. As a result, in the focal position (2), the resolution of the interferometer was limited. The interaction length of the pump pulse, in contrast, was of the order of several Rayleigh lengths. The frequency shift was accumulated over this propagation length. Thus, a clear signal at gas densities of about 10^{19} cm^{-3} has been obtained.

The interaction of the pulse with the gas was in this case also simulated in 1D-geometry. Particularly the background gas density was varied and the electric field distribution of the pump pulse was analyzed. On the left side of figure 6.23, the electric field of the 10 fs laser pulse is depicted. Here the pulse propagated for about 4 μm through a background of neon gas at a density of $1 \cdot 10^{19}$ cm^{-3}. The gas was ionized and the evolution of the electron density, $n_e(t)$, over the pulse was resolved (top). The ionization rate, dn_e/dt (bottom), has been achieved by numerical derivation. The non-zero values at the positions where the oscillation of the electric field passes through zero are an artefact of smoothing prior to the deviation. However, a high ionization rate has been observed at the leading edge of the pulse. So almost all electrons of the first ionization state ($\mathcal{E}_{\text{ion}} = 21.6$ eV) have been ionized during a single cycle (at $z \approx 5.5$ μm in the figure). Then the ionization rate decreases due to depletion of the electronic reservoir. It increases again as the intensity is appropriate to ionize the second electron ($\mathcal{E}_{\text{ion}} = 41$ eV). This happens close to the center of the pulse ($z \approx 4.2$ μm . . . 5.2 μm). It is also here, that the rate decreases faster than the pulse intensity after a few cycles. This again indicates a depletion of the level. At the trailing edge of the pulse, almost no ionization has been seen. In average, a charge state of $Z = 2$ has been obtained within about 5 fs.

The electric field distribution of the pulse after a propagation length of about 36 μm is shown on the right side of figure 6.23 for three different background gas densities. In the case of low density (top), the pulse shape remains almost unchanged. With increasing background density, the number of ionization events increases. Here a change in the phase devolution has clearly been observed as well as an elongation of the pulse width. High frequency components, in particular, have been produced at the positions of high ionization rates. This is in agreement with the model presented in [164] (compare equation (6.17)). Self-phase modulation at the position of steep electron density gradients along the pulse has been observed. Note that the change in the pulse shape also leads to a reduction in intensity (bottom). This shows, however, that even in the simplified 1D-geometry, self-phase modulation and hence ionization-induced blue-shift is a

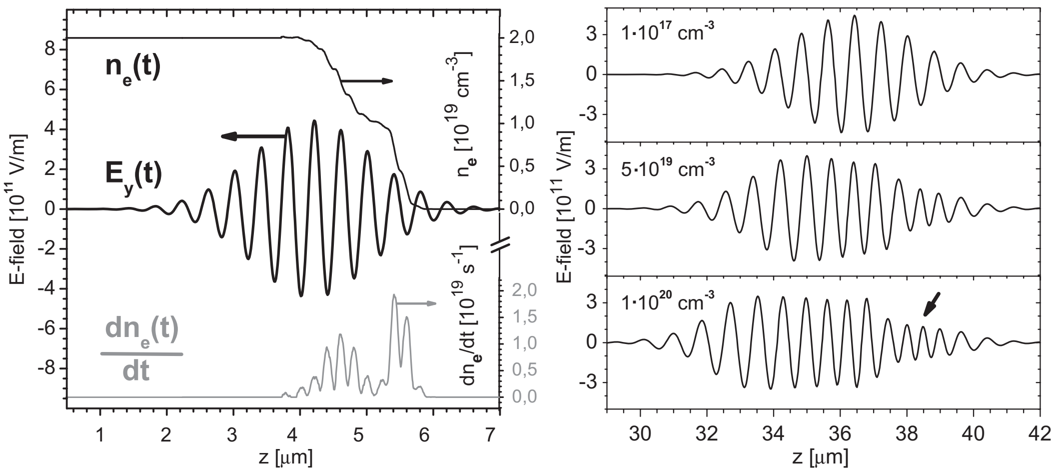

Figure 6.23: Left: Electric field of 10 fs laser pulse after entering the simulation box. The pulse propagates from left to right. The electron density that is produced during the interaction with neon and the ionization rate $\mathrm{d}n_e/\mathrm{d}t$ are plotted. Here the background gas density is $1 \cdot 10^{19}$ cm^{-3}. Right: Distribution of the field of the laser pulse after a propagation of about 36 µm through neon. Here the background gas density was varied. The strongest frequency shift as observed at the leading edge of the pulse is indicated by an arrow.

highly dynamic process due to the feedback of the pulse shape on the ionization rates. The strongest frequency shift has been found at the pulse front (indicated by an arrow) where the ionization of the outermost electron occurs.

The spectrum of the pulse after propagation of about 36 µm through the target gas was obtained by Fourier transformation of the electric field. The results are shown in figure 6.24 (solid lines). In order to compare the result with the experimental data, some of the spectra already reported above have been added (dotted line, compare figure 6.13). Note that the peak intensity in the measured spectra is shifted from the central wavelength to shorter wavelengths by about 50 nm. This is a result of self-phase modulation in the gas filled hollow fiber, due to which a non-symmetric spectrum is produced. The simulated spectra have been plotted with an offset of 50 nm, so that a direct comparison of the simulated spectra with the experimental is possible. Nevertheless, a good agreement between simulation and experiment with respect to the relative blue-shift is observed. Particularly from the experiment, the data has proved that the blue-shift increases with background gas density. This has also been observed in the simulation. In order to obtain more quantitative data on the electron density produced, however, the gas density used in the simulation has

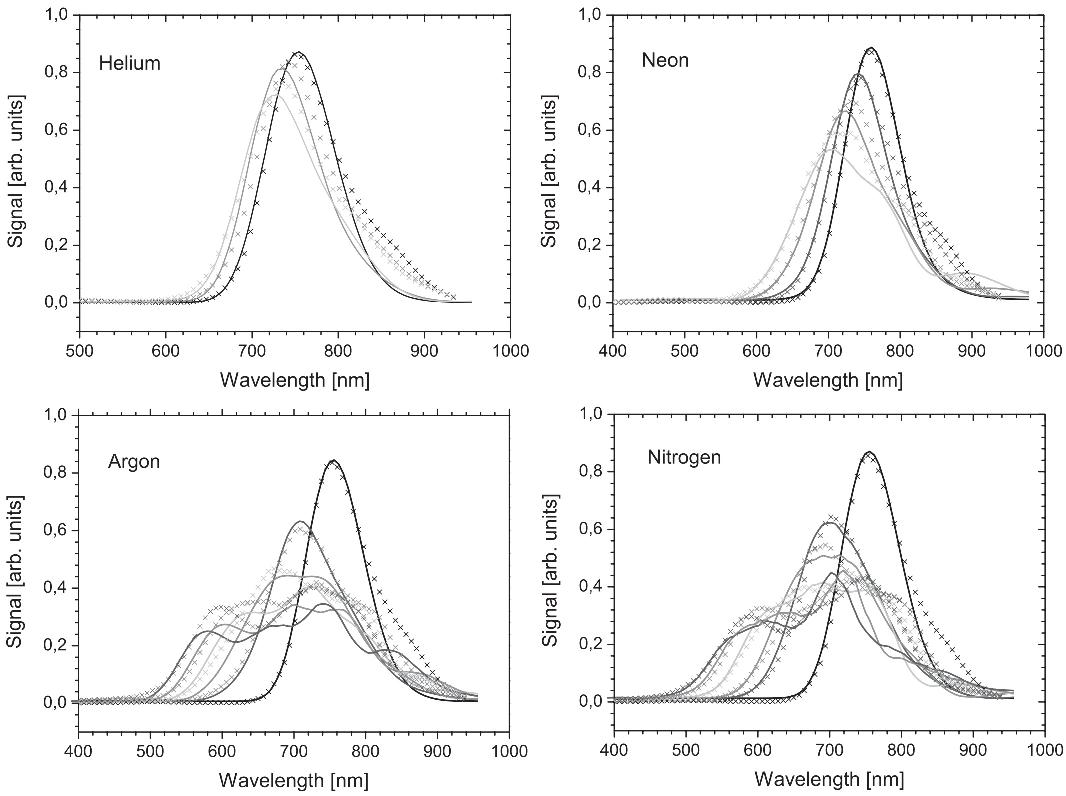

Figure 6.24: Simulated optical spectra of 10 fs pump pulse after interaction with target gas at various background densities ($I = 1 \cdot 10^{16}$ W/cm^2). To compare them with the experimental results, the measured data were added in the background (crosses). The result of the comparison is shown in in figure 6.25. Also in the simulation, the spectral blue-shift increases with gas density. Particularly a good agreement between the form of the spectra obtained in the simulation and the experiment has been achieved.

been compared with those of the experiment. The densities which correspond to a similar blue-shift are depicted in figure 6.25. On the left side of the figure, the frequency shift obtained in the experiment is repeated as a function of backing pressure. Since the intensity was kept constant during the measurement, the interaction length was constant as long as defocusing and clustering effects could be neglected. This was up to a backing pressure of about 25 atmospheres. The results obtained from the simulation are shown at the right side of the figure. Particularly the density used in the simulation is plotted as a function of background density in the experiment for two overlapping curves. It is also here that a linear relationship has been observed for pressures up to 25 atmospheres. In the case of argon and nitrogen, the deviation from the linearity is analogous to that observed experimentally. This was ascribed to the clustering of the molecules (see above). In the simulation, the density required to produce a spectrum simi-

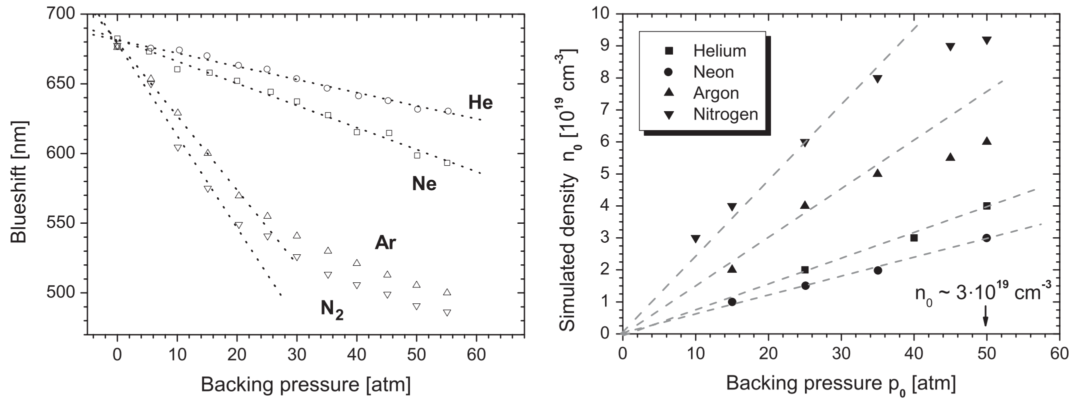

Figure 6.25: Left: Blue-shift observed experimentally for several gases. Right: Simulated background density correlated with the experiments for similar spectra.

lar to that of a given backing pressure is higher for helium than for neon. This, however, can be explained by the simulated average ionization rates (compare figure 6.21). In the case of helium, the average state increases from about $Z = 1$ to $Z = 2$ if the intensity increases from $1 \cdot 10^{16}$ W/cm^2 to $2 \cdot 10^{16}$ W/cm^2 and a 10 fs pulse is assumed. In the case of neon, the increase is from about $Z = 1$ to $Z = 1.5$. Hence, if the intensity was about $2 \cdot 10^{16}$ W/cm^2 in the experiment instead of $1 \cdot 10^{16}$ W/cm^2, a stronger increase of the blue-shift for helium than for neon can be expected. More important, however, is that for both a similar background density is needed to produce a similar blue-shift as observed in the experiment. Note that a background pressure of 50 atmospheres corresponds to a local atomic density of about $3 \cdot 10^{19}$ cm^{-3}, as indicated. For argon and especially nitrogen, a higher density has been required in the simulation to produce the same spectrum as observed experimentally. This is in agreement with the focal volume in which ionization is expected. Using particularly $I = 1 \cdot 10^{16}$ W/cm^2 and $M^2 = 2.9$, the lengths were calculated over which the laser ionizes the gas (by setting $I(z) \leq I_{\mathrm{BSI}}$, compare equation (44) in Appendix A). Here the thresholds, I_{BSI}, for single ionization have been used. For example, the distance over that helium can be ionized is about 128 μm. The distances found for the other gases follow the ratio 1 (He) : 1.4 (Ne) : 2.7 (Ar) : 3.2 (N_2). This has been compared with the slopes of the curves on the right side of figure 6.25. Here the slopes follow the ratio 1 : 1.3 : 2.4 : 3.3. Note that in the simulation the interaction length of the pulse with the gas was fixed to 36 μm and the background gas density was varied. In contrast to the simulation, the density was fixed in the experiment and the interaction length differed due to the focal geometry. Nevertheless, in both cases the relative blue-shift, $\Delta\lambda/\lambda$, has been proportional to the interaction length, L, and the background gas density, n_0 (equation (6.16) and (6.17)). Hence the relative blue-shift found in the simulation made it possible to estimate the background gas density, n_0, and with that the average ionization state, Z, of the gas and the electron density, n_e, respectively. Here the ADK ionization rates were used for this purpose. Although the relative numbers given by the ratios above are similar, the total numbers of electrons calculated are too high namely by a factor of 4. For example, the interaction length within helium that can be ionized is about 128 μm (equation (6.17)), compared to 36 μm in the simulation. So, the interaction length might be overestimated in the experiment. Therefore a rough estimation via the optical self-emission in figure 6.10 was also done. The comparison yields a neutral gas density of $1.5 \cdot 10^{19}$ cm^{-3}. The density is now underestimated by a factor of about 2 with respect to the interferometric measurement reported in chapter 5. This discrepancy might be due to the fact that the 1D-model cannot resolve spatial variation in the intensity profile or the effect of ionization induced defocusing. Moreover, blue-shifting of the spectrum is a highly-dynamic process since the part of the pulse that is undergoing a blue-shift changes with the intensity due to focusing. The spectral shift of the pulse on the optical axis is also different from that in the wings [166]. Nevertheless, the simulation of the blue-shift allows one to validate the electron density within a factor of 2 to 4. The relative blue-shift is in good agreement with the experimental data and especially the slope of the spectrum is has been reproduced in a good way.

7. Electron beam filamentation in over-dense plasmas

In the experiment described in this chapter, the propagation and filamentation of a laser-produced electron beam through over-critical plasmas were studied. Therefore a petawatt laser pulse was focused onto a thin solid target to accelerate electrons to MeV energies. While the pulse is stopped at the critical density, the electron beam can propagate through the over-critical plasma, carrying a part of the laser energy. The understanding of the transport of high energy electrons through dense plasma is of fundamental importance particularly for the Fast Ignitor (FI) concept relevant to laser fusion as proposed by Tabak *et. al.* [31]. In this scheme, an intense electron beam is used to initiate ignition in a high-density fuel pellet. In the experiment conducted here, pre-ionized CH-foam targets of various thicknesses and densities were used to investigate the spatial structure of the electron beam during the propagation. In particular, high resolution images of the optical radiation emitted by the MeV-electrons at the rear side of the target have been taken. It has been observed that the beam has broken up into filaments. The data clearly show that some of the inner filaments organize in a ring like structure. The role of the Weibel instability in initiating the filamentation process is inferred from 3D-PIC simulations and analytical considerations. By varying the thicknesses of the targets, the divergence angle of the electron beam has been obtained.

In the following, first key-features of the laser system used for this experiment are presented and the targets are described. Details of the set-up of the experiment and the optical diagnostic are explained in chapter 4. The experimental data are presented and compared with the results of 3D-PIC simulation.

7.1. The Vulcan Petawatt laser system

VULCAN is a 2.5 kJ high-versatile "large scale" Nd:glass laser located at the Central Laser Facility of the Rutherford Appleton Laboratory in Chilton, UK. In 2002 the system was successfully upgraded to deliver pulses containing 500 J of laser energy compressed to 500 fs in duration, equivalent to petawatt (10^{15} W) power. Focused to a spot of 5 μm in diameter (FWHM), an intensity on target of $1 \cdot 10^{21}$ W/cm^2 is achieved, which is sufficient for the investigation of high relativistic laser-plasma interaction physics. In the following, the laser is described and important parameters are summarized.

The original VULCAN laser is designed to fire simultaneously eight synchronized high-energy pulses of which six are typically used as heater beams delivering long pulses between 80 ps and 2 ns in duration. The set-up of the VULCAN laser and the Petawatt upgrade are presented in figures 7.1 and 7.2. Using the CPA mode of operation, one of the remaining beams delivers ultra-short pulses with a peak power of 100 TW and sub-ps duration [167, 168]. In particular up to $\sim$ 70 J on target are available, equivalent to few 10^{19} W/cm^2 intensity in focus of an f/3 parabola with a ns-contrast of better than 10^7. The eighth beam is also available in CPA configuration but at reduced intensity. It usually serves as an optical probe pulse. Three different target areas are available which are called "West" (TAW), "East" (TAE) and "Petawatt" (TAP). The distribution of the beams among the areas is highly flexible as indicated in figure 7.1 (the vacuum compressors located in TAW and TAP are not drawn here).

The heart of the system is a series of single- and double-pass, flashlamp-pumped rod and disk amplifiers, consistent of neodymium-phosphate and neodymium-silicate glass [169]. The central wavelength of operation is 1.053 nm for TAW and TAE and 1.055 nm for TAP. Before fed into VULCAN main amplification chain, the oscillator pulses are stretched to durations of several hundreds of ps and pre-amplified using 9 mm rod amplifiers from nJ to sub-100 μJ energy level [170]. The beam is then split and expanded in diameter while the pulses are amplified by rod amplifiers with increasing aperture up to 45 mm in diameter. The beams are next split into four and the rod amplifiers are followed by double pass 108 mm disk amplifiers. After a further splitting into 8 beams, the pulses are amplified by 108 and 150 mm single-pass disk amplifiers. Vacuum spatial filters are used to expand and clean the beam between each amplification stage. Finally, the pulses are distributed into the target areas. The bandwidth that can be transported by the main amplification chain is 4 nm which

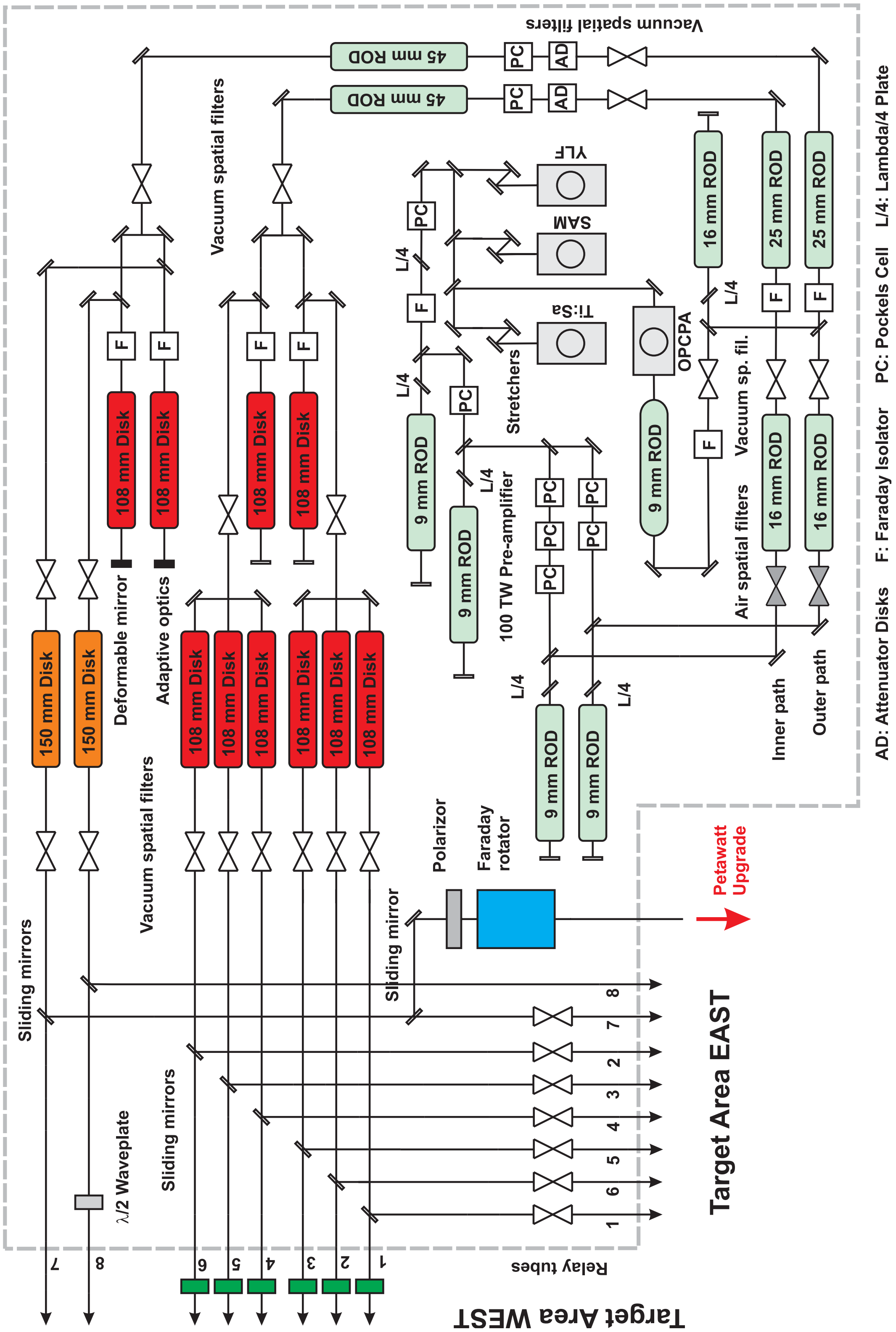

Figure 7.1: Schematic of VULCAN Laser.

is basically limited by gain narrowing during the amplification process. Note that according to the pulse-bandwidth relation, this is equivalent to 500 fs minimum pulse duration. Hence to achieve petawatt performance, both a further increase in energy and an optimization of gain narrowing were required. Therefore a separate OPCPA pre-amplifier was installed (see below).

Several front-end configurations are available to meet the requirements on bandwidth and pulse duration in the different target areas [170, 171]. For the production of 100 TW pulses in TAW, an oscillator with a saturable absorber mirror (SAM) is used which delivers pulses of 170 fs in duration and 1 nJ energy at a bandwidth of 5 nm (FWHM). TAE is usually operated with long pulses of 600 ps to 2 ns in duration. For short pulse operation of TAE, however, a Nd:YLF additive pulse mode-locked oscillator delivering 1.8 ps pulses is used and the pulses are stretched to 80 ps. The seed pulses for TAW and TAP mode of operation are produced by a Kerr-lens mode-locked Ti:Sa oscillator (120 fs, stretched to 2.4 ns for TAW and 4.8 ns for TAP, respectively). Especially for TAP mode of operation, an OPCPA pre-amplifier with high gain (10^8) and virtually no reduction in spectral bandwidth is used to amplify the pulses to mJ level. Using OPCPA, spectral narrowing in the amplifiers is optimized by a reduction of the required gain from the Nd:Glass amplifiers [172]. Using the output of the OPCPA pre-amplifier (> 13 nm) a bandwidth of larger than 5 nm

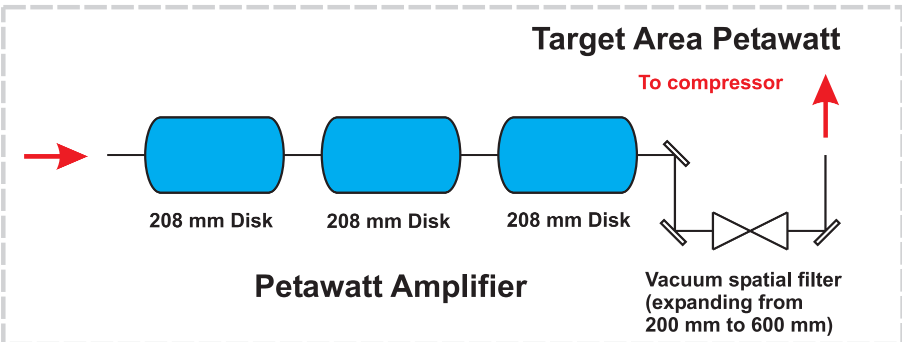

Figure 7.2: Final amplification stage of VULCAN Petawatt Upgrade.

after the Nd:Glass amplifiers was measured which is sufficient to achieve 400 fs pulses [169, 173]. In petawatt mode, one of the CPA beams is guided through another single-pass amplification chain consistent of three ex-NOVA laser 208 mm disk amplifiers. The final amplification stage is illustrated in figure 7.2. A 208 mm aperture Faraday rotator in combination with a single polarizer is used to isolate it optically from the other amplifiers. Before the pulse is compressed by two gold-coated holographic gratings of 940 mm in diameter (1480 lpmm), it is expanded to a diameter of 600 mm by passing a vacuum spatial filter operating at f/25. To sustain optimum focusing quality, an adaptive optics is included in the beam path [174]. A near diffraction limited focal spot of about 5 μm in diameter (FWHM) is achieved [175, 176].

7.2. Experimental set-up

A schematic of the experimental set-up is shown in figure 7.3. The petawatt pulse was focused with an f/3.2 parabola onto the front side of a target which is in detail described below. The pulse energy was 350 J at a central wavelength of $\lambda_0 = 1053$ nm. The spectral bandwidth of the pulse was about 2.2 nm (due to technical reasons). This gave a limit for pulse compression of about 750 fs (FWHM). The power of the laser during the campaign was hence limited to about half of a petawatt. The angle of incidence with respect to the target normal was 45° in order to avoid back-reflections of pulse into the laser. A reproducible focal spot of 6 μm in diameter was obtained that contained about 75% of the laser energy. The rear side of the target was imaged onto two cameras loaded with Ilford HP5 film using an f/2 lens system with a focal length of $f = 100$ mm. The magnification was 40×. Details of the optical diagnostic are given in chapter 4. In addition, the energies of the electrons emitted at the rear side of the target were measured with a permanent-magnet electron spectrometer along the axis of the laser beam. Details on the spectrometer can be found in [177]. The distance from the target to the 5 mm in diameter collimator was 3.7 m, resulting in a solid angle of $1.4 \cdot 10^{-6}$ sr. The electron spectra were recorded on Fujifilm image plates.

7.3. Description of multilayered laser target

For the experiment, coated foam targets (polypropylen, CH_x) with a cell size of 1 μm and densities of 100 and 200 mg/cm^3 were used. A small cell size is advantageous for a rapid homogenization of the plasma density. The thicknesses were 250, 500 and 750 μm. The front side of the target was over-coated with a 75 nm gold layer in order to generate X-rays for pre-ionization of the foam [178, 179]. The rear side of the target was over-coated with 200 nm of aluminium in order to obtain a steep density gradient important for the optical transition radiation technique [127, 180]. Also the direct propagation of the second harmonic of the laser beam was effectively blocked by the over-dense plasma and the aluminium coating at the rear side of the target. The coated foam was held by a small washer of 1 mm in diameter which could be mounted on a special target holder.

In order to pre-ionize the foam to electron densities between 15 and 30 times critical density (according to the foam density), the leading edge of the laser pulse was used. Generally, a major contribution to the pre-pulse level is due to AMPLI-

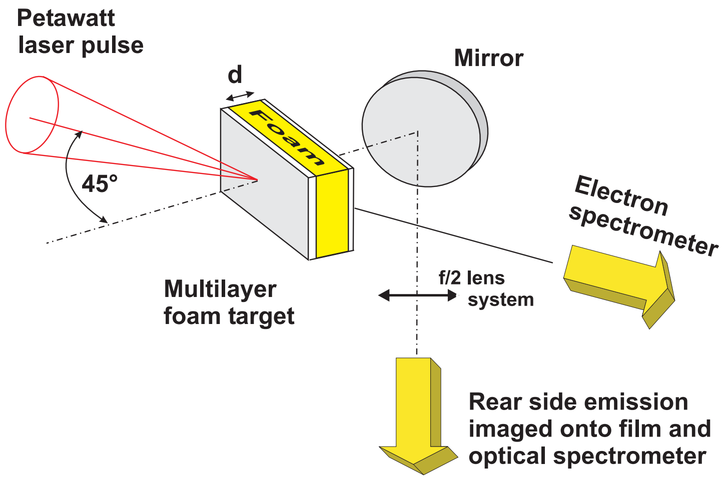

Figure 7.3: Schematic of experimental set-up and multi-layer target layout. Details on the optical diagnostic indicated are given in chapter 4.

fied spontaneous emission (ASE) and parasitic parametric fluorescence or super-fluorescence (in OPCPA mode) during the gain duration of the amplifiers, respectively. For high-power CPA lasers, pre-pulses equivalent to a contrast ratio of about 10^6 are typical on a picosecond timescale. Spectral clipping and imperfect recompression of the pulse can lead to a further decrease in pulse contrast. In the context of peak powers of 10^{20} W/cm^2, however, the target material is hence ionized before the arrival of the main pulse. The pulse contrast on target can be improved by frequency-doubling. Recently, also plasma mirrors have been used successfully [181, 182]. Here, however, pre-ionization and subsequent plasma heating before the arrival of the main pulse was of interest.

The pre-pulse level on picosecond basis of the VULCAN Petawatt beam was independently characterized using a third-order autocorrelation technique and by measuring the threshold ionization of gas clusters using optical shadowgraphy. Focal intensities of the order of $10^{12} - 10^{13}$ W/cm^2 up to 700 ps, 10^{15} W/cm^2 up to 60 ps and 10^{16}W/cm^2 at about 50 ps before the main pulse have been reported [183, 184, 185].

As a result of the pre-pulse, a pre-plasma is formed in the thin gold layer. On high-Z targets, a significant part of the incident laser energy (up to 80%) is absorbed due to inverse bremsstrahlung and causes the pre-plasma to heat up. In high-Z materials such as gold, a very large number of atomic energy levels exist, which can be excited and a large number of bound and spectral bands can be generated [155, 186]. A strong flux of X-rays is produced by the layer that can be used to pre-ionize the target. In order to estimate the temperature of the radiation field, the Stefan-Boltzmann law is used, saying that the power emitted by a black body into half space is proportional to the 4th power of its temperature,

$$P = \sigma A T^4, \tag{7.1}$$

where $\sigma = 5.67 \cdot 10^{-4}$ Wm^{-2}K^{-4}, A the area of the emitter and T its temperature in Kelvin (11.600 K $\widehat{=}$ 1 eV). For instance, a plasma temperature of approximately 100 eV is equivalent to an energy flux density of 10^{13} W/cm^2. The radiation can propagate almost unhindered through the low-Z foam target (CH). Detailed measurements of the propagation of a X-ray-induced ionization front in low density foam targets using high-Z burn-through foils are reported elsewhere [178, 187, 188, 189].

Simultaneously, as a result of the electron pressure, the pre-plasma generated at the gold surface will undergo a hydrodynamic expansion which is assumed to be spherical. To estimate the dimension of the pre-plasma generated at the moment of the pulse peak, the ion sound speed of a plasma,

$$c_s = \left(\frac{T_e + T_i}{m_i} \right)^{1/2}, \tag{7.2}$$

was used and $T_e \approx T_i \approx 100$ eV were assumed. The ion mass of gold is $m_i = 197$ u (atomic weight units, 1 $u = 1.66 \cdot 10^{-27}$ kg). An expansion velocity of roughly 10^4 m/s is expected. At this temperature, the pre-plasma will expand by the order of 10 µm within 700 ps. In addition, due to the relative small cell size of the foam target (~ 1 µm) and an atomic weight of $m_i = 12$ u for C, the foam plasma has enough time to homogenize prior the peak of the main pulse.

7.4. Data obtained

Optical images obtained from target rear side

In the moment the main pulse hits the target, plasma electrons at the location of the (relativistically corrected) critical density are accelerated to high energies. In contrast to the laser radiation, these electrons can propagate through the over-dense plasma and exit the target at the rear-side. The optical part of the transition radiation produced during the plasma-vacuum transition was imaged onto film. A typical optical image is shown in figure 7.4 a). The thickness of the foam layer was 250 μm, the density of the foam was 100 mg/cm^3. The data were processed by overlying the two images obtained on the same shot. In the raw data, an elliptical spot is observed with a horizontal elongation. This is an indication that the electron beam observed has been accelerated in the direction of the laser pulse. Note that in the set-up the optical axis of the diagnostic was perpendicular to the target rear side (see figure 7.3). This is supported by the fact that a symmetric focal spot has been reported by separate measurements [176], which was incident on a spherically expanding pre-plasma. Simultaneously, due to the high light pressure, hole-boring is expected to push the critical surface along the beam direction. At the rear plasma-vacuum boundary, however, the angle between the cone of exiting beamlets and the target surface causes an elongation in width of the images. To take this into account, the horizontal direction has been re-scaled as detailed below.

In the images, filaments with spot sizes of $\sim$ 10 μm in diameter (FWHM) are observed that are clearly organized in a ring like structure. The filaments are surrounded by a cloud of several smaller filaments, where the size of smallest observable filaments is about 2 μm. This confirms a close to diffraction limited resolving power of the optical diagnostic. Figure 7.4 b) depicts the re-processed data obtained on the camera without bandpass filter. In order to illustrate the dimensions, two concentric rings are drawn. The inner ring has a diameter of $\sim$ 40 μm and indicated the position of the larger inner filaments. The outer ring indicates the size of the entire spot. It's diameter is about 100 μm. On the left side of figure 7.5, the data obtained using a 500 μm thick foam target is shown. Also here, the filaments organize in a ring like structure.

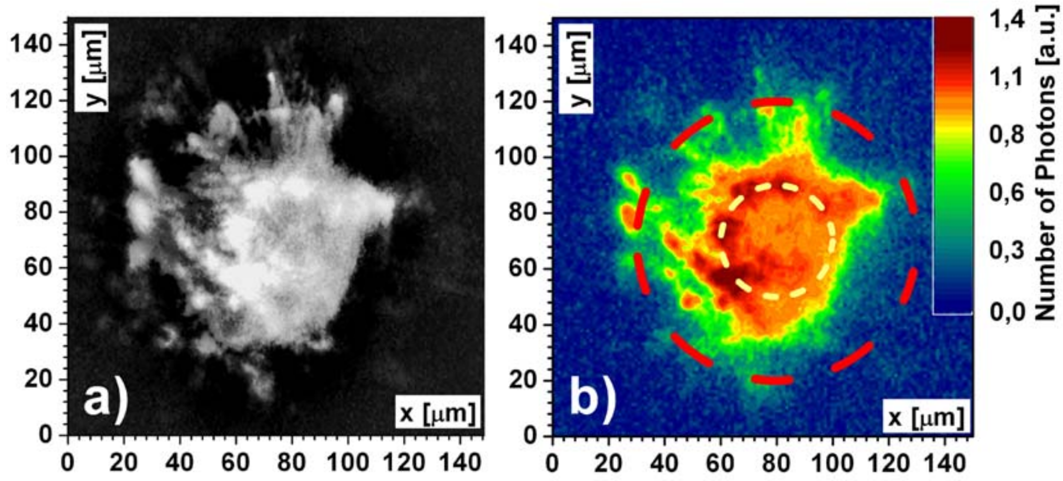

Figure 7.4: Data obtained using 250 μm foam target. a) Picture of optical emission. The image shows the reprocessed data obtained from both cameras with different grey filters by overlying in order to show the substructure of the inner circle as well as the filaments in the outer region. b) Reprocessed data of the image without bandpass filter. Two concentric rings with 100 μm (red) and 50 μm (yellow) in diameter are drawn indicating the inner ring like organization of larger filaments and the divergence of the cloud of outer filaments.

An analysis of the diameters of the inner ring and the outer structure is presented on the right side of figure 7.5. The analysis of the divergence of the filaments with increasing target thickness reveals a divergence angle of $\sim 10°$ for the inner ring and $\sim 20°$ for the cloud of outer filaments.

In order to analyze the filamentary structure more in detail, a polar representation of the circular structure seen on the 250 μm foam target was calculated. The result is presented in figure 7.6. Clearly five larger inner filaments can be observed which are organized along a circle with a radius of about 20 μm. The structure is almost periodic along the angular coordinate with a frequency of $\sim 1/50°$ as can be seen from the line-out (1). The filaments in the outer region are significantly smaller as can be observed from the line-outs (2). Note that the exposure is different. Since in the case of coherent transition radiation, the level of emitted light is proportional to the square of the number of electrons that are crossing the plasma-vacuum surface, the picture shows that most of the current is located inside a disc with a radius of $\sim 30 - 40$ μm.

Optical spectra

For each shot, the optical spectrum of the emission was recorded. The spectrum obtained on 250 μm laser irradiated foam target is shown in figure 7.7. The signal is peaked around the second harmonic of the laser frequency. This is also supported by a comparison of the images with and without the bandpass filter. In both the same structure has been observed. Following Baton *et. al.* [123] the strong emission of 527 nm light can be explained by coherent transition radiation due to hot electrons transiting the rear target-vacuum interface. Note that some contributions from synchrotron radiation cannot be excluded *a priori*. A comparison of the bandwidth of the emission ($\Delta\lambda = 4$ nm, FWHM) and the laser spectral bandwidth ($\Delta\lambda_L = 2.2$ nm, FWHM) shows that the data is not affected by second harmonic of the laser pulse. As in some shots aluminium foil targets were used (15 μm in thickness) and interference pattern have been observed in the optical images, the coherence of the emission was confirmed. These results indicate that the electrons are accelerated in bunches twice per optical cycle $\tau_0 = 2\pi/\omega_0$ of the petawatt laser pulse. This was also observed by other groups [40, 44, 123]. In those investigations, electron bunching has been attributed to either the laser ponderomotive force or resonance absorption. While the oscillating component of the ponderomotive force accelerates bunches of electrons twice every laser cycle, this happens only once per cycle in the resonance absorption case. In addition, it was observed that the signal strength located around the second harmonic was significantly decreasing with increasing target thickness. This was attributed to a dephasing of the electron bunches with increasing propagation length as a result of the energy spread of the electrons within the bunch [190]. The velocity spread leads spatially to a de-localization of the electrons with time and hence to a decrease in contrast of the modulation itself. The decrease of the coherent part of the radiation around the second harmonic is due to the fact that the emission spectrum is related to the modulation function via a Fourier transformation [127]. The optical spectrum and the decrease in signal with target thickness gives hence further evidence that the electron beam observed has predominantly been generated by $\vec{j} \times \vec{B}$ acceleration mechanism.

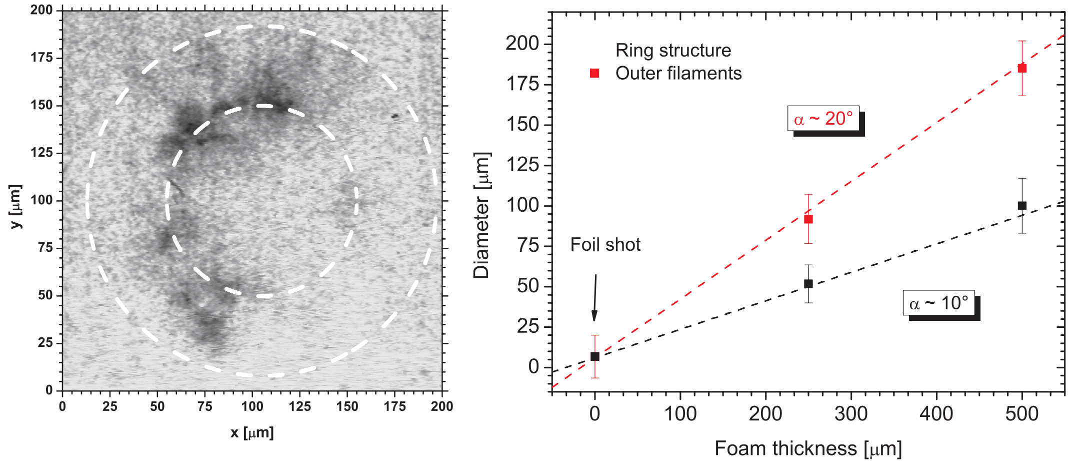

Figure 7.5: Left: Data obtained on 500 μm foam target. Also here, the filaments organize in a ring structure. Note that the intensity of the signal is low compared to that of the 250 μm target. Right: Diameter of the ring structure and the outer filaments observed for different target thicknesses.

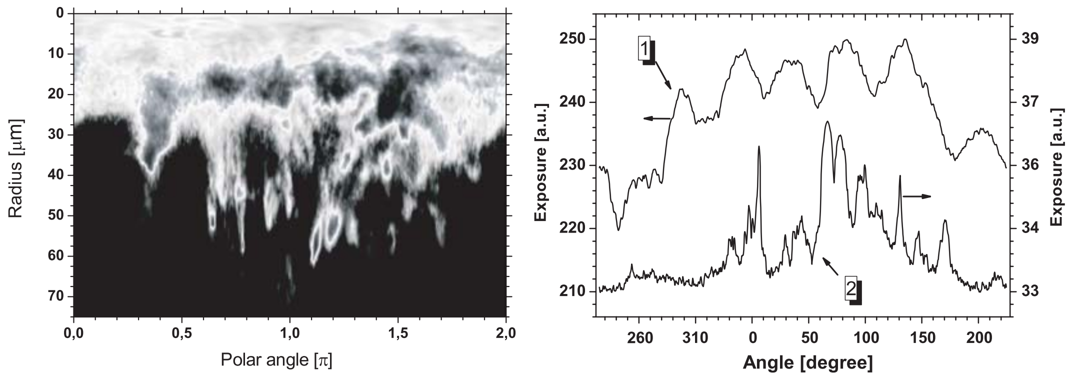

Figure 7.6: Left: Polar representation of data obtained in 250 μm foam shot. Five filaments with a spot size of about 10 μm are clearly observed at a radius of about 20 μm around the center of the spot. Smaller filaments are found up to a radius of about 60 μm. Right: film exposure analyzed along a circle of $\sim$ 20 μm (1) and $\sim$ 50 μm (2) in diameter.

Electron spectra

On the right side of figure 7.7 typical electron spectra obtained for different target conditions are shown. As can be seen, the different density targets gave similar results. A two temperature Boltzmann distribution was obtained with a "hot" temperature of around $T_h \approx 9$ MeV and a "cold" temperature of $T_c \approx 3$ MeV.

As detailed above (chapter 3), different absorption mechanisms are ascribed to produce different electron temperatures in the hot tail of the spectrum. According to the experimental geometry (p-polarization, 45° angle of incidence), resonance absorption may occur as well as $\vec{j} \times \vec{B}$ acceleration. The electron temperatures for the experimental parameters were calculated. According to the model given by Wilks *et. al.* [105] the laser ponderomotive force will lead to an electron temperature of

$$T_{\mathrm{pm}} = 0.511 \cdot \left[\left(1 + I_{18}\lambda_L^2/1.37\right)^{1/2} - 1 \right] \ \mathrm{MeV}, \tag{7.3}$$

while resonance absorption will contribute to a Boltzmann distribution with a temperature given by [103]

$$T_{\mathrm{res}} = 0.1 \cdot \left(I_{17}\lambda_L^2\right)^{1/3} \ \mathrm{MeV}, \tag{7.4}$$

with λ_L as the wavelength of the accelerating laser pulse (in μm), I_{17} and I_{18} denote the intensity in terms of 10^{17} and 10^{18} W/cm^2, respectively. Note that equation (7.4) is valid for p-polarized radiation only. It is well known that electrons accelerated by resonance absorption of the laser pulse will be directed perpendicular to the target surface (due to the direction of the density gradient), while the laser ponderomotive force basically accelerates electrons along the laser propagation axis [106, 103, 191]. The temperatures measured with those predicted according to equation (7.3) and (7.4) were compared. The intensity on the different targets was between 3.5 and $5 \cdot 10^{20}$ W/cm^2, that leads to T_h between 7.5 and 9.3 MeV and $T_c \approx 2$ MeV. The values derived from the measured spectra for the two temperatures are close to the estimated ones. The electron spectra lead hence to the conclusion that the emission observed was due ponderomotively accelerated electrons bunched at $2\omega_0$. Note that in previous experiments in which a petawatt pulse was focused on gold layered targets, a ponderomotive scaling of the electron temperatures was observed. This was ascribed to the $\vec{j} \times \vec{B}$ acceleration mechanism [192]. An additional electron temperature tail was found which was ascribed by self modulated laser wakefield acceleration or direct laser acceleration in large pre-plasma [193]. Here electrons undergo betatron-resonance in a plasma-channel and are accelerated to energies according to a scaling of

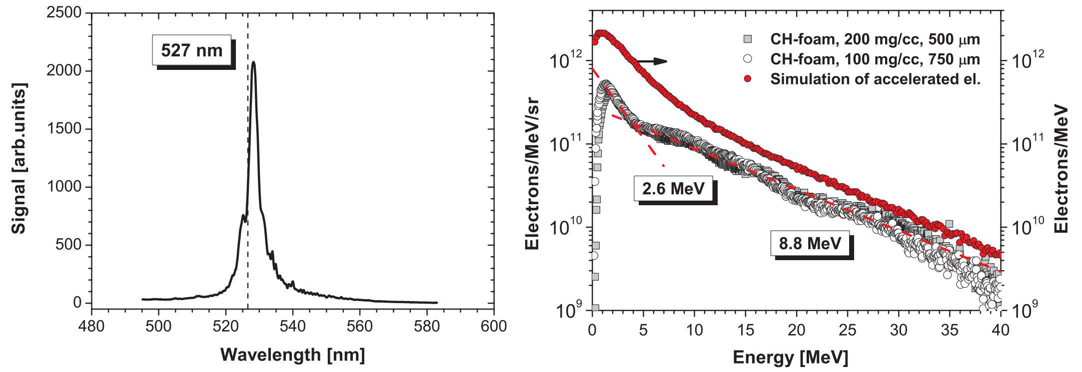

Figure 7.7: Left: Optical emission of the rear-side emission recorded using 250 μm foam target. The emission shows a strong maximum around the second harmonic of the laser frequency (reproduced with courtesy of J. Osterholz) [190]. Right: Electron spectra measured for different foam target conditions. The electron spectrum obtained from the simulation is also shown.

$T_{\mathrm{DLA}} = 1.5 \cdot (I/I_{18})^{1/2}$ MeV. This mechanism would also produce bunched electrons every optical half cycle of the pulse and thus lead to emission of coherent transition radiation with a peak at 527 nm. In the shots during this campaign, however, no electron population was observed which could be attributed to DLA scaling. The energies for all shots taken during the one-week campaign are shown in figure 7.8. Note that the energy expected for DLA-theory would be about 30 MeV.

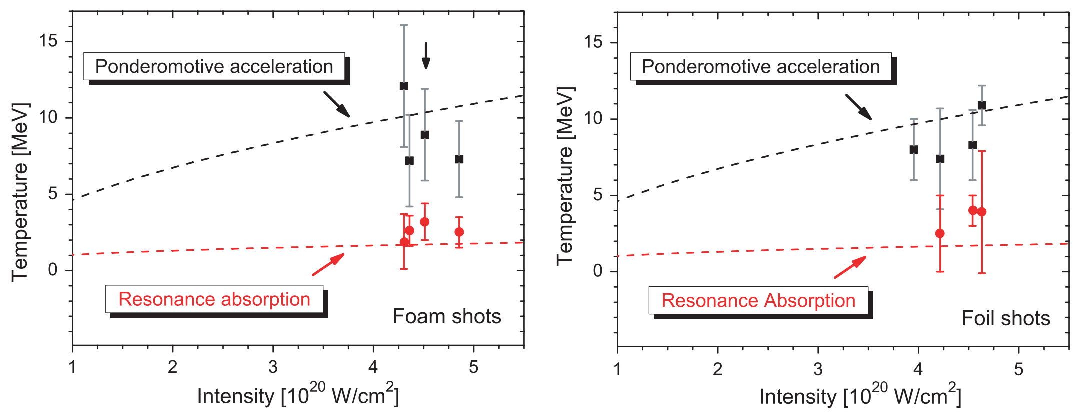

Figure 7.8: Left: Electron temperatures obtained from foam shots by fitting the "hot" and "cold" population observed in the electron spectra. The arrow indicates a shot without gold coating in front of the foam target. Right: Electron temperatures obtained on aluminium foil shots. In both the energy expected from resonance absorption and $\vec{j} \times \vec{B}$-acceleration are plotted.

7.5. Interpretation of experimental data

The occurrence of the ring like structure of the larger inner filaments is one of the key findings of this measurement. The reproducibility of the structure was confirmed as the ring was also observed on other shots with different target thicknesses (compare figure 7.5). The optical spectra of the emitted transition radiation as well as the elipticity of the spots observed in the raw data sustain that the acceleration mechanism has been ascribed to $\vec{j} \times \vec{B}$ ponderomotive heating. This is also in agreement with the electron spectra recorded, particularly with the scaling laws predicted for this acceleration mechanism. In the case that spatially the electron density of the beam generated correlates with the focal intensity of the petawatt pulse, a Gaussian density distribution will be generated (compare also chapter 3). If such a beam is started at the front side of the foam target, due to the pre-ionization, return currents can develop and hence support a high current. The system of high-energetic electron beam and low-energetic return current is sensitive to the Weibel instability. The Weibel instability is ascribed to be driven by anisotropies in the distribution function of the beam, i.e. the occurrence of (seed) magnetic fields. Thus an anisotropy is clearly given by the beam shape. Hence a break-up is expected around regions of maximum magnetic field, that is around the first derivative of the Gaussian. This leads to a ring like structure.

In the experiment, the ring structure was seen as an ellipse and the width was ascribed to the acceleration direction of the electrons parallel to the laser direction. In order to strengthen the geometrical interpretation of the observation, the angle between the beam and the target normal was derived. Therefore the model presented by Sheng *et. al.* [194] was used. The angle, Θ, under which laser-accelerated electrons will leave the rear side of a solid target that is irradiated by an intense laser pulse incident under an angle α, is determined by the relativistic gamma-factor of the electrons. Quantitatively,

$$\tan(\Theta) = \left[\frac{2}{\gamma - 1} + \frac{\gamma + 1}{\gamma - 1} \cdot \tan^{-2}(\alpha)\right]^{-1/2} . \tag{7.5}$$

Inserting the experimental conditions, i.e. $\gamma \approx 15$ and $\alpha = 45°$, it follows that the electrons leave the gold layer under an angle of $\Theta \approx 42°$. That is approximately the direction of the laser pulse.

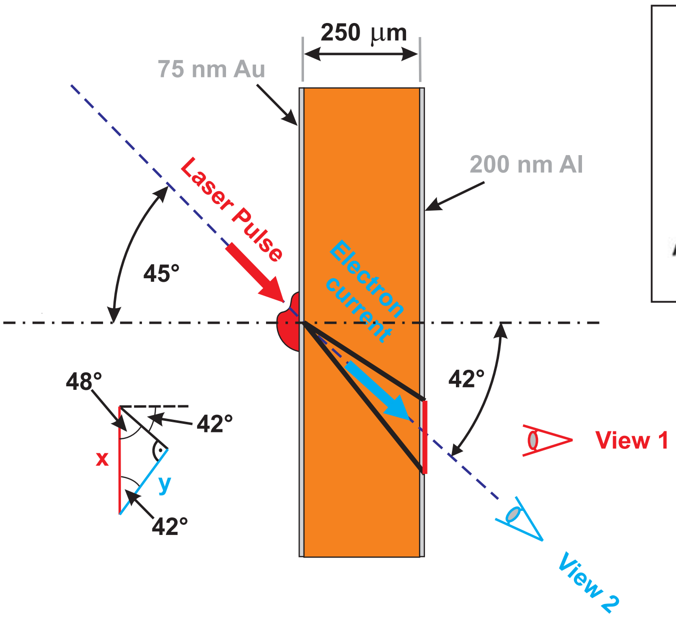

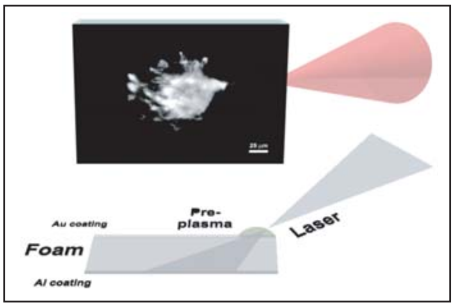

Figure 7.9: Top view of target geometry, laser pulse and electron beam. The elliptic structure seen in the images is caused by the direction of the electron current with respect to the target normal. Details are given in the text. The inset illustrates how the scenario is seen by "view 1". The original data was inserted.

The angle of divergence of the beam was experimentally found to be of about 20°. For simplicity assume that the beam has a conical shape. The aluminium coated rear side of the target, where the optical transition radiation is produced, appears under an angle of 48° with respect to the cone axis. Here the transition radiation is produced. The angle of view of imaging diagnostic with respect to the target rear side was about 90°. Hence, when the electron beam transits the metal-vacuum interface, an ellipse with an aspect ratio

$$\sin(90^\circ - \Theta) = \frac{y}{x} \approx 0.75 \tag{7.6}$$

is observed. Note that the images obtained by the optical diagnostic have been re-scaled by this factor. The geometry is illustrated in figure 7.9. The images were obtained under an angle indicated by "view 1" in the figure. After re-scaling, the electron beam is seen as indicated by "view 2". The inset shows the original data as seen by the diagnostic.

7.6. 3D-PIC simulations of current filamentation

Simulations were carried out for the experimental parameters with the 3D-PIC code Virtual Laser Plasma Laboratory (VLPL) by A. Pukhov [195]. The scenario was divided in two steps. First the laser acceleration of electrons was modeled to identify the hot electron population that is responsible for the beam observed. Therefore a laser pulse with the Gaussian profile $a = a_0 \exp(-(t/T)^2 - (r/R)^2)\cos[\omega_0(t - cz)]$, where $a_0 = 15$, $T = 314\omega_0^{-1}$ and $R = 63c/\omega_0$, was normally incident onto a plasma layer with a linear density ramp reaching the maximum $n_{\max} = 20n_c$ over the distance $L = 300c/\omega_0$, where $n_c = \omega_0^2 m/4\pi e^2$ is the critical density (for a laser wavelength of 1.055 μm, $n_c = 1.1 \cdot 10^{21}$ cm^{-3}). The linear density ramp was used to mimic the pre-plasma at the target surface. The spectrum of the total accelerated electrons is shown on the right side of figure 7.7. The calculated spectrum consists of two Boltzmann-like energy distributions with $T_{\text{eff}} \approx 8$ MeV and 3.5 MeV.

In a second step, the electron beam was injected into a plasma with $n_e = 30n_c$ and its propagation was studied. The simulations were carried out for the higher density target as the measured electron spectra were similar for the 100 and 200 mg/cm^3 targets. The transverse electron beam temperature was set to zero to keep the beam within the simulation box. Initially, the electron beam had a smooth Gaussian transverse density profile with a radius of $R_b = 10$ μm and a peak density of $n_b = 0.1n_c$. This beam transports the power $P_b = \gamma n_b mc^3 \cdot \pi R_b^2 \approx 14$ TW and the current $J = n_b ec \cdot \pi R_b^2 \approx 7J_A \approx 1.8$ MA. The electron beam current is significantly above the Alfvén limit and the beam quickly begins to filament. Figure 7.10 show transverse cuts of the electron density and the $x-$component of the quasi-static magnetic field after the beam has propagated 10, 20 and 100 μm through the foam plasma. The onset of the filamentation is observed at a radius $\sim R_b$ after the beam has propagated about 10 μm (figure 7.10 (a) and (b)). This is in agreement with the general behaviour of the Weibel instability to be most effective in the region of strongest anisotropies as a direct result of strongest magnetic fields and the subsequent magnetic repulsion of the counter-streaming beams. After a propagation distance of 20 μm, strong magnetic fields are observed at a radius of $r \approx 7$ μm and cause the inner part of the beam to filament (figure 7.10 (c) and (d)). This leads to the occurrence of

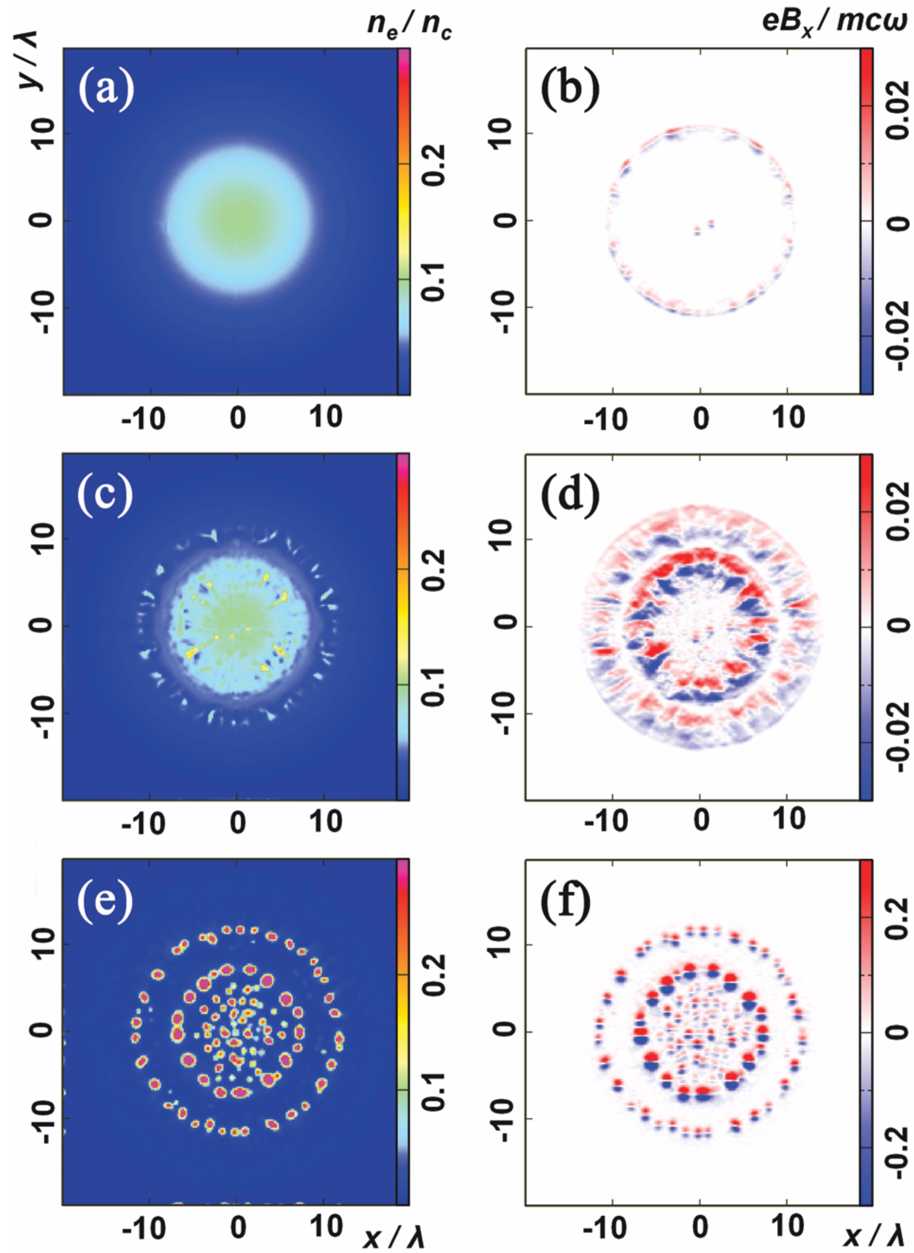

Figure 7.10: Simulation of electron density of hot electrons after 10 μm, 20 μm and 100 μm propagation ((a), (c) and (e)) and $x-$component of magnetic field surrounding the filaments ((b), (d) and (f)).

the inner current filaments observed. Then some of the filaments begin to merge while the ring like geometry survives. The ring like structure is clearly revealed in figure 7.10 (e) and (f). Here the beam has propagated over 100 μm. Note that a similar ring structure has been observed in the experiment.

The growth rate of the Weibel instability is given by equation (3.21) (refer to chapter 3). The relevant timescale on which filamentation occurs is the plasma frequency of the relativistic electron beam, ω_{be}. The growth rate of the instability, $\gamma_{\mathrm{W}} \approx \omega_{be} \cdot (n_b/(\gamma n_e))^{1/2} \cdot v/c$, scales with the root of the beam contrast n_b/n_e, where n_e is the density of the surrounding plasma [37, 196]. Using $n_b = 0.1 n_c$, $n_e = 30 n_c$ and $v \sim c$, and estimating the growth rate of the Weibel instability, one obtains $\gamma_{\mathrm{W}}^{-1} \sim 130$ fs. This corresponds to a beam propagation distance of about 40 μm which is of the same order as observed in the simulation. As expected, each small filament in figure 7.10 (e) carries a current smaller than the limiting Alfvén current J_A and is surrounded by a strong self-generated magnetic field. The B_x-field reaches 30 MG (figure 7.10 (f)). In turn, both the occurrence of dense current filaments surrounded by strong magnetic fields, allows the conclusion that it is this magnetic field that leads to beam filamentation due to the Weibel instability.

Note the density contrast scaling in the growth rate of the Weibel instability. This was the motivation for recent experiments performed by Wei *et al* [197]. They report on the observation of filamented electron beams exiting the rear of thin foils that undergo Weibel instability in low-density gas plasma. In this configuration, the growth rate of the Weibel instability is increased because the beam density is of the order of background density. The electron acceleration was identified to be the $\vec{j} \times \vec{B}$-mechanism. A similar angle of divergence as observed in this study is reported and filaments of the order 80 μm are found.

8. Summary and Outlook

In the first part of this thesis, the propagation of a laser-induced ionization front through gaseous targets and the subsequent evolution of a plasma channel were studied. Experimentally, an ultra-short, high-intensity laser pulse with a duration of sub-10-fs was focused on the edge of a gas jet under high pressure. Helium, neon, argon and nitrogen were used as target gases at densities up to few 10^{20} cm^{-3}. An intensity of few 10^{16} W/cm^2 was obtained in a focal spot with a diameter of about 5 μm. The laser wavelength was 800 nm. Due to the high electric field of the laser, the outer electrons of the target gas are rapidly removed from the ion. As the ponderomotive potential of the pulse (about 600 eV) is high compared to the ionization potentials of outer electrons of the target gas (few tens of eV), the dominant ionization process is tunneling ionization and the rates given by ADK-tunneling theory can be applied. The plasma electrons cause a change in the refractive index with respect to the neutral gas. This allowed to study the front and the channel in a pump-probe experiment via shadowgraphy and interferometry. Particularly a frequency-doubled probe pulse at variable time delays was used for probing of the channel at 90°. For the first time the front has been resolved optically with a temporal resolution of sub-10-fs. This temporal resolution has been confirmed by the motion blur seen in the images. Spatially, a high resolution of about 1 μm has been achieved.

It has been found that the front propagates with the speed of light. This has been confirmed for all four gases used. Behind the front, a plasma channel with a diameter of the order of the focal spot is produced. By increasing the delay of the probe pulse with respect to the pump pulse, the evolution of the plasma channel was studied up to about 100 picoseconds. By a careful calibration of the distance of the plane that was imaged onto the detector with respect to the plasma axis (a technique that is called "focused shadowgraphy" [135]), it was possible to obtain quantitative information from the shadowgrams. Particularly it has been observed that for some gases the electron density within the channel is increasing on a timescale of several hundreds of femtoseconds after the laser-matter-interaction. The increase was ascribed to collisional-ionization and the effect was also confirmed by interferometric measurements. A comparison of the field ionization rates and the collisional ionization rates has shown that collisional ionization is relevant on a timescale that is long compared to the pulse duration. The same holds for plasma heating due to electron-ion collisions (inverse bremsstrahlung). During the time the pulse interacts with the plasma, almost none of the pulse energy is transferred into the plasma via collisions. The kinetic energy of the electrons after the laser-gas interaction has been ascribed to the phase-mismatch between the moment of ionization with respect to the peak of the electric field (ATI energy). The initial electron temperature has been estimated to be of the order of 60 eV in the case of helium and of the order of 80 eV in the case of neon. This is in agreement with absorption measurements and PIC simulations.

The analysis of the shadowgrams has clearly shown that the channel diameter remains constant when it was probed. Only in the case of helium, the onset of a hydrodynamic expansion of the channel starts about 10 ps after the laser-matter interaction. The onset of the expansion requires that a significant amount of kinetic energy is transferred from the electrons to the ions. The efficiency of the energy transfer via binary collisions depends on the mass ratio of the collision partners. Since helium was the lightest element which was probed, the expansion has been observed here first.

Both the shadowgrams as well as the interferograms confirm that no pre-plasma was present. In order to validate that the plasma produced by a pre-pulse containing about 10 percent of the pulse energy was measureable, the Dazzler inside the laser was reprogrammed and controlled pre-pulses were produced. The pre-plasma could be well resolved in the shadowgrams on femtosecond timescale.

The optical properties of the plasma channel are such that it acts as a defocusing lens for both the pump and the probe pulse. The effect of ionization induced defocusing of the laser pulse is a well known process and usually limits the focusability of the pulse. In order to maximize the intensity in focus and to minimize ionization induced defocusing, in the experiment a tight focusing equivalent to a f-number of about f/3 and a background gas density of the order of 10^{19} cm^{-3} were chosen. Under these conditions, defocusing plays a minor role and a narrow channel has been observed. Nevertheless, it has been shown that ionization induced defocusing becomes important at high gas densities (few 10^{20} cm^{-3}) and target gases with low ionization thresholds for the outer electrons (argon and nitrogen). Here a divergent channel structure has been seen in the images. An analytic estimate of the effect is consistent with the data obtained in the interferograms and the structure of the optical self-emission of the plasma.

On the side of the channel, however, i.e. parallel to the propagation direction of the pump pulse, a Fresnel diffraction pattern was evolving. This could be explained by the occurrence of steep gradients of the electron density (laterally) that are produced as a result of strong focusing of the pump pulse. The observations are in agreement with the ADK tunneling rates and also confirm that defocusing was minimized. The Fresnel pattern has been reproduced analytically as well as by numerical simulations.

Caused by the change of the refractive index during the ionization, self-phase modulation leads to an up-shift of the frequencies contained in the pulse spectrum. From this shift, quantitative information about the average ionization state produced within the channel can be obtained. Therefore the optical spectrum of the pulse was measured after the interaction with the target. The average ionization rates observed are of the same order as predicted by ADK tunneling rates. This was shown to be in agreement with separate absorption measurements.

The propagation of the ionization front through the gas was simulated using a numerical 3D-PIC code. Particularly an intense 10 fs pulse was focused into a simulation box filled with neutral target material. Field-ionization using the ADK ionization rates was included in the code and the development of the electron density over the pulse could be resolved. Dependent on the ionization potentials of the material, subsequent liberation of outer electrons was observed at the leading edge of the pulse. Here the simulation has clearly shown that a proper integration of the rate equations over the cycles is of importance to obtain the average ionization state produced by the pulse due to its short duration. Also in the simulation, the ionization front propagates with the speed of light through the gas. Furthermore, the spectral blue-shift of the pump pulse is in good agreement with the experimental data.

As soon as an electron is liberated, its dynamics is governed by the laser electric field as a result of the high laser ponderomotive potential which the electron is exposed to. The simulation as well as the calculation of single-electron trajectories have confirmed that due to the short pulse duration, almost no acceleration of the electrons is caused by the ponderomotive force of the laser. Hence almost none of the ponderomotive potential can be transferred into kinetic energy of the electrons. Immediately after the pulse, however, the velocity distribution of the electrons is significantly non-Maxwellian. Particularly the energy gain due to the laser field that is present at the moment an electron is ionized (ATI-energy) was resolved.

As binary collisions could be included into the calculation, the development of an electron temperature after the laser interaction has been shown. The time required by the electrons to thermalize has been found to be of the order of several hundreds of femtoseconds. Here the temperature is of the order of 60 eV in the case of helium and neon. This is in agreement with absorption measurements.

In order to compare the result with the shadowgrams, the optical probe pulse was simulated as well. Its modulation in intensity caused by the optical properties of the electron density distribution inside the channel was studied. The numerical data are in excellent agreement with the shape of the front as seen in the shadowgrams. Also the Fresnel pattern was well reproduced.

The simulation confirms that during the time the pump pulse interacts with the material, binary collisions play a minor role at the densities used. Hence plasma heating due to collisions via inverse bremsstrahlung could be neglected. Also non-collisional processes such as ponderomotive heating of the electrons by the pulse are of no effect. The wakefield produced by the laser was too small to be resolved optically or to have a measurable influence on the electron velocity distribution after the pulse interaction. All these results show that the ionization front, observed with high resolution, has been well separated from laser heating. Note that the ATI energy is a direct result of the ionization process itself and comes into play at the trailing edge of the pulse. The subsequent thermalization between the electrons as well as between electrons and ions occurs on timescales that are significantly longer than the pulse duration.

According to the theory of tunneling ionization, the rate equations are functions of the instantaneous electric field strength an atom is exposed to. Hence electrons are liberated on the time scale of the duration of a half-cycle of the laser field. To resolve this sub-cycle ionization dynamics observed in the simulation also experimentally, sub-fs probe pulses would be required. Using sub-10-fs probe pulses at a wavelength of 400 nm, however, it was possible to obtain quantitative information about the ionization process using optical shadowgraphy and interferometry with high resolution. The uncertainty of the average ionization state produced in the channel arises from the fact that the interaction volume was rather small due to the tight focusing. Nevertheless, with the help of an analysis of the beam caustic, the interaction volume has been obtained. Note that in experiments using longer probe pulses (130 fs), a loss in fringe visibility was reported. This was ascribed to a pulse transit effect [16]. This has not been observed here using a sub-10-fs probe pulse. In order to further reduce the uncertainties in the measurement, in future works the interaction volume should be increased. Using an ultra-short laser pulse containing milli-Joule instead of micro-Joule of optical energy, the interaction volume could in principle be increased in such a way that the Rayleigh length is large compared to the gas jet without reducing the intensity. This would allow to increase the resolution of the optical interferometer and would also allow high-precision absorption measurements. Here potentially recent developments in laser technology, in particular the Optical parametric chirped pulse amplification technique (OPCPA), are very promising.

In the experiment, an increase of the electron density inside the plasma channel has been observed. This has been ascribed to collisional ionization. Collisions, however, require a kinetic treatment since the initial velocity distribution of the electrons was shown to be non-Maxwellian. Hence in order to quantify the increase also in the PIC simulation, collisional ionization is next to be included in the PIC code. This, however, was beyond the scope of this experimental work. Nevertheless, a simple estimate of the rate equations has allowed to confirm the observations.

In the second part of this thesis, the propagation and filamentation of a laser-produced electron beam propagation in dense plasmas were studied. The understanding of the transport of high energy electrons through ionized matter is of fundamental importance, for example for the Fast Ignitor (FI) concept relevant to laser fusion as well as astrophysics. In the FI concept, ignition of a pre-compressed pellet containing the fusion fuel is initiated by laser produced electrons with energies in the MeV range [31]. It is crucial for this scheme that a part of the energy of an ignitor laser is converted into an intense electron beam that can propagate through the high-density over-critical plasma to initiate the thermonuclear burn in the pre-compressed core [26, 198].

In the experiment, a petawatt-class laser was focused onto a thin gold layer in order to generate a strong current of relativistic electrons. In the focus, an intensity of $5 \cdot 10^{20}$ W/cm^2 was achieved. While the laser pulse is stopped at the critical density, the electron beam generated can propagate through the dense plasma. In order to study the propagation over several hundreds of microns, foam (CH) targets with various thicknesses of up to 1 mm were used. The foam was pre-ionized using the X-ray flux of the gold converter foil in front of the target. So electron densities of the order of 15 to 30 times critical were produced in the foam using the laser pre-pulse prior the electrons were accelerated at the front side. For a detection of the beam structure, the rear side of the foam target was over-coated with a thin layer of aluminium. The electrons, when they transit the boundary from the target into vacuum, emit characteristic transition radiation. The optical part of this radiation was imaged with high resolution on film plates. So it has been observed that the electron beam breaks up into filaments. A ring like inner group of larger filaments with a diameter of about 10 μm was observed. As a high-resolution optics was used, the smallest filaments that could be resolved have been of a diameter of about 2 μm.

The temperature distribution of the electrons exiting the target and optical spectra of the transition radiation have led to the finding that the electrons which form the filaments observed have been accelerated by the $\vec{j} \times \vec{B}$-mechanism. This is particularly supported by the observation of a strong peak in the optical spectrum around the second harmonic of the laser frequency, giving evidence that the electrons were accelerated in bunches twice per laser cycle. Moreover, the data show that the electron beam was propagating parallel the laser axis. Also this is an indication that the electrons were accelerated by the ponderomotive push of the laser. Resonance absorption, in contrast would preferably lead to an acceleration of electrons parallel to the target normal, i.e. under an angle of about 45° with respect to the laser k-vector.

In addition to the optical spectra of the light emitted, the energy distribution of the electron beam was measured on each shot. A two-temperature distribution was found. The distribution of the high energy tail observed in the spectrum had a temperature between 7.5 and 9.3 MeV. The colder had a temperature of about 2 MeV. The temperatures are both in agreement with those predicted by scaling laws for resonance absorption and the $\vec{j} \times \vec{B}$ acceleration mechanism if the laser intensity obtained in focus is inserted [103, 105].

The filamentation of the current has been ascribed to the Weibel instability. In order to analyze the generation of the electron beam and the subsequent dynamic of the filamentation process, 3D-PIC simulations were performed by A. Pukhov and S. Kiselev. The electron temperature and the structure seen in the data have been well reproduced. The growth rate of the instability observed in the simulation has been found to be in agreement with analytical estimates. Particularly the ring of filaments has been well reproduced.

For the Fast Ignitor, it is essential that the relativistic electrons can reach the dense fuel core in order to ignite it. As already noted by Alfvén in 1939, although in principle arbitrary high currents can be transported if the beam is neutralized by co-moving ions or a counter-streaming background current, small perturbations in the magnetic field will rapidly grow and hence will cause a limitation of the beam current (compare figure 3.3). This effect is also referred to as current filamentation instability and associated with the work of Weibel. As known from recent experiments and simulations, the Weibel instability is a strong non-resonant process which will lead to rapid filamentation of the laser produced electron beam [36, 38, 39, 47, 115, 199].

In praxis, it is however difficult to perfectly compensate Mega-Ampere currents by a return current in such a way that the instability is suppressed to grow. This is especially the fact in a laser-plasma accelerator using solid targets as particularly the beam will spatially depend on the intensity profile of the focus. This can be compared to the non-relativistic ponderomotive force. Here it was the anisotropy of the intensity distribution which led to the acceleration of electrons out of focus. In a similar way, filamentation will occur as a direct result of the spatial inhomogeneity of the beam. This has been seen in the data obtained in this thesis. Note that the experimental configuration used here is close to the actual discussed fast ignitor laser scenario - besides the energy and pulse length. The intensity distribution in focus was nearly a diffraction limited Gaussian and may be converted to more a top hat shape with the help of random phase plates. As a direct consequence of the intensity distribution in focus, especially the boundary, however, an anisotropy in the distribution function as discussed above is already generated - and hence the seed of the fast growing unstable mode. Note that this was confirmed by PIC simulations performed by Taguchi *et. al.* showing the filamentation of a cylindrical high relativistic electron beam [36].

Consequently, filamentation of a super-strong current to individual Alfvén limited beamlets will most likely in principle be unavoidable in this configuration. This is supported by the fact that simulations clearly show a rapid growth of the (Weibel) instability [36, 38, 47, 117, 200, 199]. Note that recent *collisional* 3D-PIC simulations of filamented transport observed a hollow-like structure of the filaments as a result of a balancing between plasma pressure and magnetic pressure. The current in such a filament exceeded the Alfvén limit. The filamentation process and dynamics, however, was not affected and also merging was observed [199]. This, however, must not be detrimental to the concept of fast ignition, since in principle an arbitrary high current can be produced and transported although the current is filamented. More relevant in this context is, besides a general discussion about stopping power and energy deposition of the beam into the dense fuel plasma, the divergence of the beam. In this experiment, the inner ring of filaments expanded under an angle of about 10°, the entire spot under an angle of about 20°. This behaviour was independently reported by other groups as well [197]. This angular spread is most likely a result of the interaction geometry between laser and plasma in focus since it was not seen in the simulation. The angular spread, however, and the distance from the relativistically corrected critical density to the hot spot (of about 10 μm in diameter), eventually crucially limits the energy deposition. Hence a systematic investigation of the divergence could be extremely valuable on the way to produce a stable, filamented current beam with low divergence.

Bibliography

[1] R. W. Hellwarth, *Advances in Quantum Electronics* (Columbia University Press, New York, 1961).

[2] H. W. Mocker and R. J. Collins, *Mode Competition and Self-Locking Effects in Q-switched Ruby Laser*, Applied Physics Letters **7**, 270 (1965).

[3] G. A. Mourou, T. Tajima and S. V. Bulanov, *Optics in the relativistic regime*, Review of Modern Physics **78**, 309 (2006).

[4] F. Gires and G. Mayer, *Action dune onde lumineuse intense sur lindice de refraction des liquides*, Compt. Rend. **258**, 2039 (1964).

[5] D. Strickland and G. Mourou, *Compression of amplified chirped optical pulses*, Op. Commun. **56**, 219 (1985).

[6] P. Maine, D. Strickland, D. Bado, M. Pessot and G. Mourou, *Generation of ultrahigh peak power pulses by chirped-pulse amplification*, IEEE Journal of Quantum Electronics **24**, 389 (1988).

[7] D. E. Spence, P. N. Kean and W. Sibbett, *60-fs pulse generation from a self-mode-locked Ti:sapphire laser*, Optics Letters **60**, 42 (1990).

[8] S. Sartania, Z. Cheng, M. Lenzner, G. Tempea, Ch. Spielmann, F. Krausz and K. Ferencz, *Generation of 0.1-TW 5-fs optical pulses at a 1-kHz repetition rate*, Optics Letters **22**, 1562 (1997).

[9] J. J. Macklin, J. D. Kmetec and C. L. Gordon III, *High-Order Harmonic Generation Using Intense Femtosecond Pulses*, Phys. Rev. Lett. **70**, 766 (1993).

[10] A. L'Huillier and Ph. Balcou, *High-Order Harmonic Generation in Rare Gases with a 1-ps 1053-nm Laser*, Phys. Rev. Lett. **70**, 774 (1993).

[11] P. M. Paul, E. S. Toma, P. Breger, G. Mullot, F. Auge, Ph. Balcou, H. G. Muller and P. Agostini, *Observation of a Train of Attosecond Pulses from High Harmonic Generation*, Science **292**, 1689 (2001).

[12] M. Hentschel, R. Kienberger, Ch. Spielmann, G. A. Reider, N. Milosevic, T. Brabec, P. Corkum, U. Heinzmann, M. Drescher and F. Krausz, *Attosecond metrology*, Nature **414**, 509 (2001).

[13] R. Kienberger, E. Goulielmakis, M. Uiberacker, A. Baltuska, V. Yakoviev, F. Bammer, A. Scrinzi, Th. Westerwalbesloh, U. Kleineberg, U. Heinzmann, M. Drescher and F. Krausz, *Atomic transient recorder*, Nature **427**, 817 (2004).

[14] S. Baker, J. S. Robinson, C. A. Haworth, H. Teng, Smith R. A., C. C. Chirila, M. Lein, J. W. G. Tisch and J. P. Marangos, *Probing Proton Dynamics in Molecules on an Attosecond Time Scale*, Science **312**, 424 (2006).

[15] A. Zewail, *Femtochemistry: atomic-scale dynamics of the chemical bond*, J. Phys. Chem. A **104**, 5660 (2000).

[16] L. A. Gizzi, M. Galimberti, A. Giulietti, P. Koester, L. Labate, P. Tomassini, Ph. Martin, T. Ceccotti, P. De Oliveira and P. Monot, *Femtosecond interferometry of propagation of a laminar ionization front in a gas*, Phys. Rev. E **74**, 036403 (2006).

[17] H. Ruhl, in *Introduction to Computational Methods in Many Particle Body Physics*, edited by M. Bonitz and D. Semkat (Rinton Press, Paramus, New Jersey, 2006).

[18] M. Seif, *Fusion Power: Progress and Problems*, Science **173**, 802 (1971).

[19] C. L. Olson, in *Z-Pinch Inertial Fusion Energy*, *Landhold-Boerstein Handbook on Energy Technologies*, edited by W. Martienssen (Springer, Berlin, 2004).

[20] R. C. Arnold and J. Meyer-ter-Vehn, *Inertial confinement fusion driven by heavy-ion beams*, Reports on Progress in Physics **50**, 559 (1987).

[21] M. G. Haines, *Review of Inertial Confinement Fusion*, Astrophysics and Space Science **256**, 125 (1998).

[22] J. H. Nuckolls, L. Wood, A. Thiessen and G. B. Zimmermann, *Laser compression of matter to super-high densities: thermonuclear (CTR) applications*, Nature **239**, 129 (1972).

[23] J. Lindl, *Development of the indirect-drive approach to inertial confimement fusion and the target physics basis for ignition and gain*, Physics of Plasmas **2**, 3933 (1995).

[24] J. D. Lindl, R. L. McCrory and E. M. Campbell, *Progress towards ignition and burn propagation in inertial confinement fusion*, Physics Today **45**, 32 (1992).

[25] S. Atzeni and M. L. Ciampi, *Burn performance of fast ignited, tritium-poor ICF fuels*, Nucl. Fusion **37**, 1665 (1997).

[26] C. Deutsch, *Fast ignition schemes for inertial confinement fusion*, Eur. Phys. J. Appl. Phys. **24**, 95 (2003).

[27] M. Tabak, D. S. Clark, S. P. Hatchett, M. H. Key, B. F. Lasinski, R. A. Snavely, S. C. Wilks, R. P. J. Town, R. Stephens, E. M. Campbell, R. Kodama, K. Mima, K. A. Tanaka, S. Atzeni and R. R. Freeman, *Review of progress in Fast Ignition*, Physics of Plasmas **12**, 57305 (2005).

[28] A. Pukhov and J. Meyer-ter-Vehn, *Laser Hole Boring into Overdense Plasma and Relativistic Electron Currents for Fast Ignition of ICF Targets*, Phys. Rev. Lett. **79**, 2686 (1997).

[29] K. Takahashi, R. Kodama, K. A. Tanaka, H. Hashimoto, Y. Kato, K. Mima, F. A. Weber, T. W. Barbee and L. B. Da Silva, *Laser-Hole Boring into Overdense Plasmas measured with Soft X-Ray Laser Probing*, Phys. Rev. Lett. **84**, 2405 (2000).

[30] W. Yu, M. Y. Yu, J. Zhang and Z. Xu, *Model for the boring of ultraintense lasers into overdense plasmas*, Phys. Rev. E **58**, 6553 (1998).

[31] M. Tabak, J. Hammer, M. E. Glinski, W. L. Kruer, S. C. Wilks, J. Woodworth, E. M. Campbell, M. D. Perry and R. J. Mason, *Ignition and high gain with ultrapowerful lasers*, Physics of Plasmas **1**, 1626 (1994).

[32] O. Willi, *Inertial-confinement fusion by fast ignition*, Phil. Trans. R. Soc. Lond. A **357**, 555 (1999).

[33] R. Kodama, P. A. Norreys, K. Mima, A. E. Dangor, R. G. Evans, H. Fujita, Y. Kitagawa, K Krushelnik, T. Miyakoshi, N. Miyanaga, T. Norimatsu, S. J. Rose, T. Shozaki, K. Shigemori, A. Sunahara, M. Tampo, K. A. Tanaka, Y. Toyama, T. Yamanaka and M. Zepf, *Fast heating of ultrahigh-density plasma as a step towards laser fusion ignition*, Nature **412**, 798 (2001).

[34] H. Alfvén, *On the Motion of Cosmic Rays in Interstellar Space*, Phys. Rev. Lett. **55**, 425 (1938).

[35] E. S. Weibel, *Spontaneous Growing Transverse Waves in a Plasma Due to an Anisotropic Velocity Distribution*, Phys. Rev. Lett. **2**, 83 (1959).

[36] Toshihiro Taguchi, Thomas M. Antonsen, Chuan S. Liu and Kunioki Mima, *Structure Formation and Tearing of an MeV Cylindrical Electron Beam in a Laser-Produced Plasma*, Phys. Rev. Lett. **86**, 5055 (2001).

[37] M. Honda, J. Meyer-ter-Vehn and A. Pukhov, *Collective Stopping and Ion Heating in Relativistic-Electron-Beam Transport for Fast Ignition*, Phys. Rev. Lett. **85**, 2128 (2000).

[38] Y. Sentoku, K. Mima, Sheng. Z. M., P. Kaw, K. Nishihara and K. Nishikawa, *Three-dimensional particle-in-cell simulations of energetic electron generation and transport with relativistic laser pulses in overdense plasma*, Phys. Rev. E **65**, 46408 (2002).

[39] M. Tatarakis, F. N. Beg, E. L. Clark, A. E. Dangor, R.D. Edwards, R. G. Evans, T. J. Goldsack, K. W. D. Ledingham, P. A. Norreys, M. A. Sinclair, M-S Wei, M. Zepf and K Krushelnik, *Propagation Instabilities of High-Intensity Laser-Produced Electron Beams*, Phys. Rev. Lett. **90**, 175001 (2003).

[40] J. Zheng, K. A. Tanaka, T. Sato, T. Yabuuchi, T. Kurahashi, Y. Kitagawa, R. Kodama, T. Norimatsu and T. Yamanaka, *Study of Hot Electrons by Measurement of Optical Emission from the Rear Surface of a Metallic Foil Irradiated with Ultraintense Laser Pulse*, Phys. Rev. Lett. **92**, 165001 (2004).

[41] T. A. Hall, S. Ellwi, D. Batani, A. Bernardinello, V. Masella, M. Koenig, A. Benuzzi, J. Krishnam, F. Pisani, A. Djaoui, P. A. Norreys, D. Neely, S. J. Rose, M. H. Key and P. Fews, *Fast Electron Deposition in Laser Shock Compressed Plastic Targets*, Phys. Rev. Lett. **81**, 1003 (1998).

[42] H. Teng, J. Zhang, Z. L. Chen, Y. T. Li, X. Y. Peng and J. X. Ma, *Propagation of hot electrons through high-density plasmas*, Phys. Rev. E **67**, 026408 (2003).

[43] J. Fuchs, T. E. Cowan, P. Audebert, H. Ruhl, L. Gremillet, A. Kemp, M. Allen, A. Blazevic, J.-C. Gauthier, M. Geissel, M. Hegelich, S. Karsch, P. Parks, M. Roth, Y. Sentoku, R. Stephens and E. M. Campbell, *Spatial Uniformity of Laser-Accelerated Ultrahigh-Current MeV Electron Propagation in Metals and Insulators*, Phys. Rev. Lett. **91**, 255002 (2003).

[44] J. J. Santos, F. Amiranoff, S. D. Baton, L. Gremillet, M. Koenig, E. Martinolli, M. Rabec Le Gloahec, C. Rousseaux, D. Batani, A. Bernardinello, G. Greison and T. Hall, *Fast Electron Transport in Ultraintense Laser Pulse Interaction with Solid Targets by Rear-Side Self-Radiation Diagnostics*, Phys. Rev. Lett. **89**, 025001 (2002).

[45] M. Borghesi, A. J. Mackinnon, A. R. Bell, G. Malka, C. Vickers, O. Willi, J. R. Davies, A. Pukhov and J. Meyer-ter-Vehn, *Observations of Collimated Ionization Channels in Aluminum-Coated Glass Targets Irradiated by Ultraintense Laser Pulses*, Phys. Rev. Lett. **83**, 4309 (1999).

[46] D. Giulietti, M. Galimberti, A. Giulietti, L. A. Gizzi, R. Numico, P. Tomassini, M. Borghesi, V. Malka, S. Fritzler, M. Pittman, K. Ta Phouc and A. Pukhov, *Production of ultracollimated bunches of multi-MeV electrons by 35 fs laser pulses propagating in exploding-foil plasmas*, Physics of Plasmas **9**, 3655 (2002).

[47] M.-C. Firpo, A. F. Lifshits, E. Lefebvre and C. Deutsch, *Early Out-Of-Equilibrium Beam-Plasma Evolution*, Phys. Rev. Lett. **96**, 115004 (2006).

[48] B. W. Boreham and H. Hora, *Debye-Length Discrimination of Nonlinear Laser Forces Acting on Electrons in Tenuous Plasmas*, Phys. Rev. Lett. **42**, 776 (1979).

[49] K Burnett, V. C. Reed and P.L. Knight, *Atoms in ultra-intense laser fields*, J. Phys. B - At. Mol. Opt. Phys. **26**, 561 (1993).

[50] R. R. Freeman and P. H. Bucksbaum, *Investigations of above-threshold ionization using subpicosecond laser pulses*, J. Phys. B - At. Mol. Opt. Phys. **24**, 325 (1991).

[51] G. Mainfray and C. Manus, *Multiphoton ionization of atoms*, Rep. Mod. Phys. **54**, 1333 (1991).

[52] M. Protopapas, C. H. Keitel and P. L. Knight, *Atomic physics with super-high intensity lasers*, Reports on Progress in Physics **60**, 389 (1997).

[53] Y. Gontier, M. Poirier and M. Trahin, *Multiphoton absorption above the ionization threshold*, J. Phys. B-At. Mol. Opt. **13**, 1381 (1980).

[54] A. L. Schawlow and C. H. Townes, *Infrared and Optical Masers*, Phys. Rev. **112**, 1940 (1958).

[55] T. H. Maiman, *Optical and Microwave-Optical Experiments in Ruby*, Phys. Rev. Lett. **4**, 564 (1960).

[56] T. H. Maiman, *Stimulated Optical Radiation in Ruby*, Nature **187**, 493 (1960).

[57] P. A. Franken, A. E. Hill, C. W. Peters and G. Weinreich, *Generation of Optical Harmonics*, Phys. Rev. Lett. **7**, 118 (1961).

[58] J. L. Hall, E. J. Robinson and L. M. Branscomb, *Laser Double-Quantum Photodetachment of I-*, Phys. Rev. Lett. **14**, 1013 (1965).

[59] N.B. Delone G.S. Voronov, *Ionization of Xe atom by electric field of ruby laser emission*, Sov. Phys. JETP Lett. **1**, 66 (1965).

[60] P. Agostini, G. Barjot, J. F. Bonnal, G. Mainfray, C. Manus and J. Morellec, *Multiphoton ionization of hydrogen and rare gases*, IEEE Journal of Quantum Electronics **4**, 667 (1968).

[61] M. Göppert-Mayer, *Elementary processes with two-quantum transitions*, Annalen der Physik **9**, 273 (1931).

[62] A. Einstein, *Über einen die Erzeugung und Verwandlung des Lichts betreffenden heuristischen Gesichtspunkt*, Annalen der Physik **17**, 132 (1905).

[63] P. Agostini, F. Fabre, G. Mainfray, G. Petite and N. K. Rahman, *Free-Free Transitions Following Six-Photon Ionization of Xenon Atoms*, Phys. Rev. Lett. **42**, 1227 (1979).

[64] L. V. Leldysh, *Ionization in the field of a strong electromagnetic wave*, Sov. Phys. JETP Lett. **20**, 1307 (1965).

[65] F. H. M. Faisal, *Multiple absorption of laser photons by atoms*, J. Phys. B - At. Mol. Opt. Phys. **6**, L89 (1973).

[66] B. Chen, F. H. M. Faisal, S. Jetzke, H. O. Lutz and P. Scanzano, *Above-Threshold Electron Ejection Spectra*, Phys. Rev. A **36**, 4091 (1987).

[67] H. R. Reiss, *Effect of an intense electromagnetic field on a weakly bound system*, Phys. Rev. A **22**, 1786 (1980).

[68] H. R. Reiss, *Electron spectrum in intense-field photoionization*, Journal of the optical Society of America B **4**, 726 (1987).

[69] B. W. Shore and P. L. Knight, *Enhancement of high optical harmonics by excess-photon ionization*, J. Phys. B - At. Mol. Opt. Phys. **20**, 413 (1987).

[70] A. McPherson, G. Gibson, H. Jara, U. Johann, T. S. Luk, I. A. McIntyre, K. Boyer and C. K. Rhodes, *Studies of multiphoton production of vacuum ultraviolett-radiation in rare gases*, Journal of the Optical Society of America B **4**, 595 (1987).

[71] M. Ferray, A. L'Huillier, X. F. Li, L. A. Lompré, G. Mainfray and C. Manus, *Multiple-harmonic conversion of 1064-nm radiation in rare gases*, J. Phys. B - At. Mol. Opt. Phys. **21**, L31 (1988).

[72] X. F. Li, A. L'Huillier, M. Ferray, L. A. Lompré and G. Mainfray, *Multiple-harmonic generation in rare gases at high laser intensity*, Phys. Rev. A **39**, 5751 (1989).

[73] J. Seres, P. Wobrauschek, Ch. Streli, E. Seres, F. Krausz and Ch. Spielmann, *Generation of coherent keV X-rays with intense femtosecond laser pulses*, New Journal of Physics **8**, 251 (2006).

[74] H. A. Bethe and E. E. Salpeter, *Quantum Mechanics of One- and Two Electron Atoms* (Plenum, New York, 1977).

[75] T. Auguste, P. Monot, L. A. Lompré, G. Mainfray and C. Manus, *Multiply charged ions produced in noble gases by a 1 ps laser pulse at* $\lambda = 1053$ *nm*, J. Phys. B - At. Mol. Opt. Phys. **25**, 4181 (1992).

[76] A. M. Perelomov, V. S. Popov and M. V. Terentev, *Ionization of atoms in an alternating electric field, I*, Sov. Phys. JETP Lett. **23**, 924 (1966).

[77] A. M. Perelomov, V. S. Popov and M. V. Terentev, *Ionization of atoms in an alternating electric field, II*, Sov. Phys. JETP Lett. **24**, 207 (1967).

[78] L. D. Landau and A. F. Lifshits, *Classical Theory of Fields*, 2nd edition ed. (Addison-Wesley, Reading. Mass., 1962).

[79] G. L. Yudin and M. Y. Ivanov, *Nonadiabatic tunnel ionization: Looking inside a laser cycle*, Phys. Rev. A **64**, 013409 (2001).

[80] M. V. Ammosov, N. B. Delone and V. P. Krainov, *Tunnel ionization of complex atoms and of atomic ions in an alternating electromagnetic field*, Sov. Phys. JETP Lett. **64**, 1191 (1896).

[81] S. Augst, D. Strickland, D. D. Meyerhofer, S. L. Chin and J. H. Eberly, *Tunneling ionization of noble gases in a high-intensity laser field*, Phys. Rev. Lett. **63**, 2212 (1989).

[82] G. Petite, P. Agostini, R. Trainham, E. Mevel and P. Martin, *Origin of the high-energy electron emission from metals under laser irradiation*, Phys. Rev. B **45**, 12210 (1992).

[83] Paul Gibbon, *Short Pulse Laser Interactions with Matter* (Imperial College Press, London, 2005).

[84] W. L. Kruer, *The Physics of Laser Plasma Interactions*, Vol. 73 of *Frontiers in Physics* (Addison-Wesley, New York, 1988).

[85] C. E. Max and J. Arons, *Self-Modulation and Self-Focusing of Electromagnetic Waves in Plasmas*, Phys. Rev. Lett. **33**, 209 (1974).

[86] R. L. Carman, D. W. Forslund and J. M. Kindel, *Visible Harmonic Emission as a Way of Measuring Profile Steepening*, Phys. Rev. Lett. **46**, 29 (1980).

[87] N. A. Ebrahim, C. Joshi and H. A. Baldis, *Electron acceleration below quarter-critical density in CO_2 laser-produced plasmas*, Physics Letters **84**, 253 (1981).

[88] J. J. Sanderso, *Corrections to Thompson Scattering for Intense Laser Beams*, Physics Letters **18**, 114 (1965).

[89] J. H. Eberly and A. Sleeper, *Trajectory and Mass Shift of a Classical Electron in a Radiation Pulse*, Phys. Rev. **176**, 1570 (1968).

[90] T. W. B. Kibble, *Frequency Shift in High-Intensity Compton Scattering*, Phys. Rev. **138**, B 740 (1965).

[91] O. Buneman, *Inversion of the Helmholtz (or Laplace-Poisson) operator for slab geometry*, J. Comp. Phys. **26**, 124 (1973).

[92] D. Bauer, P. Mulser and W.-H. Steeb, *Relativistic Ponderomotive Force, Uphill Acceleration, and Transmission to Chaos*, Phys. Rev. Lett. **75**, 4622 (1995).

[93] B. Quesnel and P. Mora, *Theory and simulation of the interaction of ultraintense laser pulses with electrons in vacuum*, Phys. Rev. E **58**, 3719 (1998).

[94] S. C. Rae and K. Burnett, *Possible production of cold plasmas through optical-field-induced ionization*, Phys. Rev. A **46**, 2077 (1992).

[95] B. M. Penetrate and J. N. Bardsley, *Residual energy in plasmas produced by intense subpicosecond lasers*, Phys. Rev. A **43**, 43 (1991).

[96] L. Schlessinger and J. Wright, *Inverse-bremsstrahlung absorption rate in intense laser field*, Phys. Rev. A **20**, 1934 (1979).

[97] T. P. Hughes, *Plasma and Laser Light* (Adam Hilger, New York, 1975).

[98] Shalom Eliezer, *The Interaction of High-Power Lasers with Plasmas* (Institute of Physics Publishing, Bristol, 2002).

[99] N. G. Denisov, *On a singularity of the field of an electromagnetic wave propagated in an inhomogenous plasma*, Sov. Phys. JETP Lett. **4**, 544 (1957).

[100] V. L. Ginzburg, *The Properties of Electromagnetic Waves in Plasma* (Pergamon, New York, 1964).

[101] J. P. Freidberg, R. W. Mitchel, R. L. Morse and L. I. Rudsinski, *Resonant Absorption of Laser Light by Plasma Targets*, Phys. Rev. Lett. **28**, 795 (1971).

[102] O. Willi, *Lecture Notes*, (2006), (unpublished).

[103] F. N. Beg, A. R. Bell, A. E. Dangor, C. N. Danson, A. P. Fews, M. E. Glinski, B. A. Hammel, P. Lee, P. A. Norreys and M. Tatarakis, *A study of picosecond laser-solid interactions up to* 10^{19} W/cm^2, Physics of Plasmas **4**, 447 (1997).

[104] J. Osterholz, F. Brandl, T. Fischer, D. Hemmers, M. Cerchez, G. Pretzler, O. Willi and S. J. Rose, *Production of Dense Plasmas with sub-10-fs Laser Pulses*, Phys. Rev. Lett. **96**, 085002 (2006).

[105] S. C. Wilks, W. L. Kruer, M. Tabak and A. B. Langdon, *Absorption of ultra-intense laser pulses*, Phys. Rev. Lett. **69**, 1383 (1992).

[106] G. Malka and J. L. Miquel, *Experimental Confirmation of Ponderomotive-Force Electrons Produced by an Ultrarelativistic Laser Pulse on a Solid Target*, Phys. Rev. Lett. **77**, 75 (1996).

[107] S. C. Wilks, *Simulations of ultraintense laser-plasma interactions*, Phys. Fluids B **5**, 2603 (1993).

[108] R. B. Miller, *An Introduction to the Physics of Intense Charged Particle Beams* (Plenum Press, New York, 1982).

[109] R. A. Fonseca, L. O. Silva, J. W. Tonge, W. B. Mori and J. M. Dawson, *Three-dimensional Weibel instability in astrophysical scenarios*, Physics of Plasmas **10**, 1979 (2003).

[110] M. V. Medvedev and A. Loeb, *Generation of Magnetic Fields in the Relativistic Shock of Gamma-Ray Burst Sources*, The Astrophysical Journal **526**, 697 (1999).

[111] L. O. Silva, R. A. Fonseca, J. W. Tonge, J. M. Dawson, W. B. Mori and M. V. Medvedev, *Interpretating plasma shells: near-equipartition magnetic field generation and nonthermal particle acceleration*, The Astrophysical Journal **596**, L121 (2003).

[112] M. V. Medvedev, L. O. Silva, M. Fiore, R. A. Fonseca and W. B. Mori, *Generation of magnetic fields in cosmological shocks*, Journal of the Korean Astronomical Society **37**, 533 (2004).

[113] Y. Sentoku, K. Mima, S. Kojima and H. Ruhl, *Magnetic instability by the relativistic laser pulses in overdense plasmas*, Physics of Plasmas **7**, 689 (2000).

[114] B. F. Lasinski, A. B. Langdon, S. P. Hatchett, M. H. Key and M. Tabak, *Particle-in-cell simulations of ultra intense laser pulses propagating through overdense plasma for fast-ignitor and radiography applications*, Physics of Plasmas **6**, 2041 (1999).

[115] L. Gremillet, G. Bonnaud and F. Amiranoff, *Filamented transport of laser-generated relativistic electrons penetrating a solid target*, Physics of Plasmas **9**, 941 (2002).

[116] J. R. Davies, A. R. Bell and M. Tatarakis, *Magnetic focusing and trapping of high-intensity laser generated fast electrons at the rear side of solid targets*, Phys. Rev. E **59**, 6032 (1998).

[117] F. Califano, F. Pegoraro and S. V. Bulanov, *Spatial structure and time evolution of the Weibel instability in colissionless inhomogeneous plasmas*, Phys. Rev. E **56**, 963 (1997).

[118] F. Califano, F. Pegoraro, S. V. Bulanov and A. Mangeney, *Kinetic saturation of the Weibel instability in a collisionless plasma*, Phys. Rev. E **57**, 7048 (1998).

[119] Y. Sentoku, K. Mima, P. Kaw and K. Nishikawa, *Anomalous resistivity resulting from MeV-electron transport in overdense plasma*, Phys. Rev. Lett. **90**, 155001 (2003).

[120] Y. B. Fainberg, V. D. Shapiro and V. I. Shevchenko, *Nonlinear theory of interaction between a monochromatic beam of relativistic electrons and a plasma*, Sov. Phys. JETP Lett. **30**, 528 (1970).

[121] A. Bret, M.-C. Firpo and C. Deutsch, *Electromagnetic instabilities for relativistic beam-plasma interaction in whole k space: Nonrelativistic beam and plasma temperature effects*, Phys. Rev. E **72**, 16403 (2005).

[122] L. O. Silva and R. A. Fonseca, *On the role of purely transverse Weibel instability in fast ignitor scenarios*, Physics of Plasmas **9**, 2458 (2002).

[123] S. D. Baton, J. J. Santos, F. Amiranoff, H. Popescu, L. Gremillet, M. Koenig, E. Martinolli, O. Guilbaud, C. Rousseaux, M. Rabec Le Gloahec, T. Hall, D. Batani, E. Perelli, F. Scianitti and T. E. Cowan, *Evidence of Ultrashort Electron Bunches in Laser-Plasma Interactions at Relativistic Intensities*, Phys. Rev. Lett. **91**, 105001 (2003).

[124] U. Happek, A. J. Sievers and E. B. Blum, *Observation of coherent transition radiation*, Phys. Rev. Lett. **67**, 2962 (1991).

[125] P. Kung, H.-C. Lihn, Wiedemann H. and D. Bocek, *Generation and Measurement of 50-fs (rms) Electron Pulses*, Phys. Rev. Lett. **73**, 967 (1994).

[126] V. L. Ginzberg and I. M. Frank, *Radiation of a uniformly moving electron due to its transition from one medium into another*, Sov. Phys. JETP Lett. **16**, 15 (1946).

[127] C. B. Schroeder, E. Esarey, J. van Tilborg and W. P. Leemans, *Theory of coherent transition radiation generated at a plasma-vacuum interface*, Phys. Rev. E **69**, 016501 (2004).

[128] M. L. Ter-Mikaelian, *High-Energy Electromagnetic Processes in Condensed Media* (Wiley-Interscience, New York, 1972).

[129] L. Levi, *Applied Optics* (John Wiley and Sons, New York, 1968).

[130] M. Born and E. Wolf, *Principles of Optics* (Cambridge University Press, Cambridge, 1999).

[131] *Handbook of Optical Systems*, edited by H. Gross (Wiley-VCH, Weinheim, 2005), Vol. Volume 1.

[132] W. Singer, M. Totzeck and H. Gross, in *Handbook of Optical Systems*, edited by H. Gross (Wiley-VCH, Weinheim, 2005), Vol. Volume 2.

[133] F. Cattani, A. Kim, D. Anderson and M. Lisak, *Threshold of induced transparency in the relativistic interaction of an electromagnetic wave with overdense plasmas*, Phys. Rev. E **62**, 1234 (2000).

[134] B. Shen and Z. Xu, *Transparency of an overdense plasma layer*, Phys. Rev. E **64**, 56406 (2001).

[135] G. S. Settles, *Schlieren and Shadowgraph Techniques* (Springer, Berlin, 2001).

[136] S. Semushin and V. Malka, *High density gas jet nozzle design for laser target production*, Review of Scientific Instruments **72**, 2961 (2001).

[137] V. Malka, C. Coulaud, J. P. Geindre, V. Lopez, Z. Najmudin, D. Neely and F. Amiranoff, *Characterization of neutral density profile in a widely range of pressure of cylindrical pulsed gas jets*, Review of Scientific Instruments **71**, 2329 (2000).

[138] R. Jung, J. Osterholz, O. Willi, M. Galimberti, L. Gizzi, M. Borghesi, S. Kar, C. A. Ceccetti, R. Heathcote and D. Neely, Annual Report RAL-TR-2005-025, Central Laser Facility, Rutherford Appleton Laboratory (unpublished).

[139] T. Hosokai, K. Kinoshita, T. Watanabe, K. Yoshii, T. Ueda, A. Zhidokov and M. Uesaka, *Supersonic gas jet target for generation of relativistic electrons with 12 TW - 50 fs laser pulse*, Proceedings of EPAC 981 (2002).

[140] D. Rist, *Dynamik realer Gase* (Springer, Berlin, 1996).

[141] M. J. Zucrow, *Gas dynamics* (John Wiley and Sons, New York, 1976).

[142] www.parker.com.

[143] R. Benattar, C. Popovics and R. Sigel, *Polarized light interferometer for laser fusion studies*, Review of Scientific Instruments **50**, 1583 (1979).

[144] J.-C. Diels and W. Rudolph, *Ultrashort Laser Pulse Phenomena: Fundamentals, Techniques, and Applications on a Femtosecond Time Scale, Optics and Photonics Series*, 2nd ed. (Elsevier, New York, 2006).

[145] G. Pretzler, *Höchstleistungs-Kurzpulslaser*, (2000), lecture notes (unpublished).

[146] A. E. Siegman, *Lasers* (University Science Book, Sausalito, 1986).

[147] R. Szipöcs, Kárpát, Ch. Spielmann and F. Krausz, *Chirped multilayer coatings for broadband dispersion control in femtosecond lasers*, Optics Letters **19**, 201 (1994).

[148] A. Stingl, M. Lenzner, Ch. Spielmann, F. Krausz and R. Szipöcs, *Sub-10-fs mirror-dispersion-controlled Ti:sapphire laser*, Optics Letters **20**, 602 (1994).

[149] M. Nisoli, S. DeSilvestri and O. Svelto, *Generation of high energy 10 fs pulses by a new pulse compression technique*, Applied Physics Letters **68**, 2793 (1996).

[150] M. Nisoli, S. Stagira, S. DeSilvestri, O. Svelto, S. Sartania, Z. Cheng, M. Lenzner, Ch. Spielmann and F. Krausz, *A novel high energy pulse compression system: Generation of multigigawatt sub-5-fs pulses*, Applied Physics B - Lasers and Optics **65**, 189 (1997).

[151] F. Brandl, Dissertation, Universität Düsseldorf, 2006.

[152] M. Cerchez, R. Jung, J. Osterholz, T. Toncian, O. Willi, P. Mulser and H. Ruhl, *Absorption of ultrashort laser pulses in strongly overdense targets*, (2007), (submitted to Phys. Rev. Lett.).

[153] P. Tournois, *Acousto-optic programmable dispersive filter for adaptive compensation of group delay time dispersion in laser systems*, Opt. Commun. **140**, 245 (1997).

[154] A. E. Siegman, in *Laser resonators and coherent optics: Modeling, technology, and applications; Proceedings of SPIE*, Vol. Volume 1868 of *Lasers and Masers*, SPIE (Society of Photo-Optical Instrumentation Engineers, Los Angeles, 1993), S. 2.

[155] Ya. B. Zel'dovich and Yu. P. Raizer, in *Physics of Shock Waves and High-Temperature Hydrodynamic Phenomena*, edited by W. D. Hayes and R. F. Probstein (Dover Publications, New York, 2002).

[156] NIST Database for electron-impact cross-sections for ionization and excitation, www-amdis.iaea.org.

[157] A. Kemp, R. E. W. Pfund and J. Meyer-ter-Vehn, *Modeling ultrafast laser-driven ionization dynamics with Monte Carlo collisional particle-in-cell simulations*, Physics of Plasmas **11**, 5648 (2004).

[158] R. E. W. Pfund, Dissertation, TU Berlin, Berlin, 1999.

[159] P. Monot, T. Auguste, L. A. Lompré, G. Mainfray and C. Manus, *Focusing limits of a terawatt laser in an underdense plasma*, Journal of the Optical Society of America B **9**, 1579 (1992).

[160] E. E. Fill, *Focusing limits of ultrashort laser pulses: analytical theory*, Journal of the Optical Society of America B **11**, 2241 (1994).

[161] Jan Posthumus, *Molecules and Clusters in Intense Laser Fields* (Cambridge University Press, New York, 2001).

[162] T. Ditmire, *Interaction of intense laser pulses with atomic clusters*, Phys. Rev. A **53**, 3379 (1996).

[163] M. Omieczynski, Diplomarbeit, Universität Düsseldorf, 2007.

[164] S. P. Le Blanc, R. Sauerbrey, S. C. Rae and K. Burnett, *Spectral blue shifting of a femtosecond laser pulse propagating through a high pressure gas*, Journal of the Optical Society of America B **10**, 1801 (1993).

[165] C. Birdsal and A. B. Langdon, *Plasma Physics via Computer Simulation* (Adam Hilger, Bristol, 1991).

[166] S. P. Le Blanc and R. Sauerbrey, *Spectral, temporal, and spatial characteristics of plasma-induced spectral blue-shifting and its application to femtosecond pulse measurement*, Journal of the Optical Society of America B **13**, 72 (1996).

[167] C. N. Danson, J. Collier, D. Neely, L. J. Barazanti, A. Damerell, R.B. Edwards, M. H. R. Hutchionson, M. H. Key, P. A. Norreys, D. A. Pepler, I. N. Ross, P. F. Taday, W. T. Toner, M. Trentelman, F. N. Walsh, T. B. Winstone and R. W. W. Wyatt, *Well characterized* 10^{19} *W/cm*^{2} *operation of VULCAN - an ultra-high power Nd:glass laser*, Journal of Modern Optics **45**, 1653 (1998).

[168] C. N. Danson, R. Allott, G. Booth, J. Collier, C. Edwards, P. S. Flintoff, S. J. Hawkes, M. H. R. Hutchionson, C. Hernandez-Gomez, J. Leach, D. Neely, P. A. Norreys, M. Notley, D. A. Pepler, I. N. Ross, J. A. Walczak and T. B. Winstone, *Generation of focused intensities of* 5×10^{19} *Wcm*$^{-2}$, Laser and Particle Beams **17**, 341 (1999).

[169] S. Hawkes, J. Collier, C. N. Danson and C. Hernandez-Gomez, Annual Report RAL-TR-2004-025, Central Laser Facility, Rutherford Appleton Laboratory (unpublished).

[170] S. J. Hawkes, C. Hernandez-Gomez and D. A. Pepler, Annual Report RAL-TR-2005-025, Central Laser Facility, Rutherford Appleton Laboratory (unpublished).

[171] C. Hernandez-Gomez, J. Collier and J. Smith, Annual Report RAL-TR-2002-013, Central Laser Facility, Rutherford Appleton Laboratory (unpublished).

[172] C. Hernandez-Gomez, Coll, M. Csatari and J. Smith, Annual Report RAL-TR-2002-013, Central Laser Facility, Rutherford Appleton Laboratory (unpublished).

[173] C. Hernandez-Gomez, I. O. Musgrave, S. J. Hawkes, B. Fell, T. B. Winstone, R. J. Clarke and C. N. Danson, Annual Report RAL-TR-2005-025, Central Laser Facility, Rutherford Appleton Laboratory (unpublished).

[174] J. Collier, C. Hooker, S. Hawkes and C. Edwards, Annual Report RAL-TR-2002-013, Central Laser Facility, Rutherford Appleton Laboratory (unpublished).

[175] C. N. Danson, P. A. Brummitt, R. J. Clarke, J. Collier, B. Bell, A. J. Frackiewicz, S. Hancock, S. Hawkes, C. Hernandez-Gomez, P. Holligan, M. H. R. Hutchionson, A. Kidd, W. J. Lester, I. O. Musgrave, D. Neely, D. R. Neville, P. A. Norreys, D. A. Pepler, C. J. Reason, W. Shaikh, T. B. Winstone, R. W. W. Wyatt and B. E. Wyborn, *Vulcan Petawatt - an ultra-high intensity interaction facility*, Nucl. Fusion **44**, 239 (2004).

[176] C. N. Danson, P. A. Brummitt, R. J. Clarke, J. Collier, B. Fell, A. J. Frackiewicz, S. Hawkes, C. Hernandez-Gomez, P. Holligan, M. H. R. Hutchionson, A. Kidd, W. J. Lester, I. O. Musgrave, D. Neely, D. R. Neville, P. A. Norreys, D. A. Pepler, C. J. Reason, W. Shaikh, T. B. Winstone, R. W. W. Wyatt and B. E. Wyborn, *Vulcan petawatt: Design, operation and interactions at* 5×10^{20} W/cm^2, Laser and Particle Beams **23**, 87 (2005).

[177] P. A. Norreys, K. L. Lancaster, C. D. Murphy, H. Habara, S. Karsch, R. J. Clarke, J. Collier, R. Heathcote, C. Hernandez-Gomez, S. J. Hawkes, D. Neely, M. H. R. Hutchionson, R. G. Evans, M. Borghesi, L. Romagnani, M. Zepf, K. Akli, J. A. King, B. Zhang, R. R. Freeman, A. J. MacKinnon, S. P. Hatchett, P. Patel, R. Snavely, M. H. Key, A. Nikroo, R. Stephens, C. Stoeckl, K. A. Tanaka, T. Norimatsu, Y. Toyama and R. Kodama, *Integrated implosion/heating studies for advanced fast ignition*, Physics of Plasmas **11**, 2746 (2004).

[178] T. Afshar-rad, M. Desselberger, M. Dunne, Edwards J., J. M. Foster, D. Hoarty, M. W. Jones, S. J. Rose, P. A. Rosen, R. Taylor and O. Willi, *Supersonic Propagation of an Ionization Front in Low Density Foam Targets Driven by Thermal Radiation*, Phys. Rev. Lett. **73**, 74 (1994).

[179] M. Desselberger, M. W. Jones, Edwards J., M. Dunne and O. Willi, *Use of X-Ray Preheated Foam Layers to Reduce Beam Structure Imprint in Laser-Driven Targets*, Phys. Rev. Lett. **74**, 2961 (1995).

[180] V. Ginzburg and V. Tsytovich, *Transition Radiation and Transition Scattering* (Hilger, Bristol, 1990).

[181] Y. Nomura, L. Veisz, K. Schmid, T. Wittmann, J. Wild and F. Krausz, *Time-resolved refectivity measurements on a plasma mirror with few-cycle laser pulses*, New Journal of Physics **9**, 9 (2007).

[182] I. Watts, M. Zepf, E. Clark, M. Santala, M. Tatarakis, K. Krushelnick, A. E. Dangor, A. C. Machacek, J. S. Wark, P. A. Norreys, R. J. Clarke,

R. Allott, C. N. Danson and D. Neely, Annual Report RAL-TR-1999-062, Central Laser Facility, Rutherford Appleton Laboratory (unpublished).

[183] C. Hernandez-Gomez, D. Canny, I. O. Musgrave and J. Collier, Annual Report RAL-TR-2005-025, Central Laser Facility, Rutherford Appleton Laboratory (unpublished).

[184] J. Lazarus, P. M. Nilson, Smith R. A., A. S. Moore, E. L. Clark, R. T. Eagleton, R.D. Edwards, E. T. Gumbell and R. J. Clarke, Annual Report RAL-TR-2005-025, Central Laser Facility, Rutherford Appleton Laboratory (unpublished).

[185] I. O. Musgrave, C. Hernandez-Gomez, D. Canny, R. Heathcote, R. J. Clarke, J. Collier and Bandyopadhyay, Annual Report RAL-TR-2005-025, Central Laser Facility, Rutherford Appleton Laboratory (unpublished).

[186] J. Castor, *Radiation hydrodynamics* (Cambridge University Press, Cambridge, 2006).

[187] R. G. Watt, J. Duke, C. J. Fontes, P. L. Gobby, R. V. Hollis, R. A. Kopp, R. J. Mason, D. C. Wilson, C. P. Verdon, T. R. Boehly, J. P. Knauer, D. D. Meyerhofer, V. Smalyuk, R. P. J. Town, A. Iwase and O. Willi, *Laser Imprint Reduction Using a Low-Density Foam Buffer as a Thermal Smoothing Layer at 351-nm Wavelength*, Phys. Rev. Lett. **81**, 4644 (1998).

[188] M. Dunne, M. Borghesi, A. Iwase, M. W. Jones, R. Taylor, O. Willi, G. Gibson, S. R. Goldman, J. Mack and R. G. Watt, *Evaluation of a Foam Buffer Target Design for Spatially Uniform Ablation of Laser-Irradiated Plasmas*, Phys. Rev. Lett. **75**, 3858 (1995).

[189] D. Hoarty, Dissertation, Imperial College, London, 1997.

[190] J. Osterholz, Priv. Comm.

[191] M. I. K. Santala, M. Zepf, I. Watts, F. N. Beg, E. Clark, M. Tatarakis, K. Krushelnick, A. E. Dangor, T. McCanny, I. Spencer, R. P. Singhal, K. W. D. Ledingham, S. C. Wilks, A. C. Machacek, J. S. Wark, R. Allott, R. J. Clarke and P. A. Norreys, *Effect of the Plasma Density Scale Length on the Direction of Fast Electrons in Relativistic Laser-Solid Interactions*, Phys. Rev. Lett. **84**, 1459 (2000).

[192] T. E. Cowan, A. W. Hunt, T. W. Phillips, S. C. Wilks, M. D. Perry, C. Brown, W. Fountain, S. P. Hatchet, J. Johnson, M. H. Key, T. Parnell, D. M. Pennington, R. A. Snavely and Y. Takahashi, *Photonuclear Fission from High Energy Electrons from Ultraintense Laser-Solid Interactions*, Phys. Rev. Lett. **84**, 903 (1999).

[193] C. Gahn, G. D. Tsakiris, A. Pukhov, J. Meyer-ter-Vehn, G. Pretzler, P. Thirolf, D. Habs and K. J. Witte, *Multi-MeV Electron Beam Generation by Direct Laser Acceleration in High Density Plasma Channels*, Phys. Rev. Lett. **83**, 4772 (1999).

[194] Sheng. Z. M., Y. Sentoku, K. Mima, J. Zhang, W. Yu and J. Meyer-ter-Vehn, *Angular Distributions of Fast Electrons, Ions, and Bremmsstrahlung x/gamma-Rays in Intense Laser Interaction with Solid Targets*, Phys. Rev. Lett. **85**, 5340 (2000).

[195] A. Pukhov, *Three-dimensional electromagnetic relativistic particle-in-cell code VLPL (Virtual Laser Plasma Lab)*, J. Plasma Physics **61**, 425 (1999).

[196] R. G. Evans, L. O. Silva, J. R. Davies and W. B. Mori, Annual Report RAL-TR-2003-018, Central Laser Facility, Rutherford Appleton Laboratory (unpublished).

[197] M. S. Wei, F. N. Beg, E. L. Clark, A. E. Dangor, R. G. Evans, A. Gopal, K. W. D. Ledingham, P. McKenna, P. A. Norreys, M. Tatarakis, M. Zepf and K Krushelnik, *Observations of the filamentation of high-intensity laser-produced electron beams*, Phys. Rev. E **70**, 056412 (2004).

[198] C. Deutsch, H. Furukawa, K. Mima, M. Murakami and K. Nishihara, *Interaction Physics of the Fast Ignitor Concept*, Phys. Rev. Lett. **77**, 2483 (1996).

[199] H. Ruhl, *3D kinetic simulation of super-intense laser-induced anomalous transport*, Plasma Sources Sci. Technol. **11**, A154 (2002).

[200] F. Califano, D. Del Sarto and F. Pegoraro, *Three-Dimensional Magnetic Structures Generated by the Development of the Filamentation (Weibel) Instability in the Relativistic Regime*, Phys. Rev. Lett. **96**, 105008 (2006).

[201] A. Pukhov, *Particle acceleration in relativistic laser channels*, Physics of Plasmas **6**, 2847 (1999).

[202] S. C. Wilks and W. L. Kruer, *Absorption of ultrashort, ultra-intense laser light by solids and overdense plasmas*, IEEE Journal of Quantum Electronics **33**, 1954 (1997).

[203] B. M. Penetrate, J. N. Bardsley, W. M. Wood, C. W. Siders and M. C. Downer, *Ionization-induced frequency shifts in intense femtosecond laser pulses*, J. Phys. B - At. Mol. Opt. Phys. **9**, 2032 (1992).

[204] D. Batani, M. Manclossi, J. J. Santos, V. T. Tikhonchuk, J. Faure, A. Guemnie-Tafo and V. Malka, *Transport of intense laser-produced electron beams in matter*, Plasma Physics and Controlled Fusion **48**, B211 (2006).

[205] R. E. Kidder, *Energy gain of laser-compressed pellets - simple model calculations*, Nucl. Fusion **16**, 405 (1976).

[206] S. P. Hatchett, C. G. Brown, T. E. Cowan, E. A. Henry, J. S. Johnson, M. H. Key, J. A. Koch, A. B. Langdon, B. F. Lasinski, R. W. Lee, A. J. MacKinnon, D. M. Pennington, M. D. Perry, T. W. Phillips, M. Roth, T. C. Sangster, M. S. Singh, R. A. Snavely, M. A. Stoyer, S. C. Wilks and K. Yasuike, *Electron, photon, and ion beams from the relativistic interaction of Petawatt laser pulses with solid targets*, Physics of Plasmas **7**, 2076 (2000).

[207] F. F. Chen, *Introduction to Plasma Physics and Controlled Fusion*, 2nd ed. (Plenum Press, New York, 1984), Vol. 1.

[208] P. Mora and T. M. Antonsen Jr., *Kinetic modeling of intense, short laser pulses propagating in tenuous plasmas*, Physics of Plasmas **4**, 217 (1997).

[209] M. Perry, *Crossing the Petawatt Threshold*, LLNL Science and Technology Review 4 (1996).

[210] A. Baltuska, Th. Udem, M. Uiberacker, M. Hentschel, E. Goulielmakis, Ch. Gohle, R. Holzwarth, V. Yakoviev, A. Scrinzi, T. W. Hänsch and F. Krausz, *Attosecond control of electronic processes by intense light fields*, Nature **421**, 611 (2003).

[211] R. R. Freeman, P. H. Bucksbaum, H. Milchberg, S. Darack, D. Schumacher and M. E. Geusic, *Above-Threshold ionization with Subpicosecond Laser Pulses*, Phys. Rev. Lett. **59**, 1092 (1987).

[212] P. H. Bucksbaum, L. D. Van Woerkom, R. R. Freeman and D. W. Schumacher, *Nonresonant above-threshold ionization by circular polarized subpicosecond pulses*, Phys. Rev. A **41**, 4119 (1990).

[213] C. Kim, G.-H. Kim, J.-U. Kim, I. S. Ko and H. Suk, *Characterizations of symmetry and asymmetry high-density gas jets without Abel inversion*, Review of Scientific Instruments **75**, 2865 (2004).

[214] M. H. Key, M. D. Cable, T. E. Cowan, K. G. Estabrook, B. A. Hammel, S. P. Hatchett, E. A. Henry, D. E. Hinkel, J. D. Kilkenny, J. A. Koch, W. L. Kruer, A. B. Langdon, B. F. Lasinski, R. W. Lee, B. J. MacGowan, A. J. MacKinnon, J. D. Moody, M. J. Moran, A. A. Offenberger, D. M. Pennington, M. D. Perry, T. J. Phillips, T. C. Sangster, M. S. Singh, M. A. Stoyer, M. Tabak, G. L. Tietbohl, M. Tsukamoto, K. Wharton and S. C. Wilks, *Hot electron production and heating by hot electrons in fast ignitor research*, Physics of Plasmas **5**, 1966 (1998).

[215] M. Honda, *Eigenmodes and growth rates of relativistic current filamentation instability in a collisional plasma*, Phys. Rev. E **69**, 16401 (2004).

[216] Christoph Ernst Trump, Dissertation, TU Berlin, 2000.

[217] Michael G. Schätzel, Dissertation, LMU München, 2006.

[218] Tobias Kampfrath, Dissertation, FU Berlin, 2006.

[219] Satyabrata Kar, Dissertation, Queen's University of Belfast, 2005.

Appendix A: Laser Pulse Propagation

In this paragraph, important physical properties of the laser pulse are summarized. In particular, the analytic expressions for an optical lowest-order Gaussian beam propagating in free space (i.e. vacuum) are reviewed. An analytic derivation of the formulas can be found in numerous books and articles covering the physics of lasers and laser beams. The key results summarized here are taken from [146, 144, 154].

One of the most important properties of a laser beam is the intensity that can be obtained in the focus. Generally, the intensity, $\mathcal{I}$, is defined by the amount of optical energy, $\mathcal{E}$, that is deposited during the time Δt into an area, A,

$$\mathcal{I} = \frac{\mathcal{E}}{\Delta t \cdot A}. \tag{1}$$

Following classical electrodynamics, it can be derived via the energy density flow vector, $\vec{S} = \vec{E} \times \vec{H}$ (Poynting vector), of an electro-magnetic wave with the electric and magnetic field components $\vec{E}(t)$ and $\vec{H}(t)$. Using the vacuum speed of light, $c = 1/\sqrt{\epsilon_0 \mu_0}$, where ϵ_0 denotes the dielectric constant of vacuum and μ_0 the magnetic permittivity, the Poynting vector is given by

$$\vec{S} = c^2 \epsilon_0 \cdot \vec{E} \times \vec{B}. \tag{2}$$

Using furthermore the relation $\left|\vec{B}\right| = c^{-1} \left|\vec{E}\right|$ between the electric and the magnetic field strengths of the wave, at a time t the intensity is given by the amplitude of the Poynting vector,

$$\mathcal{I} = \left|\vec{S}\right| = c \cdot \epsilon_0 \cdot E^2, \tag{3}$$

which in the case of linearly polarized light shows a fast oscillatory behaviour. Note that in the case of circular polarized light, it is constant but reduced by a factor of 2. Writing the electric component of the wave with a frequency ω_0 and (potentially time-dependent) phase $\varphi(t)$ in the form

$$\vec{E}(t) = \vec{E_A}(t) \cdot \cos(\omega_0 t + \varphi(t)), \tag{4}$$

the pulse shape in the time domain can be defined by the envelope, $E_A(t)$. In the slowly varying envelope approximation (SVEA), the change of the

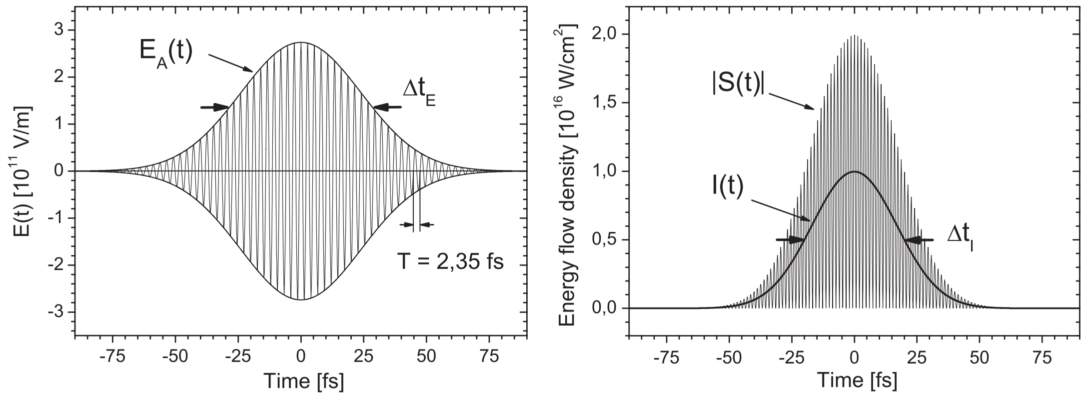

Figure 1: Left: Electric field of a linearly polarized laser pulse with a duration of $\Delta t_I = 40$ fs ($\mathrm{FWHM_I}$) and a peak intensity of $I_0 = 1.0 \cdot 10^{16}$ W/cm^2. The wavelength of the pulse is 800 nm. Right: Intensity in form of the amplitude of the POYNTING vector using the SLOWLY VARIING ENVELOPE APPROXIMATION.

envelope of the electric field in equation (4) is assumed to be slow compared to the oscillation. Then the intensity can be defined by the time-averaged energy flow density. Using $\langle sin(\omega_0 t)\rangle_{\mathrm{cycle}} = 0.5$, the intensity, $I(t)$, as used throughout this work, is given by

$$I(t) = \frac{c \cdot \epsilon_0}{2} \cdot E_A(t)^2. \tag{5}$$

The PEAK INTENSITY, I_0, is given by the maximum of the electric field $E_A(t) = \left|\vec{E}_A(t)\right|$ and is labeled E_0. In practical units, equation (5) reads

$$E_0 = 2.74 \cdot 10^3 \sqrt{I_0\ [\mathrm{W/cm^2}]}\ \ \frac{\mathrm{V}}{\mathrm{m}}. \tag{6}$$

If the SVEA is invalid, one has to use the definition given by equation (3). Note that in this case the peak value of the intensity, $\mathcal{I}_0$, is defined without the factor 1/2 (see also figure 1). The pulse is called a GAUSSIAN PULSE if its shape follows

$$E_A(t) = E_0 \cdot e^{-\left(\frac{t-t_0}{w_t}\right)^2} \tag{7}$$

with a GAUSSIAN WIDTH $w_t = E_0/e$ in the time domain. The Gaussian width is connected to the full width at half maximum of the field strength ($\mathrm{FWHM_E}$) by

$$\Delta t_E = 2 \cdot \sqrt{\ln 2} \cdot w_t. \tag{8}$$

Together with equation (7), the intensity of the laser pulse is given by

$$I(t) = \frac{\epsilon_0 \cdot c}{2} E_0^2 \cdot e^{-8 \cdot \ln 2 \cdot \left(\frac{t-t_0}{\Delta t_E}\right)^2}. \tag{9}$$

Using $\Delta t_E/\Delta t_I = \sqrt{2}$, whereas Δt_I denotes the full width at half maximum of intensity ($\mathrm{FWHM_I}$), one obtains finally

$$I(t) = \frac{\epsilon_0 \cdot c}{2} \cdot E_0^2 \cdot e^{-4 \cdot \ln 2 \cdot \left(\frac{t-t_0}{\Delta t_I}\right)^2}. \tag{10}$$

The relationship between the amplitudes of the electric field, $E(t)$, the envelope, $E_A(t)$, the POYNTING vector, $S(t)$, and the intensity profile, $I(t)$, of an ultra-short laser pulse with a duration Δt_I ($\mathrm{FWHM_I}$) and Δt_E ($\mathrm{FWHM_E}$), respectively, is illustrated in figure 1. Due to the fact that detectors used for pulse measurements are sensitive to the intensity rather than the electric field, the subscript "I" is usually dropped.

Spatially, the electric field of a Gaussian beam transverse to the optical axis follows the profile

$$E(r) = E_0 \cdot e^{-\left(\frac{r}{w}\right)^2}, \tag{11}$$

where r denotes the distance to the optical axis. In analogy to the definition of a Gaussian pulse in the time domain, an important characteristic length in the definition in the spatial domain is the GAUSSIAN BEAM RADIUS, w. It denotes the position off the optical axis where the electric field strength drops to $1/e$ of its maximum value, E_0. Here the intensity decreases accordingly to I_0/e^2. Furthermore, the propagation of a Gaussian beam through free space is fully characterized by its minimum beam radius at the beam waist, w_0, plus the wavelength, λ, of the radiation. Let z be the coordinate parallel to the optical axis of the beam and z_0 the position of the beam waist. The beam radius, w, at any point z is given by

$$w(z) = w_0 \cdot \left[1 + \left(\frac{\lambda(z - z_0)}{\pi w_0^2}\right)^2\right]^{\frac{1}{2}}. \tag{12}$$

Let in the following be $z_0 = 0$. As can be seen, the beam radius increases out of the waist due to diffraction. The radii of the wave fronts follow

$$R(z) = z \cdot \left[1 + \left(\frac{\pi w_0^2}{\lambda z}\right)^2\right], \tag{13}$$

which means that at large distance from the beam waist, the divergence half-angle is given by

$$\Theta = \lim_{z\to\infty} \left(\frac{w(z)}{z}\right) = \frac{1}{\pi} \cdot \frac{\lambda}{w_0}. \tag{14}$$

In the NEAR FIELD, i.e. close to the beam waist, the RAYLEIGH length is defined by the distance where the area covered by the beam (laterally) is twice that at the position of the waist,

$$z_R = \frac{\pi \cdot w_0^2}{\lambda}. \tag{15}$$

This length is of particular importance, because within $\pm z_R$ diffraction effects of optical components are minimized. E.g. if the pulse is focused onto matter, here the plasma formation is expected to be most homogeneous. Moreover, within the Rayleigh length the intensity of the beam is at least 80 % of its maximum [131].
At large distance from the beam waist, however, the $1/e$ spot size in the FAR FIELD is given by

$$w_0 \cdot w(z) \approx \frac{\lambda \cdot z}{\pi}. \tag{16}$$

This leads to the important result that the spot size can be transformed by an (ideal) focusing lens at the position z_L in the beam via

$$w(z_L + f) \approx \frac{\lambda \cdot f}{\pi \cdot w(z_L)}, \tag{17}$$

where f is the focal length of a thin, ideal lens and Δz the distance between the lens and the beam waist of an initially collimated Gaussian beam. Note that as a result of the diffraction limit, the distance between the geometrical and the diffraction limited focus is given by [146]

$$\Delta f = f - \Delta z \approx \frac{z_R^2}{f}. \tag{18}$$

This is illustrated in figure 2. The radius of curvature of the beam just beyond the lens is then equal to the focal length. Using focusing optics with long focal lengths (cm) compared to the Rayleigh length (μm), the focal shift towards the focusing element is usually negligible.

If the diameter, D, of the focusing element is $D = \pi \cdot w(z)$, then about 99% of the incident energy is transferred and the effective diameter of the focal spot is $d = 2 \cdot w(z + f)$. The spot contains 86% of the focused energy of the beam. At larger distance from the focus, the energy distribution can become extremely complex due to diffraction effects of the optical components and can in most cases only be computed numerically [130].

The free space propagation of an ideal Gaussian beam, however, and further transformation by paraxial optical systems are fully characterized by its waist spot size w_0 and the waist location z_0 with a far-field angular spread for $w^2(z)$ given by $\lambda/(\pi w_0)$ [154].

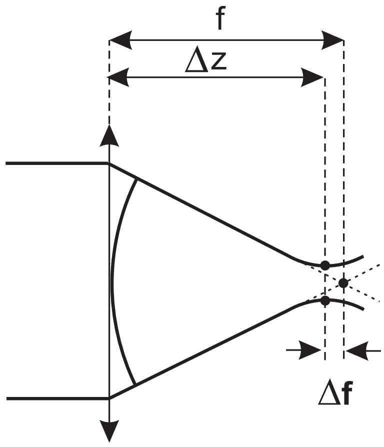

Figure 2: Shift in position between geometrical focus of a Gaussian beam and its beam waist (after [146]).

Note that using real lasers, the quality of the output beam from the laser oscillator will differ from a perfect Gaussian beam, i.e. it usually will have a larger divergence in the far field and a larger focus in the near field. It has been shown that for arbitrary real laser beams[1] the usual rules for Gaussian beam propagation correctly describe the evolution if a correction factor, $M^2 \geq 1$, is introduced [154]. This BEAM QUALITY FACTOR is given by the ratio of the divergence of the real laser beam to the theoretical diffraction limited beam of the same waist size

$$M^2 = \frac{\Theta_{\text{real beam}}}{\Theta_{\text{Gaussian beam}}}, \tag{19}$$

saying that in the far field the angular size of the beam will be $M^2\times$ larger than calculated for a perfect Gaussian beam. The axial variation of the spot size for arbitrary real beams in free space is given by

$$w_M(z) = w_{0M} \cdot \left[1 + \left(\frac{z - z_0}{z_{RM}}\right)^2\right]^{1/2}, \tag{20}$$

which is defined by the real beam spot size, denoted by w_{0M}, and the size of the beam waist given by the Rayleigh length,

$$z_{RM} = \frac{\pi w_{0M}^2}{M^2 \lambda}. \tag{21}$$

The focusability of a real laser beam is characterized by the BEAM PARAMETER PRODUCT,

$$\Theta w_{0M} = M^2 \frac{\lambda}{\pi}, \tag{22}$$

[1]also non-Gaussian, either fully coherent or partially incoherent, single-mode or multi-mode, smooth or distorted real beams in free space!

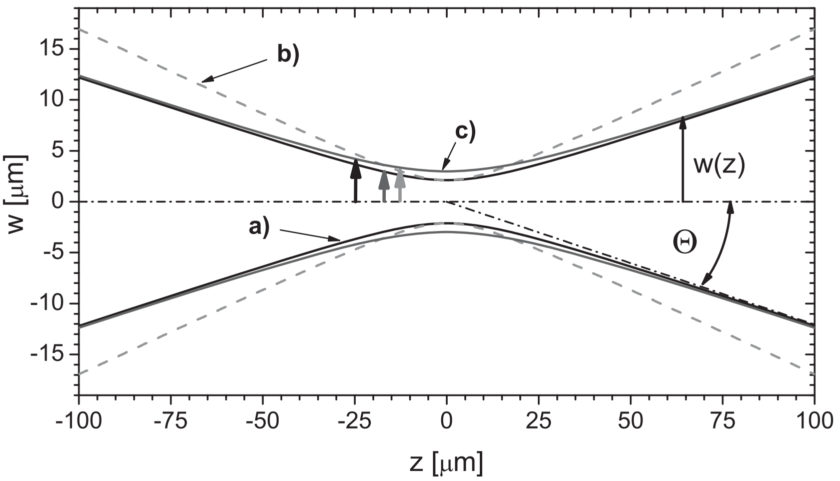

Figure 3: Effect of beam parameter M^2: a) Gaussian beam with $w_0 = 2.12$ μm and $M^2 = 1$, b) with $M^2 = 1.4$, c) $w_{0M} = 2.97$ μm and $M^2 = 1.4$. The Rayleigh length is 17.68 μm, 12.63 μm and 17.68 μm, respectively.

which states that the focus diameter scales with the factor M^2. Thus the beam quality is often called "M^2 times diffraction limited".

In general, the closer a beam is to an ideal Gaussian, the more tightly it can be focused, the larger its Rayleigh length (field of view) and the smaller the diameter of the optics needed to transmit it. In experimental praxis, however, the minimum diameter of the focus that can be achieved is usually limited by numerical apertures clipping the beam and thus raising the M^2-factor due to diffraction.

The (maximum) intensity on axis of a laser pulse with the peak power P_0 is obtained by integrating the spatial intensity profile over the full area of the beam,

$$P_0 = \int_0^\infty I(r) \cdot 2\pi r \, \mathrm{d}r = \int_0^\infty \frac{c_0 \epsilon_0}{2} \cdot E_0^2 \cdot e^{-2\left(\frac{r}{w}\right)^2} \cdot 2\pi r \, \mathrm{d}r = \frac{\pi I_0 w^2}{2} \tag{23}$$

This means that the on-axis intensity is given by

$$I_0(z) = \frac{2}{\pi} \frac{P_0}{w(z)^2}, \tag{24}$$

where equation (12) can to be used to derive $w(z)$. Physically, the maximum intensity depends distinctly on the focusability of the beam, given by the beam waist $w(z)^2$.

Usually the pulse duration, Δt_I, is known (e.g. by separate autocorrelation measurements), so it is more convenient to calculate the intensity as function of calorimetric energy $\mathcal{E}$ measured for a typical shot.

Assuming that the sensitive area, A, of a calorimeter is large enough, i.e. the radius of a circular aperture is at least twice the beam radius at that position, i.e. $r > 2w$, then 99.9% of the pulse energy is collected (and the integration to ∞ is justified). Furthermore assuming that the temporal intensity profile is given by equation (10), one yields

$$\mathcal{E} = \int_{-\infty}^{+\infty} P(t)\ \mathrm{d}t = \frac{\pi w^2}{2} \cdot I_0 \cdot \int_{-\infty}^{+\infty} e^{-4\cdot\ \ln 2 \cdot \left(\frac{t-t_0}{\Delta t_I}\right)^2} \mathrm{d}t. \tag{25}$$

The relation between the peak intensity, I_0, of a temporally and spatially Gaussian pulse with a duration Δt_I and Δx_I ($\mathrm{FWHM_I}$ of intensity) containing the energy $\mathcal{E}$ and a spot size of a radius $w = w(z)$, is given by

$$\mathcal{E} = \pi w^2 \cdot I_0 \cdot \Delta t_I \cdot \frac{\sqrt{\pi}}{4 \cdot \sqrt{\ln 2}}, \tag{26}$$

what is equivalent to

$$I_0 = \ln 2 \cdot \frac{\mathcal{E}}{\Delta t_I \pi \left(\frac{\Delta x_I}{2}\right)^2}. \tag{27}$$

In practical terms this yields

$$I_0 \approx 1.88 \cdot 10^{20} \times \frac{\mathcal{E}[\mathrm{J}]}{\Delta t_I[\mathrm{ps}] \cdot \pi \cdot (w[\mu\mathrm{m}])^2}\ \mathrm{W/cm^2}. \tag{28}$$

This is an important result since formulas (26) - (28) connect the peak intensity of the pulse with standard laboratory measures, i.e. the energy, $\mathcal{E}$, the duration, Δt_I (FWHM of intensity), and the focal diameter, Δx_I and w, respectively.

The E_0/e-radius, w, at focal position can experimentally be verified by imaging the spatial intensity profile of the beam onto a detector such like a linear working CCD. If the profile is Gaussian, an intensity profile according to

$$I(r) = I_0 \cdot e^{-2\cdot\left(\frac{r}{w}\right)^2} \tag{29}$$

is found, yielding the 1/e spot size of the pulse where the intensity drops to 13.5 % of the peak value. In turn, due to $\Delta x_I / \Delta x_E = \sqrt{2}$, the full width at half maximum of intensity ($\mathrm{FWHM_I}$), Δx_I, is given by

$$\Delta x_I = \frac{2 \cdot \sqrt{\ln 2}}{\sqrt{2}} \cdot w \approx 2 \cdot 0.589 \cdot w \tag{30}$$

The beam quality factor, M^2, can be estimated by the factor between the ideal Gaussian spot size and the measured one, respectively. Alternatively, it can experimentally be determined by measuring the divergence half-angle Θ (equation (14)) of the beam.

It is also convenient to specify an average intensity, I_{av}, instead of the peak intensity, I_0. Since any diagnostic trace of the pulse will give a detector response in form of a spatial and temporal intensity profile, respectively, the full widths at half maximum values can be used. Particularly averaging in the time domain and in space has to be considered. Using the fact that 50% of the total power (and energy, respectively) is deposited within a spot size of Δx_I in diameter, the spatial integration yields

$$\langle P\rangle_{\text{spot}} = \int_{\psi=0}^{2\pi}\int_{r=0}^{\Delta x_I/2} I_0 \cdot e^{-2\cdot\left(\frac{r}{w}\right)^2} \cdot r \text{ d}r \text{ d}\psi = 0.5 \cdot P_0 \tag{31}$$

Averaging the intensity over the spot yields (compare equations (23)-(25))

$$\langle I\rangle_{\text{spot}} = \frac{P_0}{\pi \cdot w^2} = \frac{\ln 2}{2} \cdot \frac{P_0}{\pi \cdot \left(\frac{\Delta x_I}{2}\right)^2}. \tag{32}$$

On the other hand, the fraction of the energy that is deposited on a detector during the time interval Δt_I is given by

$$\langle E\rangle_{\Delta t_I} = \int_{-\frac{\Delta t_I}{2}}^{+\frac{\Delta t_I}{2}} P(t) \text{ d}t = 0.761 \cdot \mathcal{E}. \tag{33}$$

Defining the time-averaged power to

$$\langle P\rangle = \frac{\langle E\rangle_{\Delta t_I}}{\Delta t_I} = \frac{0.761 \cdot \mathcal{E}}{\Delta t_I}, \tag{34}$$

the average intensity, that is expected within a spot size Δx_I of a pulse with a duration of Δt_I (both FWHM_I of intensity) is given by

$$I_{\text{av}} = 0.761 \cdot \frac{\mathcal{E}}{\Delta t_I \cdot \pi \cdot w^2} = 0.381 \cdot I_0. \tag{35}$$

In practical terms this reads (using equation (30))

$$I_{\text{av}} = 0.264 \cdot \frac{\mathcal{E} \text{ [J]}}{\Delta t_I \text{ [ps]} \cdot \pi \cdot \left(\frac{\Delta x_I}{2} \text{ [µm]}\right)^2} \cdot 10^{20} \text{ W/cm}^2. \tag{36}$$

Example: (Focal spot produced by Ti:Sa laser which was used in this thesis)

$$w_{0M} = 3,64 \text{ µm} \tag{37}$$
$$\Delta t_I = 10 \text{ fs} \tag{38}$$
$$\mathcal{E} = 60 \text{ µJ} \tag{39}$$
$$I_{\text{av}} = 1.1 \cdot 10^{16} \text{ W/cm}^2 \tag{40}$$
$$I_0 = 2.88 \cdot 10^{16} \text{ W/cm}^2 \tag{41}$$
$$I_0 \cdot \lambda^2 = 1.84 \cdot 10^{16} \text{ W/cm}^2 \cdot \text{µm}^2 \tag{42}$$

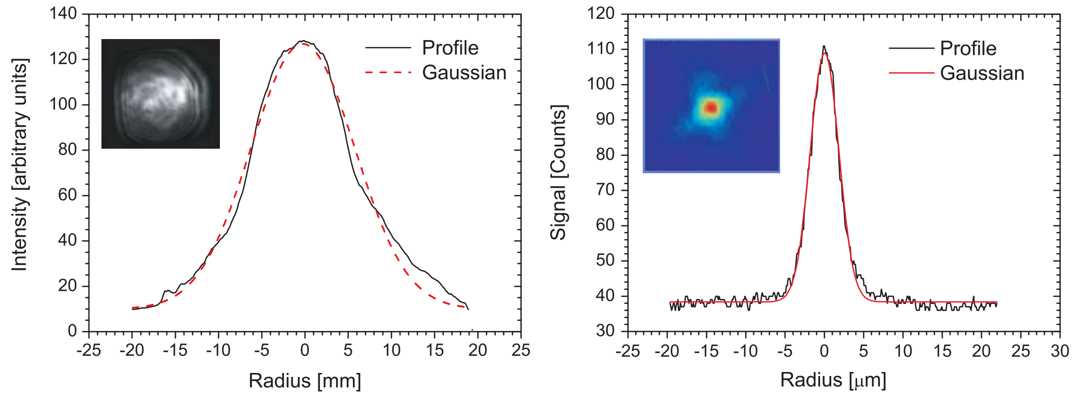

Figure 4: Left: Beam profile in front of the focusing parabola using the Ti:Sa laser at full power. Right: ASE profile at focal position. The parameters of the fits are: $w_0 = 12.04$ mm on parabola and $w_0 = 3.64$ μm at focal position. The insets show images of the beam obtained with film and with the focus diagnostic (8 bit CCD camera).

To define an effective f-number of the focusing optic, the beam size on the focusing element (parabola), $w(f)$, and the 99%-criterion for the energy transferred can be used, particularly

$$D = \pi \cdot w(f), \quad (f/\sharp)_{\mathrm{eff}} = f/D. \tag{43}$$

In the experiment performed to study the propagation of an ionization front in gaseous targets (chapter 6), an effective f-number of $(f/\sharp)_{\mathrm{eff}} = 3.15$ was used. The effective focal length of the parabola was $f = 119$ mm. A beam radius of $w(f) = 12.04$ mm was measured on the parabola using film.

For a volumetric description of the focus, however, not only the lateral but also the longitudinal dimension has to be considered. This is of fundamental importance in the case of gas targets, since a plasma is produced at a distance from the vacuum focus of several times of the Rayleigh length. Here the depth of focus (determined by the Rayleigh length and the beam quality parameter, M^2, respectively) defines the interaction volume. To describe the spatial variation of laser intensity in the region of the focus, first the axial intensity distribution is needed, which is given by

$$I(z) = I_0 \cdot \left(1 + \left(\frac{\lambda z M^2}{\pi w_{0M}^2}\right)^2\right)^{-1}. \tag{44}$$

The transverse profile is given by equation (29). Note that the beam radius, w, is also a function of z (equation (12) and (20), respectively). Together, the intensity is given by

$$I(r,z) = I_0 \cdot \left[1 + \left(\frac{\lambda z M^2}{\pi w_{0M}^2}\right)^2\right]^{-1} \cdot \exp\left[\frac{-2r^2}{w_{0M}^2 \cdot \left(1 + \left(\frac{\lambda z M^2}{\pi w_{0M}^2}\right)^2\right)}\right]. \tag{45}$$

The average ionization state of the target gas depends on the local laser intensity. Spatially, higher ionization states occur closer to the center of the beam waist. Hence different ionization states of the material will generally occur in different focal volumes. A method to quantify these volumes is to relate the iso-surfaces of intensity to the thresholds given by ionization theory such as BSI. The volumes have a double-blackjack shape which are extended with respect to the optical axis and symmetrically centered around the geometric focus (refer for example to figure 2.2). To determine the volume, however, the 3-dimensional intensity distribution given equation (45) with $r = \sqrt{x^2 + y^2}$ and Rayleigh length (equation (21)) can be used. Assuming that $z_0 = 0$, the focal volume where the intensity $I(r,z)$ is above a certain value I_i is given by [161]

$$V = \int \left|\pi r^2\right| \mathrm{d}z = \int \pi w_{0M}^2 \left[1 + \left(\frac{z}{z_{RM}}\right)^2\right] \cdot \ln\left(\frac{I_0}{I_i}\left[1 + \left(\frac{z}{z_{RM}}\right)^2\right]^{-1}\right) \mathrm{d}z \tag{46}$$

The integration limits are given by $\pm z(r = 0)$, or

$$z = z_{RM}\sqrt{\frac{I_0}{I_i} - 1} \quad (I > I_I) \tag{47}$$

Evaluating the integral yields

$$V = \frac{\pi w_{0M}^2 z_{RM}}{M^2}\left(\frac{4}{3}\beta + \frac{2}{9}\beta^3 - \frac{4}{3}\arctan\beta\right), \quad \beta = \sqrt{\frac{I_0 - I_i}{I_i}}. \tag{48}$$

The result is particularly important in order to determine the fraction of energy that is used for ionization. If the beam waist, w_{0M}, the beam quality factor M^2 and the wavelength are known, e.g. by scanning the beam caustic in the near field of the focus, the interaction volume can be obtained analytically using equation (48) and (21).

Appendix B: Table of ionization thresholds predicted by BSI-theory

The following table shows ionization thresholds predicted by BSI-theory for the gases used in the experiment (equation (2.9)).

Ionization process	*Ionisation potenzial* [eV]	*Threshold* [W/cm^2]
$H \rightarrow H^+$	13.6	$1.4 \cdot 10^{14}$
$He \rightarrow He^+$	24.6	$1.5 \cdot 10^{15}$
$He^+ \rightarrow He^{2+}$	54.4	$8.8 \cdot 10^{15}$
$Ne \rightarrow Ne^+$	21.6	$8.7 \cdot 10^{14}$
$Ne^+ \rightarrow Ne^{2+}$	41.0	$2.8 \cdot 10^{15}$
$Ne^{2+} \rightarrow Ne^{3+}$	63.5	$7.2 \cdot 10^{15}$
$Ne^{3+} \rightarrow Ne^{4+}$	97.1	$2.2 \cdot 10^{16}$
$Ne^{4+} \rightarrow Ne^{5+}$	126.2	$4.1 \cdot 10^{16}$
$Ne^{5+} \rightarrow Ne^{6+}$	157.9	$6.9 \cdot 10^{16}$
$Ar \rightarrow Ar^+$	15.8	$2.5 \cdot 10^{14}$
$Ar^+ \rightarrow Ar^{2+}$	27.6	$5.8 \cdot 10^{14}$
$Ar^{2+} \rightarrow Ar^{3+}$	40.7	$1.2 \cdot 10^{15}$
$Ar^{3+} \rightarrow Ar^{4+}$	59.8	$3.2 \cdot 10^{15}$
$Ar^{4+} \rightarrow Ar^{5+}$	75.0	$5.1 \cdot 10^{15}$
$Ar^{5+} \rightarrow Ar^{6+}$	91.0	$7.6 \cdot 10^{15}$
$Ar^{6+} \rightarrow Ar^{7+}$	124.3	$1.9 \cdot 10^{16}$
$Ar^{7+} \rightarrow Ar^{8+}$	143.5	$2.6 \cdot 10^{16}$
$N \rightarrow N^+$	14.5	$1.8 \cdot 10^{14}$
$N^+ \rightarrow N^{2+}$	29.6	$7.7 \cdot 10^{14}$
$N^{2+} \rightarrow N^{3+}$	47.4	$2.3 \cdot 10^{15}$
$N^{3+} \rightarrow N^{4+}$	77.5	$9.0 \cdot 10^{15}$
$N^{4+} \rightarrow N^{5+}$	97.9	$1.5 \cdot 10^{16}$
$N^{5+} \rightarrow N^{6+}$	552.1	$1.0 \cdot 10^{19}$

Acknowledgement

First of all, I would like to thank Prof. Oswald Willi for his supervision of this thesis, his never-ending encouragement and infectious enthusiasm. I also would like to thank Prof. Georg Pretzler for thousands of very fruitful discussions. I grateful acknowledge the support provided by Prof. Hartmut Ruhl and Prof. Alexander Pukhov on which the numerical simulations in this thesis are based. I especially would like to thank Prof. Jürgen Uhlenbusch for his mentorial support during the years since I entered the Institute for Laser and Plasma Physics. I would also like to thank Helmut Kempkens for his support and friendship.

My colleagues at the institute helped me greatly, in particular Toma and Monika Toncian, Jens Osterholz, Andreas Pistelok and Manfred Tamminga. A lot of ideas are based on discussions with colleagues from the theoretical group, in particular Julia Schweitzer, Christoph Karle and Sergey Kiselev. A special thanks to László Veisz and his support performing the FLUENT simulations. Nevertheless, this work would not have been possible without the help of Manfred Rosemann and his team, Christoph Bolten and Helmut Borrmann. Especially their support in technical issues is acknowledged. I would like to thank Renate ter Horst and Claudia Dingle for their abundant support and always encouraging help.

I would like to thank the staff of the Central Laser Facility for their support during the experiments at the VULCAN laser. In particular David Neely, Rob Clarke, Robert Heathcote, Margaret Notley, Sujit Bandyopadhyay and Martin Tolley. A special thank to David Hoarty for a great time during the experiments at the HELEN laser at AWE Aldermaston.

I would like to particularly thank Marco Borghesi for all the support and being a great teacher. And of course I would like to thank a lot all the colleagues from abroad for having a great time together doing experiments at Rutherford Appleton Laboratory and elsewhere. In particular Satyabrata Kar, Carlo Alberto Cecchetti and Marco Galimerti.

I grateful acknowledge the funding of this work provided by the Düsseldorf Entrepreneurs Foundation.

Finally I would like to thank my parents and friends for their infinite supply of support and understanding.

List of publications

Published and submitted papers

- R. Jung, J. Osterholz, K. Löwenbrück, S. Kiselev, G. Pretzler, A. Pukhov, O. Willi, S. Kar, M. Borghesi, W. Nazarov, S. Karsch, R. Clarke, D. Neely
  Study of electron-beam propagation through preionized dense foam plasmas
  Physical Review Letters 94 (19), 195001, 2005

- R. Fischer, C. H. Keitel, R. Jung, G. Pretzler, O. Willi
  Impact of a static magnetic field on high-order harmonic spectra
  Physical Review A 75, 0334901, 2007

- M. Borghesi, S. Kar, L. Romagnani, T. Toncian, P. Antici, P. Audebert, E. Brambrink, F. Ceccherini, C. A. Cecchetti, J. Fuchs, M. Galimberti, L. A. Gizzi, T. Grismayer, T. Lyseikina, R. Jung, A. Macchi, P. Mora, J. Osterholz, A. Schiavi, O. Willi
  Impulsive electric fields driven by high-intensity laser matter interactions
  Laser and Particle Beams, 25 (1), 161, 2007

- S. Kar, M. Borghesi, C. A. Cecchetti, L. Romagnani, F. Ceccherini, T. V. Liseykina, A. Macchi, R. Jung, J. Osterholz, O. Willi, L. A. Gizzi, A. Schiavi, M. Galimberti and R. Heathcote
  Dynamics of laser charge-displacement channeling in intense laser-plasma interactions
  New Journal of Physics **9**, 402, 2007

- M. Cerchez, R. Jung, J. Osterholz, T. Toncian, O. Willi, P. Mulser and H. Ruhl, *Absorption of ultrashort laser pulses in strongly overdense targets*
  submitted to Phys. Rev. Lett.

Patents

- R. Jung
  Verfahren und System zur reproduzierbaren Positionierung eines Zielobjektes in das Wirkvolumen einer Laserstrahlung
  Deutsche Patentanmeldung, Nummer DE 10 2007 018 140.1

Die hier vorgelegte Dissertation habe ich eigenständig und ohne unerlaubte Hilfe angefertigt. Die Dissertation wurde in der vorgelegten oder in ähnlicher Form noch bei keiner anderen Institution eingereicht. Ich habe bisher keine erfolglosen Promotionsversuche unternommen.

Düsseldorf, den 09.05.2007